Sintering of oxide-supported Pt and Pd nanoparticles in air studied by in situ TEM

Simonsen, Søren Bredmose

Publication date:
2011

Document Version
Publisher's PDF, also known as Version of record

Ph.D. Thesis

Sintering of oxide-supported Pt and Pd nanoparticles in air studied by in situ TEM

Søren Bredmose Simonsen

June 2011

Center for Individual Nanoparticle Functionality
Department of Physics
Technical University of Denmark

Haldor Topsøe A/S

Preface

This thesis is submitted in candidacy of the Ph.D. degree from the Technical University of Denmark (DTU). It represents results obtained during my work at the R&D division, Haldor Topsøe A/S and at the Center for Individual Nanoparticle Functionality (CINF), Department of Physics, Technical University of Denmark. The work was carried out from February 2008 to June 2011 under supervision of Professor Ib Chorkendorff from CINF, Technical University of Denmark, Stig Helveg from Haldor Topsøe A/S and Søren Dahl from CASE, Technical University of Denmark. Financial support was provided by Haldor Topsøe A/S and the Danish Agency for Science, Technology and Innovation through the Industrial Ph.D. Programme. The sample preparation and part of the sample characterization was carried out at Department of Microtechnology and Nanoscience (MC2) in cooperation with Competence Centre for Catalysis at Chalmers University of Technology. My stay and work at Chalmers University was partly financed by Competence Centre for Catalysis and though the MC2 Access Programme. A part of the characterization was also carried out at the Interdisciplinary Nanoscience Center (iNANO), Aarhus University.

For excellent supervision, many great input and fruitful discussions, I would especially like to thank my supervisors Stig Helveg, Søren Dahl and Ib Chorkendorff.

At Haldor Topsøe, I would like to thank all my colleagues for creating a fantastic working environment and for contributing to this project in many of ways. Especially I would like to thank everyone in the Microscopy Department for the conversations, the inspiration and for helping me with the microscopy work. Thanks to Stig Helveg for practical training, for STEM work and for great inspiration throughout the project. Thanks to Sven Ullmann for helping me to solve any sudden problems around the microscopes. Thanks to Sven Ullmann and Chi-Manh Tran for assisting on the SEM-EDS work. Thanks to Jens Sehested for fruitful discussions and input on the data analysis.

At DTU, thanks to Lone Bech and John Larsen for XPS work. Thanks to David Norman McCarthy, Christian Ejersbo Strebel and Anders Ulrik Fregerslev Nierhoff for sample preparation with the cluster source. Thanks to Chris Boothroyd for assisting with STEM elemental mapping. Thanks to Lionel Cervera Gontard for assisting with electron tomography.

At Chalmers University, thanks to Magnus Skoglundh for great collaboration and for taking very good care of me during my stays in Gothenburg. Thanks to Bengt Kasemo and Ann Grant for providing the ideas and basic substrates for my samples. Thanks to Elin Larsson for kind introduction to and help with the sample preparation techniques. Thanks to Laurent Feuz for assisting with ellipsometry. Thanks to Henrik Frederiksen for help with PVD. Thanks to Ulf Södervall for helping me with the practical challenges regarding a fast access to tools in the cleanroom. Thanks to the Department of Applied Physics for kindly lending me a TEM for preliminary sample characterization.

At Aarhus University, thanks to Kristoffer Meinander, Thomas Nørregaard Jensen and Jeppe Vang Lauritsen for AFM work.

Especially thanks to my beloved Anne for supporting me throughout this project.

Søren Bredmose Simonsen
Kgs. Lyngby, June 2011

Abstract

This thesis presents a fundamental study of the sintering of supported nanoparticles in relation to diesel oxidation catalysts. The sintering of supported nanoparticles is an important challenge in relation to this catalyst, as well as many other catalyst systems, and a fundamental understanding of the sintering mechanisms of nanoparticles is important for making improvements to their long term catalytic activity.

Diesel oxidation catalysts are usually composed of noble metal nanoparticles on a complex three-dimensional high surface area oxide. The complex support structure makes it difficult to directly observe dynamical processes such as particle sintering with the present state of the art microscope techniques, and consequently it is difficult to relate experimental observations and theoretical sintering models. To reduce the complexity, the present study uses planar model catalysts. These are composed of Pt, Pd and bimetallic Pt-Pd nanoparticles supported on a flat and homogeneous Al_2O_3 or SiO_2 surface. By using in situ TEM on the planar model catalysts it was possible to directly monitor the detailed dynamical changes of the individual nanoparticles during exposure to oxidizing conditions at elevated temperatures. The time-resolved TEM images are presented and these offer direct insight into the fundamental dynamics of the sintering process at the nano-scale.

For Pt, Pd and bimetallic Pt-Pd nanoparticles it is shown that the sintering process is governed by the Ostwald ripening mechanism in an oxidizing environment. The observations compare well with predictions from mean-field kinetic models for ripening, but deviations are revealed for the time-evolution for the individual nanoparticles. A better description of the individual nanoparticle ripening is obtained by kinetic models that include local correlations between neighbouring nanoparticles in the atom-exchange process. The sintering process was also presented statistically by particle size distributions extracted from the TEM images. The statistical data agreed only partly with the mean-field kinetic models for ripening, but the deviations could be accounted for by including more detailed information into the models, such as an observed size-dependence of the three-dimensional shape of the supported nanoparticles and the local correlations between the nanoparticles.

Resumé

Denne afhandling præsenterer et grundlæggende studium i sintringen af nanopartikler i relation til dieseloxidationskatalysatorer. Sintring af nanopartikler er en stor udfordring for at opnå en høj aktivitet for denne og for mange andre heterogene katalysatorer, og en grundlæggende forståelse af sintringsmekanismerne er afgørende for at kunne udvikle mere stabile katalysatorer.

En dieseloxidationskatalysator består oftest af nanopartikler af et eller flere ædelmetaller som er distribueret på et oxidisk bæremateriale med et højt overfladeareal og en kompleks tredimensionel struktur. På grund af den komplekse struktur af bæreren kan det være vanskeligt at undersøge dynamiske processer, så som sintring, selv ved hjælp af de bedste mikroskopiteknikker. Blandt andet derfor kan det være udfordrende at opnå eksperimentelle observationer der kan sammenlignes med de teoretiske modeller for sintring. For at reducere kompleksiteten, arbejdes der i dette studium med plane modelkatalysatorer. De består af nanopartikler af Pt, Pd og bimetallisk Pt-Pd på en flad, homogen Al_2O_3- eller SiO_2-overflade. Ved at undersøge de plane modelkatalysatorer med in situ TEM er det muligt direkte og i detalje at observere dynamiske forandringer af de individuelle nanopartikler mens de eksponeres til et oxiderende gasmiljø ved høje temperaturer. De tidsopløste TEM-billeder som præsentes, giver direkte indsigt i de fundamentale dynamikker som på nanoskala karakteriserer sintringsprocessen.

For Pt-, Pd- og for de bimetalliske Pt-Pd-nanopartikler vises det at sintringen i et oxiderende miljø domineres af ”Ostwald ripening”-mekanismen. De eksperimentelle observationer stemmer godt overens med kinetiske middelfeltmodeller for ripening, men afvigelser afsløres også på det individuelle partikelniveau. Det vises at en bedre overensstemmelse kan opnås mellem observationen af de individuelle partikler og de teoretiske modeller hvis lokale påvirkninger mellem nabopartikler integreres i modellerne. Sintringsprocessen præsenteres desuden statistisk ved brug af partikelstørrelsesfordelinger som ekstraheres fra TEM-billederne. Den statistiske repræsentation viser en delvis overensstemmelse med de kinetiske sintringsmodeller, og det vises at der kan gøres rede for afvigelserne ved at integrere en mere detaljeret information i modellerne som f.eks. de lokale korrelationer mellem nabopartikler eller en observeret sammenhæng mellem partiklernes størrelse og form.

List of included publications in relation to this study

Paper I
S.B. Simonsen, I. Chorkendorff, S. Dahl, M. Skoglundh, J. Sehested, S. Helveg, "Direct Observations of Oxygen-induced Platinum Nanoparticle Ripening Studied by In Situ TEM", *J. Am. Chem. Soc.* 132 (2010) 7968

Paper II
S.B. Simonsen, I. Chorkendorff, S. Dahl, M. Skoglundh, J. Sehested, S. Helveg, "Ostwald ripening in a Pt/SiO_2 model catalyst studied by in situ TEM", J. Catal. 281 (2011) 147

Paper III
S.B. Simonsen, I. Chorkendorff, S. Dahl, M. Skoglundh, K. Meinander, T.N. Jensen, J.V. Lauritsen, and S. Helveg, "Effect of particle shape on the ripening of supported Pt nanoparticles", *submitted 2011*

Other publications

A.B. Laursen, K.T. Højholt, L.F. Lundegaard, S.B. Simonsen, S. Helveg. F. Schüth, M. Paul, J.-D. Grunwaldt, S. Kegnæs, C.H. Clausen, K. Egeblad: "Substrate Size-Selective Catalysis with Zeolite-Encapsulated Gold Nanoparticles", *Angew. Chem. Int. Ed.* 49 (2010) 3504

S.B. Simonsen, S. Dahl, E. Johnson, S. Helveg: "Direct Observations of Catalytic Soot Oxidation on a Nano-Scale using Environmental Transmission Electron Microscopy", *SAE Int. J. Mater. Manuf.* 1 (2009) 199

S.B. Simonsen, S. Dahl, E. Johnson, S. Helveg: "Ceria-catalyzed soot oxidation studied by environmental transmission electron microscopy", *J. Catal* 255 (2008) 1

Contents

”An ideal way of distinguishing between crystallite migration and atomic diffusion mechanisms would be to sinter a catalyst while observing it in the electron microscope, using a heated grid holder”

– P. C. Flynn and S. E. Wanke, 1975

1. Introduction

This study addresses the sintering of oxide supported noble metal nanoparticles in relation to the diesel oxidation catalyst, and aims at providing a fundamental understanding which is needed for the future development of more stable diesel oxidation catalysts. Here, a brief introduction is given to the diesel oxidation catalyst and to the related challenge of sintering.

Catalysts for diesel exhaust abatement

The diesel engine has the advantage of a better fuel economy and less carbon dioxide production per driven kilometer compared to the petrol engine [1]. Especially in Europe, there has been much focus on the fuel-efficient diesel vehicles [2], and sales of diesel passenger cars are rising in Europe and in the rest of world [1]. The exhaust after-treatment poses a different task for the diesel vehicles than for petrol engines, where the well-established 3-way catalyst is used [3,4]. Increasingly stricter limits for carbon monoxide (CO), hydrocarbon (HC), nitrogen oxides (NOx) and particulate matter (diesel soot) emissions has led to the development of a whole series of catalytic units: the diesel oxidation catalyst (DOC), the catalyzed diesel particle filter (cDPF), the selective catalytic reduction unit (SCR) and the ammonia slip catalyst (ASC) or lean NOx trap (LNT) [5] (fig 1.1).

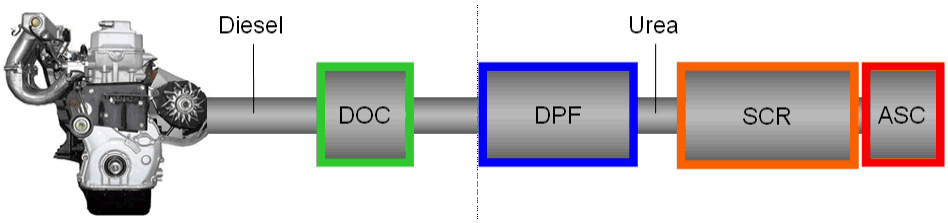

Fig 1.1: Illustration of a diesel engine exhaust after-treatment system composed of several units.

The diesel oxidation catalyst

The purpose of the DOC is to oxidize CO into carbon dioxide (CO_2), to complete the oxidation of remains from the diesel fuel (HC) into CO_2 and H_2O and to oxidize NO into NO_2. The first two reactions directly result in a less toxic exhaust gas. The oxidation of NO does this indirectly because NO_2 is an active reactant for soot oxidation and an optimized ratio between NO and NO_2 enhances the activity of the SCR [5].

The active phase in a DOC is often Pt, which is distributed as nanoparticles to obtain a large reactive surface area and thereby a high catalytic efficiency [6]. The support material for the nanoparticles is typically a high surface area oxide support, such as alumina (ca. 150 m2/g [7]), possibly mixed with a zeolite. The zeolite acts as an absorption buffer for HC when the exhaust temperature is low [5].

The main challenges for the further development of the diesel oxidation catalyst

For the development of modern DOCs, the main challenges are the cost, the catalytic efficiency at low temperatures during cold engine start (well below 200ºC), and the durability of a catalytic coating that may be exposed to high exhaust temperatures at normal engine operation during the lifetime of the vehicle [5]. The exhaust gas temperature is typically below 300ºC for light-duty vehicles [8]. For heavy-duty vehicles it is usually below 400ºC [9] with a maximum temperature of ca. 600ºC [7]. While the oxide support is relatively stable at these conditions, the supported nanoparticles will tend to aggregate into larger structures i.e. the nanoparticles will sinter [10-12].

High temperatures and reactive gas conditions will accelerate the sintering, resulting in a reduction of the active surface area of the nanoparticles, causing an undesirable catalyst deactivation [10-19].

The focus of the present study

The present study addresses the challenge of sintering related to the DOC. The sintering of oxide-supported noble metals in an oxidizing environment is studied experimentally with a main focus on Al_2O_3-supported Pt nanoparticles, while Pt/SiO_2, Pd/Al_2O_3 and bimetallic $Pt\text{-}Pd/Al_2O_3$ are studied for comparison. The sintering of Pt/Al_2O_3 has already been studied intensely for at least four decades [10-18], but even though the previous studies have provided significant insight, full consensus has not been reached regarding some fundamental aspects, such as which theoretical sintering models are applicable and which nano-scale mechanism that dominates the sintering. The aim of the present study is to provide fundamental insight into the sintering, i.e. to convincingly determine the dominating sintering mechanism and to offer a detailed comparison of experimental observations with the theoretical models. In situ transmission electron microscopy (TEM) has proven to be capable of directly monitoring dynamical changes at the nano-scale, such as gas-induced sintering of supported nanoparticles [20-38], and is thereby one of the most promising techniques for obtaining insight into the fundamental dynamics. For this reason in situ TEM was chosen as the primary experimental technique for this study, while post mortem characterization with a variety of techniques such as TEM, STEM and AFM were applied complementary.

2. Theory

This chapter introduces the theory of sintering and transmission electron microscopy in relation to the present study.

2.1. Sintering

Sintering in heterogeneous catalysis generally refers to a deactivation process where the active surface area of metal nanoparticles is reduced due to particle growth [12]. The supported nanoparticles inevitably tend to aggregate into larger structures due to their excess surface free energy [10-18]. The high temperature and reactive gas conditions encountered during catalysis can accelerate the sintering, causing the undesired catalyst deactivation. The sintering of supported nanoparticles is typically attributed to mass transport mechanisms involving particle or atom migration [10-18].

The particle migration mechanism refers the migration of entire nanoparticles and subsequent coalescence between the nanoparticles [39] (fig. 2.1a). The migration of the particles is explained by thermally activated atomic diffusion on the particle surface that leads to an accumulation of diffusing atoms on one side of the particle which thereby slightly shifts the centre of the whole particle. Brownian motion of the particles results from this process when it is repeated randomly many times [11]. The particle diffusivity of a supported particles decreases exponentially with the particle radius, so that particles above a certain radius limit effectively becomes immobile [11]. Based on a model for particle migration [11], it can be estimated that the limiting particle radius is ca. 4 nm for the model catalysts presented in this study, when thermally aged at T = 650ºC. Since the initial particle radii is ca. 1.5 nm for the present model catalysts (section 3.1.2), this a priori suggests that particle migration could influence the sintering in the present experiments.

Atom migration, also referred to as Ostwald ripening, is when sintering is mediated by the diffusion of atoms or atomic species between immobile nanoparticles either on the surface of the support or through the gas phase [40,41] (fig. 2.1b). As will become clear from the chapters 4 - 8, this mechanism dominates entirely for the sintering of the present model catalysts and the focus will therefore be on the ripening mechanism in the introduction of the relevant sintering models.

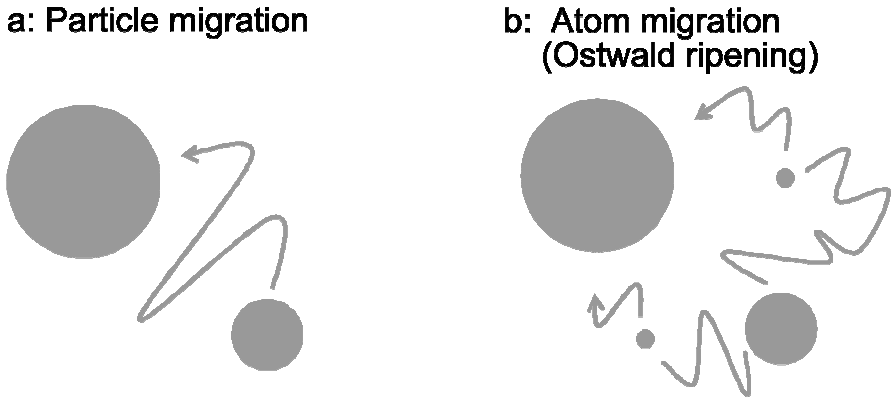

Fig. 2.1: Illustration of particle migration and Ostwald ripening.

2.1.1. Models for Ostwald ripening

The Gibbs-Thomson relation

In Ostwald ripening, the transport of atomic species is explained by the Gibbs-Thomson relation, which describes the equilibrium concentration of adatoms at the particle edge, c_p to the particle radius of curvature, R illustrated in fig. 2.2 [11,13].

$$c_p = c_p^{\infty} \exp\left(\frac{2\gamma\Omega}{kTR}\right) \tag{2.1}$$

where c_p^{∞} is the equilibrium concentration of atomic species at the particle edge on an infinitely large particle, γ the particle surface energy, Ω the atomic volume, k Boltzmann's constant and T the temperature. According to eq. 2.1, the concentration of atomic species is higher at the boundary of small particles than at larger particles. As a result of the gradient in concentration, a net flux will proceed where atomic species diffuse from smaller to larger particles, so that the larger particles eventually grow at the expense of the smaller ones. Accordingly, a critical radius of curvature, R^* must exist for any particle ensemble, for which particles neither shrink nor grow. It has been shown that R^* approximates the mean arithmetic radius of curvature of the particle ensemble [42], but for sufficiently small particles, R^* deviates from the mean radius of curvature [43].

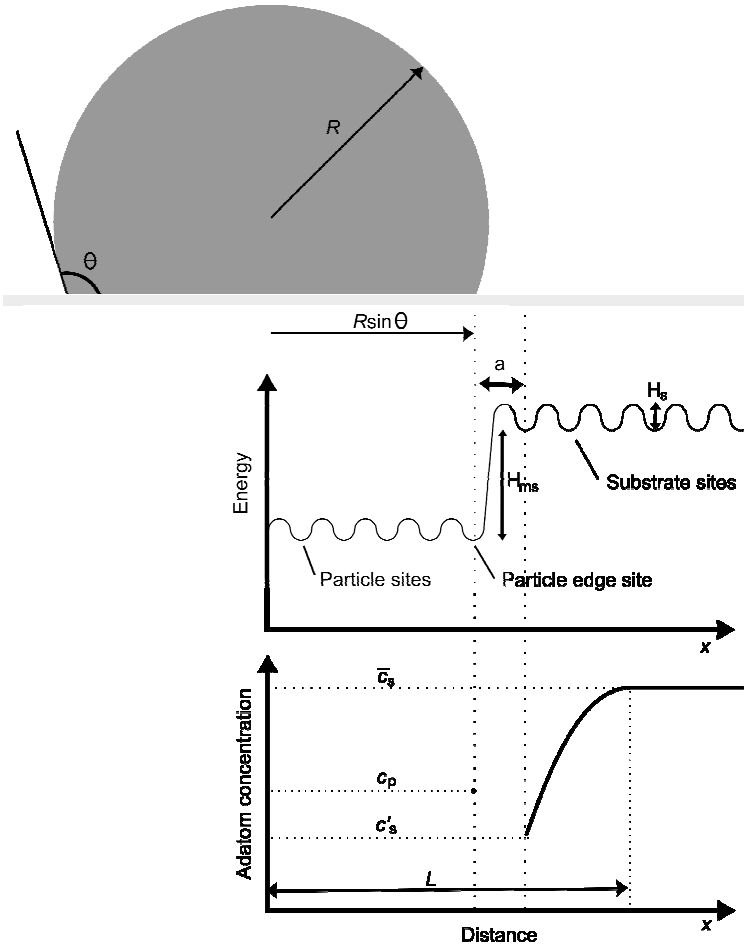

Fig. 2.2: Illustration of a simplified energy-distance and concentration-distance diagram for a three-dimensional metal particle, with a spherical cap shape, on a flat support.

The mean-field assumption

The growth or decay of the nanoparticles is often described by kinetic models relying on the mean-field assumption of the concentration of atomic species. That is, the concentration of atomic species is constant, $\bar{c}_s$ on the support beyond the screening distance, L (fig. 2.2) from the edge of the particle and this mean-field concentration is governing the atom-exchange for each particle in the ripening process [11,13].

The LSW model

By applying the Gibbs-Thomson relation and the mean-field assumption, Lifshitz and Slyozov [44] and Wagner [45] independently developed the so-called LSW model which statistically describes the Ostwald ripening for three-dimensional systems of particles in a homogeneous medium, such as spherical grains in a solid solution. According to this model, an asymptotic particle size distribution (PSD) develops as the sintering proceeds. The asymptotic PSD is a) independent of the initial PSD and b) independent of time (stationary) after a transitional period. Figure 2.3 presents a reprint of the stationary PSD from the original paper by Lifshitz and Slyozov [44]. Chakraverty adapted the model to two-dimensional systems consisting of three-dimensional particles on a flat, homogenous support, and showed that the modeled ripening of the two-dimensional systems lead to a similar stationary PSD [40]. The LSW model thus predicts a characteristic asymmetrical PSD shape with a tail to the small particle side of the main peak.

On the contrary it has been suggested that the particle migration mechanism would lead to a PSD with a sharp cutoff at the small particle side and a tail toward the large particle side of the main peak [13,46]. It has been found that a lognormal distribution will fit the PSD characteristic of particle migration [46]. The characteristic differences between the modeled PSD shapes for the two mechanisms suggest that one route for determining the sintering mechanism for a given catalyst, would be to analyze the shape of the PSD after sintering. However, the distinct PSD shape described by the LSW model has not previously been reported for technical catalysts. Even after severe aging in oxygen at ambient pressures, log-normal like shapes are typical for PSDs of technical catalysts [47,48], and this has spurred some debate on the actual relation between the sintering mechanisms and the resulting PSD shapes [11,12,39,46-54].

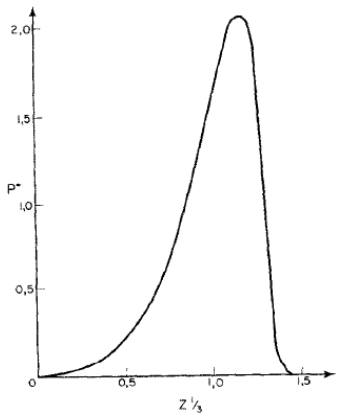

Fig. 2.3: The stationary PSD shape according the LSW model. The plot shows the fraction of particles plotted as a function of R/R*. The figure is reprinted from [44].

Modeling the growth or decay of single particles

While the LSW model addresses the statistical characteristics of particle ensembles, a model for the growth of individual particles supported on flat and homogeneous catalyst supports was developed by Wynblatt and Gjostein [11]. The use of in situ TEM offers the offers the possibility of describing

the individual nanoparticles during sintering. Therefore, in this thesis the model proposed by Wynblatt and Gjostein will be used extensively for comparison with the experimental data. To give the reader a full understanding of the parameters used in this model, it's derivation is reproduced below.

First, it is assumed that the particles can be approximated by spherical caps supported on a flat homogeneous support [11] as illustrated by fig. 2.2. The Ostwald ripening consists of two types of dynamical processes a) attachment of atomic species to and detachment of atomic species from the particles, i.e. interface related processes and b) diffusion of the atomic species on the support or through the gas phase. Here, it is assumed that the diffusion through the gas phase can be neglected, and this assumption is verified for the present systems in chapter 4.

Regarding a), the flux of atomic species crossing the particle-support interface, J_i can be related to the concentration of atomic species at the particle edge, c_p and at the adjacent support sites, c'_s (fig. 2.2):

$$J_i = 2\pi R \sin\theta a \beta' \left(c'_s - c_p \beta \right) \tag{2.2}$$

where R is the radius of curvature, θ the metal-support contact angle, a the atomic spacing at the support at the particle edge, all defined in fig. 2.2, and

$$\beta' = \nu_s \exp\left(-H_s / kT \right) \tag{2.3}$$

$$\beta = \nu_p / \nu_s \exp\left(-H_{ms} / kT \right) \tag{2.4}$$

where ν_s and ν_p are the vibrational frequencies of the atomic species on the support and on the particle, respectively. H_s is the energy barrier between support sites, H_{ms} the energy barrier between a support site and the particle edge site, respectively (fig. 2.2). k is Boltzmann's constant and T is the temperature. A positive J_i-value corresponds to a flux onto the particle.

Regarding b), in a steady state regime, Fick's second law in polar coordinates can be used to describe the diffusion rate atomic species on the support, dc_s/dt as a function of the radial distance, x (fig. 2.2),

$$\frac{dc_s}{dt} = \frac{1}{r} \frac{d}{dx} \left(xD \frac{dc_s}{dx} \right) = 0 \tag{2.5}$$

where D is the diffusivity for the atomic species on the specific support. Eq. 2.5 has the solution, $c_s(x) = k_1 \ln(x) + k_2$. Applying the mean-field assumption by inserting the boundary conditions $c_s(L) = \bar{c}_s$ and $c_s(R\sin\theta) = c_s'$ as defined in fig. 2.2 leads to:

$$c_s(x) = \bar{c}_s + \frac{\bar{c}_s - c'_s}{\ln(L) - \ln(R\sin\theta)} \left[\ln(x) - \ln(L) \right] \tag{2.6}$$

By using Fick's first law and integrating around the particle perimeter, the diffusion flux towards a particle, J_d can now be described as:

$$J_d = 2\pi R \sin\theta \cdot D \frac{dc_s}{dx} = \frac{2\pi D}{\ln\left(R\sin\theta / L\right)}\left[\bar{c}_s - c'_s\right] \tag{2.7}$$

The flux across the particle-support interface, J_i must match J_d, and it can be shown that, $J_i = J_d$ leads to,

$$J_i = \frac{2\pi R \sin\theta a\beta' \dfrac{2\pi D}{\ln\left(R\sin\theta / L\right)}}{2\pi R \sin\theta a\beta' + \dfrac{2\pi D}{\ln\left(R\sin\theta / L\right)}}\left[\bar{c}_s - c_p\beta\right] \tag{2.8}$$

The mean-field concentration, $\bar{c}_s$ is related to the radius of curvature for particles that neither grow nor shrink, R^* through the Gibbs-Thomson relation:

$$\bar{c}_s = c_s^\infty \exp\left(\frac{2\gamma\Omega}{kTR^*}\right) \approx c_s^\infty\left(1 + \frac{2\gamma\Omega}{kTR^*}\right) \tag{2.9}$$

where c_s^∞ is the concentration at the support in equilibrium with an infinitely large particle, and γ, Ω, k and T are defined in relation to eq. 2.1. Recalling that c_p^∞ (eq. 2.1) is defined as the equilibrium concentration of atomic species at the particle edge on an infinitely large particle and that β (eq. 2.4) describes the energy barrier and vibrational frequency for moving an atomic specie from the particle edge to the support, it can be recognized that $c_s^\infty = \beta c_p^\infty$. By also applying the Taylor expansion shown for eq. 2.9 on eq. 2.1 and inserting both in eq. 2.8 leads to:

$$J_i = \frac{2\pi R \sin\theta a\beta' \dfrac{2\pi D}{\ln\left(R\sin\theta / L\right)}}{2\pi R \sin\theta a\beta' + \dfrac{2\pi D}{\ln\left(R\sin\theta / L\right)}} \frac{2c_p^\infty \beta\gamma\Omega}{kT}\left[\frac{1}{R^*} - \frac{1}{R}\right] \tag{2.10}$$

The change in volume for a given particle with the assumed particle geometry (fig. 2.2) is,

$$\frac{d}{dt}\left(\frac{4}{3}\pi R^3 \cdot \left(\frac{1}{2} - \frac{3}{4}\cos\theta + \cos^3\theta\right)\right) = 4\pi R^2\left(\frac{1}{2} - \frac{3}{4}\cos\theta + \cos^3\theta\right)\frac{dR}{dt} = \Omega J_i \tag{2.11}$$

where, $1/2 - 3/4\cos\theta + \cos^3\theta$ is the factor that transforms the volume of a sphere with a radius R into a spherical cap with a radius of curvature, R and a metal-support contact angle, θ defined in fig. 2.2. Combining eq. 2.10 with 2.11 finally leads to an expression for the growth rate for a given particle with the radius of curvature, R:

$$\frac{dR}{dt}=\frac{2\pi R\sin\theta a\beta'\dfrac{2\pi D}{\ln\left(L/R\sin\theta\right)}}{2\pi R\sin\theta a\beta'+\dfrac{2\pi D}{\ln\left(L/R\sin\theta\right)}}\frac{2c_p^{\infty}\beta\gamma\Omega^2}{4\pi R^2\left(1/2-3/4\cos\theta+\cos^3\theta\right)kT}\left[\frac{1}{R^*}-\frac{1}{R}\right] \qquad (2.12)$$

According to eq. 2.12, the growth rate of a given particle is related to parameters such as the temperature, the metal-support contact angle, θ, the diffusivity, D, the energy barriers for crossing the metal-support interface, through β and β', the so-called screening distance, L and R^* which is equal to the mean radius of curvature, $\overline{R}$ when applying the Taylor approximation. It should be noticed, that consistent with the definition of R^*, $dR/dt \rightarrow 0$ for $R \rightarrow R^*$. Also, it should be emphasized that a stationary PSD consistent with the LSW model can be extracted from eq. 2.12 [11,55].

The rate of the two types of processes a) the interface processes and b) the diffusion, is not necessarily identical, which means that the ripening process is either limited by the interface processes (corresponding to $2\pi D/\ln(L/R\sin\theta) > 2\pi R\sin\theta a\beta'$) or by the diffusion processes (corresponding to $2\pi R\sin\theta a\beta' > 2\pi D/\ln(L/R\sin\theta)$) which is referred to as interface control and diffusion control, respectively. For interface controlled ripening eq. 2.12 can be simplified to:

$$\frac{dR}{dt}=\frac{\sin\theta}{\left(1/2-3/4\cos\theta+\cos^3\theta\right)}\frac{a\beta'\beta c_p^{\infty}\gamma\Omega^2}{kTR^2}\left[\frac{R}{R^*}-1\right]=\alpha_i\frac{\alpha_i'}{R^2}\left[\frac{R}{R^*}-1\right] \qquad (2.13)$$

For diffusion controlled ripening eq. 2.12 can be simplified to:

$$\frac{dR}{dt}=\frac{1}{\left(1/2-3/4\cos\theta+\cos^3\theta\right)\ln\left(L/R\sin\theta\right)}\frac{D\beta c_p^{\infty}\gamma\Omega^2}{kTR^3}\left[\frac{R}{R^*}-1\right]=\alpha_d\frac{\alpha_d'}{\ln\left(L/R\sin\theta\right)R^3}\left[\frac{R}{R^*}-1\right] \qquad (2.14)$$

In eqs. 2.13 and 2.14 α_i and α_d describes the influence of the particle shape on the ripening through, θ. α_i' and α_d' describes the other system specific parameters.

Eqs. 2.12 – 2.14 model the growth rates of individual supported nanoparticles, only for idealized catalyst systems. For real industrial catalysts, the modeling will be further complicated by a number of additional parameters. Firstly, the partial pressure of reactive gasses may influence, γ, β and D. Secondly, faceting of the supported nanoparticles will influence, R, α_i and α_d. Thirdly, the often highly complex support structure of industrial catalysts violates the basic assumption of the model of a flat, homogenous support. For these reasons, it is not straight forward to relate eqs. 2.12 – 2.14 to experimental observations of real catalytic systems.

Modeling ensemble averaged parameters

Most experimental studies of sintering do not offer the possibility of following the growth rates of the individual nanoparticles, which further complicates the comparison of the eqs. 2.12 – 2.14 with experimental observations. Instead, observations of ensemble averaged parameters such as the metal dispersion (as measured e.g. by chemisorption or temperature programmed desorption) or the mean particle size (measured by XRD or TEM) obtained as a function of either time or temperature have often been compared with the models. For this purpose, Wynblatt and Gjostein in their original presentation showed that eqs. 2.12 – 2.14 are consistent with the so-called general growth law (GGL) [11,56]:

$$\overline{R}^n(t) - \overline{R}^n(0) = Kt \tag{2.15}$$

where $\overline{R}(t)$ and $\overline{R}(0)$ are the mean radius of curvature at time, t and t = 0, respectively, K a rate constant and n the sintering order. GGL is consistent with a well-known empirical model, the so-called simple power law equation (SPLE) [12,13,15,16,39,41,57]:

$$\frac{dS}{dt} = -kS^n \tag{2.16}$$

where S is the metal surface area, t time, k a rate constant and n the sintering order. S is related to the surface area averaged particle radius, $\bar{r}$ and the dispersion, Δ by $S(t)/S(0) = \bar{r}(0)/\bar{r}(t) = \Delta(t)/\Delta(0)$. GGL and SPLE apply to both particle migration and Ostwald ripening and it has been suggested that the two mechanism can be distinguished by different characteristic value ranges of n, which thereby suggest a simple method of determining the dominating sintering mechanism [13,15,56]. The success of this approach has been debated [13,15]. Eqs. 2.15 and 2.16 are presented here, because of their frequent appearance in the sintering literature, but since the present study offers the possibility of a more detailed comparison with PSDs and with the temporal evolution of individual nanoparticles, the GGL and SPLE models expressing the observation by only one variable ($\overline{R}$, Δ or S) are not used.

2.1.2. A brief overview of results from previous sintering studies

As described in chapter 1, the DOC typically consists of Pt nanoparticles on an oxide support, such as Al_2O_3. The sintering in an oxidizing environment of oxide supported Pt nanoparticles has been studied intensively for at least four decades. In this section, a brief overview will be given of the most imported observations.

The effect of temperature and gas environment on the sintering

The sintering rate of oxide supported Pt nanoparticles in an oxidizing environment is highly dependent on the temperature [10,12,16]. For Pt/Al_2O_3 (but not for Pt/SiO_2) increasing metal dispersion have been reported during aging at temperatures near 500ºC [10,12,15,16,58-61]. For higher temperatures, it is well-known that oxidizing environments enhance the sintering of supported Pt nanoparticles compared with H_2, N_2, Ar or vacuum [10,12,15,16,56,61], and that the sintering rate increases with the partial pressure of O_2 [10,15,58], although a few studies have reported differently [21,60]. Beside ca. 10 – 20 % of O_2, a DOC will be exposed to ppm levels of NO and CO [62], and all three gasses enhance the sintering [19]. The effect of CO is weaker than the effect of O_2, but NO enhances the sintering considerably more than O_2, while a combination of CO and NO has a weaker effect than pure NO [19]. Explanations for the enhanced sintering could be a) a lowering of the metal surface energy, γ by oxygen coverage [61,63], as mentioned above in relation to eqs. 2.12 – 2.14, b) gas-induced variations in the equilibrium particle shape for example by wetting [15,19,64-66]. This would influence α_i and α_d in eqs. 2.13 and 2.14, respectively, and c) formation of $Pt\text{-}O_2$ or Pt-NO complexes which are more volatile than pure Pt adatoms [12,15,19,56,65]. The last effect has been demonstrated by in situ STM for Pt-H complexes at a Pt(110) surface [67].

According to Berry's diagram Pt should be in the metallic phase for temperatures above ca. 500ºC in 1 bar air [68], and this could suggest that Pt-oxygen formation would not be involved in the sintering of Pt/oxide catalysts. However, Berry's diagram applies to bulk, but not necessarily to supported nanoparticles. Al_2O_3-supported Pt nanoparticles in an oxidizing environment are bulk oxidized at 500ºC [19] and surface oxidized or at least covered with oxygen at higher temperatures [19,69-71]. It has also been reported that the degree of oxidation depend on the nanoparticle size [69,70,72].

The effect of the initial particle characteristics on the sintering

The sintering depends on the type of metal, for example via differences in the metal-support interactions [16] and the following decreasing order of stability in O_2 has been reported: Rh > Pt > Ir > Ru [15]. It appears that no studies directly compare the sintering of alumina supported Pt and Pd in oxygen. An in situ study of Pd/Al_2O_3 in oxygen reports relatively complex dynamical changes as a function of temperature, including redispersion at temperatures below 650ºC and rapid growth above 800ºC [28]. It has also been found that alloying of Pt with Pd [16,73,74] or Au [75] leads to a lower degree of sintering in O_2.

The distribution and loading of the metals also influence the sintering: a) an early theoretical study by Flynn and Wanke suggests that the sintering rate depends on the width of the PSD [49] and b) from experimental studies it has been reported that the sintering rate increases for increasing metal loadings [15,58].

The effect of the support on the sintering

Generally, variations in the surface morphology, such as the pore structures characteristic for many industrial catalysts, has a stabilizing effect because a) of the large support surface area and thereby the relatively long distances between the particles [10] and b) particles can be stabilized by cavities in the support material such as support pores [76] because of a lower chemical potential for particles at concave regions relative to particles at convex regions [11]. Also surface defects, steps and other irregularities impede the diffusion of atomic species [15].

The degree of sintering of Pt/SiO_2 at $T \geq 600$ºC in O_2 is reported to be higher than [53,77] or comparable to [59] the degree of sintering for Pt/Al_2O_3. The effect of the support is, however, difficult to establish experimentally because of the high degree of variation (both morphological and chemical) on the support surface when comparing two support materials [10]. Impurities on the support can influence the sintering for example by strong localized chemical interactions, which suggests that a route for stabilization is to introduce chemical "traps" on the support [15,23]. Relatively low sintering rates for a Pt/Al_2O_3-based catalyst have for example been obtained by addition of Ge to the support [78] or by mixing with MgO [79], Ba-CeO_2 [80], Ce-Zr-based oxide powders [38,81,82] or zeolites [83].

The dominating sintering mechanism of oxide supported Pt in oxygen

Ostwald ripening is commonly reported to be the dominant mechanism for the sintering of Pt nanoparticles supported on oxides, such as Al_2O_3 [19,21,59,61] or SiO_2 [53,59] in an oxidizing environment. However, particle migration has also been reported (Pt/Al_2O_3 [33,84], Pt/SiO_2 [76]), and some studies suggest that particle migration may dominate at low temperatures or for short aging times while ripening dominates at higher temperatures and longer aging times (Pt/Al_2O_3 [56,85,86]).

Most of these studies depend on indirect statistical information, typically, the mean particle size, the dispersion, PSDs, or structural information from TEM images obtained post mortem [19,56,59,61,85,86]. As mentioned, the veracity of using ensemble-averaged properties or PSDs in

order to verify a particular sintering mechanism is debatable, and the route for determining the dynamical history of the supported particles from a TEM image obtained post mortem is not obvious. A few studies present time-resolved images obtained post mortem [53,84] or in situ [21,33]. The interpretation of the dynamical changes of the supported nanoparticles is thereby apparently not as challenging. However, these approaches can be challenged by artifacts induced by the characterization methods. For the post mortem approach, it has to be assumed that all the properties of the catalysts are fixated during temperature ramping, sample transfer and for a different gas environment, such as in the vacuum of the TEM, which is not always the case [28,64]. Also, it is critical that the characterization is exactly repeated. For the in situ experiments, the applied probing method may induce artifacts (such as electron beam effects) which can be difficult to fully avoid. In general, it is not straight forward to extract convincing evidence from the experiments for the dynamical mechanisms, and this may explain why full consensus regarding the dominant sintering mechanisms has not been reached.

2.2. Transmission electron microscopy

Since most characterization in this study is performed with TEM, this section gives a description of TEM and in situ TEM. In total, five different TEMs were used during this study, but the description will particularly refer to a CM300 FEG SuperTwin (Philips/FEI Company) since most characterization and all in situ TEM experiments were carried out using this microscope. The section will end with a brief description of energy dispersive spectroscopy (EDS), which is used both in combination with TEM, scanning electron microscopy (SEM) and scanning transmission electron microscopy (STEM). Introductions to the theory of the additionally applied techniques, such as physical vapor deposition (PVD) [87], cluster source deposition [88,89], SEM [90], STEM [91-93], atomic force microscopy (AFM) [94,95], Ellipsometry [96] and x-ray photoelectron spectroscopy (XPS) [94,95,97] are found in the references.

2.2.1. The TEM principle

The TEM is, analogous to the optical light microscope, forming two-dimensional images of a three-dimensional sample. The resolution of the projected images is limited by the wavelength of the probing wave, λ and atomic resolution can be obtained by accelerating the electron beam with high voltages, according to the de Broglie equation [91,92,98],

$$\lambda = \frac{h}{p} \tag{2.17}$$

where p is the electron momentum. The intensity and focus of the beam of electrons is controlled by electromagnetic lenses, which can be considered as thin, convex lenses. The objective lens is the first lens after the electron beam interacts with the sample, and this lens creates an enlarged real space image and a diffraction image of the sample (fig. 2.4). The diffraction image is formed in the back focal plane of the lens, because a convex lens will focus parallel rays in a single spot in this plane. The real space image is also formed, since a convex lens ideally focuses rays from a single point, *A* in the object plane, into one point, *A'* in the images plane (fig. 2.4). Two operation modes are therefore characteristic for TEM: image and diffraction mode.

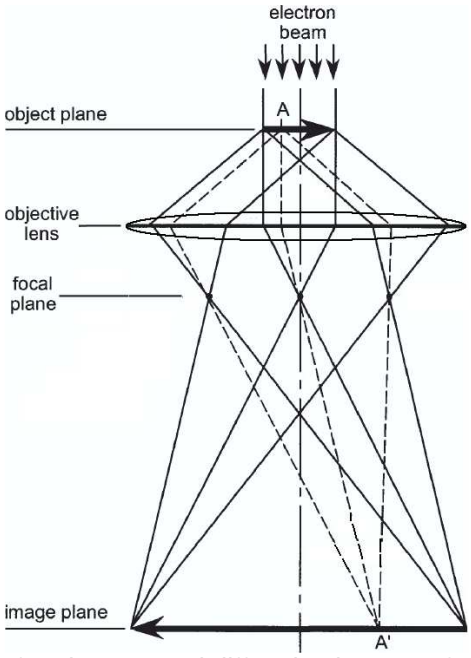

Fig. 2.4: Illustration of the formation of real space and diffraction images after the objective lens.

Because the electrons interact strongly with the sample, a thin sample (preferably below 100 nm) is needed for the transmission of the electrons [91,98]. Most of the electrons are scattered elastically (Ignoring the low energy losses for phonon creation) and the energy lost by in-elastically scattering is converted to x-rays, secondary electrons, Auger electrons, electron-hole pairs and plasmons [91]. After interaction with the sample, the intensity differences in the electron beam are monitored at a viewing screen or with a CCD-camera.

2.2.2. Imaging theory

Phase contrast theory explains high resolution phenomena in the images such as Pt lattice fringes and the Fresnel fringes surrounding the particles in the images. The mathematical formulation is based on Fraunhofer diffraction were the incident beam is assumed to be a planar uniform wave: $\psi(\mathbf{r}) = A\exp(i\mathbf{k}\cdot\mathbf{r})$. The sample is assumed to be a so-called weak phase object, WPO. In this approximation the sample is thought to be so thin that its interaction with the electron beam can be described by the projected scattering potential of the sample, V_p where higher order terms of the projected potential are ignored (kinematical scattering). The image contrast results from interference of transmitted and scattered waves leaving the sample, ignoring Fresnel diffraction within the sample. Using the WPO approximation, the equation for a scattered wave is simplified to [91],

$$\psi(\mathbf{r}) \approx 1 - i\sigma V_p(\mathbf{r}) \tag{2.18}$$

where σ is an interaction constant which depends on the mass and wave length of the electrons in the beam. The intensity of the electron beam leaving the sample is then described with respect to phase contrast by the following equation [91]:

$$I(\mathbf{r}) = \psi(\mathbf{r})\psi^*(\mathbf{r}) \approx 1 + 2\sigma V_p \otimes F^{-1}\left(A(\mathbf{u})E(\mathbf{u})\sin(\chi(\mathbf{u}))\right) \quad (2.19)$$

where F^{-1} is the inverse Fourier transform, **u** is the spatial frequency, $A(\mathbf{u})$ is the objective aperture function, $E(\mathbf{u})$ is the envelope function and $\chi(\mathbf{u})$ is sometimes called the phase distortion function [91]. While the first part of eq. 2.19, $2\sigma V_p$ describes the interaction between the electron beam and the sample, the last part describes how the electron beam is influenced by the lens system. This term is called the contrast transfer function (CFT) when the WPO approximation is applied [91]. The phase distortion function describes the influence of objective lens defocus and aberrations. To the first order in one dimension it can be described as [91],

$$\chi(u) = \pi\Delta f\lambda u^2 + \frac{1}{2}\pi C_s\lambda^3 u^4 \quad (2.20)$$

where Δf is the defocus and C_s is the spherical aberration constant. Spherical aberration, which is a lens defect, and defocus of the objective lens are therefore important parameters for image formation. Additional parameters are temporal and spatial incoherency of the beam, described by the envelope function, $E(\mathbf{u})$ and the effect of objective aperture, described by $A(\mathbf{u})$. The CFT is plotted in figure 2.5 with parameters characteristic for the FEI CM300 at the so-called Scherzer defocus, which is an optimization of the defocus value, Δf by balancing the effect of spherical aberration against the defocus [91]. The function values oscillate giving the maximum image contrast at CFT_{max} and no contrast when CFT = 0. Rows of atoms can appear as bright or dark lattice fringes depending on the sign of CFT [91]. Below the point resolution, defined as the first crossover in the CTF (fig. 2.5), direct interpretation of high resolution TEM images of weak phase objects is possible, meaning that in this region all atoms will appear dark on a bright background. The point resolution at Scherzer defocus for the CM300 is [91],

$$r_{Sch} = 0.66 C_s^{\frac{1}{4}} \lambda^{\frac{3}{4}} = 0.21nm \quad (2.21)$$

Information of higher spatial frequencies is, however, available. The information limit, defined as the highest spatial frequency transferred through the imaging lenses (fig. 2.5), is a result of the $E(\mathbf{u})$, describing the spatial and temporal incoherence, dampening the CFT. In the region above the point resolution, one must be careful when interpreting the images, because the atoms may appear dark or bright depending on the sign of the CTF. Figure 2.5 shows which of the Pt lattice distances it is possible to resolve using the CM300.

Most of the TEM images in the present study are recorded at low magnification, where lattice fringes are not visible and phase differences play a minor role for the image contrast. In these images, the sample regions with a large scattering potential will generally appear darker than regions where the scattering potential is smaller. The sample scattering potential depends on the mass and the thickness of the sample. In terms of mass-thickness contrast in the TEM images, the Pt or Pd nanoparticles (Z_{Pt} = 78, Z_{Pd} = 46) are identified as the darker contrast features which are superimposed at the brighter background that corresponds to the amorphous oxide support (Z_{Al} = 13, Z_{Si} = 14, Z_O = 8, Z_O = 7). The mass-thickness contrast theory focuses on the sample scattering potential i.e. the first part of eq. 2.19. To first approximation the mass-thickness contrast, C can be described as [91],

$$C = 1 - \exp(-Q\Delta x) \quad (2.22)$$

where Δx is the thickness of the sample and $Q = N_0\rho\sigma/M$ is the total elastic scattering cross section specific for the sample material, where N_0 is Avogadro's number, ρ the density, σ the scattering cross section per atom, and M is the molar mass [99]. Q increases approximately linearly with the atom number Z [99].

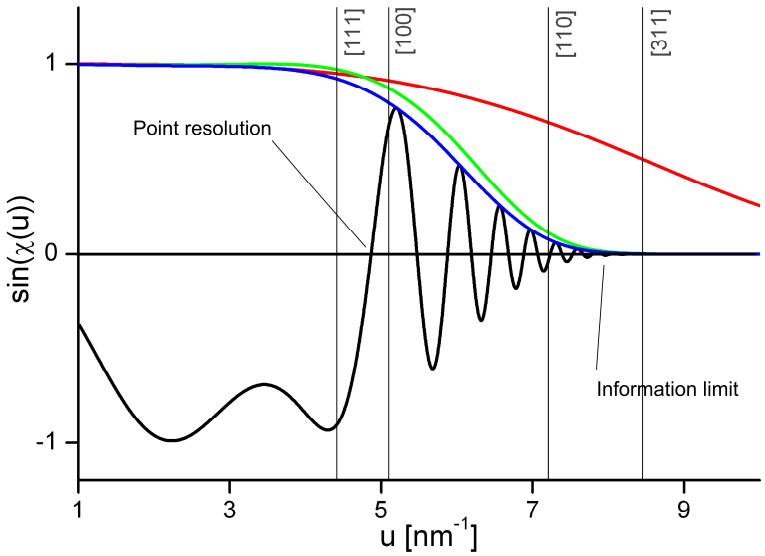

Fig. 2.5: The contrast transfer function is plotted in one dimension (black) as a function of the spatial frequency. The parameters used are characteristic for the CM300 microscope: V = 300 kV, C_s = 1.4 mm, C_c = 2.0 mm, Energy spread = 0.6 kV, Convergence = 0.3 mrad, Δf_{Sch} = -67 nm. The temporal (red), spatial (green) and the total (blue) envelope is presented and the point resolution and the information limit are defined. The vertical lines denote the lattice space distances for Pt with indices [*hkl*].

2.2.3. The experimental setup

An overview of the CM300 FEG SuperTwin (Philips/FEI Company) microscope is now given.

The electron source

The CM300 (fig. 2.6a) has a field emission gun (FEG) consisting of a tungsten cathode from which electrons are extracted by applying an electric potential difference between the cathode tip and an anode. Unfortunately the tungsten cathode tip gets unstable by adsorbed gasses since adsorbents change the tip work function. For this reason a FEG requires ultrahigh vacuum (~10^{-9} mbar) [91,98]. The electrons are accelerated by a second anode using the high tension characteristic for the gun. For the CM300 the acceleration voltage accelerates the extracted electrons to an energy of 300 keV.

Lenses and Apertures

An overview of the several lenses and apertures used in the CM300 TEM is given by fig. 2.6b. The condenser system consists of two condenser lenses and apertures that create a condensed and parallel beam [91]. The magnification system in the CM300 consists of a SuperTwin objective lens, a minicondenser lens, a diffraction lens, an intermediate lens and two projector lenses. The operator focuses the image by using the objective lens. A cross-over in the front focal point of the objective lens is created by the minicondenser producing coherent illumination of the sample [100]. At the back focal plane of the objective lens, where a diffraction pattern is formed, the objective aperture

can be inserted to enhance contrast by blocking of scattered electrons. In the image plane of the objective lens where the first real image is formed, the selected-area aperture can be inserted to control the sample area from which a diffraction pattern is recorded [98]. The diffraction pattern or the real image is magnified by the intermediate and the projector lenses.

Detectors

The viewing screen (fig. 2.6a) acts as the primary detector and is a plate coated with a ZnS scintillator. When lifting the viewing screen, the beam is sent further down the microscope column to meet one of two detectors: A Tietz F114 Fastscan CCD or a Gatan imaging filter (GIF2000). All images were recorded with the Tietz system because its high sensitivity makes it capable of creating images from low intensity beams which is important for the present in situ experiments as will be described in detail in section 3.2.1.3.

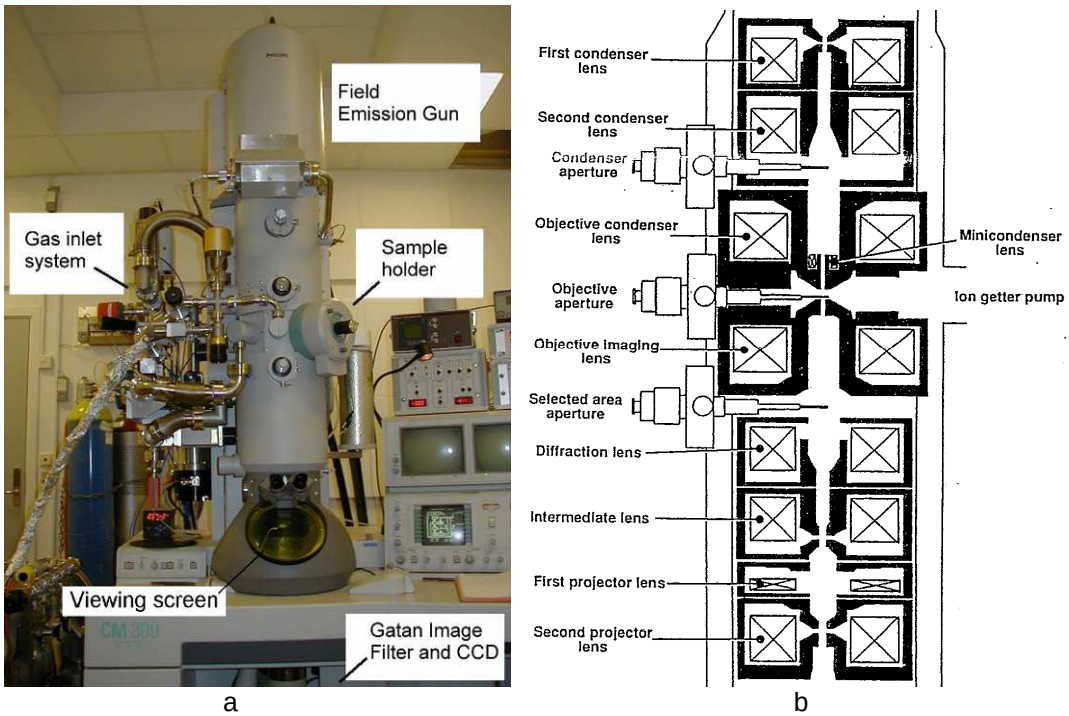

Fig. 2.6: (a) The CM300 FEG SuperTwin (Philips/FEI Company) TEM. (b) Illustration of the lenses and apertures on a FEI CM microscope. The illustration in (b) is reprinted from [100].

2.2.4. In situ TEM

In situ TEM refers to a broad class of experiments carried out during observation in a TEM from heating experiments [101] to experiments with electric or magnetic forces [102]. In this study the term in situ TEM refers to experiments in the TEM where samples are exposed to reactive gases and elevated temperatures, also sometimes referred to as environmental TEM (ETEM) [14,31,103-106]. During the in situ experiments, a reduced spatial image resolution results from scattering of the electron beam by the gas molecules in the microscope column [31,105]. The CM300, is equipped with an environmental cell and a differential pumping system for in situ studies and was in fact the first in situ TEM microscope capable of resolving distances below 0.2 nm in a gas phase [31].

An illustration and a photo of the differential pumping system are presented in fig. 2.7a-b. When running in in situ mode, a steady flow of gas is let into the sample region from the gas inlet system. The gas pressure is ramped down from the gas flask pressure (~50-100 bar) over the in situ box (~500 mbar) into the microscope gas inlet. Here the gas is introduced into the sample region through a needle valve, adjusting the final pressure (up to 15 mbar) [105]. Two apertures, *a* enclose the sample volume that corresponds to the cell where the sample is exposed to the reactive atmosphere. From this cell, gases can diffuse away through the apertures. A molecular drag pump is connected to the region between apertures *a* and *b*. This region makes up pumping level 1. The diameter of the aperture *a* is 0.2 mm which is the half of the diameter of *b* [105]. Pumping level 2 is evacuated by turbo molecular pumps. In the upper part of the column (pumping level 3), an ion-getter pump is connected above condenser aperture C1. Two further ion getter pumps are operating in the FEG region above pumping level 3. The result is that the gas pressure drops gradually from the sample region and up (and down) the column [31]. In this study, typical gas pressures during in situ experiments were ca. 10 mbar, $7 \cdot 10^{-2}$ mbar, $8 \cdot 10^{-5}$ mbar and 10^{-9} mbar for the sample region and the three pumping levels, respectively. The gas flow through the system was ca. 5 – 10 mL/min [105].

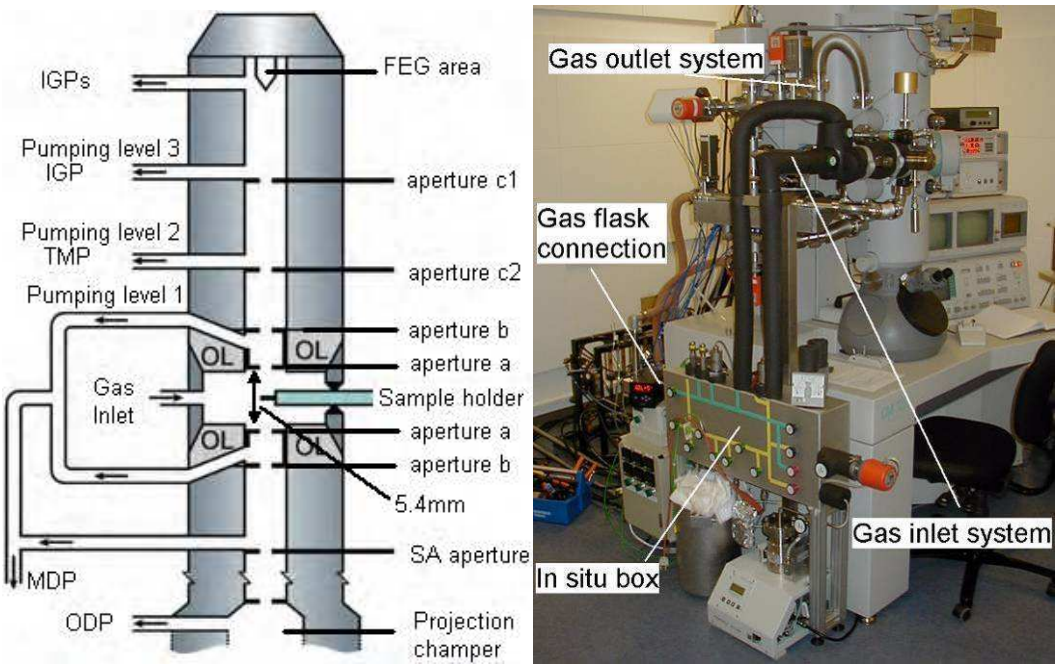

a b

Fig. 2.7: (a) Illustration of the differential pumping system [105] and (b) photo of the in situ gas inlet system.

The heating holder

For the thermal aging of the samples, a Gatan Single Tilt Heating Holder 628 (fig. 2.8a-b) and a Gatan Model 901 SmartSet Hot Stage Controller was used.

This particular holder was chosen because its materials remain stable when exposed to an oxidizing atmosphere at elevated temperatures. The heater element was a platinum filament placed inside an Inconel cup, which acted as support and heating furnace for the sample (fig. 2.8).The temperature was measured by using a Pt-Pt/Rh (13 %) thermocouple spot-welded on the side of the furnace. The cup was suspended by zirconia spheres to isolate it thermally from the frame of the holder. The maximum temperature for the holder is ~900ºC depending on the surrounding gas. In

10 mbar air the temperature could not be raised further than 740ºC, but this was sufficient to activate the sintering of the oxide-supported Pt nanoparticles.

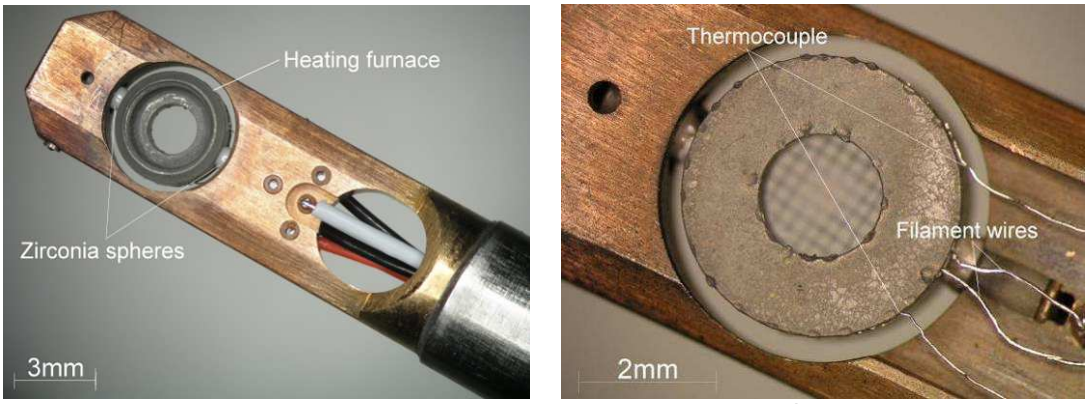

a b

Fig. 2.8: Photos of the Gatan heating holder tip.

2.2.5. EDS

The energy of the x-rays generated from inelastic scattering of the electron beam corresponds to the characteristic energy for the elements in the sample, when the x-rays are produced by relaxation of exited atoms [90,91]. These x-rays therefore contain information of the sample composition, which is typically measured by semiconducting silicon detectors, where the x-ray energy is converted into electron-hole pairs, measured as an amplified current and analyzed with a multichannel analyzer [90]. The result is a histogram that represents the intensity of intervals of the x-ray energy. The peaks in the spectrum correspond to the characteristic energies for the elements and the background signal to Bremsstrahlung [90,91]. For a single element there are multiple characteristic energies, but in the recorded spectra this complexity reduces because the intensities for certain energies are much more intense than for others. The K_α lines are for example ca. 8 times more intense than the K_β lines [90].

To reduce noise from background current in the semiconducting silicon, the detector is typically cooled with liquid nitrogen, and therefore thin (= few micrometers) windows made of light elements such as carbon (Z_C = 6) or beryllium (Z_{Be} = 4) protect the detector from condensation of gasses (mostly H_2O) in the microscopy column [90]. A significant faction of the x-rays with energies below 1 keV are absorbed by the window [90], and therefore EDS is generally best for analysis of higher energies corresponding to the heavier elements, for example Pt and Pd for which EDS is applied in this study.

Elemental mapping

Combining EDS with a scanning probe (SEM or STEM) offers the possibility of recording a three-dimensional dataset where each pixel in the scanned areas corresponds to a full EDS spectrum. Two-dimensional projections of this dataset can visualize the spatial distribution of the peak intensities for a chosen energy range, and for example present an image of the characteristic energies for Pt on the sample. A challenge when performing the elemental maps is the often severe beam damage induced to the sample because the focused electron beam has to scan the sample relatively slowly to achieve a satisfactory high EDS signal count.

Quantitative analysis

To quantitatively analyze the concentration of a given element, the peak intensity of this can be compared to the peak intensity from a standard with a known concentration measured under the exact same conditions [90]. The quantitative analysis relies on a reasonable peak background fitting and for bulk analysis (SEM-EDS) the comparison with standards normally has to be corrected by the so-called ZAF corrections, describing the efficiency with which an element produce x-rays (Z), x-ray energy loss by absorption in the sample (A) and x-ray energy loss from fluorescence (F) [90]. For thin samples (TEM-EDS) the concentration fraction between two elements approximately corresponds to the integrated peak intensity fraction times a calibration factor, *k*, which can be found by comparison with standards or from models [90]. In the present study, the *k*-factors were determined from the model by Nestor Zaluzec.

3. Methods

3.1. Model catalysts

The first part of this chapter describes the preparation and characteristics of the catalysts. In the second part, details of the sintering experiments and data analysis are given.

3.1.1. Motivation for using model systems

Industrial diesel oxidation catalysts are typically composed of Pt nanoparticles with a mean radius of a few nanometers dispersed on a highly porous oxide support, typically γ-Al_2O_3 [6]. A highly complex support structure is characteristic for such catalysts as illustrated by the electron tomogram of a Pt/γ-Al_2O_3 (after thermal aging, hence the relatively large Pt nanoparticles) in figure 3.1.

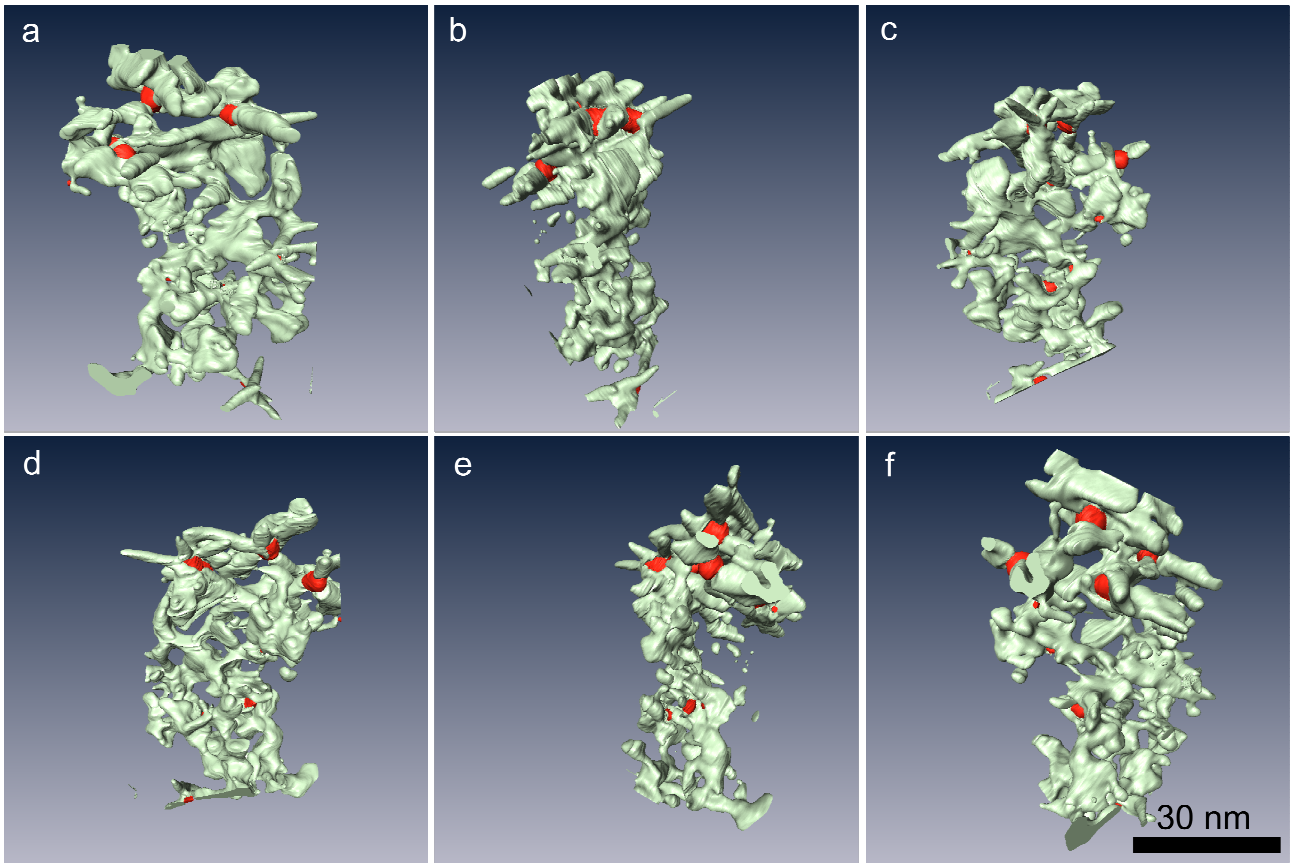

Fig. 3.1: (a-f) Electron tomography reconstruction of a Pt/γ-Al_2O_3 diesel oxidation catalyst. In the segmentation, the volumes of Pt and Al_2O_3 are marked by red and green colors, respectively. Each image corresponds to the catalyst rotated by 60 degrees with respect to the previous images in the series.

An in situ study of nanoparticle sintering in such complex support structures will meet the following challenges: a) the three-dimensional dynamical changes of nanoparticles in a complex support structure are difficult to track and analyze from time-resolved two-dimensional images, b) the complex support structure will induce a high degree of variation in the mass-thickness contrast of the TEM images so that the small Pt nanoparticles are difficult to detect in image regions corresponding to thick support layers. The presence of a gas phase during in the situ experiments will enhance this problem, c) as described in the chapter 2, the theoretical models for sintering assume a flat and homogeneous support. In a fundamental study of sintering where experimental data is compared with the theoretical models, it is more appropriate to work with catalytic model systems that mimic the assumptions of the theoretical models as closely as possible.

For these reasons, the present study focuses on the sintering of Pt nanoparticles dispersed on a flat, homogeneous Al_2O_3 support. To study effects of the type of oxide support on sintering, it was decided also to work with a model catalyst with a flat, homogeneous SiO_2 support. Also, the sintering of Pd nanoparticles and bimetallic Pt-Pd nanoparticles on a flat oxide support is addressed.

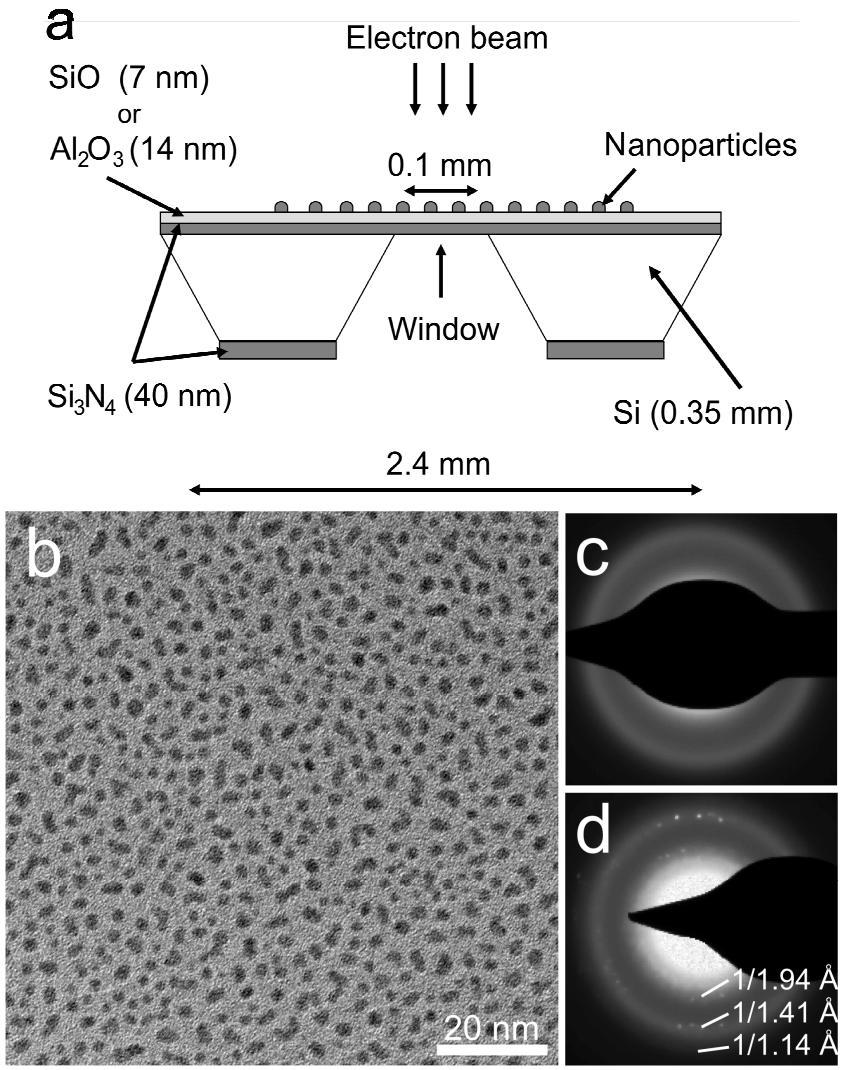

Fig. 3:2: (a) Schematic side-view of the model catalyst. (b) TEM image of the as-prepared Pt/Al_2O_3 model catalyst. (c) Electron diffraction pattern of the bare Si_3N_4-supported alumina film. (d) Electron diffraction pattern of the model catalyst. Diffraction spots corresponding to the Pt (111), (200) and (220) lattice planes are indicated.

3.1.2. The metal-oxide model catalysts

The model catalysts in this study consist of Pt, Pd and bimetallic Pt-Pd nanoparticles dispersed on a flat, amorphous Al_2O_3 and SiO_2 support that were prepared on 40 nm thick, amorphous Si_3N_4 electron transparent windows supported on Si wafers (fig. 3.2a) [107]. The route mean square roughness [108] of the Si_3N_4 layer is < 0.5 nm over a 400 μm^2 area [107]. The windows are stable under strong electron beam irradiation and in temperatures up to 1000°C at atmospheric pressure [107].

The preparation of the oxide layers

Following the Si_3N_4 window preparation [107], the Al_2O_3 support was formed by PVD from an Al_2O_3 target of 99.99 % nominal purity (Kurt J. Lesker Company) using an electron beam evaporator (AVAC HVC600) operated with a base vacuum pressure of $4 \cdot 10^{-6}$ mbar and a deposition rate of 0.05 nm/s. The SiO_2 layer was formed by oxidizing the Si_3N_4 using a microwave plasma processor (TePla 300PC) operated at 1 kW for 40 min in 1 mbar O_2.

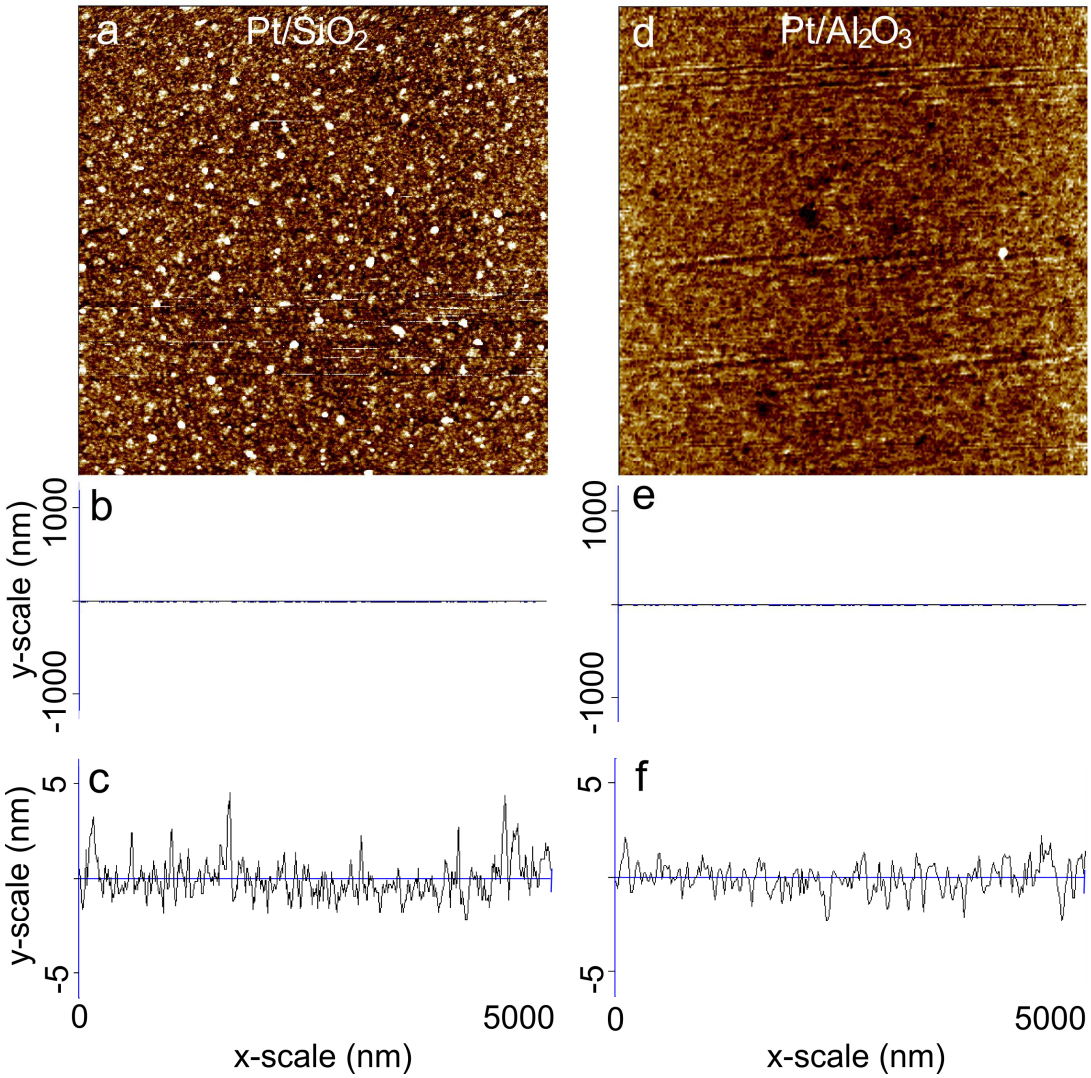

Fig. 3.3: (a,d) AFM images and (b,c,e,f) vertical line scans of (b-c) the SiO_2 substrate and (e-f) the Al_2O_3 substrate. The image widths are 5 µm and the color scale covers 5 nm. All line scans are performed horizontally from edge to edge at the center for the vertical axis. For (b,e), the y-axis has a 1x1 ratio to the x-axis.

The thickness of the oxide layers

The thickness of the oxide layers and the Si_3N_4 window was determined by ellipsometry (J.A. Woollam M2000). The thicknesses given with an error of ±1 nm are; Al_2O_3 = 14 nm on Si_3N_4 = 36 nm, and SiO_2 = 7 nm on Si_3N_4 = 28 nm. The ellipsometry measurements were carried out with assistance from Laurent Feuz from the Department of Applied Physics at Chalmers University.

The surface morphology of the oxide layers

The surface morphology of the oxide layers was determined by using atomic force microscopy (AFM) (DI Nanoscipe 3000). The AFM images in figure 3.3a,d show that the oxide layers are relatively flat and that the Al_2O_3 layer is less rough than the SiO_2 layer. Figure 3.3b,e present line scans with a 1x1 ratio between x- and y-scales, which show that the samples are flat on the micrometer level. If the y-scales are exaggerated relative to the x-axis, as presented in figure 3.3c,f, it appears that the surface height varies by ca. ±3 nm for Pt/SiO_2 and ca. ±1 nm for Al_2O_3. The route mean square roughness over a 100 μm^2 area was < 0.6 nm for SiO_2 and < 0.4 nm for Al_2O_3. This shows that preparation of the oxide layer by oxidation (SiO_2) creates a slightly rougher surface than preparation by PVD, but that the initial surface roughness (route mean square roughness < 0.5 nm for Si_3N_4 [107]) is not dramatically changed by the creation of the oxide layers. The AFM measurements were carried out with assistance from Elin Larsson, Competence Centre for Catalysis at Chalmers University.

The composition of the oxide layers

XPS was used to verify the sample composition and to determine the degree of impurities for the two sample types before the deposition of the metals (fig. 3.4a-b). All major peaks in the XPS spectra were identified and the spectra were calibrated using the characteristic O 1s, N 1s and C 1s peak. The spectrum for the SiO_2-sample reveals a characteristic peak at 103.5 eV (fig. 3.4a), which corresponds to the reference value for the Si 2p 3/2 peak in SiO_2 [97]. For the Al_2O_3-sample XPS reveals a characteristic peak at 74,6 eV (fig. 3.4b) which corresponds to the reference value for the Al 2p 3/2 peak in pure Al_2O_3 (74,7 eV) [97].

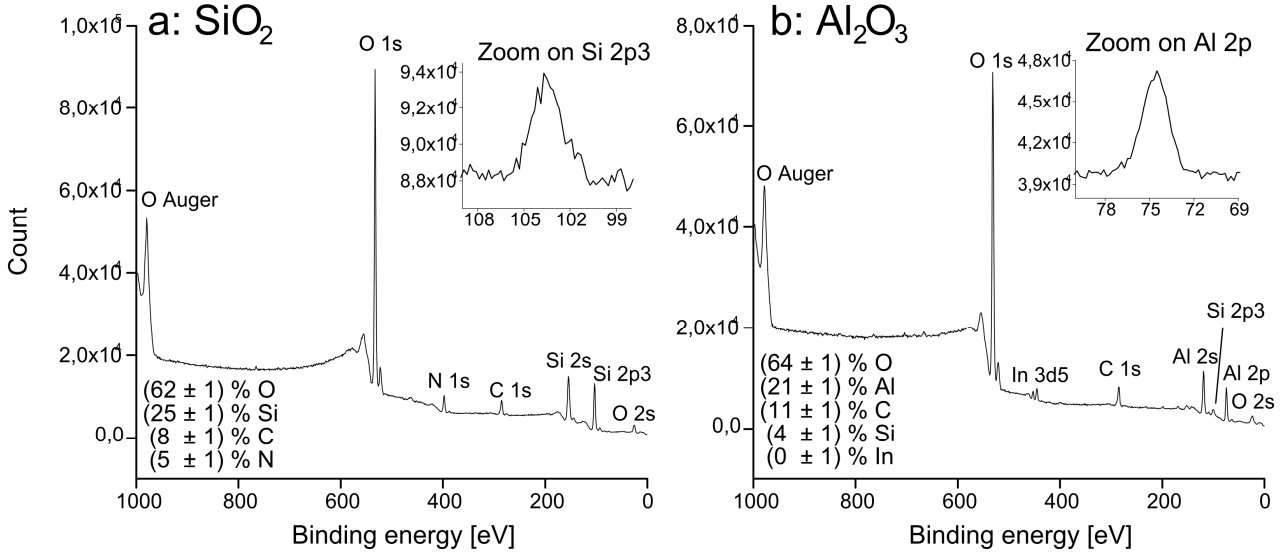

Fig. 3.4: XPS spectra of the (a) SiO_2 and (b) Al_2O_3 substrate. In both graphs a high energy resolution spectrum on the relevant metal peak (Si and Al) is inserted. The quantified atomic concentration for each element is inserted in the figure.

From the insert of figure 3.4a, it is seen that there could be a shoulder on the main peak near the value 101,9 eV, which corresponds to the reference values for the Si 2p3 peak in SiO. This could indicate that the SiO_2 is not fully oxidized, but the shoulder could very well result from poor statistics. The shoulder could also be explained by the presence of the compounds SiC or SiN with the binding energies 101,0 eV and 101,5 eV respectively. The reference values for the Al 2p3 peak of partly oxidized Al varies from 72-76 eV and can therefore be difficult to determine exactly. The peak identified as the Al 2p3 peak from Al_2O_3 does not have any shoulders, which may indicate that the Al is fully oxidized. According to the quantitative analysis presented in figure 3.4a,b, oxygen is overrepresented (O/Si = 2.5, O/Al =3.0) compared to the stoichiometric oxide relation (O/Si = 2, O/Al = 1.5) indicating a full oxidation.

XPS also reveals ca. 10 % atomic concentration of carbon contamination on the as-prepared substrates and a trace of In below 1 % on the Al_2O_3 sample (fig. 3.4a,b). The In most probably results from a contamination from previous samples in the AVAC HVC600 electron beam evaporator. It is difficult to pinpoint the exact source of the carbon contamination. It may be remnants from the sample production, or a result of the exposure to ambient conditions during transfer from the clean room to the vacuum chamber hosting the XPS facility. Based on the results presented previously [109] and in section 3.2.1.2, it is most likely that the carbon contamination will react and/or desorbs during temperature ramping or during the first few minutes at the constant temperature of the in situ TEM or tube furnace sintering experiments. The XPS work was carried out with assistance from John Larsen and Lone Bech at CINF, Technical University of Denmark.

The crystallinity of the oxide layers

Selected electron area diffraction patterns of the Si_3N_4-supported oxide layers demonstrate only broad and diffuse bands of diffracted electrons consistent with an amorphous structure. This is shown for the Al_2O_3 sample in figure 3.2c.

The Pt and Pd nanoparticles

In a final preparation step, the metals were deposited onto the oxide layers by PVD using an electron beam evaporator (AVAC HVC600) operated with a base vacuum pressure of $2 - 4 \cdot 10^{-6}$ mbar and with a deposition rate of 0.05 nm/s. In total four sample types were prepared: 1) Pt/Al_2O_3, 2) Pt/SiO_2 3) Pd/Al_2O_3 and 4) $Pt\text{-}Pd/Al_2O_3$. The nominal Pt or Pd thickness was 0.5 nm. For the bimetallic $Pt\text{-}Pd/Al_2O_3$ sample, a nominal thickness of 0.2 nm Pt was first deposited followed by the deposition of Pd also with a nominal thickness of 0.2 nm. The used Pt and Pd targets had 99.99 % nominal purity (Nordic High Vacuum AB). For all samples, the as-deposited metal particles are present as irregularly shaped and crystalline islands, as presented for the Pt/Al_2O_3 sample in figure 3.2b,d. The Pt nanoparticles are homogenously distributed over both oxide supports, as seen for Pt/Al_2O_3 in figure 3.2b.

Figure 3.5 presents PSDs based on automatic measurements (section 3.3.1) of the nanoparticle sizes from the TEM images of the as-prepared samples (full black). The Pt nanoparticles have a mean projected radius of approximately 1.5 nm for all samples and the PSDs representing the Pt/SiO_2 sample is wider than the distributions of Pt, Pd and Pt-Pd nanoparticles supported on Al_2O_3.

Particle deposition with a cluster source

For some of the Pt/SiO_2-samples, Pt nanoparticles were also deposited with a cluster source (Mantis Deposition Ltd) in a multichamber UHV system (Omicron Multiscan Lab) with a base pressure of ca. 10^{-11} mbar. The Pt nanoparticles were formed by gas-phase condensation from a flux of platinum atoms, which are sputtered from a 99.99% purity platinum target by a magnetron sputtering head, located inside a liquid nitrogen cooled enclosure. Argon gas is used to provide the

plasma at the magnetron sputtering head. The Pt nanoparticle sizes were controlled by the sputtering power, the gas (Ar and He) flow in the aggregation zone and by filtering of the nanoparticles according to their mass-to-charge ratio with quadrupole mass filter [89]. The cluster source was applied to produce Pt/SiO_2 model catalysts which were similar to those prepared by PVD, i.e. similar Pt particles sizes, but with a lower particle density. In addition Pt/SiO_2 model catalysts were produced with a bimodal PSD by first depositing small nanoparticles (radii = ca. 1.5 nm) with either PVD (resulting in a high particle density) or with the cluster source (resulting in a low particle density) followed by the deposition of larger particles (radii = ca. 6 nm) with the cluster source. The SiO_2-samples were degassed at 500ºC for 1 hour prior to the deposition with the cluster source, except the sample with Pt nanoparticle already deposited with PVD, which was degassed at the lower temperatures of 150ºC to avoid sintering of the Pt nanoparticles.

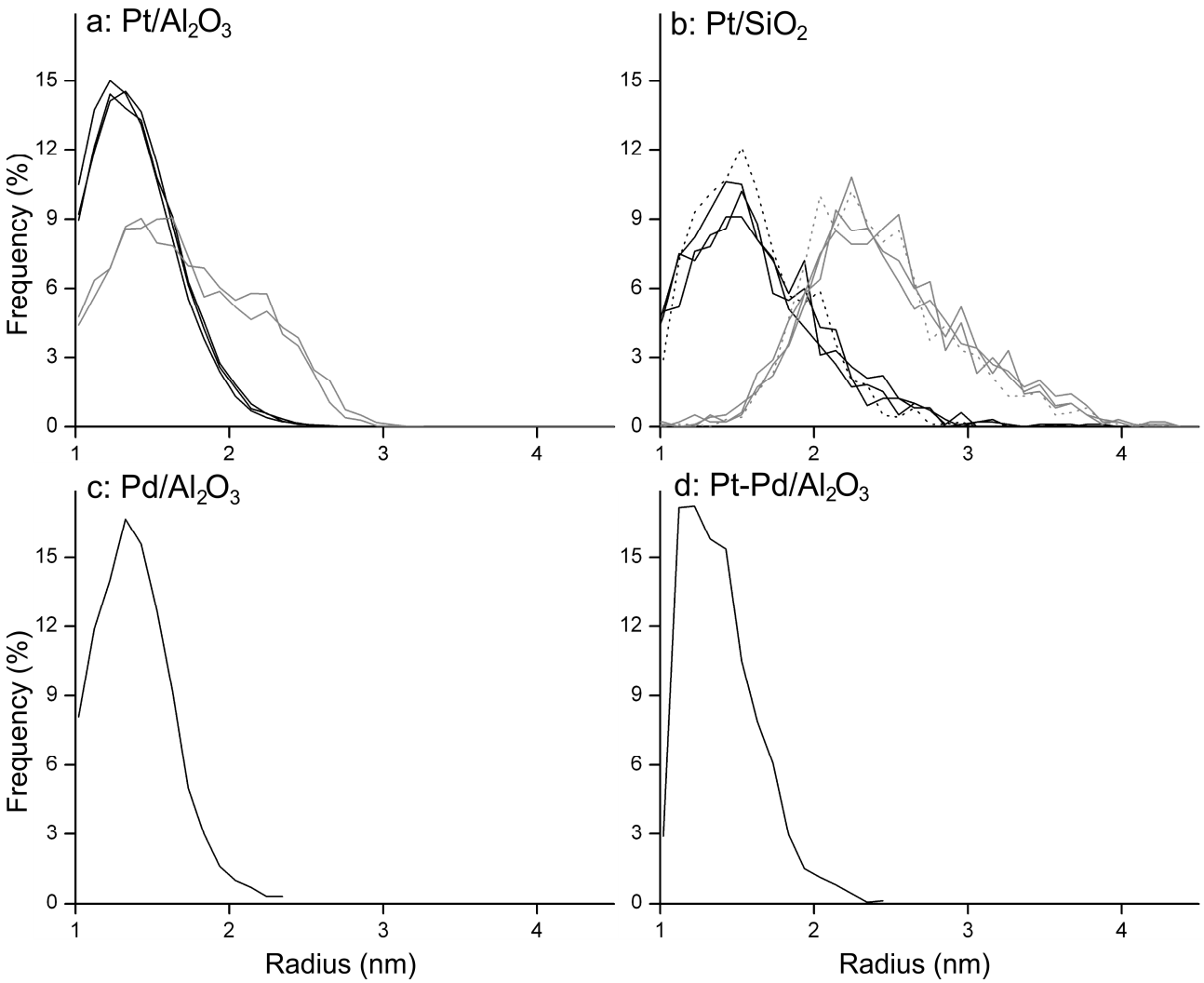

Fig. 3.5: The lines corresponds to PSDs for (a) Pt/Al_2O_3, (b) Pt/SiO_2, (c) Pd/Al_2O_3 and (d) $Pt\text{-}Pd/Al_2O_3$ representing the samples as-prepared (full black) and after aging in a tube furnace in 1 bar 0.2 % O_2 in N_2 for 3 hours at 600℃ (full grey). The particles were automatically measured as describe in section 3.3.1. Identical bin sizes are used for all PSDs. For comparison, PSDs from manually measured radii are added for the Pt/SiO_2 sample (dotted lines). The number of particles is ≥ 1000 for each PSD.

Uniformity of the as-prepared samples
From figure 3.5 (full black) it can be seen for Pt/Al_2O_3 (a) and Pt/SiO_2 (b) that the main peak value and the width of the PSDs are identical for different as-prepared samples of the same type. This means that the statistical characteristics of the Pt nanoparticles on the as-prepared samples are identical for each of these samples.

Reproducibility
Figure 3.5 also presents PSDs for the Pt/Al_2O_3 (a) and Pt/SiO_2 (b) samples after thermal aging in a tube furnace in 1 bar 0.2 % O_2 in N_2 for 3 hours at 600°C (full grey). Both Pt/Al_2O_3 samples were aged in the same experiment and similarly all three Pt/SiO_2 sample were aged in the same experiment. According to the figure, the PSDs are exactly reproduced when the samples are exposed to exactly the same conditions. This means that the samples are suitable for a statistical study of sintering.

Sample storage and stability
After preparation the samples were stored in a glove box with ppm levels of O_2 and H_2O. The measured degree of sintering could not be reproduced for the Pt/Al_2O_3 samples stored in air at ambient pressure for longer periods (months). The reason for the reduced reproducibility after storing in air could not be determined from TEM or XPS.

3.2. The sintering experiments

The sintering of the model catalysts was carried out and directly monitored by use of in situ TEM. For comparison, the sintering was studied by post mortem TEM after thermal aging in a tube furnace. Details for the sintering experiments are described in this section.

3.2.1. In situ TEM

3.2.1.1. Experimental details

In situ TEM experiments were performed using the CM300 electron microscope described in section 2.2. In the electron microscope, the model catalysts were exposed to 10 mbar technical air composed of 21 % O_2 and 79 % N_2 (class 2 from Air Liquide). Each sample exposed to this environment was mounted with the metal-oxide side facing the bottom of the heating holder. The holder facilitated the heating of the samples in the gas environment at a rate of 30°C/min. to a temperature in the range 200-740°C where the temperature was kept constant within ca. 3°C for up to 6 hours. An objective aperture wit scattering semi-angle of 7.5 mrad was used.

3.2.1.2. Temperature calibration

It can not be guaranteed that the temperature of the sample is identical to the furnace temperature measured by the thermo-couple (section 2.2.4). For heating experiments without a gas phase, one approach for the temperature calibration is to rely on reference values e.g. melting points, thermal expansion of a crystal lattice or phase transition [92], which, however, can be difficult since the

reference values often refer to bulk materials and are not always precisely given for nanoparticles. For in situ TEM in a gas phase, as in the present study, the temperature calibration is further complicated by gas-induced effects on the demarcation parameters. Another challenge in the temperature calibration of in situ TEM is that the temperature of the gas phase may be different from the temperature of the sample.

In this study the temperature of the sample and the gas near the sample surface is calibrated by comparing the results from in situ TEM experiments with non-catalytic oxidation of carbon black (CB), with reference experiments from a plug-flow reactor where the temperature measurements are expected to be reliable. The data of the reference experiments were taken from a previous study [110]. The oxidation of CB on a SiO_2 sample without Pt nanoparticles was also compared to oxidation of CB on stainless steel to determine if the lower heat conductance of $SiO_2/Si_3N_4/Si$ relative to stainless steel would result in lower temperatures at the SiO_2 surface over the electron transparent window (fig. 3.2a). Specifically, CB powder (Printex U, Degussa GmbH) was dispersed dryly on a stainless steel TEM grid and on the SiO_2 sample without Pt nanoparticles. In the later case the CB was suspended in ethanol, treated with ultrasound and a droplet of the suspension was added to the SiO_2 sample. The sample was allowed to dry in air. In the TEM, the CB/stainless steel sample was exposed to 2 mbar O_2 (99.998%) and the temperature was ramped with a rate of 2°C/min until 600°C was reached. The CB/SiO_2 sample was exposed to 10 mbar technical air (class 2 from Air Liquide) and the temperature was ramped as described for the CB/stainless steel sample. For the reference experiment in the plug-flow reactor, 0.1 g CB was mixed with α-Al_2O_3 powder (CB/Al_2O_3 mass fraction = 0.1) and oxidized in 2 mbar O_2 in N_2 in a flow = 50 Nml. In the reference experiment, the temperature was ramped to 600°C with the same ramping rate as in the in situ TEM experiments. The progress of the reaction was followed by monitoring the CO and CO_2 levels using a Binos 1 dual channel infrared sensor (Leybold-Heraeus GmbH). The temperature was measured with a thermocouple in the reactor ca. 10 mm below the sample bed.

From time-resolved in situ TEM images, the diameters of 10 CB particles on the CB/stainless steel (squares) and the CB/SiO_2 (circles) sample were measured and the mean shrinkage is presented as a function of temperature in figure 3.6. To compare the measurements of CO and CO_2 from the plug-flow reactor with results from in situ TEM the following considerations were made: The CB particles will decrease in volume as carbon is removed from the particles in the process of CO and CO_2 production. The mean particle shrinkage is estimated by assuming that the particles are spherical, composed of 100% carbon and that carbon is removed layer by layer of from the outer surface so that no oxidation inside the CB particles takes place. These assumptions only represent a first approximation, since the CB particles are not perfect spheres, contain up to 10% of hydrogen [111] and the oxidation can probably take place in the particle pore system [112,113].

According to figure 3.6, the temperature dependent decrease in mean particle diameter is similar for the two in situ TEM experiments and for the results from the plug-flow reactor: For all three experiments the decrease in diameter is detectable at temperatures above 500°C, and the diameter shrinking rate, caused by non-catalytic oxidation of the particles [109], is high near 600°C. This shows a) that the temperature near the CB particles are not substantially lower when supported on a film of SiO_2 and Si_3N_4 than when supported on stainless steel which is known to be a good heat conductor, and b) that the gas and sample temperature correspond to the temperature measured by the thermo-couple at the heating holder furnace. Because of the relatively large error bars in the figure the temperature can, however, only be determine within a precision of ca. 50°C (fig. 3.6).

In addition the temperature was also calibrated directly from the sintering results, by comparing the mean particle radius after the Pt/SiO_2 samples were aged either in the microscope or in a thermally equilibrated external tube reactor in 10 mbar technical air at 740°C for 3 hours. The temperature ramping rate was identical for these two experiments and the electron beam was turned

off throughout the thermal ageing in the microscope. Because the mean Pt particle size after heat treatment only differed by 2 % for the samples, the temperature measured on the furnace is concluded to be similar to the temperature of the sample and gas environment near the sample surface during the in situ TEM experiments.

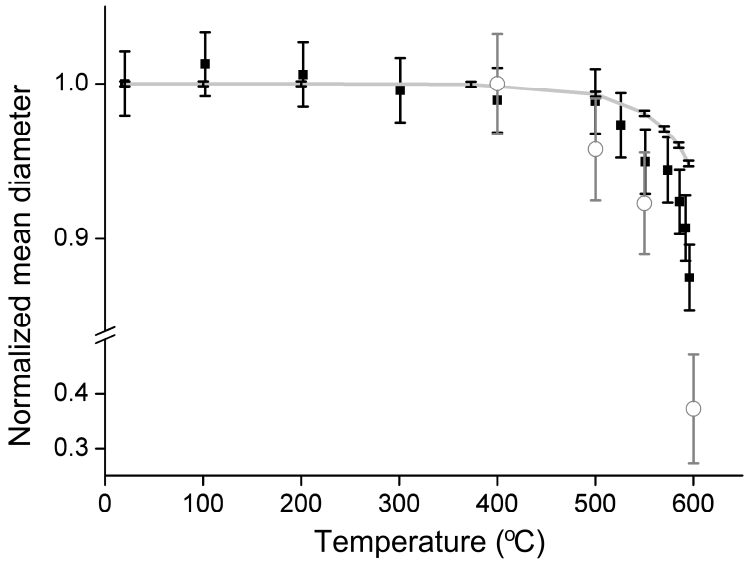

Fig. 3.6: Normalized mean diameters of 10 CB particles from the CB/stainless steel sample (squares) and the CB/SiO_2 sample (circles) presented as a function of temperature. For comparison the mean diameter is estimated based on measurements of CO and CO_2 from a plug flow reactor (grey line). The error bars represent the estimated measuring errors.

3.2.1.3. Electron beam effects

Before performing the actual sintering experiments it is necessary to understand and control the artifacts that may be induced by the electron beam so that they can be eliminated.

Electron beam effects - overview

To obtain an overview of the possible effects of the electron beam in combination with the gas phase the Pt/SiO_2 model catalyst was exposed to the very high electron beam current density of 16 A/cm^2 in 2 mbar O_2 and at a temperature of 300°C which is well below the onset temperature for sintering of Pt/SiO_2 [53,59]. Figure 3.7 presents time-resolved in situ TEM images of the same region of the sample, and from the image series the beam induced dynamical changes of the Pt particles can be observed such as a) particle migration (e.g. particle no. 1), b) coalescence between migrating particles (e.g. particles no. 2 and 3), c) particle splitting (e.g. particle no 4), d) decreasing particle radius and contrast (e.g. particle no. 5). Several of these dynamical changes can easily be mistaken for sintering mechanisms such as particle migration and Ostwald ripening. For the sintering experiments it is therefore critical that proper experimental conditions are found so that the observed dynamical changes are not dominated by such beam induced artifacts.

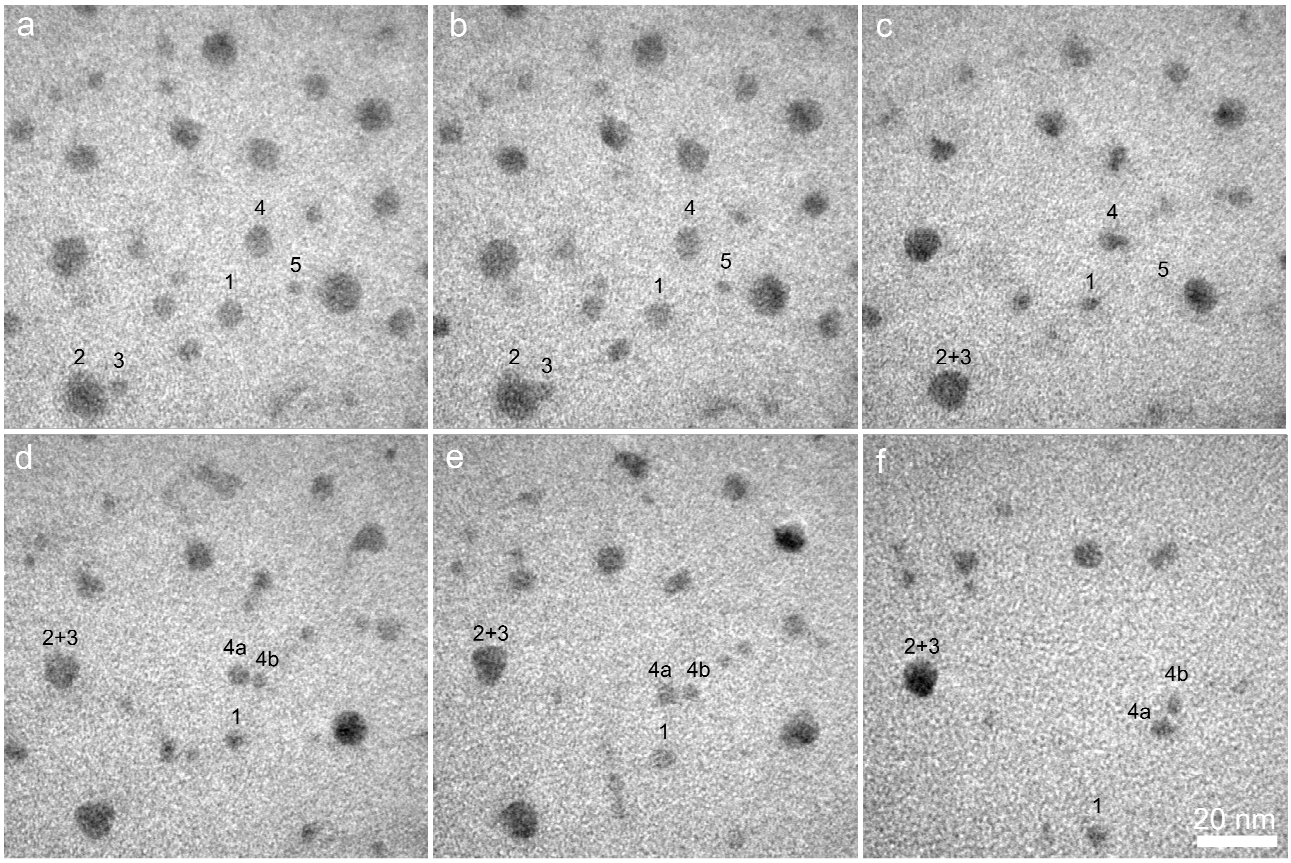

Fig. 3.7: Time-resolved in situ TEM images of Pt nanoparticles supported on SiO_2 during exposure to the high electron beam current density of 16 A/cm^2 in 2 mbar O_2 at T = 300ºC. The images are acquired (b) 18 s, (c) 2 min, (d) 4 min, (e) 10 min and (f) 20 min after the acquisition of time of (a).

Electron beam effects at low beam current densities

To find the optimal illumination conditions for the in situ TEM experiments, the electron beam effects were examined for all four types of model catalysts (Pt/Al_2O_3, Pt/SiO_2, Pd/Al_2O_3 and Pt-Pd/Al_2O_3) by exposing the samples to various low beam current densities (< 1 A/cm^2) in 10 mbar technical air and at a temperature of 400°C. The regions were initially unexposed to the electron beam and were subsequently imaged with a frame rate of 1.4 frames/s (exposure time = 0.5 s) for 30 min. At the lower beam current densities, the image series revealed two main effects of the electron beam; the shrinkage of the projected nanoparticle areas and the coalescence of neighboring Pt nanoparticles.

To address the shrinkage, the radii of at least 30 nanoparticles were manually measured in the first and last frame of the image series. For particles that eventually disappeared during the 30 min. of exposure to the electron beam, the final radius measurements were obtained from the last frame where the particles were clearly visible, and the shorter beam exposure time was taken into account.

Figure 3.8 shows the mean nanoparticle radius shrinkage rate as a function of the electron beam current density for Pt/Al_2O_3 (filled black squares), Pt/SiO_2 (filled grey squares), Pd/Al_2O_3 (open grey squares) and Pt-Pd/Al_2O_3 (open black squares) and reveals an approximately linear increase in the mean radius shrinkage rate with beam current densities increasing up to 1 A/cm^2.

Figure 3.8 also presents the fraction of coalescing particles for Pt/Al_2O_3 (filled black circles), Pt/SiO_2 (filled grey circles), Pd/Al_2O_3 (open grey circles) and Pt-Pd/Al_2O_3 (open black circles). Only a minor fraction of ca. 1 % of the total number of nanoparticles apparently coalesced in the oxidizing gas environment irrespective of the electron beam current density (fig. 3.8). Specifically,

the coalescence events involved only particles located in close vicinity with their center of mass separated by ca. 3 nm and did not involve migration of particles over longer distances. The events could be coalescence events or a localized, fast ripening effect in accordance with [114].

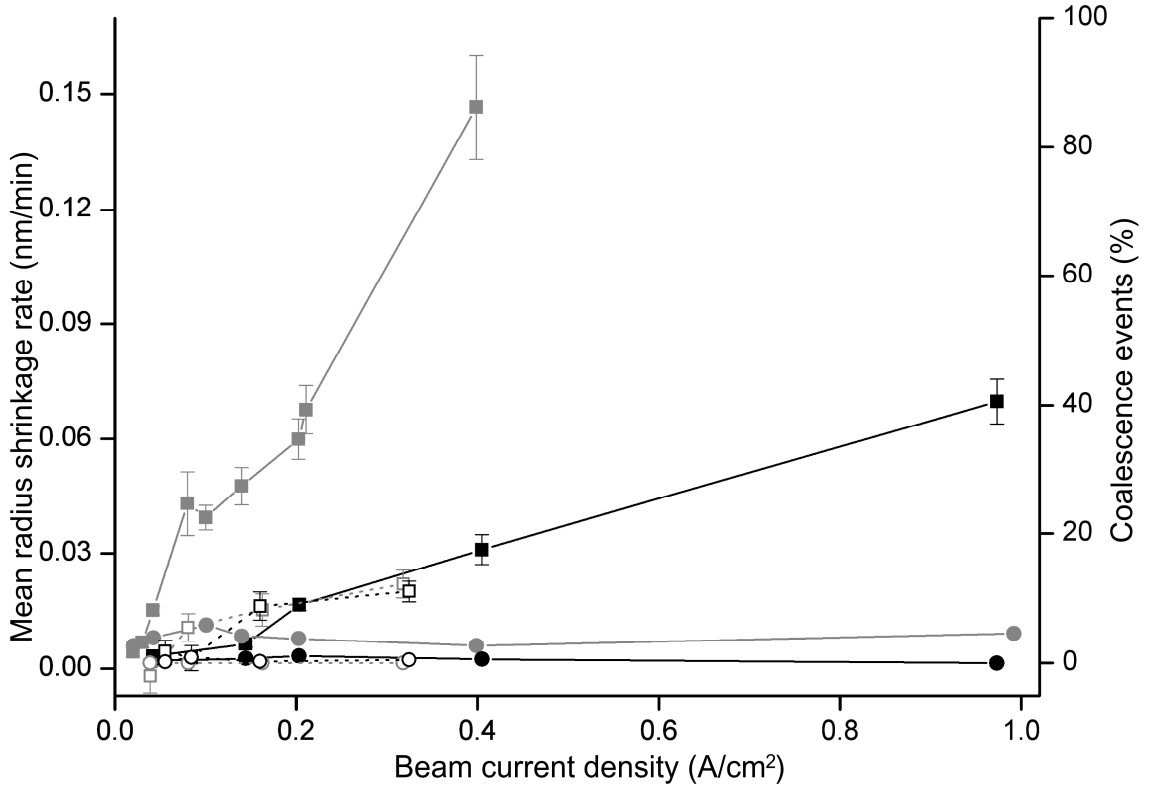

Fig. 3.8: The mean particle radius shrinkage rate (squares) and the fraction of coalescence events (circles) for Pt/Al_2O_3 (filled black), Pt/SiO_2 (filled grey), Pd/Al_2O_3 (open grey) and $Pt\text{-}Pd/Al_2O_3$ (open black) model catalysts during exposure to 10 mbar air at 400°C presented as a function of beam current density. The fraction of coalescing particles is calculated after exposure of the sample to the electron beam for 30 min. For each data point, the mean radius shrinkage rate is based on measurements on more than 30 particles and the percentage of coalescence events is calculated from 200 - 500 particles per point. Error bars refer to the standard deviation of the mean radius (eq. B.2, Appendix B).

Electron beam effects in different gas environments

To address the mechanisms of the electron beam effects, the Pt/SiO_2 sample was exposed to the electron beam in different gas environments. The radius shrinkage was absent in high vacuum (10^{-7} mbar) or 10 mbar N_2 as well as in the experiments with technical air, but with the electron beam blinded off between the first and last frame, as shown by figure 3.9 (squares). Hence, the radius shrinkage is a combined effect of the electron beam and the oxidizing gas environment.

Ca. 1 % coalescence events were also observed at 400°C in the high vacuum of 10^{-7} mbar in the electron microscope (fig. 3.9, circles) and even at the same conditions at room temperature (not shown). Interestingly, for the Pt/SiO_2 sample the coalescing particles increased to 80 % in pure N_2 even though the model catalyst is stable in pure N_2 i.e. when not exposed to the electron beam, as will be presented in detail in section 4.3.1. This shows that the artifacts from the electron beam depend on the gas composition in combination with the electron beam, and that it is necessary to evaluate the electron beam effects while exposing the catalyst to environments that are relevant for the sintering experiments.

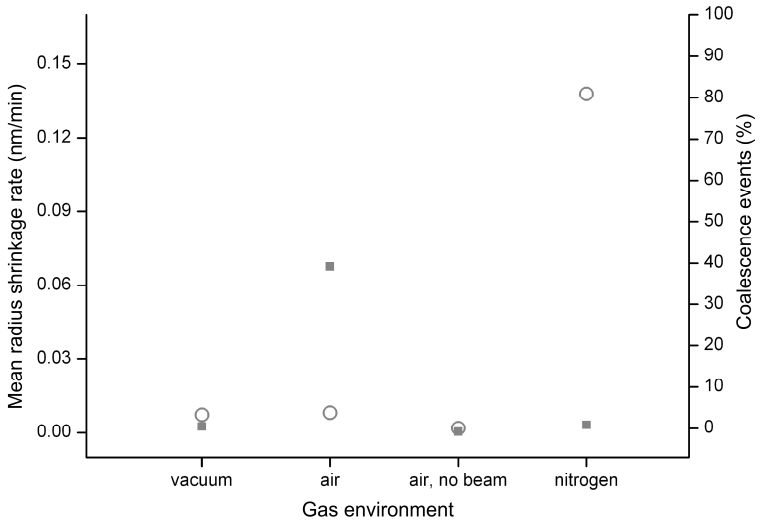

Fig. 3:9: The mean particle radius shrinkage rate (squares) and the fraction of coalescing particles (circles) for the Pt/SiO_2 model catalyst during exposure to 0.21 A/cm^2 at 400 °C in different gas environments for 30 min. For each data point, the mean radius shrinkage rate is based on measurements on 100 particles (69 particles for N_2).

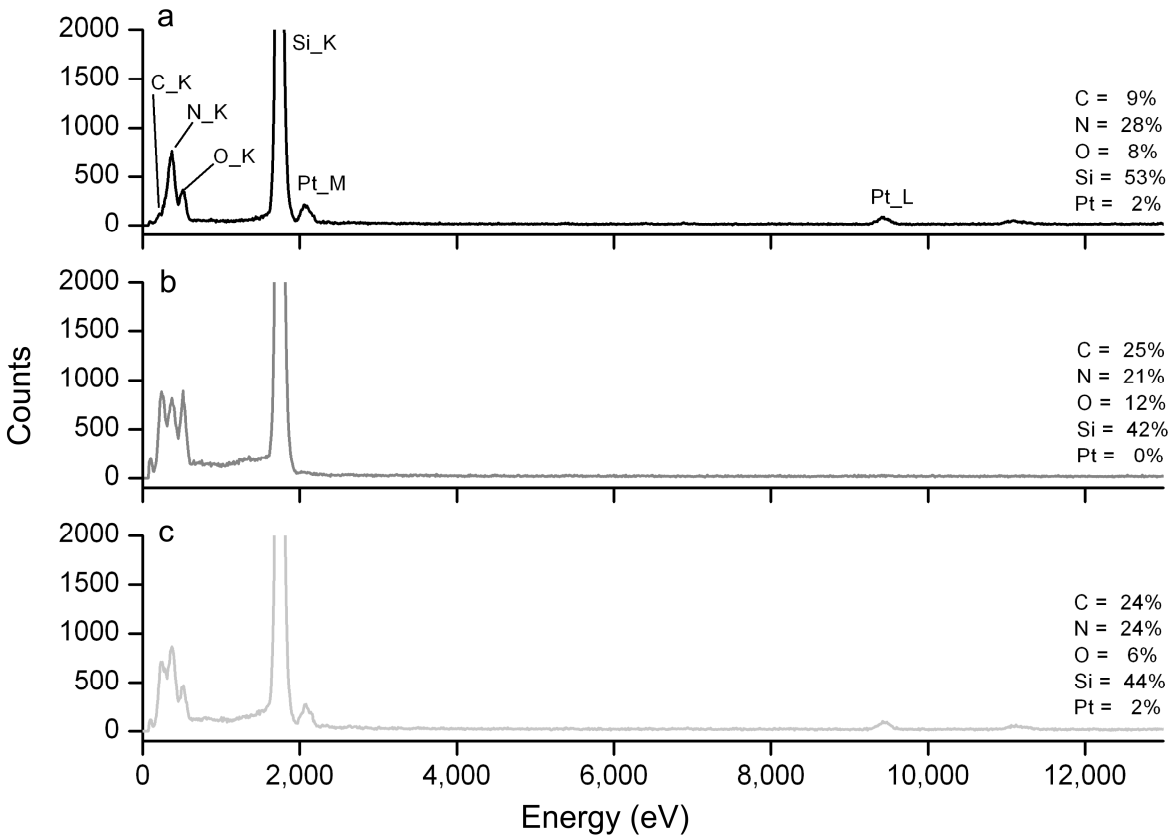

Fig. 3:10: EDS spectra of the Pt/SiO_2 sample (a) before and (b) after exposure to the electron beam at a beam current of 0.21 A/cm^2 at the same region for 2 hours in 10 mbar technical air at 400℃. (c) An EDS spectrum recorded after the treatment, but representing a region which was un-exposed to the electron beam. The quantified atomic concentration for each element is inserted in the figure.

Electron beam effects – Loss of Pt

The exposure of the Pt/SiO_2 model catalyst to 10 mbar technical air at 400°C and 0.21 A/cm^2 was repeated with a new sample for a prolonged period of 2 hours. A TEM-EDS analysis of the same region on a sample in it's as-prepared state (fig. 3.10a) and after the 2 hours beam exposure (fig. 3.10b), was performed by using a CM200 FEG UltraTwin TEM (Philips/FEI Company) with an EDS detector (EDAX). The experiments revealed a loss of Pt as seen from a reduction in the Pt L and M peak intensity. Also, a decrease in the particle density could be observed for the exposed region as illustrated in figure 3.11. The particle density did not increase when the sample was afterwards treated in H_2 at 500°C for 40 min. The Pt is therefore probably removed from the sample by the electron beam as volatile Pt-oxygen species.

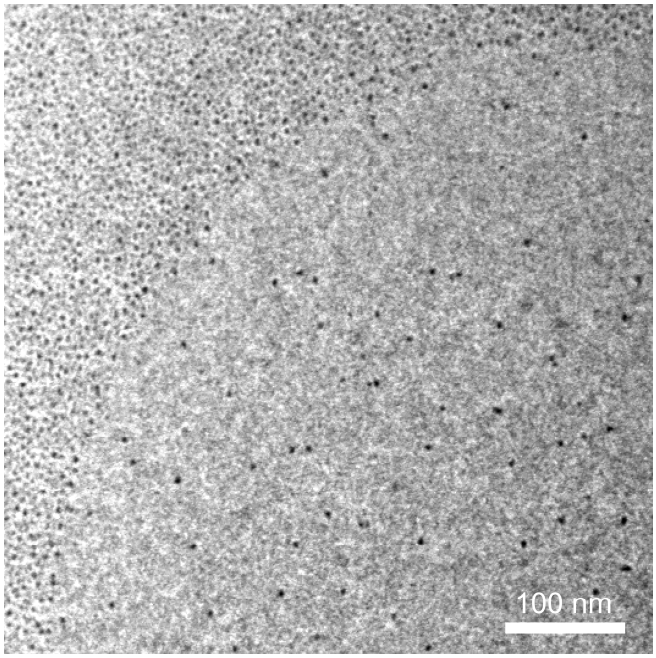

Fig. 3.11: TEM image of a region of the sample after exposure to the electron beam at a beam current density of 0.21 A/cm^2 for 1 hour in 10 mbar technical air at 400℃. A lower density of particles is observed in the region exposed to the electron beam.

In regions of the sample which were not directly exposed to the electron beam, the quantified atomic concentration was constant (fig. 3.10c), and the particle density changes abruptly at edges of the regions that were exposed to the electron beam (fig. 3.11). This shows that the dominating effects of the electron beam are not mediated through ionization of the gas phase surrounding the sample, but is localized to the surface of the exposed regions. During the sintering experiments it is therefore possible to compare regions of the sample exposed to the electron beam with un-exposed regions.

The temperature dependence of the electron beam effects

The study of the electron beam effects was repeated to address the influence of temperature variations by exposing the Pt/Al_2O_3 (filled black), Pt/SiO_2 (filled grey), Pd/Al_2O_3 (open grey) and $Pt\text{-}Pd/Al_2O_3$ (open black) samples to a constant beam current density of 0.21 A/cm^2 in 10 mbar technical air at a temperature of 200°C and 600°C (fig. 3.12). Figure 3.12 shows that the shrinkage

(squares) and the coalescence (circles) were independent of temperature in this interval for the Pt-oxide samples and approximately independent for the Pd/Al_2O_3 and $Pt\text{-}Pd/Al_2O_3$ samples.

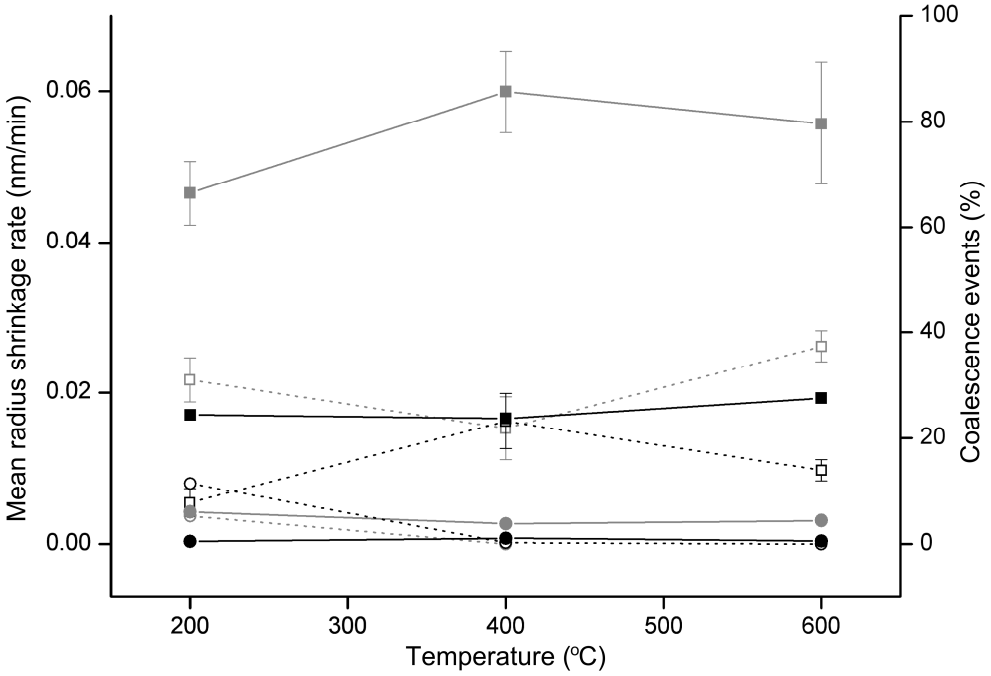

Fig. 3.12: The mean particle radius shrinkage rate (squares) and the fraction of coalescence events (circles) for Pt/Al_2O_3 (filled black), Pt/SiO_2 (filled grey), Pd/Al_2O_3 (open grey) and $Pt\text{-}Pd/Al_2O_3$ (open black) model catalysts during exposure to 10 mbar air presented as a function of temperature at constant beam current density (0.21 A/cm^2). For each data point, the mean radius shrinkage rate is based on measurements on > 30 particles and the percentage of coalescence events is calculated from 200-500 particles for each data point. Error bars refer to the standard deviation of the mean radius (eq. B.2, Appendix B).

Estimating the electron beam effects for the sintering experiments

The present series of experiments demonstrates the importance of minimizing the electron dose on the samples in order to quantitatively compare the changes in the ensemble of supported nanoparticles with sintering models with a negligible effect of the electron beam. Hence, during the sintering experiment, in situ TEM was performed using a low electron beam current density of ca. 0.07 A/cm^2 for the Pt/Al_2O_3, Pd/Al_2O_3 and $Pt\text{-}Pd/Al_2O_3$ model catalysts and 0.03 A/cm^2 for the more sensitive Pt/SiO_2 model catalyst, according to figure 3.8, in order to minimize the effect of the electron beam. To further minimize the beam dose for sample regions monitored over the prolonged periods of up to 6 hours, TEM images were only acquired every 30 min. In the intervening period, the electron beam was removed from the region and blanked. Also, for each sample, a corner of the sample window was exposed to the electron beam during the time used for alignment of the microscopes, and it was made sure that this region was not used for imaging. For the sintering experiment with the Pt/Al_2O_3 sample, the same sample regions were exposed to the electron beam for ca. 1.3 min. per image giving a total exposure time of ca. 17 min including the time needed for searching and focusing. From figure 3.8, the total Pt particle radius shrinkage caused by the electron beam can therefore be estimated to ca. 0.1 nm. For Pt/SiO_2, the total exposure time was ca. 9 min for the same region followed over time, and the beam-induced decrease in the mean Pt particle radius is also estimated to ca. 0.1 nm. Similarly the beam induced decrease in the mean radius of Pd and Pt-Pd particles was estimated to 0.1 nm for both samples. For all model catalysts the beam-induced decrease in the mean particle radius is negligible compared to the particle sizes.

Possible effects of the electron beam on the oxide support
Above, the effects of the electron beam on the supported nanoparticles have been discussed in detail. However, it could also be suggested that the electron beam induce changes in the structure of the support oxide. Such changes may influence the sintering experiment since changes in the support may change the binding energy and the diffusion rate of Pt-species at the oxide support. Also, the electron beam may induce evaporation of Pt adatoms present on the oxide support, which are not visible in the TEM images and therefore not accounted for by the analysis in this section. Despite the effort to minimize the combined effects of the gas phase and the electron beam, it is therefore possible that the influence of electron beam effects can be observed in the sintering experiments. For the sintering experiments, regions of the sample which are successively exposed to the electron beam are therefore compared to regions which were previously un-exposed to the electron beam. This comparison will be described in detail in chapter 4.

3.2.2. Ex situ TEM, STEM, AFM and SEM-EDS

Thermal aging in a tube furnace
A series of thermal aging experiments at the temperatures 450°C - 750°C were carried out with the Pt/Al_2O_3 and Pt/SiO_2 samples in 0.2 % O_2 in N_2 with a total pressure of 1 bar and a flow of 120 ml/min by using a tube furnace (Carbolite CFT). The glass tube had a diameter of 3.5 cm and a length of 110 cm. Masterflex Tygon 06409-24 tubing's were used for gas in- and outlet. Before temperature ramping, the samples were placed in a porcelain boat in the centre of the tube furnace. By using an ADM2000 universal gas flow meter (Agilent Technologies) the gas flow was measured with an estimated error of 3 ml/min at room temperature before the ramping of the temperature and after the sintering experiment when room temperature again was reached. To obtain ca. 0.2 % O_2 in N_2, a flow 20 – 25 ml/min 1 % O_2 (class 2 from Air Liquide) was added to a flow of 100 ml/min N_2 from liquid nitrogen. Based on the total gas flow, the tube dimensions and the expression for the mean squared displacement by diffusion, $x^2 = 2Dt$, with $D = 0.27$ cm^2/s the diffusion length of the O_2 was estimated to ca. 12 cm at the centre of the tube, which means that the gasses are fully mixed when reaching the samples. The temperature was ramped by 5°C/min until the chosen maximum temperature was reached which was maintained for 3 hours. The temperature was ramped down by turning off the heater current resulting in a decreasing ramping rate of ca. -2°C/min for the first 200°C. Information of the temperature was given by the tube furnace display with an estimated error of ± 7°C as determined by using an additional thermocouple which in one experiment was inserted in the tube furnace near the sample.

Post mortem characterization
The samples were mounted in a Phillips TEM standard holder and TEM images were acquired using the CM300 TEM for the Pt/SiO_2 samples and an image aberration corrected Titan 80-300ST TEM (FEI Company) for Pt/Al_2O_3. It was mainly for practical reasons that two different microscopes were used for the TEM imaging. No objective apertures were inserted. The TEM images were acquired at many different regions on the samples to make sure that the images were representative for the whole sample. In addition, the samples were inspected at low magnification, to verify the homogeneity of the particle sizes across the sample.

STEM was performed using a Titan 80-300ST TEM on the Pt/Al_2O_3 and Pt/SiO_2 model catalysts after thermal aging in the tube furnace at 650°C. The microscope was operated at primary electron energy of 300 kV and with the electron probe size less than 0.23 nm, as calibrated from the Pt(111) lattice fringe spacing. A high-angle annular dark field (HAADF) detector was used to collect

scattered electrons and ensure high contrast of the Pt nanoparticles. Images were recorded at a magnification, corresponding to a pixel size of 0.16 nm. Furthermore all images were recorded with the same contrast and brightness level for proper comparison of the different images. In the microscope, the samples were mounted with the Pt/oxide side facing upwards towards the electron beam source. The STEM imaging was carried out with assistance from Stig Helveg, Haldor Topsøe A/S.

STEM-EDS elemental mapping was performed on the bimetallic Pt-Pd/Al_2O_3 model catalyst to determine the distribution of the two metals. This was done by using a Titan 80-300ST TEM operated at 300kV with a CEOS probe corrector. The elemental mapping was carried out on an as-prepared sample as well as on a sample after an in situ sintering experiment in 10 mbar technical air at 650ºC for 6 hours. The electron probe size was less than 0.24 nm, as calibrated from the Au(111) lattice fringe spacing. A HAADF and an Oxford Inca EDX detector were used. In the microscope, the samples were mounted with the Pt/oxide side facing upwards towards the electron beam source and the holder was tilted towards the EDX detector by 20.4 degrees. The STEM-EDS elemental mapping was carried out with assistance from Chris Boothroyd, CEN, Technical University of Denmark.

Non-contact AFM (nc-AFM) was performed at room temperature on the Pt/Al_2O_3 sample after thermal aging at 650°C in an ultra-high vacuum (UHV) chamber with a base pressure below 1×10^{-10} mbar using a beam deflection nc-AFM described in [115]. The very sensitive non-contact operation mode of the AFM was chosen in order to minimize tip-induced movements of the nanoparticles. The sample was fixed on a standard Ta sample plate and introduced to the UHV through a vacuum load lock. No further sample processing was performed. The nc-AFM images were recorded in the topography mode by keeping the mean frequency shift (Δf), due to the tip-surface interaction, constant relative to a preset frequency shift value and recording the feedback signal of the tip-surface distance control as it traces the surface. A voltage was applied to the tip, relative to the sample holder, U_{bias}, which was adjusted to minimize the electrostatic forces arising from the contact potential difference [116]. To optimize the AFM resolution and to reduce the risk of mechanically pushing the clusters, high aspect ratio carbon nanotube (CNT) terminated silicon probes (Nanosensors, CNT-NCH type) with cantilever spring constants of ~42 N/m and resonance frequencies of ~330 kHz [117] were used. The AFM measurements were carried out by the AFM group at iNANO, Aarhus University.

To measure the relative amount of Pt on the model catalyst as a function of aging temperature, SEM-EDS was performed on the Pt/SiO_2 samples after thermal aging in the TEM or in the tube furnace at different temperatures with a XL30 ESEM-FEG (FEI Company) and a Quanta 600 (FEI Company) both equipped with EDAX EDS detectors. Because the Pt is only situated at the oxide surface, the surface sensitivity was increased both by recording the spectra from a 6600 μm^2 area at the thin Si_3N_4 window and by using a low acceleration voltage of 5 kV. The Pt M-line of 2.0 keV was used for quantification. The samples were fixated on an Al stub holder with plastic conductive carbon cement. To reduce charging of the samples, the measurements were conducted in wet mode with a pressure of 0.7 torr and a 500 micron pressure limiting aperture. The SEM-EDS measurements were carried out with assistance from Sven Ullmann and Chi-Manh Tran, Haldor Topsøe A/S.

3.3. Data analysis

3.3.1. Image processing and measurements

Due to the low electron beam current density in the in situ experiments, the signal-to-noise ratio (SNR) of the raw TEM frames was found by using eq. 3.1 to be ca. 2.6 which is below the SNR-value of 3-5 which is a minimum criterion for a significant signal according to the Rose condition [92].

$$SNR = \frac{n_{mean}}{\sigma_n} \tag{3.1}$$

Here n_{mean} is the mean pixel intensity and σ_n is the standard deviation of the pixel intensities [92]. To improve the signal-to-noise ratio as well as to reduce the effect of thermal drift of the sample in the TEM images, each TEM image from the in situ experiments presented in the following chapters represents the average of 6 (10 for Pt-Pd/Al_2O_3) aligned TEM frames recorded successively with an exposure time of 0.5 s and a frame rate of 1.4 frames/s, as illustrated in Fig. 3.13: (a-b). The processing increased the SNR-value to 4.5 so that the image used for the analysis approximately fulfils the Rose condition.

From the TEM images, the particle sizes were measured by manually or automatically by outlining the particle perimeters, using the software ImageJ, and the corresponding projected areas of the particles were converted to particle diameters using a circular approximation. To check the consistency of the automatic approach, images with 1000 particles were automatically and manually analyzed and the best agreement was obtained for an automatic analysis of the images processed by a Gaussian blur filter (Sigma = 3.0), and subsequently, by a Minimum (Radius = 2.0 pixels) filter (fig. 3.13c). The close agreement between the radii from manual (dotted line) and automatic (full line) measurements is illustrated for the Pt/SiO_2 sample in figure 3.5b.

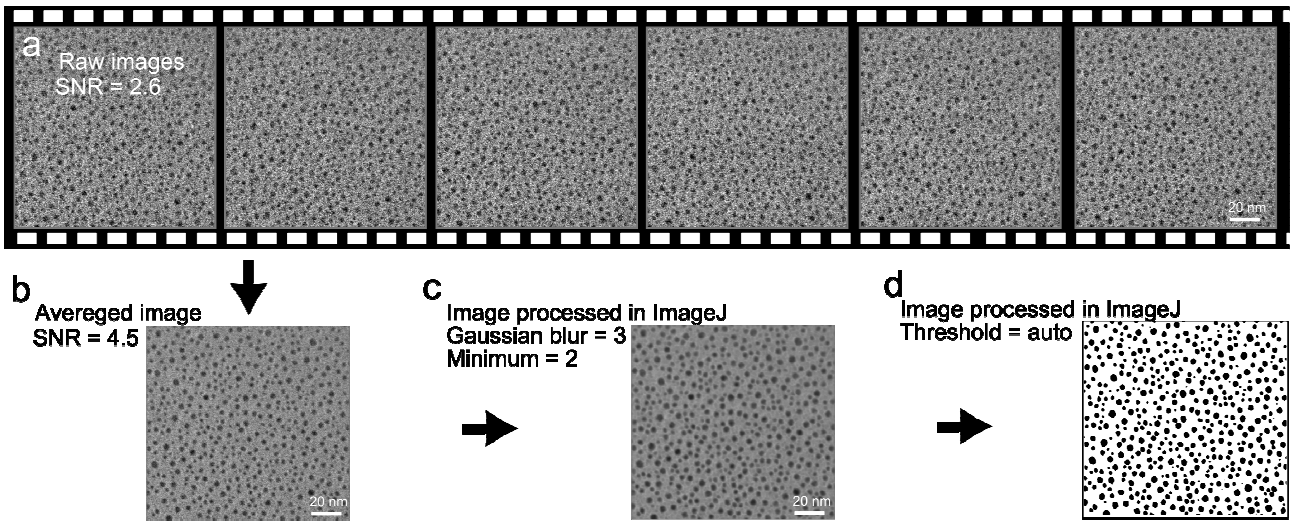

Fig. 3.13: (a) Six frames recorded successively with an exposure time of 0.5 s and a frame rate of 1.4 frames/s are (b) aligned and averaged which improves the signal-to-noise ratio from 2.6 to 4.5. For the automatic particle measurements the averaged image is processed in ImageJ with (c) the filters Gaussian blur = 3 and Minimum = 2 and (d) with automatic threshold.

The particle radii corresponding to the automatic measurements are typically presented in the form of PSDs with an optimum bin size calculated according to [118]. Due to sintering, the optimum bin size changes during the experiment and, as a compromise, the bin size is therefore calculated using the particle size measurements after 3 hours in the in situ experiment and after thermal aging at 600°C in the tube furnace experiments.

3.3.2. TEM calibration

The calibration of the TEM was carried out in the following way. A TEM image was recorded for every magnification of Au particles on a carbon film. For the highest magnifications, reference lattice distances for Au were compared with measured lattice distances from the images. The microscope post-magnification value was corrected if the distances differed more than 10 %. For low magnification images where lattice fringes were not visible, a distance of a recognizable feature was compared with the distance of the same feature on an image with higher resolution that was already calibrated.

3.3.3. Error analysis

Estimated errors

As mentioned above, the TEM was calibrated to monitor distances with a precision within at least 10 %. The contribution to the error on a measured distance, x, such as the particle radius from the TEM calibration, δx_{TEM_cal} is therefore 10 % of the measured distance, which is a conservative estimate. This error is systematic and applies for the absolute distances.

The information limit for the CM300 and the Titan TEM is ca. 0.14 nm and ca. 0.10 nm, respectively. For the sintering experiments, the TEM images were acquired using a pixel binning of 1024 x 1024 (CM300) and 2048 x 2048 (Titan) pixels and typically at magnifications corresponding to pixels sizes of 0.13 nm and 0.09 nm, respectively. This means that the image resolution is ultimately determined by the information limit of the microscopes.

For the in situ TEM sintering experiments, the gas phase, the additional drift induced by the elevated temperature and the inserted objective aperture (7.5 mrad) to enhance contrast will degrade the resolution by reducing the information limit (section 2.2.2). According the a Young's fringe test [92] the effective information limit is 0.21 nm in 10 mbar technical air at 500ºC when the objective aperture is inserted (fig. 3.14).

As described in section 3.3.1, the particle averaged diameter was found from the projected particle area by outlining the perimeter. The lack of an objective definition of the particle perimeter in the images results in a random error, $\delta x_{manual\_measure}$. The particle sizes of 10 particles were measured two times, and $\delta x_{manual\_measure}$ was estimated as the mean deviation in the measurements. Since $\delta x_{manual\_measure}$ depends on the pixel resolution and on the signal-to-noise ratio, it is estimated separately for every magnification and signal-to-noise ratio. For the in situ TEM sintering experiments $\delta x_{manual\_measure}$ typically equals the effective information limit. In cases where the estimated value of $\delta x_{manual\_measure}$ is lower than the effective information limit, the effective information limit is used as the measurement error.

To estimate the error from the automatic measurements, $\delta x_{automatic\_measure}$, particle sizes of the same 10 particles were measured automatically and manually, and $\delta x_{automatic\_measure}$ is estimated as the mean deviation in the automatic and manual measurements. The approach was used for groups of particles with different sizes, to determine the possible size dependence of the error. For particles

with diameters larger than 2 nm, $\delta x_{automatic\_measure}$ is ca. 0.5 nm and random. A disadvantage of the image processing applied for the automatic measurements (section 3.3.1) is that the sizes of the very small particles (diameters < 2 nm) are systematically overestimated. For this reason, particles with a diameter smaller than 2 nm were omitted in the present analysis. In some cases it was necessary to measure diameters below the limit of 2 nm, and in these cases manual measurements were applied.

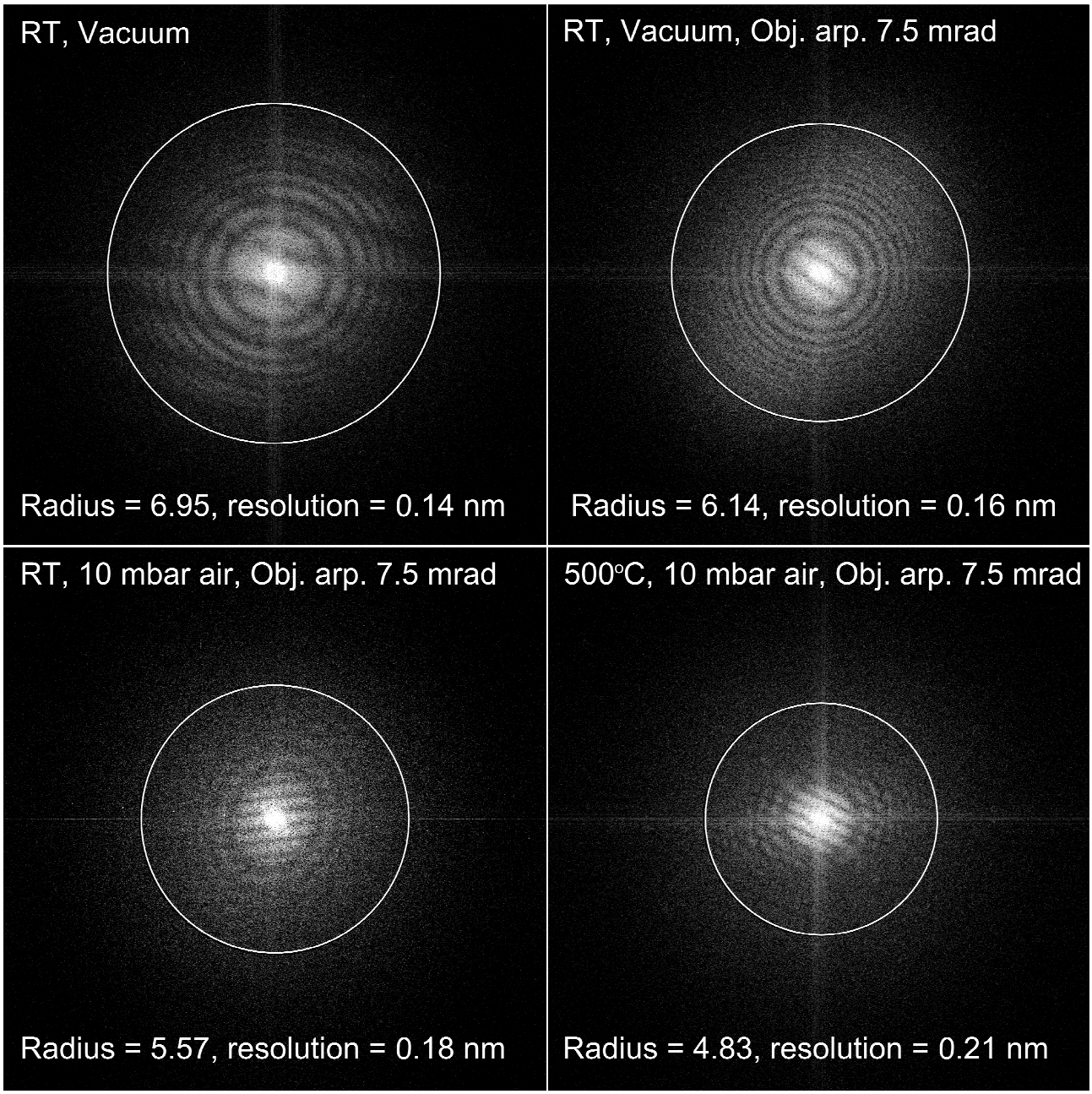

Fig. 3.14: Results from a Young's fringe resolution test. The effect on the information limit of a 7.5 mrad objective aperture, a gas pressure of 10 mbar air and of raising the temperature to 500ºC is indicated by the radius of information in reciprocal space and by the corresponding resolution in real space.

Error calculations

When absolute distances are compared, the conservative estimate, δx_{TEM_cal} is used as the estimated measuring error. When only relative distances are compared within the same experiment, δx_{TEM_cal} is not taken into account and the estimated measuring error is identical to $\delta x_{automatic\_measure}$ or

$\delta x_{manual\_measure}$. When other values are calculated from the measured diameters, such as the particle radii, the mean particle radius or the particle growth rate, dr/dt, the propagated error, δq is calculated using the standard formula [119]:

$$\delta q = \sqrt{\left(\frac{\partial q}{\partial x_1}\delta x_1\right)^2 + \ldots + \left(\frac{\partial q}{\partial x_N}\delta x_N\right)^2} \tag{3.2}$$

In theses calculations the measurement error of the image acquisition time, t and the beam current density were found to contribute insignificantly, and were therefore ignored. For figures where the error analysis deviates from this, the calculations are described in detail in Appendix B.

4. Ostwald ripening of oxide-supported Pt nanoparticles in air

This chapter presents an overview of the main in situ and post mortem results for the sintering the Pt/Al_2O_3 and Pt/SiO_2 model catalysts. Parts of these results are described in the papers I, II and III (See List of included publications)

4.1. In situ results

Sintering of the Pt nanoparticles was activated by heating the Pt/Al_2O_3 and Pt/SiO_2 model catalysts at 30°C/min. up to 650°C in an atmosphere of 10 mbar air. The TEM images were acquired after the establishment of isothermal conditions (corresponding to time t = 0 min.) and the stabilization of sample drift. The aging temperature of 650ºC was chosen for the in situ experiments because it approximately matches the maximum operation temperature of a DOC (See chapter 1) and because the relatively high aging temperature results in sintering rates sufficiently high to allow for the nano-scale dynamical changes in the model catalysts to be followed on a reasonable time scale.

4.1.1. Images of the same region as a function of time

To monitor the dynamical changes of the Pt nanoparticles in the course of time, consecutive TEM images were recorded in situ from the same region of the Pt/Al_2O_3 (fig. 4.1a-f) and the Pt/SiO_2 (fig. 4.2a-f) sample. Immediately after temperature ramping and stabilization of sample drift, the irregular shapes of the as-prepared Pt nanoparticles (fig. 3.2b) were transformed to predominantly circular projected shapes (fig. 4.1a, fig. 4.2a). Furthermore, for both samples the image series directly revealed that the Pt particles remained immobile during the experiment and that the projected areas of the Pt particles either increased or decreased. The observations cannot be due to a morphological transformation of the Pt particles, such as a wetting/non-wetting transformation [64], because the smaller particles eventually disappear and the larger particles obtain a more pronounced dark contrast, consistent with an increased particle height along the electron beam direction according to the theory of mass-thickness contrast (eq. 2.22). Hence, the observations unequivocally demonstrate that the Pt nanoparticles on both oxides sintered and that the sintering was governed by the Ostwald ripening mechanism.

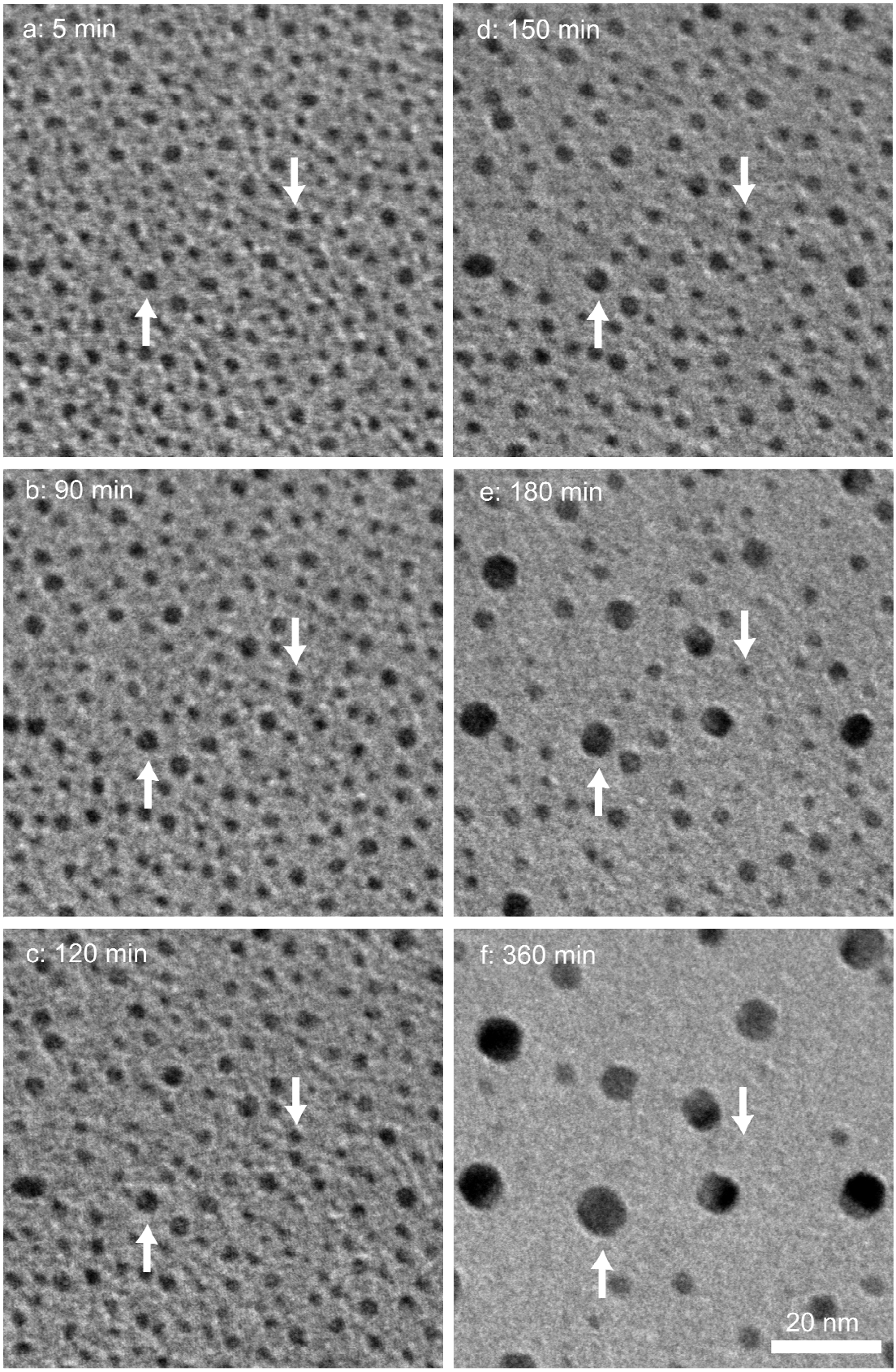

Fig. 4.1: (a-f) Time-resolved TEM images recorded in situ at the same region of a Pt/Al_2O_3 model catalyst during exposure to 10 mbar air at 650ºC. The denoted times are relative to the time at which the temperature reached 650ºC. To guide the eye, arrows indicate examples of a growing particle, and a decaying particle.

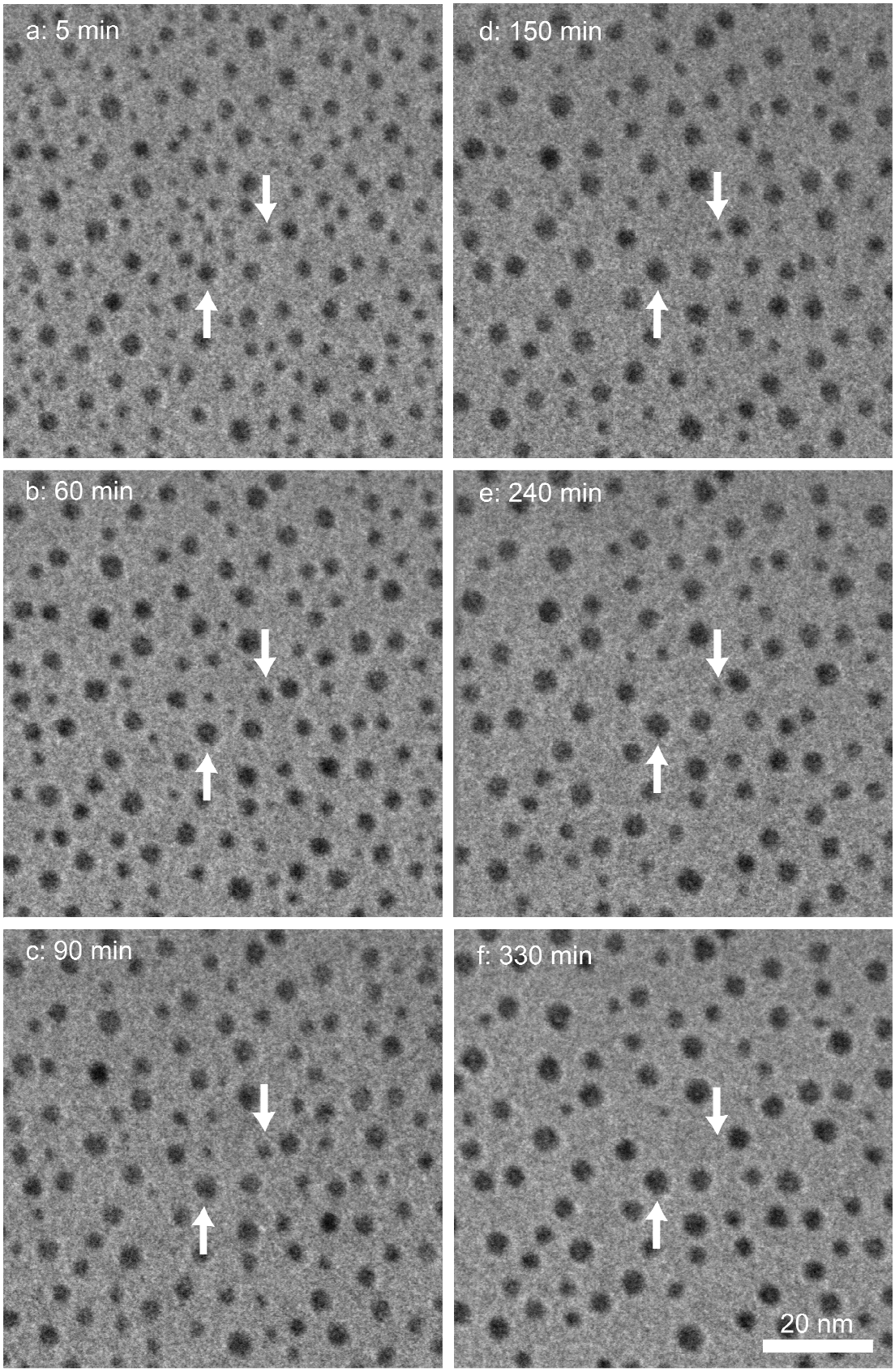

Fig. 4.2: (a-f) Time-resolved TEM images recorded in situ at the same region of the Pt/SiO_2 model catalyst during exposure to 10 mbar air at 650ºC. The denoted times are relative to the time at which the temperature reached 650ºC. To guide the eye, arrows indicate examples of a growing particle, and a decaying particle.

4.1.2. Ensemble averaged data as a function of time

To get an overview of the dynamical changes of the Pt nanoparticles observed in figure 4.1 and 4.2, the sintering process is described in the following via ensemble averaged parameters such as the mean radius, the particle density, the spread in the particle sizes and the total metal volume per support area. However, the number of particles in the fixed field of view of the full TEM images corresponding to figure 4.1 and 4.2 drops with time (from 571 to 62 particles for Pt/Al_2O_3 and from 321 to 158 particles for Pt/SiO_2) and an analysis with a high counting statistics can therefore not be based on these alone. Therefore, the observations are complemented by a more thorough statistical analysis. This analysis is based on a larger number of TEM images that were acquired during the in situ experiment, but at regions on the sample that were previously un-exposed to the electron beam. A benefit of this approach is also, that effects of the electron beam which still may influence the data for the region followed over time, even after the careful minimization procedure undertaken, are eliminated in the statistical analysis (section 3.2.1.3). For the ensemble averaged parameters obtained from the additional images, the counting statistics is high (ca. 600-2000 particles for Pt/Al_2O_3 and ca. 700-2000 particles for Pt/SiO_2) relative to the data obtained from the regions followed over time.

Figure 4.3a presents the mean particle radius for Pt/Al_2O_3 (black) and for Pt/SiO_2 (grey) obtained from (open symbols) the images of the region followed over time and (filled symbols) the images of the additional regions. For both samples, the overall time-dependent trend of the mean radius is similar for the regions followed over time and the additional regions, but for Pt/Al_2O_3, the mean radius increases slower with time than for the region followed over time relative to the additional regions. This deviation is discussed below in section 4.1.6, and the following discussion of the ensemble averaged parameters is focused on the larger statistical dataset obtained from the additional regions.

For the Pt/Al_2O_3 model catalyst, the mean radius remains almost stable in the initial period, but increases rapidly after ca. 100 min and subsequently becomes roughly constant with time. The reported time-dependence of the averaged sintering rate is usually characterized by an initial stage with a high growth rate, followed by a decreasing growth rate [11,12,15,16,19,21,23,26,53]. But for Pt/Al_2O_3 in an oxidizing environment, an initial stage with a low sintering rate followed by higher rates has previously been reported [11] in agreement with the result presented in figure 4.3a. Figure 4.3b shows that the particle density of Pt/Al_2O_3 (black filled symbols) is high in the initial stage and is reduced with time until it stabilizes when the mean radius stabilizes. The figures 4.3a-b therefore agree that the sintering rate slows down in the final sintering stage. That the mean radius is almost stable in the initial stage (fig. 4.3a, black filled symbols) does not indicate that the sintering has not initiated at this stage, since the sintering process indeed proceeds as can be seen from the decrease in particle density (fig. 4.3b, black filled symbols). The standard deviation of the particle radius for Pt/Al_2O_3 is presented in figure 4.3c (black, filled symbol). Initially, the standard deviation is small reflecting a narrow spread in the particle sizes. The spread in the particle sizes increases at the onset of the increase in the mean particle radius. Finally both the mean radius and the particle spread remain almost constant. The similarity between the trend of the mean radius vs. time and the standard deviation vs. time shows that the sintering process results in a spread in the particles sizes, and could furthermore suggest that the sintering rate is related to the spread of particle sizes.

For Pt/SiO_2 the increase in the mean radius is almost linear as a function of time (fig. 4.3a, grey filled symbols). The increase in the mean radius of Pt/SiO_2 is much smaller compared to Pt/Al_2O_3, which apparently indicates that the sintering rate for Pt nanoparticles on SiO_2 is lower than on Al_2O_3 at 650ºC in the oxidizing environment. Also, the particle density for Pt/SiO_2 (fig. 4.3b, grey filled symbols) decreases with time as was observed for Pt/Al_2O_3, but with a lower rate, consistent

with the lower sintering rate (fig. 4.3a). The lower sintering rate for Pt/SiO_2 relative to Pt/Al_2O_3 is surprising, since a higher [53,77] or comparable [59] degree of sintering was previously reported for Pt/SiO_2 relative to Pt/Al_2O_3 at $T \geq 600$ºC in oxygen. The deviation could either result a) from differences in the structure of the two model catalysts, such as the slightly higher degree of the surface roughness of the SiO_2 relative to the Al_2O_3 (fig. 3.3) or b) from a difference in the experimental conditions in the present study and in the previous, such a very low total pressure in the in situ experiment (10 mbar) compared with that of the post mortem studies (1 bar) [53,59,77]. In section 4.3.1 it will become clear that the deviation is likely explained by the difference in the total gas pressure.

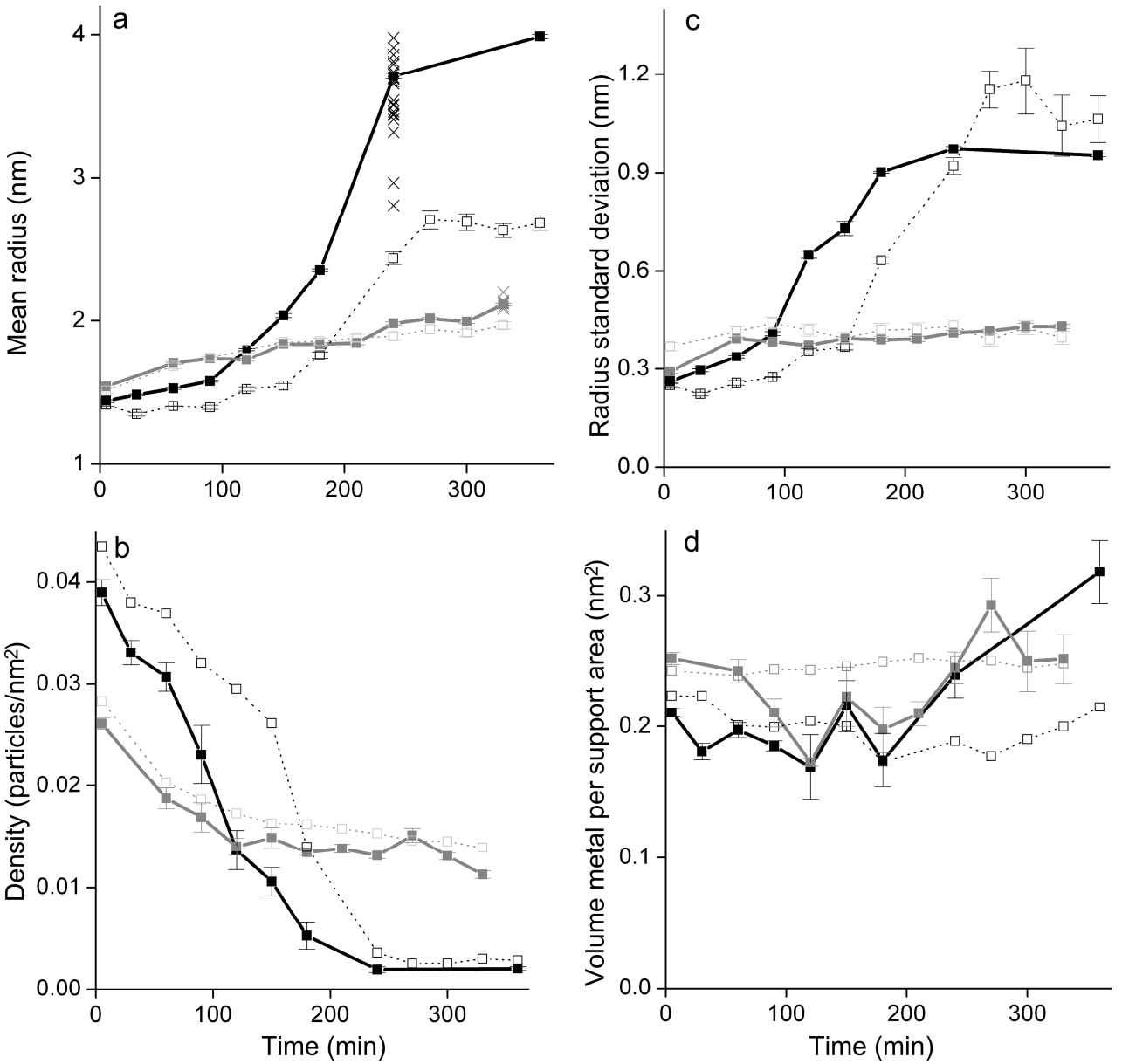

Fig. 4.3: (a) The mean particle radius, (b) the particle density, (c) the standard deviation of the radii and (d) the Pt metal volume per support area as a function of aging time for particles in an region followed over time (open symbols) and for regions previously unexposed to the electron beam (filled symbols) for Pt/Al_2O_3 (black) and Pt/SiO_2 (grey). (a) An example of the statistical spread in mean particle radius for different regions on the sample is presented for Pt/Al_2O_3 at 240 min (black x's) and for Pt/SiO_2 at 330 min (grey x's). Error bars: See Appendix B.

It is interesting to observe that the sintering rate is similar for both model catalysts (or slightly higher for Pt/SiO_2) during the initial stage, where the spread in particle sizes is similar (or slightly higher for Pt/SiO_2) and that the sintering rate becomes higher for Pt/Al_2O_3 relative to Pt/SiO_2 after the spread in the particle sizes of Pt/Al_2O_3 becomes higher than for Pt/SiO_2 (fig. 4.3a,c). This observation is consistent with the suggestion from an early theoretical study that the sintering rate scales with the spread in particle sizes [49]. The coupling between narrow PSDs and low initial sintering rates suggests that one route to slow down the deactivation of industrial catalysts through sintering could be to aim for very narrow initial PSDs. This may prolong the meta-stable initial state, resulting in higher total activity.

4.1.3. PSDs as a function of time

To obtain more detailed information from the statistical data than what is presented by the temporal evolution of the mean radius, time-resolve PSDs were generated. The PSDs can be generated from the images of the region followed over time or from the additional images. Figure 4.4a-f presents PSDs derived from measurements on TEM images of in the region followed over time for the Pt/Al_2O_3 sample. According to figure 4.4, a tail of larger particles develops on the large particle side of the mean peak of the PSD and consequently the distribution broadens as a function of time. However, since the number of particles in the fixed field of view drops with time the shape of the PSDs become less well defined.

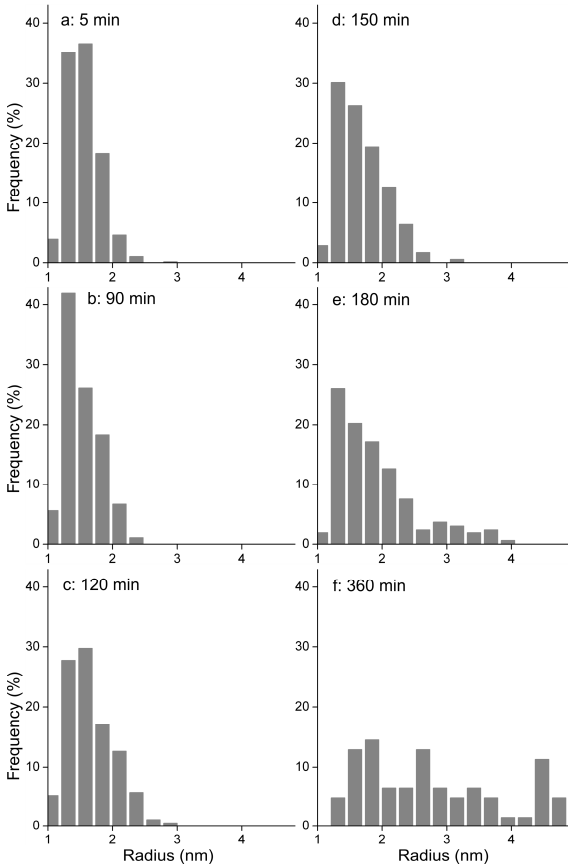

Fig. 4.4: (a-j) PSDs for the Pt/Al_2O_3 model catalyst based on measurements from the full TEM images of figure 4.1. The number of measured particles included in each distribution is (a) 571, (b) 370, (c) 403, (d) 355, (e) 158 and (f) 62.

PSDs for Pt/Al_2O_3 and Pt/SiO_2 based on the additional regions are presented in figure 4.5 and 4.6, respectively. Qualitatively, figure 4.5 reveals changes in the Pt nanoparticle sizes similar to the observations in figure 4.4. The number of particles in the PSDs in figure 4.5 (and figure 4.6) is, however, considerably higher than for figure 4.4 (the exact numbers are given in the figure caption), which makes it possible to characterize the shape of the PSDs of figure 4.5 and figure 4.6 in detail. The following discussion will therefore focus on the larger statistical dataset (fig. 4.5, fig. 4.6) instead of the PSDs generated from the region followed over time for Pt/Al_2O_3 (figure 4.4) and Pt/SiO_2 (not shown).

For both samples, the PSD broadens as a function of time and the main peak is shifted towards the larger particle sizes (fig. 4.5 and 4.6). For Pt/Al_2O_3, the PSD obtains a shoulder to the large particle side of the main peak. The shoulder grows over time while the main peak decreases, so that the PSD almost obtains a bimodal character. By the end of the experiment an asymmetric PSD with one main peak and a tail towards the small particles sizes is observed. For Pt/SiO_2, a moderate shift and broadening of the main peak is observed. The larger shift in position of the main peak for Pt/Al_2O_3 relative to Pt/SiO_2 is consistent with figure 4.3a. A shoulder, a bimodal character, or an asymmetric shape is not clearly observed for Pt/SiO_2, but it cannot be excluded that such features would be observed for Pt/SiO_2 if this catalyst was aged long enough to obtain a similar shift in the position of the main peak.

4.1.4. Comparison with the LSW model

As described in the section 2.1.1, the LSW model was established to describe Ostwald ripening, but the reported PSD shapes of industrial catalyst after thermal aging do not match the stationary PSD shape as described by the LSW model. Since a) the sintering of the Pt nanoparticles on both oxides is governed by the Ostwald ripening mechanism (fig. 4.1, fig. 4.2) and b) the present model catalysts mimic the basic assumption of the theoretical models (a flat, homogeneous support layer), it should in principle be possible to test if the Ostwald ripening mechanism actually leads to the PSD shape described by the LSW model. It should be noticed that such a test assumes that the samples are aged for a sufficiently long time to obtain the stationary PSD shape.

In the figures 4.5f and 4.6f, a two-dimensional version of the LSW model [120] is fitted to the final PSDs for Pt/Al_2O_3 and Pt/SiO_2, respectively (black line). For Pt/Al_2O_3, the PSD shape at the end of the experiment has the characteristic shape described by the LSW model, i.e. an asymmetric shape with a tail towards the small particle sizes and the fit matches closely to the experimental data (fig. 4.5f). For Pt/SiO_2 the LSW model can also be fitted to the data. Because of the more symmetrical PSD shape for Pt/SiO_2, the LSW model does not fit the experimental data as well at the large particle size side of the main peak. It is possible that the aging time for Pt/SiO_2 was to short for this sample to obtain a stationary PSD shape.

The comparison between the LSW model and the experimental observations (fig. 4.5f, fig. 4.6f) shows that the Ostwald ripening mechanism can lead to the PSD shape described by the LSW model. An explanation for why the PSD shape described by the LSW model is found in this study in contrast to studies on technical catalysts could therefore be that the present uniform support resemble the assumptions underlying the LSW model closer than the inhomogeneous support structures of technical catalysts.

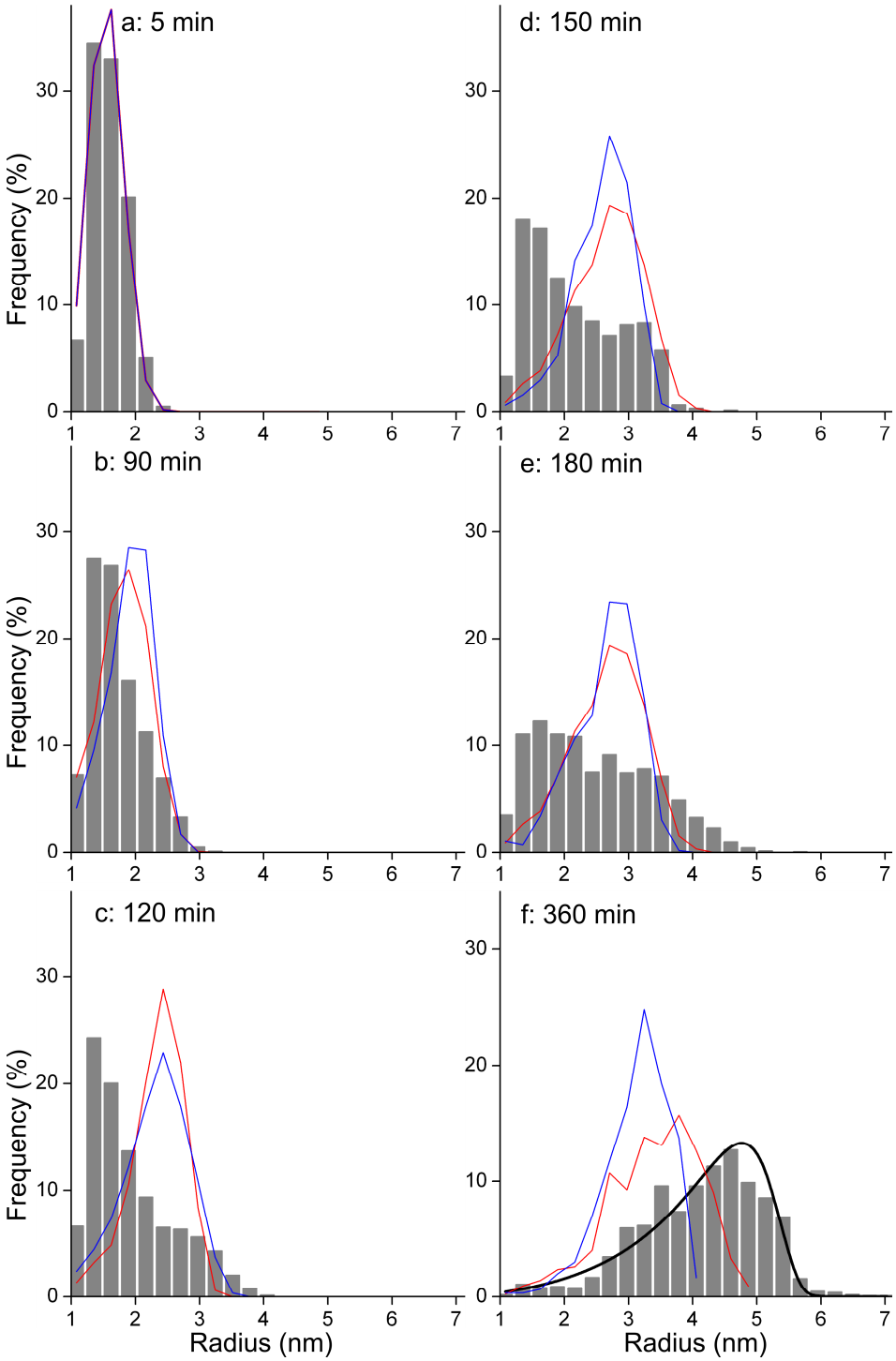

Fig. 4.5: (a-f) PSDs from Pt/Al_2O_3 based on TEM images of regions previously unexposed to the electron beam recorded during the exposure to 10 mbar air at 650ºC. The indicated aging times correspond to the aging times in figure 4.1. The number of measured particles included in each distribution is (a) 2078, (b) 1697, (c) 1800, (d) 600, (e) 1312 and (f) 1001. (f) The LSW model is fitted to the data (black). (a-f) Simulated histograms based on the interface-controlled (red) and diffusion-controlled (blue) ripening models (Eqs. 2.13 and 2.14, respectively) are indicated by lines. The initial PSDs used for the simulations are Gaussian distributions with mean and width corresponding to the PSD in (a). The number of particles drops throughout the simulation from (a) 4950 to (b) 2865, (c) 1367, (d) 910, (e) 788, and (f) 421 for the interface-controlled model and from (a) 4950 to (b) 2128, (c) 964, (d) 643, (e) 564, and (f) 299 for the diffusion-controlled model.

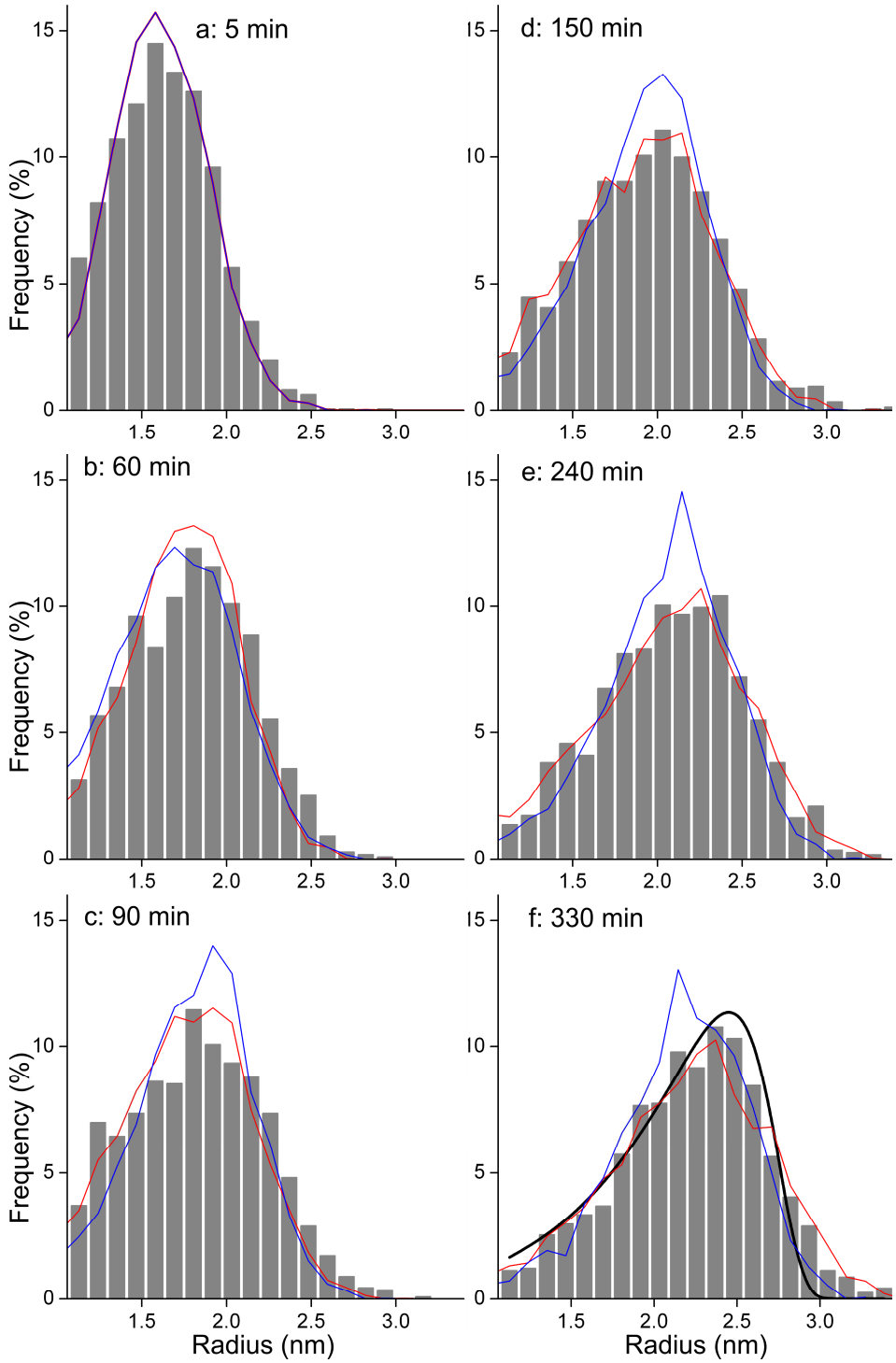

Fig. 4.6: (a-f) PSDs from Pt/SiO_2 based on TEM images of regions previously unexposed to the electron beam recorded during the exposure to 10 mbar air at 650ºC. The indicated aging times correspond to the aging times in figure 4.2. The number of measured particles included in each distribution is (a) 1593, (b) 2059, (c) 1101, (d) 1225, (e) 1095 and (f) 1134. (f) The LSW model is fitted to the data (black). (a-f) Simulated histograms based on the interface-controlled (red) and diffusion-controlled (blue) ripening models (Eqs. 2.13 and 2.14, respectively) are indicated by lines. The initial PSDs used for the simulation are Gaussian distributions with mean and width corresponding to the PSD in (a). The number of particles drops throughout the simulation from (a) 4933 to (b) 4013, (c) 3545, (d) 2853, (e) 2209, and (f) 1804 for the interface-controlled model and from (a) 4933 to (b) 3520, (c) 3019, (d) 2369, (e) 1814, and (f) 1503 for the diffusion-controlled model.

Since the LSW model only describes the stationary PSD shape, it should not be expected that the model can be fitted to the PSD in the transition stages before the stationary shape. This is the reason for only fitting the model to the final PSD in the experiments (Pt/Al_2O_3: 360 min, Pt/SiO_2: 330 min). Also, it can immediately be seen that the characteristic asymmetric PSD shape with a long tail towards the small particle sizes as described by the LSW model does not fit the observed transitions shapes (fig. 4.5b-e, fig. 4.6b-e). The mismatch is especially obvious between the LSW model and the transition shapes of Pt/Al_2O_3 (fig. 4.5b-e). This shows that the method of deducing the sintering mechanism from observations of specific PSD shapes, as suggested and discussed in the literature [11,12,39,46-54] may not be straight forward because one specific sintering mechanism can result in several different transition shapes (fig. 4.5b-e) before the characteristic shape predicted by the LSW model is obtained.

4.1.5. Comparison with computer simulations

The comparison of the theoretical models for Ostwald ripening with the experimental observations can be carried out in more detail by using of computer simulations, because the simulations of the temporal evolution of the PSD allows for comparison for the sintering stages before the stationary PSD shape is obtained.

By using eqs. 2.13 and 2.14 the time-evolution of the PSD was calculated numerically following the procedure described by De Smet et al. [55]. Specifically, Gaussian PSDs with mean values and widths equal to the initial PSDs of Pt/Al_2O_3 (fig. 4.5a) and Pt/SiO_2 (fig. 4.6a) were used as the initial PSDs and discrete time steps of 0.5 min were chosen. The simulations were performed with $\alpha_i = \alpha_d = 1$ corresponding to a constant particle shape (hemisphere), and by iteratively varying the constants α_i' and α_d'/ln(L/r) in eqs. 2.13 and 2.14, until the mean particle radius of the simulated distribution fitted the observed mean particle radius in figure 4.3a best for all times. Simulated particles with radii shrinking to values below a limit of 0.05 nm were removed from the dataset. For Pt/Al_2O_3, the iterative procedure resulted in α_i' = 0.16 $nm^{-1} \cdot min^{-1}$ and α_d'/ ln(L/r) = 0.38 $nm^{-1} \cdot min^{-1}$ for the interface- and diffusion-controlled ripening models respectively. For Pt/SiO_2, the iterative procedure resulted in α_i' = 0.035 $nm^{-1} \cdot min^{-1}$ and α_d'/ ln(L/r) = 0.067 $nm^{-1} \cdot min^{-1}$ for the interface- and diffusion-controlled ripening models respectively. In the present PSD simulations, the term ln(L/r) is considered constant for the following reasons: (a) the relation between r and L is not a priori known (b) using a constant L for all particles sizes, relies on the assumption that $L > r$ at all times for all particles, or else $dr/dt \rightarrow \pm\infty$ for $r \rightarrow L$ (eq. 2.14). This leads to an inconsistency with the mean-field assumption, since the size of the largest particles (Pt/Al_2O_3: $r \approx 2.2$ nm at $t = 5$ min, Pt/SiO_2: $r \approx 2.5$ nm at $t = 5$ min) exceeds the mean distance between the edges of the nearest neighboring particles (Pt/Al_2O_3: ca. 1.4 nm at $t = 5$ min, Pt/SiO_2: ca. 1.5 nm at $t = 5$ min). The colored lines in figure 4.5 and 4.6 indicate the simulated PSDs for the interface-controlled (red) and the diffusion-controlled (blue) ripening.

For Pt/Al_2O_3, the shape of the simulated PSDs over time transforms by gradually shifting the main peak towards larger particle sizes and by developing a tail towards the small particles sizes. By the end of the simulation, the simulated PSDs (fig. 4.5f, red or blue) therefore have shapes that resemble the PSD shape described by the LSW model (fig. 4.5f, black), which is also characteristic for the observed PSD for Pt/Al_2O_3 by the end of the experiment (fig. 4.5f). The simulations and experimental observations also deviate: the simulated PSDs do not develop a shoulder to the right side of the main peak or the bimodal character as observed for the Pt/Al_2O_3, and the position of the main peak is different for the simulated and experimentally observed PSDs. The experimentally

observed transition PSDs are therefore not expected from the theoretical models even though the PSD by the end of the experiment is well-described by the LSW model.

For Pt/SiO_2, the simulated PSDs match the experimental observations well for all aging times (fig. 4.6a-f, red and blue) since both simulated and experimentally observed PSDs gradually shift their main peaks towards the larger particles sizes, and become slightly asymmetric with tails towards the small particle side. The theoretical models (fig. 4.6f, red and blue) therefore describe the sintering of Pt/SiO_2 very well, which was not as clearly observed from the fit of the LSW model alone (fig. 4.6f, black).

The PSDs, based on the diffusion-controlled ripening model, are slightly narrower for most aging times (fig. 4.5, fig. 4.6, blue) than the PSDs based on the interface-controlled model (fig. 4.5, fig. 4.6, red), consistent with previous studies [11,121]. For Pt/SiO_2 interface controlled Ostwald ripening (fig. 4.6a-f, red) seems to fit the experimental observation slightly better than the diffusion controlled ripening (fig. 4.6a-f, blue). According to an early theoretical study, this is expected since the interface-controlled ripening should dominate over diffusion controlled ripening for catalysts with a relatively high metal loading and thus small diffusion distances between the nanoparticles as is characteristic for the present model catalysts [49]. The differences between the simulated interface and diffusion controlled ripening is most pronounced by the end of the simulation where the number of simulated particles is relatively low (fig. 4.5, fig. 4.6, figure captions) and the difference may therefore not be statistically significant. Both the diffusion and the interface-controlled process may therefore contribute to the ripening in the present experiments.

4.1.6. Deviations: the region followed over time vs. the additional regions.

The regions followed over time have been exposed to the same experimental conditions as the additional regions, except that the region followed over time was exposed to the electron beam every 30 min, while the additional regions were not exposed to the electron beam before image acquisition. As described, a number of precautions were taken to minimize the combined effects of the electron beam and the gas phase (section 3.2.1.3). Effects of the electron beam, that may influence the region followed over time in spite of these precautions, should be revealed by a comparison of the TEM images of these regions with images of the additional regions, provided that the regions followed over time are statistically representative.

In figure 4.3a-c the mean radius, the particle density and the radius standard deviation for the regions followed over time (open symbols) were compared to the same parameters for the additional regions (filled symbols) for Pt/Al_2O_3 (black) and for Pt/SiO_2 (grey). The mean particle radius obtained from the single TEM images of the additional regions is presented at one aging time (fig. 4.3a, Pt/Al_2O_3: 240 min, Pt/SiO_2: 330 min, x's) which indicates how statistically representative the region followed over time can be expected to be.

For Pt/SiO_2, the mean radius is almost identical throughout the experiment for the region followed over time and for the additional regions. Also the particle density and the radius standard deviation generally agree for the two types of regions. The combined effects of the electron beam and the gas phase must therefore be negligible for this catalyst under the present conditions.

For Pt/Al_2O_3, the overall trend of the time-dependence of the mean radius for the region followed over time equals the time-dependence of the same parameter for the additional regions, but quantitatively the mean radius is lower for the regions followed over time. It should be noticed that the statistical spread is much higher for the Pt/Al_2O_3 compared to Pt/SiO_2 (fig. 4.3a, x's), and likely the statistical spread is the reason for the discrepancy between the region followed over time and the additional regions. However, it can not be ruled out that the difference also partly results

from beam-induced changes in the structure of the support oxide in such a way that the diffusion rate over the support is decreased or from the removal of free diffusing Pt-oxygen species from the sample by the electron beam as discussed in section 3.2.1.3.

To investigate the possibility of beam-induced evaporation of Pt, the Pt volume per support area was estimated by using a hemispherical shape approximation to the projected Pt particle outlines in the TEM images. As presented in figure 4.3d (Pt/Al_2O_3: black, Pt/SiO_2: grey), this estimate does not reflect a significant loss of the Pt amount over time. For Pt/Al_2O_3, an apparent volume increase is observed after 300 min for the dataset obtained from the additional regions (fig. 4.3d, black, filled symbols). Because heavy constituents were not added to the catalyst during the ageing treatment, the difference most likely reflects the crudeness of the shape approximation. Variations of size-dependent particle shapes could falsely indicate an apparent coverage increase. From the current data it is not possible to address the three-dimensional particle shapes due to the projected geometry of the images. However, figure 4.3d gives a rough indication that significant amounts of Pt are not lost as a result of the exposure to the electron beam.

Despite the volume calculations, minor effects due to the electron beam can not fully be ruled out, but it should be recognized that there is consistency in the qualitative and quantitative trends of the data for the regions followed over time and the additional regions. This confirms that the electron beam effects cannot be dominating the sintering. Specifically, the Ostwald ripening mechanism, which is directly suggested by the time-resolved TEM images of the regions followed over time (fig. 4.1, fig. 4.2) is not dominated by beam effects, and the statistical data from the additional TEM images (fig. 4.3, solid symbols, fig. 4.5, fig. 4.6) is not influenced by the beam effects (section 3.2.1.3). Thus the approach of acquiring images of both the regions followed over time and the additional regions in combination gives a) direct evidence of the sintering mechanism (fig. 4.1, fig. 4.2) and b) statistical data for comparison with theory which is not influenced by electron beam effects (fig. 4.3 filled symbols, fig. 4.4, fig. 4.5).

4.2. Post mortem results

For comparison with the in situ results described above, the Pt/SiO_2 and Pt/Al_2O_3 samples were thermally aged in a tube furnace during exposure to a similar O_2 partial pressure as in the in situ experiments. Specifically, the samples were exposed to 1 bar 0.2 % O_2 in N_2 for 3 hours at 450°C, 550°C, 600°C or 650°C. After thermal aging the samples were transferred to the TEM for post mortem image acquisition. The samples were exposed to air during transfer and during storing.

4.2.1. Images and PSDs as a function of temperature

Figure 4.7 shows TEM images of the as-prepared and aged Pt/SiO_2 (a-e) and Pt/Al_2O_3 (f-j) model catalysts. The thermal ageing procedure results in an increase of the particle sizes and a reduction of the particle density (fig. 4.7b-e, g-j). The TEM images reveal that the onset temperature of sintering is ca. 550°C for Pt/SiO_2 and 600°C for Pt/Al_2O_3 in agreement with [10,13,16,19,21,47,53,56,58-60]. The lower onset for sintering in an oxidizing environment for SiO_2-supported Pt relative to Pt supported on Al_2O_3 is consistent with [59]. Thus Al_2O_3 appears to better stabilize the Pt nanoparticles than SiO_2 in the low temperature range.

While the images of the as prepared samples show irregular particle shape projections (fig. 4.7a, e), images of both Pt/SiO_2 and Pt/Al_2O_3 after aging at 450°C show generally circular projected shapes (fig. 4.7b, g). After aging the Pt/SiO_2 sample at higher temperatures (600°C - 650°C), variations from the circular shape, such as triangular and square shapes can be observed for the larger particles (fig. 4.7d – e, inserts). For the Pt/Al_2O_3 sample, the square particle projection shape is also observed (fig. 4.7i-j, inserts), but the triangular shape is not clearly observed and the facetted shapes are generally less pronounced.

To quantitatively describe the extent of the nanoparticle sintering, PSDs were generated from the TEM images corresponding to the different aging conditions in figure 4.7. Figure 4.8 presents the PSDs from the Pt/SiO_2 samples (a-e) and the Pt/Al_2O_3 samples (f-j). As a function of ageing temperature, the main peak of the PSDs broadens and shifts towards the larger particles sizes. Moreover, the shape of the PSDs changes differently for the two model catalysts as the temperature increases.

For Pt/Al_2O_3, the PSD shape broadens toward larger particle sizes and obtains a shoulder to the large particle side of the main peak (fig. 4.8i). At 650°C the PSD shape flips over so that a main peak at ca. 2.6 nm is associated with a tail toward smaller sizes (fig. 4.8j). These shape changes are qualitatively similar to the shape changes observed for the PSDs of Pt/Al_2O_3 from the in situ experiment (fig. 4.5).

For Pt/SiO_2, the PSD broadens, develops a long tail to the large particle side at 550°C (fig. 4.8c) and obtains a more symmetrical shape at higher temperatures (fig. 4.8d,e). The tail to the large particle side of the main peak (fig. 4.8c) is associated with the formation of larger particles with a significantly diminished particle density in their vicinity (fig. 4.7c). The observation suggests that Pt sintering was influenced by local correlations between a Pt nanoparticle and its nearest neighbors. The effect of the local correlations appears to be less pronounced at higher temperatures, because the PSD obtains the more symmetrical shapes (fig. 4.8d,e) and because the particle density appears uniform over the support (fig. 4.7d,e). The long tail to the large particle side was not observed from the in situ experiments, but the more symmetrical shapes observed at 650ºC resemble qualitatively the PSD shapes observed in situ (fig. 4.6).

4.2.2. Comparison with the LSW model

The LSW model for a two-dimensional system [120] is fitted to the PSDs for Pt/SiO_2 (fig. 4.8e, solid line) and for Pt/Al_2O_3 (fig. 4.8j, solid line) after thermal ageing at 650ºC.

The theoretical model describes the PSD corresponding to Pt/Al_2O_3 well at 650ºC (fig. 4.8j, solid line), which shows that the experimental observations are consistent with an Ostwald ripening mechanism. This result is also consistent with the in situ observations (fig. 4.5f, black line). The LSW model will obviously not describe the PSD shapes at the lower ageing temperatures well, in particular not the PSD at 600°C (fig. 4.5i) which suggests that this PSD is not stationary.

Because of the more symmetrical shape of the PSD corresponding to Pt/SiO_2 at 650ºC, the LSW model does not fit the data for Pt/SiO_2 as well as the data for Pt/Al_2O_3. Possibly, the PSD has not obtained its stationary shape which explains the symmetrical shape. This explanation is consistent with the comparison of the in situ observations with computer simulations presented in section 4.1.5. The present post mortem observations, however, also suggest an alternative explanation: the deviation from the PSD shape described by the LSW model at 650ºC (fig. 4.8e, solid line) could possibly result from the local correlations between the nanoparticles, which is not included in the fitted LSW model, but was clearly observed at lower temperatures (fig. 4.7c, fig. 4.8c). Including

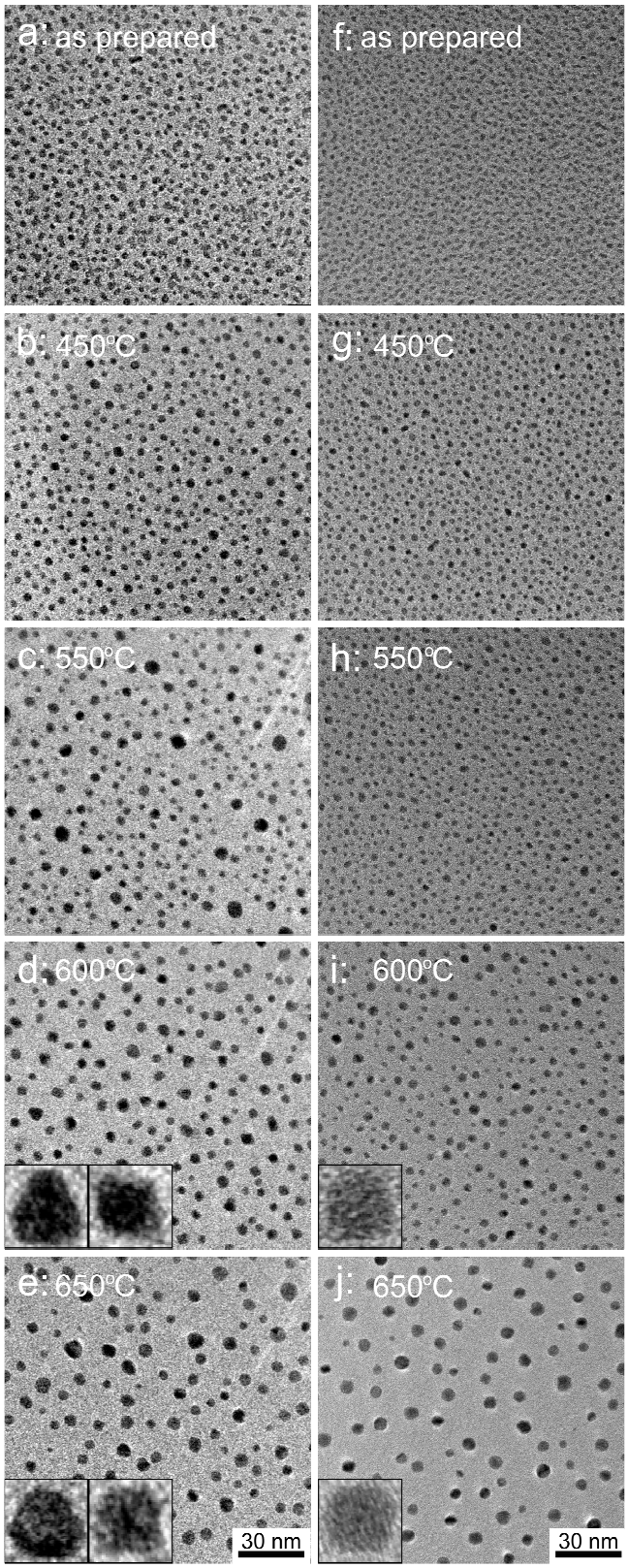

Fig. 4.7: Representative TEM images of the Pt/SiO_2 (a-e) and the Pt/Al_2O_3 (f-j) samples after aging in a tube furnace in 1 bar 0.2 % O_2 in N_2 for 3 hours. The samples were aged at 450ºC, 550ºC, 600ºC, 650ºC as indicated in the figure. The inserts show examples of particles with triangular and square projections. The white marks in the upper corner of (c-e) and the large dark patch in (b) are due to artifacts from the CCD.

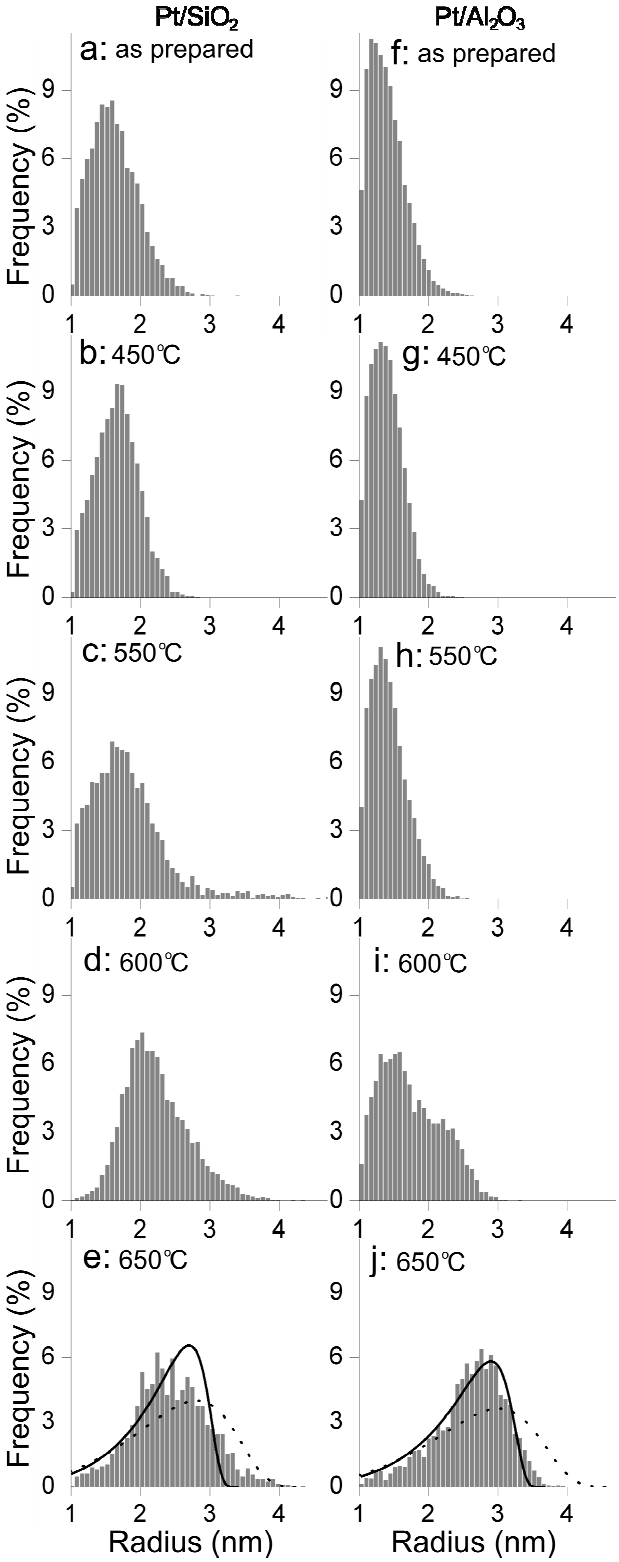

Fig. 4.8: PSDs based on measurements from a number of TEM images of the Pt/SiO_2 (a-e) and the Pt/Al_2O_3 (f-j) samples after aging in a tube furnace in 1 bar 0.2 % O_2 in N_2 for 3 hours. The samples were aged at 450ºC, 550ºC, 600ºC, 650ºC as indicated in the figure. The number of measured particles are (a) 6387, (b) 5222, (c) 2205, (d) 4566, (e) 2119, (f) 14243, (g) 11204 (h) 8310, (i) 7606 and (j) 2954. For the aging temperature 650℃, a two-dimensional LSW distributi on function [120] (solid) as well as a modified two-dimensional version of the LSW distribution which includes local interactions between the particles [122] (dotted), is fitted to the data (e,j).

the local correlations between neighboring nanoparticles will lead to a broadening and a more symmetrical shape of PSD [122-130]. Indeed, a modified version of the LSW model, including localized particle interactions [122] fits the experimental data from Pt/SiO_2 slightly better (fig. 4.8e, dotted line).

The modified version of the LSW model which includes the local particle correlations [122] does not improve the fit to the PSD of Pt/Al_2O_3 (fig. 4.8j, dotted line), and the effect of local correlations between the Pt nanoparticles on ripening therefore seems less pronounced for the Pt/Al_2O_3 model catalyst.

4.2.3. Ensemble averaged data as a function of temperature

In figure 4.9 the mean radius (a), the particle density (b), the standard deviation of the particle radius (c) and the metal volume per support area (d) is presented at a function of temperature for Pt/Al_2O_3 (black squares) and Pt/SiO_2 (grey squares). According to figure 4.9a, the mean radius is stable up to at least 450ºC and the onset for sintering is 550ºC - 600ºC for both model catalysts. The mean radius for Pt/Al_2O_3 increases more rapidly with temperature than for Pt/SiO_2. Consistently, the particle density decreases more rapidly with temperature for Pt/Al_2O_3 (fig. 4.9b). According to figure 4.9c, the particle size spread, expressed by the radius standard deviation increases for the temperatures above the onset for the sintering, consistent with figure 4.8.

4.3. Comparison of in situ and post mortem results

In the tube furnace and in the in situ experiments the model catalysts were exposed to similar O_2 partial pressures during the thermal ageing at 650ºC. Though the N_2 pressure (in situ TEM: $P_{Nitrogen}$ = 8 mbar, tube furnace: $P_{Nitrogen}$ = 1 bar) and the flow (in situ TEM: ca. 5 – 10 ml/min, tube furnace: ca 120 ml/min) were different. Because the total sample area is very small (ca. 6 mm^2), it is reasonably to assume that the change in partial pressure of O_2 by adsorption and reaction with the sample is negligible and that the difference in flow should therefore not influence the results. Aging at 650ºC for 3 hours in the tube furnace and in the TEM should therefore give comparable results, assuming that the samples do not change significantly when the tube furnace temperature is ramped down and the samples are transferred to the microscope and that the difference in the partial pressure of N_2 does not influence the results.

To make the comparison of the in situ and ex situ results, the ensemble averaged results from in situ TEM after aging the Pt/Al_2O_3 (black) and Pt/SiO_2 (grey) for 3 hours is included in figure 4.9a-d (filled circles). Approximately the in situ and post mortem results agree which means that the results from in situ TEM can generally be reproduced by the tube furnace experiments. Deviations are, however, observed, especially for the mean radius for the Pt/SiO_2 sample and the standard deviation of the radius for the Pt/Al_2O_3 sample. The agreement between the in situ and ex situ results is clearly not as good as could have been expected from fig. 3.5 which showed that the sintering of the samples can be almost exactly reproduced, if the aging conditions are exactly identical. The deviations between the in situ and post mortem results observed in figure 4.9 therefore shows that the sintering of the samples is sensitive to the minor differences in the aging conditions in the two types of experiment. A possible explanation for the different results is the

large difference in N_2 total pressure for the tube furnace and in situ experiments, which is examined in the following.

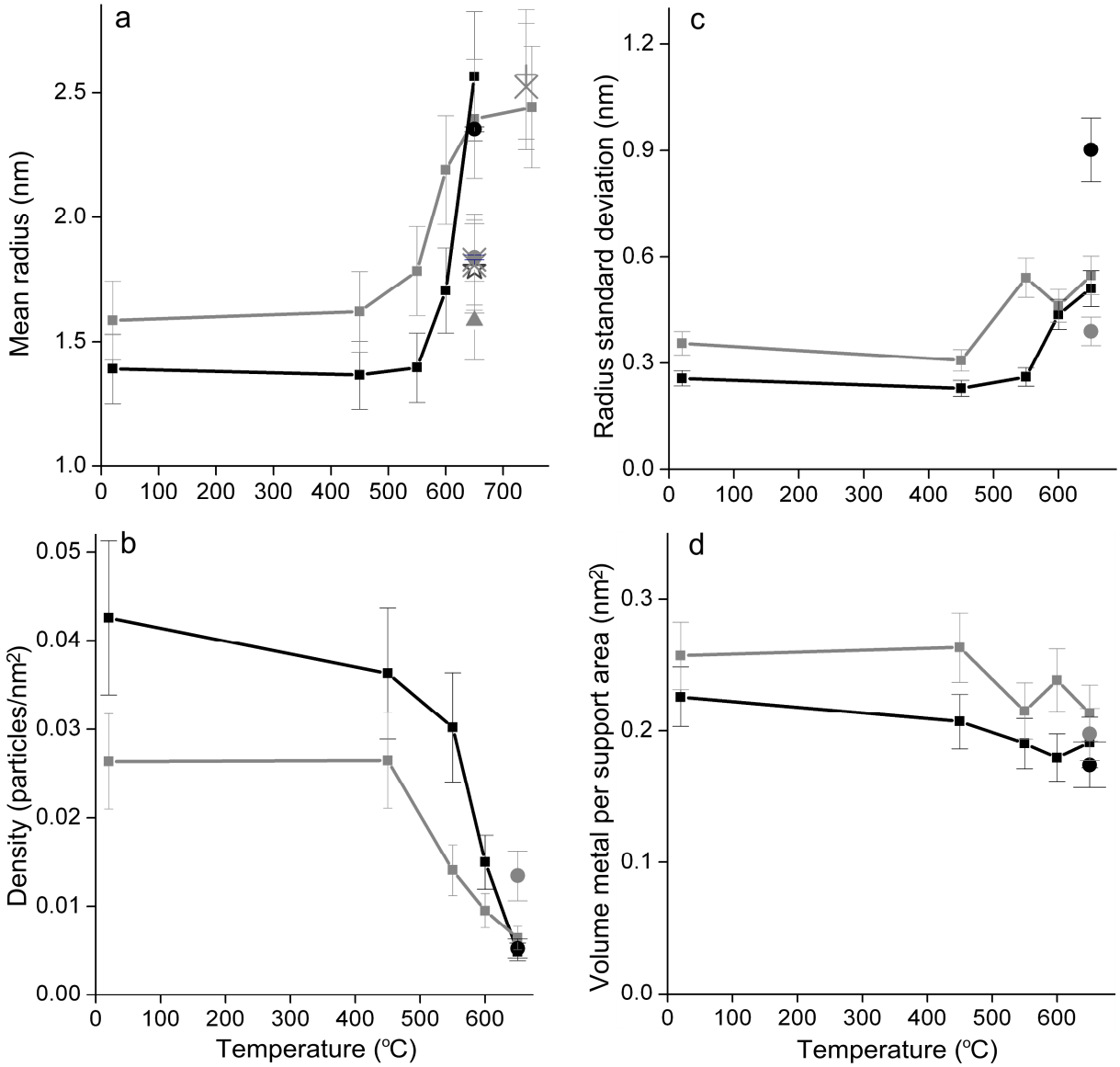

Fig. 4.9: (a) The mean particle radius, (b) the particle density, (c) the standard deviation of the radius measurements and (d) the Pt metal volume per support area as a function of aging temperature for Pt/Al_2O_3 (black) and Pt/SiO_2 (grey) after thermal aging in 1 bar 0.2 % O_2 in N_2 for 3 hours. (a-d) For comparison, the corresponding values for Pt/Al_2O_3 (black, filled circle) and Pt/SiO_2 (grey, filled circle) after aging in 3 hours in the in situ experiment are presented in the figure. (a) Additional data points represent the mean particle radius for Pt/SiO_2 after thermal aging for 3 hours in the tube furnace in 1 bar N_2 (triangle), in the tube furnace in 1 bar 0.2 % O_2 in Ar (star), in the tube furnace in 10 mbar technical air (+) and in the TEM in 10 mbar technical air where the electron beam was turned off throughout the experiment (x). Error bars: see Appendix B.

4.3.1. The effect of gas type and pressure on the sintering

To determine the influence of the O_2 and the N_2 partial pressure on the Ostwald ripening process, a number of additional thermal aging experiments were carried out in the microscope and in the tube furnace for comparison with the previously described experiments.

First a Pt/SiO_2 sample was aged in the tube furnace in 1 bar N_2 at 650ºC for 3 hours. According to figure 4.9a (triangle) the Pt nanoparticles are stable in pure N_2. According to figure 4.9a even a relatively low partial pressure 2 mbar of oxygen enhance the sintering of the oxide-supported Pt nanoparticles (10 mbar air: grey circle; 1 bar N_2: grey triangle), in agreement with several previous studies [10,12,15,16,19,56,61]. The mass-transport during the sintering of Pt/Al_2O_3 and Pt/SiO_2 is therefore likely mediated by Pt-oxygen species [10,15], which are too small or too fast to be directly detected in the in situ TEM images (fig. 4.1, fig. 4.2).

Since Pt/SiO_2 is stable in pure N_2 (fig. 4.9a, triangle), and since the degree of sintering is higher in the tube furnace experiment where the partial pressure of N_2 is high (fig. 4.9a, grey square), compared to the in situ experiment (fig. 4.9a, grey circle), the difference between the mean radii from the in situ and post mortem experiment either shows a) that the electron beam after all influenced the degree of sintering, even in regions not exposed to the electron beam in contradiction to the conclusions from section 3.2.1.3 or b) that the partial pressure of N_2, in a O_2/N_2-mixture, influences the sintering rate of Pt/SiO_2.

To test a), Pt/SiO_2 samples were aged in the TEM in 10 mbar technical air while the electron beam was turned off throughout the aging experiment. In these experiments the slower temperature ramping from the tube furnace experiments was mimicked to make the experiments fully comparable. Two such experiments were carried out at 650ºC. TEM images were acquired at RT in vacuum after the thermal aging. The results are presented in figure 4.9a (x's) and they perfectly match the result from the previous in situ experiment (grey circle). This shows that the influence of the electron beam is negligible as expected from section 3.2.1.3 and in addition that the results from in situ TEM are reproducible.

To test b), a Pt/SiO_2 sample was aged in the tube furnace in 1 bar 0.2 % O_2 in Ar for 3 hours at 650ºC. The resulting mean particle radius after thermal aging is presented in figure 4.9a (star). This tube furnace experiment reproduces the results from the in situ experiments, where the N_2 partial pressure is low. The observed difference in the degree of sintering for Pt/SiO_2 at different N_2 partial pressures can therefore not be explained by differences in the experimental setups, and it can be concluded that the sintering of Pt/SiO_2 depends, not only as expected on the partial pressure of O_2, but also on the partial pressure of N_2.

To test a possible temperature-dependence of the effect of the N_2-partial pressure on the sintering of Pt/SiO_2, the following three experiments were carried out at the higher temperature of ca. 750ºC: 1) a sample was aged in the tube furnace in 1 bar 0.2 % O_2 in N_2 for 3 hours at 750°C, 2) a sample was aged in the TEM in 10 mbar technical air at 740ºC (with full power on the furnace in the TEM heating holder, the temperature could not be raised to 750ºC in 10 mbar air) while the electron beam was turned off throughout the experiment, and the temperature was ramped similar to that of the tube furnace experiment. 3) A roughing pump and a pressure gauge were mounted at the exit from the tube furnace and a needle valve was introduced at the entrance. By adjusting the gas flow with the needle valve, it was possible to maintain a total pressure of 10 mbar technical air in the tube furnace during the thermal aging of a Pt/SiO_2 sample for 3 hours at 740ºC. The resulting mean particle radii are presented in figure 4.9a (grey square, x and +), which shows a comparable degree of sintering from all three experiments at the higher temperature of ca. 750ºC. The dependence of the degree of sintering on the partial pressure of N_2 is therefore restricted to a temperature range below 750ºC.

From the experiments it is not obvious how N_2 in combination with O_2 can boost the sintering of Pt/SiO_2, but a chemical reaction involving N_2 is strongly suggested, since the sintering is not increased by the same partial pressure of Ar. This means that the strong triple bond of N_2 must be broken by the Pt/SiO_2 catalyst when exposed to a mixture of O_2 and N_2 at temperatures near 650ºC. Since NO strongly enhance the sintering of oxide supported Pt nanoparticles [19], it can further be

speculated that such species are formed at the Pt surface and that the Ostwald ripening is mediated by Pt-NO species. In the present study, it was prioritized not to pursue the role of N_2 for the sintering of Pt nanoparticles further.

4.3.2. Degree of Pt mass conservation as a function of temperature

For the in situ experiments, Pt was not lost as a function of aging time according to the estimate for the Pt volume per support area (fig. 4.3d). For the tube furnace experiment, a similar estimate indicates a slight decrease in the Pt volume as a function of temperature (fig. 4.9d). These results are not fully consistent, which is could be related to the crudeness of the estimate. To address the degree of Pt mass conservation as a function of aging temperature, SEM-EDS was performed on the Pt/SiO_2 model catalyst (section 2.2.5 and 3.2.2). Figure 4.10 presents the Pt weight concentration as determined from the quantification of the EDS spectra as a function aging temperature after aging the sample in 1 bar 0.2 % O_2 in N_2 (squares), in the TEM in 10 mbar technical air (X) and in the TEM in 2 mbar O_2 (triangles). The electron beam was turned of throughout the thermal aging experiments in the TEM. According to figure 4.10, the Pt weight concentration is constant for aging temperatures up to 750°C, but decreases above this temperature. The loss of Pt at temperatures above 750°C is most probably caused by evaporation of Pt or Pt-oxides from the sample. This conclusion is consistent with results from earlier studies indicating loss of Pt from flat Pt/SiO_2 [53] and Pt/Al_2O_3 [21] model catalysts by a decreasing mean particle size at temperatures above 750°C and 800°C, respectively. The result shows that the Pt mass is conserved in the sintering experiments of the present study for aging temperatures up to 750°C. The result also indicates that the Ostwald ripening at temperatures up to 750°C is dominated by Pt-oxide diffusion on the oxide support, while Ostwald ripening at higher temperatures is also influenced by diffusion in the gas phase.

4.4. Deviations between theory and observations

It should be noted that although the present model systems were generated to match closely the assumptions underlying the theoretical mean-field ripening models (section 2.1.1), the experimental situation still may deviate from the model assumptions, and this may be the explanation for the discrepancies between the experimental observations and the theoretical models, for example for Pt/Al_2O_3 (fig. 4.5). Firstly, oxygen was found to induce the sintering since the experiments with only nitrogen resulted in a stable ensemble of Pt nanoparticles (fig. 4.9a). The oxygen adsorption may, however, vary on the Pt nanoparticles of varying size [69,70,72]. Also, for the very small Pt clusters the energy per metal atom may be dependant on the particle size [131]. These effects may influence the particle shape and the formation of diffusing Pt-oxide complexes. Secondly, the mean-field ripening model assumes a homogeneous metal-support adhesion energy. Although the use of flat and amorphous oxides approaches a homogeneous support, surface inhomogeneities or defects were observed at the atomic scale (fig. 3.3). These sites may act as anchoring sites for Pt (section 2.1.2), thereby influencing the diffusion of atomic species or the shape and orientation of the metal nanoparticles. These detailed structural features may also be important for sintering rates in the presence of a reactive gas environment. Thirdly, local correlations between the nanoparticles as observed for the Pt/SiO_2 after thermal aging at 550°C could more generally influence the sintering

and result in deviations between the experimental observations and for example the simulated PSDs.

At the atomic level, the degree of inhomogeneities is higher for the SiO_2 surface relative to the surface of Al_2O_3 (fig. 3.3) which also complicates the direct comparison of the two model catalyst and could partly explain the differences in the sintering rates (fig. 3.3)

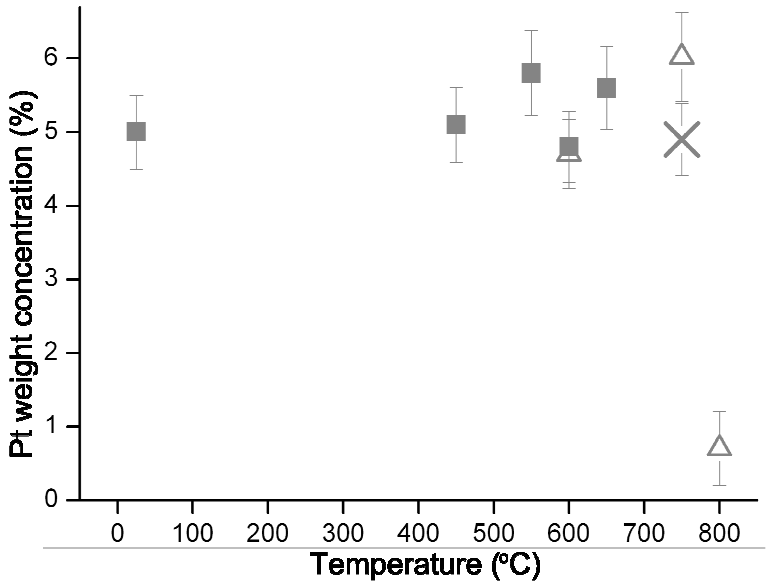

Fig. 4.10: Pt weight concentration measured with SEM-EDS presented as a function of aging temperature after thermal aging for 3 hours in the tube furnace in 1 bar 0.2 % O_2 in N_2 (squares), in the TEM in 10 mbar technical air (X) and in the TEM in 2 mbar O_2 (triangles). Error bars: See Appendix B.

4.5. Chapter summary

Sintering of Pt nanoparticles supported on Al_2O_3 and SiO_2 was studied in situ as a function of time at 650°C in 10 mbar air and ex situ as a function of temperature in a similar oxygen partial pressure. The onset temperature for the sintering is 550°C - 600°C on both oxides. Time-resolved in situ TEM images unequivocally demonstrate that the sintering of the Pt nanoparticles was governed by the Ostwald ripening mechanism on both oxide supports. Comparison in different gas environments showed that the sintering is severely boosted by oxygen, which suggests that the mass-transport is mediated by Pt-oxygen species. Mass conservation for Pt was determined for aging temperatures below 750°C according to SEM-EDS, indicating that for the present sintering experiments, the diffusion mainly takes place at the oxide support, while for higher aging temperatures the ripening may also be mediated by diffusion in the gas phase. Also for temperatures below 750ºC, the sintering of Pt/SiO_2 was found to depend on the partial pressure of N_2, which can explain the observed differences in the degree of sintering of Pt/SiO_2 in the in situ and ex situ experiments.

Furthermore, the in situ results show a similarity between the trend of the mean radius as a function of time and the spread in the particle sizes as a function of time. This result is consistent with an early suggestion from a theoretical study that the sintering rate is related to the spread of the particle sizes. The relation between the characteristics of the PSD and the sintering rate is discussed

further in chapter 7 where the sintering is compared for Pt/SiO_2 model catalysts with different initial PSDs.

In the present chapter, PSDs were extracted from the TEM images and presented as a function of time or temperature. For the Pt/Al_2O_3 model catalyst, similar evolutions of the PSD shape was observed as a function of time and temperature and the PSD shapes at the end of the in situ experiment and after sintering at the highest temperature in the ex situ experiment could be fitted well by the LSW model, consistent with the theory for Ostwald ripening. However, in both the time- and temperature-resolved PSD series, transition shapes appear which cannot be fitted well by the LSW model and which do not agree with computer simulations based on the mean-field kinetic model for Ostwald ripening. For Pt/SiO_2, the evolution in the PSD shape as a function of time is described well by the computer simulations, but significant changes in the PSD shape are not observed due to the lower degree of sintering in the relatively low N_2 partial pressure. Significant, changes are observed for the temperature-resolved PSD series for Pt/SiO_2, and the shape changes are different from that of Pt/Al_2O_3. Specifically, a tail appears to the large particle side of the main peak. This tail was associated with the formation of large particles in the TEM images with a significantly diminished particle density in their vicinity. These observations suggest that the sintering of Pt/SiO_2 was influenced by local correlations between the nanoparticles. The PSD corresponding to Pt/SiO_2 at the highest sintering temperature is relatively symmetrical and the LSW model does not fit the data for Pt/SiO_2 as well as the data for Pt/Al_2O_3. The fit of the LSW model can be slightly improved by including localized particle interactions in the model, so local effects may partly, but not fully, explain the apparent inconsistency with the theory for Ostwald ripening. A possible explanation for the deviations between the observed PSD shapes and the theoretical models for the Pt/Al_2O_3 and Pt/SiO_2 model catalysts is discussed in chapter 6. In the following chapter, the influence of the local correlations between the nanoparticles is discussed in detail for Pt/SiO_2 where this effect seemed to be more pronounced.

5. Effects of local particle correlations on Ostwald ripening

In chapter 4 it was suggested that local correlations between the oxide supported Pt nanoparticles influence the Ostwald ripening. In the present chapter, this suggestion is studied in detail for the Pt/SiO_2 model catalyst for which the effect was most pronounced according to the analysis in chapter 4. First the observed growth rates for individual nanoparticles are compared to the expected rates from the mean-field ripening model (eq. 2.12), to determine whether the observations can be accounted for without including assumptions of possible local correlations. Second, a more detailed analysis follows the time-dependence of the radii of individual Pt nanoparticles. Finally, the experimental observations are compared with ripening models which include local particle correlations. These results are described in paper II (See List of included publications).

5.1. Local particle correlations

The applicability of the mean-field Ostwald ripening models (2.1.1) for heterogeneous catalysts has been subject to debate [46-48,50,54,123,131-133]. For instance, as discussed by Voorhees [123] and Dadyburjor et al. [133], the mean-field assumption (section 2.1.1) should mostly be useful for catalysts with low metal loadings, because the metal particles on average are sufficiently far apart on the support compared to the screening distance (L, section 2.1.1). But, even for such catalysts, the actual preparation route may result in regions of high local particle density with a mean particle separation that is comparable to the particle size. As the particle separation approaches the screening distance, the particles will alter the concentration of atomic species close to the neighbor particles as compared to the uniform mean-field concentration. In this case, a nanoparticle should experience an effective concentration of atomic species, depending on the location and size of the neighbor nanoparticles, and the ripening should correlate with the local conformation of nanoparticles. For the present Pt/Al_2O_3 and Pt/SiO_2 model catalysts, the particle density is relatively high (0.03 - 0.04 particles/nm^2) and it could therefore be expected that local ripening effects can be observed. Indeed, large particles with a significantly diminished particle density in their vicinity indicated a local ripening effect for the Pt/SiO_2 model catalyst after thermal aging at 550°C (fig. 4.7c, fig. 4.8c).

Previous studies have demonstrated that local correlations in ripening are present in homoepitaxial systems, including Si-islands on Si(001) [121,134] and Ag-islands on Ag(111) [135]. These studies used time-resolved microscopy to monitor the ripening of two-dimensional islands with radii larger than ca. 5 nm under ultra-high vacuum conditions and revealed a size-dependency of the island ripening that is not well-described by a mean-field kinetic model, whereas kinetic models that incorporate local correlations provide a better description. Recently, in situ STM of three-dimensional Au nanoparticles on TiO_2(110) during CO oxidation [136], revealed that local correlations between the metal nanoparticles may also affect ripening processes in heterogeneous catalysts. However, a detailed description of the correlated ripening effect was not pursued. To

determine the effects of the local particle correlations on the ripening for the present Pt/SiO_2 model catalyst in detail, the time-resolved dynamical changes of the individual nanoparticles are measured. To compare the differences in the growth rates of individual nanoparticles, a high precision in the measurements is needed. All results presented in this chapter are therefore based on manually measured particle sizes with an estimated error of ca. 0.2 nm on the particle diameter.

5.2. Growth and decay rates of individual nanoparticles

The growth rates, dr/dt of the individual nanoparticles was obtained from the time-resolved image series of Pt/SiO_2 (fig. 4.2) by measuring the change in radius, r over the time interval, t = 60 - 120 min, for each individual particle in the image. For normalization, the mean radius, r_{mean} was calculated from the particle radii measured at t = 60 min. Figure 5.1a presents dr/dt as a function of the normalized radius, r/r_{mean}. For the majority of the nanoparticles, the growth rates are found in the first or third quadrant, corresponding to a positive dr/dt for $r/r_{mean} > 1$ or a negative dr/dt for $r/r_{mean} < 1$. Thus, particles larger or smaller than the mean particle size grew or shrank respectively, as predicted by the mean-field ripening models, eqs. 2.13 and 2.14. However, a minor fraction of the nanoparticles is associated with growth rates in the second and fourth quadrant. As these rates are not accounted for by the propagated measurement error, it seems that the mean-field models are not sufficient to account for the observed ripening.

To further elaborate on deviations from the mean-field models, the rates in figure 5.1a are re-plotted in figure 5.1b as a function of $1/r^2 \cdot (r/r_{\mathrm{mean}} - 1)$. For interface-controlled ripening, eq. 2.13 predicts a linear relationship for figure 5.1b with a slope corresponding to α_i' (assuming a constant particle shape, here $\alpha_i = 1$), and an offset $dr/dt = 0$ at $r = r_{mean}$. Figure 5.1b includes the best linear fit to the rates, which was obtained for $\alpha_i' = 0.025\ \mathrm{nm^{-1}} \cdot \mathrm{min^{-1}}$, in approximate agreement with the α_i'-value for the PSD simulation ($0.035\ \mathrm{nm^{-1}} \cdot \mathrm{min^{-1}}$) in section 4.1.5, and with an offset of 0.0005 nm/min. close to the origin. Figure 5.1b shows an overall linear trend of the data, but the data spread further emphasizes the deviations from the mean-field model. A similar analysis based on the diffusion-controlled ripening model, eq. 2.14, is included in figure 5.1c. That is, figure 5.1c shows the rates in figure 5.1a re-plotted as a function of $1/r^3 \cdot (r/r_{mean} - 1)$. Assuming a constant particle shape (here $\alpha_d = 1$) and that the term $\ln(L/r)$ in eq. 2.14 is constant (section 4.1.5), the best linear fit to the data in figure 5.1c has a slope $\alpha_d'/\ln(L/r) = 0.027\ \mathrm{nm^{-1}} \cdot \mathrm{min^{-1}}$, which is in reasonable agreement to $\alpha_d'/\ln(L/r) = 0.067\ \mathrm{nm^{-1}} \cdot \mathrm{min^{-1}}$ from the PSD simulation in section 4.1.5, and an offset of 0.0002 nm/min. which is close to the origin. The mean-field model for diffusion-controlled ripening also captures an overall linear trend of the observations, but a significant data spread is apparent.

Consistent with the results in chapter 4, figure 5.1 shows that the general trends of the ripening of the SiO_2-supported Pt nanoparticles are captured by the mean-field ripening model. The present analysis, however, shows deviations on the individual nanoparticle level between the experimental observations and the models which do not include local particle correlations.

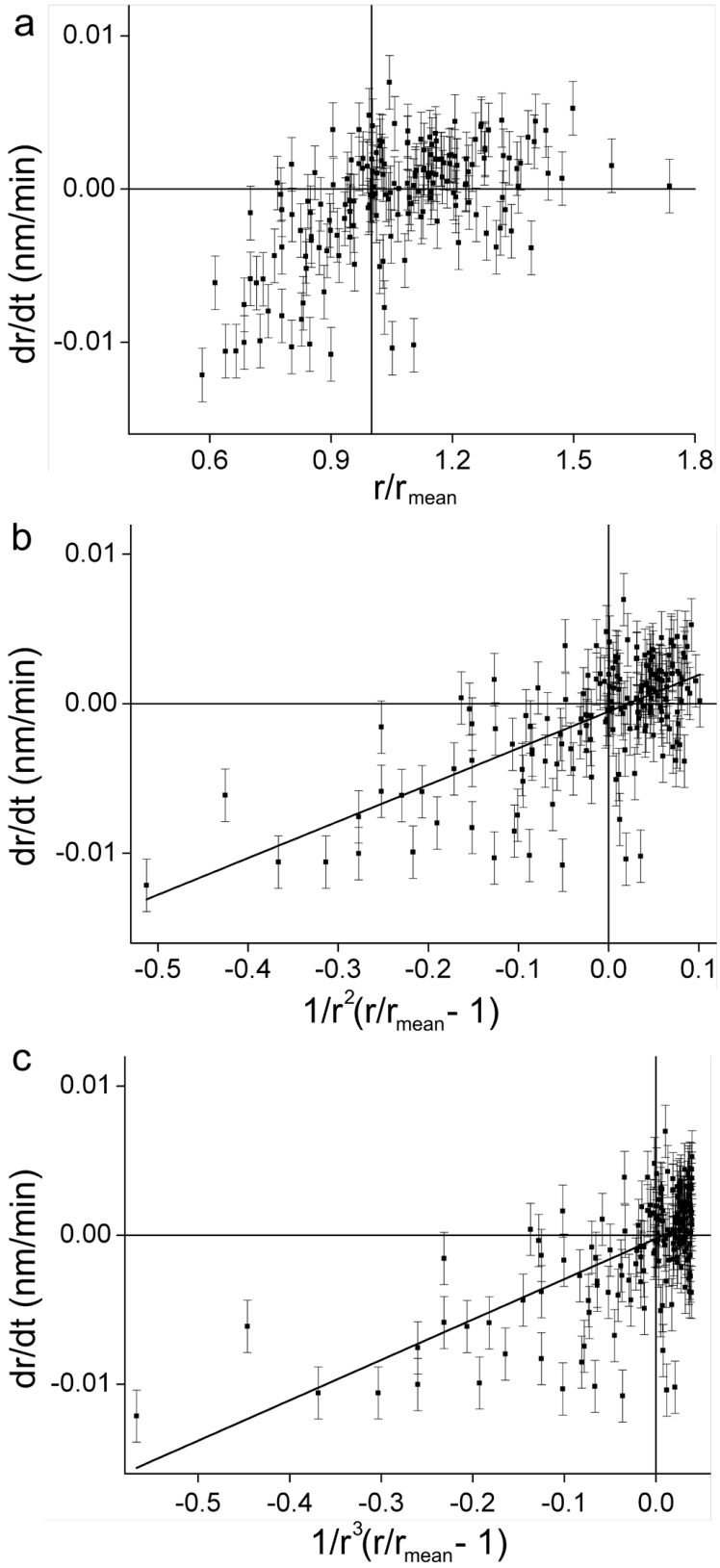

Fig. 5.1: The growth rate, *dr/dt*, for individual Pt nanoparticles presented as a function of (a) the normalized radius, r/r_{mean}, (b) $1/r^2(r/r_{mean} - 1)$, corresponding to eq. 2.13, and (c) $1/r^3(r/r_{mean} - 1)$, corresponding to eq. 2.14. The rates are obtained from the measurement of the radius at t = 60 and 120 min for 185 particles. The error bars represent the propagated measuring error based on $\delta x_{manual\_measure}$ (section 3.3.3). For the best fitted line included in (b) and (c), the R^2-value is 0.42 and 0.39 respectively.

5.3. Temporal evolution of individual nanoparticles

To further examine the discrepancies between the observed dynamical changes of the individual Pt nanoparticles and the mean-field model, a selection of Pt nanoparticles was examined throughout the entire time-resolved image series (fig. 4.2). Figure 5.2a shows the selected particles in the TEM image from fig. 4.2a. For each particle, the projected radius, r, of these particles as well as the mean radius for the entire TEM image, r_{mean}, was determined as a function of time. Figure 5.2b shows that the mean particle radius increased over time and that nanoparticles with $r > r_{mean}$ grew and nanoparticles with $r < r_{mean}$ decayed. These general trends are consistent with the mean-field models. However, discrepancies become apparent by comparing the observed particle radii with calculated radii. The time-dependence of the particle radii was calculated using the interface-controlled mean-field model (eq. 2.13) with the observed radii of particles 1-9 at t = 5 min (fig. 5.2b) as initial radii, $\alpha_i = 1$ and $\alpha_i' = 0.03$ nm^{-1} · min^{-1}. Figure 5.2c shows the calculated time-dependency of the particle radii and demonstrates that the growth rates are directly related to the particle size. However, the pattern differs from the observations: Despite comparable initial radii, the particles 4-6 decayed significantly slower than particles 7-9. Moreover, the observed order by which particles 4-9 decay also differs from the calculated order.

5.4. Comparison with local ripening models

In the following, the observations in figure 5.2 will be compared to kinetic ripening models modified by the incorporation of local particle correlations [121,134,137]. Bartelt et al. established such a ripening model for interface-controlled ripening [121,134] and Zheng and Bigot developed a model for diffusion-controlled ripening [137]. Both models are considered because both interface- or diffusion-controlled ripening was consistent with the experimental observations (section 4.1.5 and 5.2).

For both models, the size-evolution of a particle, i, is calculated on the basis of the contribution to the concentration of atomic species from i's nearest neighbor particles. Here we adopt the approach used by Bartelt et al. and define the nearest neighbors by the Voronoi construction [121,134]. In the Voronoi construction, the support plane is decomposed into cells in such a way that the Voronoi cell of particle i consists of the inner envelope of all line segments of points being equidistantly located between the centers of i and any other particle [138]. Figure 5.3 illustrates the Voronoi construction for a region of the Pt/SiO_2 sample. The nearest neighbors of a particle i are those particles j with a Voronoi cell which have a segment in common with the cell of i. Moreover, the Voronoi construction has a time-dependency, because cells vanish as the decaying particles eventually disappear (fig. 5.3).

The interface-controlled ripening model derived by Bartelt et al. concerns two-dimensional islands [121,134]. Here a similar model for ripening of three-dimensional particles on a two-dimensional support is considered based on the expression for the net flux of atomic species, J_i onto the particle, i (eq. 2.2),

$$J_i = 2\pi r_i a \beta' \left(c_s^{local} - c_p^i \beta \right) \tag{5.1}$$

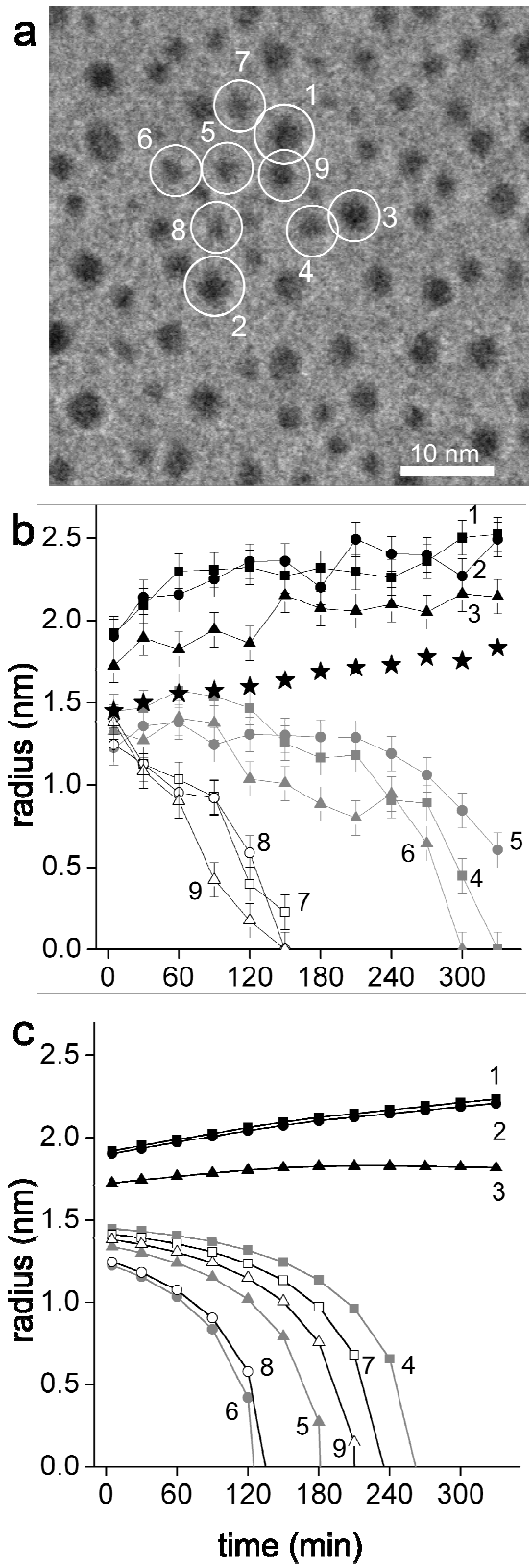

Fig. 5.2: (a) An outline of the nine selected particles in figure 4.2a (white circles). (b) The measured particle radii for the particles 1-9 as a function of time. The mean radius for the whole TEM image (stars) is also presented. (c) Calculated time-dependent particle radii for the particles 1-9. The calculations are based on eq. 2.13. The error bars indicate $\delta x_{manual\_measure}$.

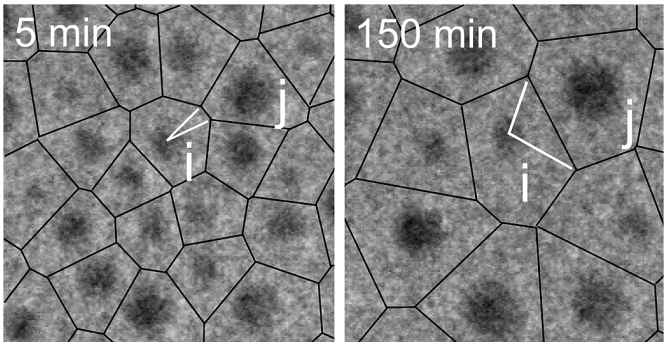

Fig. 5.3: The Voronoi construction (black lines) superimposed on a close-up on fig. 5.2a. For the Voronoi cell of particle *i*, the opening angle Φ_{ij} (indicated by white lines) with respect to the neighbor particle *j* is defined by the common line of the two adjacent cells with respect to the center of mass of particle *i*. *i* corresponds to particle no. 5 in fig. 5.2a.

where, *a* is the inter-atomic spacing defined in fig. 2.2, r_i the radius of particle *i* with constant shape ($\theta = \pi/2$, corresponding to at hemisphere), c_p^i the surface concentration of diffusing species at the edge of particle, *i* according to eq. 2.1. β and β' are defined in eq. 2.3 – 2.4. c_s^{local} is the mean local surface concentration of atomic species on the support, which only depends on *i*'s nearest neighbor particles. The contributions to c_s^{local} from each nearest neighbor, *j*, is approximated by the mean of $c_p^i\beta$ for *i* and *j*, weighted by the opening angle, Φ_{ij}, of the Voronoi cell of particle *i*, as defined in figure 5.3:

$$c_s^{local} = \sum_j \tfrac{1}{2}\left(c_p^i\beta + c_p^j\beta\right)\frac{\Phi_{ij}}{2\pi} \tag{5.2}$$

Thus, the model effectively operates with a "local" mean concentration of atomic species, determined by the nearest neighbor particles, contrary to "global" mean-field concentration, $\bar{c}_s$ underlying eqs. 2.13 and 2.14, which is spatially invariant and determined through the average particle size. The particle volume change rate can now be calculated from eqs. 5.1 and 5.2:

$$\frac{dV_i}{dt} = \Omega J_i \tag{5.3}$$

Here, Ω is the atomic volume of bulk Pt ($\Omega = 1.5 \cdot 10^{-2}$ nm^3). By using eq. 5.3, $r(t)$ can be calculated numerically for the particles 1 - 9 in figure 5.2, as described in detail in the following.

The diffusion-controlled ripening model developed by Zheng and Bigot is based on the following expression for the diffusion-limited flux from a particle *i* to a neighbor particle *j* [137]:

$$J_{ij} = \frac{2\pi D}{\ln\left(l_{ij}^2 / r_i r_j\right)}\left(c_p^i\beta - c_p^j\beta\right) \tag{5.4}$$

where *D* is the surface diffusivity for Pt on SiO_2, l_{ij} the distance between the particle centers, c_p^i the surface concentration of diffusing species at the edge of particle, *i* according to eq. 2.1 and β is defined in eq. 2.4. Notice the similarity with the equation describing the diffusion flux from the mean field to the particle, eq. 2.7. This model operates with a pair-wise atom-exchange from a

particle, *i*, to its neighbors, *j*, instead of describing the particle ripening as a result of the interaction with a local mean concentration of atomic species established by the neighbors. For consistency, the model by Zheng and Bigot is weighted by using the Voronoi geometry. Thus, the change in volume of a given particle, *i* can be described as:

$$\frac{dV_i}{dt} = -\Omega J_i = \sum_j J_{ij} \frac{\Phi_{ij}}{2\pi} \tag{5.5}$$

Here, Ω is the atomic volume of Pt and Φ_{ij} is the opening angle of the Voronoi cell of particle *i*. Eqs. 5.3 and 5.5 allows $r(t)$ to be calculated numerically for the nine particles of fig. 5.2 under the assumption of a constant particle shape (the exact shape assumption e.g. spherical or hemispherical does not influence the result as long as a constant shape assumption is applied).

The two ripening models presented here include correlations between neighboring particles with a weighting scheme based on the Voronoi construction. The Voronoi construction treats the particles as point sources or sinks for atomic species, so only the distances between the particle centers play a role. However, for the present model catalyst, the distances between the particles were comparable to their sizes. As the exchange of Pt is considered to occur at the particle edges, the correlated ripening of particle *i* may therefore be expected to depend on both the separation and the size of the neighboring particles, *j*. For a pair of neighboring particles with radii, r_i and r_j, and a center separation, l_{ij}, the inter-particle distance may therefore be better represented by the distance between the edges, l_{ij}-r_i-r_j, than l_{ij}. Moreover, for the exchange of atomic species, the particle *i* effectively interacts with sites at *j*'s edge; the number of which scales with the *j*'s circumference, $2\pi r_j$. Based on these considerations, an alternative weighting scheme is proposed in which the contributions to the correlated ripening of *i* is weighted by the ratio of the circumference of the neighbor particle *j* to the distance between the edges of the particles *i* and *j*. In the following, this scheme is referred to as the "size-dependent" weighting method and it is included in eqs. 5.3 and 5.5 by the transformation,

$$\frac{\Phi_{ij}}{2\pi} \rightarrow \frac{2\pi r_j \Big/ \left(l_{ij} - r_i - r_j\right)}{\sum_{j'} 2\pi r_{j'} \Big/ \left(l_{ij'} - r_i - r_{j'}\right)} \tag{5.6}$$

where both *j* and *j'* denote the nearest neighbors to a particle, *i* as defined by the Voronoi construction and the sum in the denominator normalizes the weights.

Based on eqs. 5.3, 5.5 and 5.6, the time-evolution of the radii of particles 1 - 9 (fig. 5.2) can be calculated with four schemes based on the interface- or diffusion-controlled ripening models including local correlations based on the Voronoi or size-dependent weighting methods. Specifically, for each scheme, $r(t)$ is calculated using the rate for the volume change, dV_i/dt, an assumption of hemispherically shaped particles, and initial radii corresponding to the measured radii at t = 5 min (fig. 5.2b). The calculations progressed with time-steps of 30 min. corresponding to the time-steps in the time-resolved image series. The calculations rely on a determination of the surface energy, γ and the parameters $\beta'\beta \cdot \rho_\infty$ (interface-controlled schemes) or $D \cdot \beta' \cdot \rho_\infty$ (diffusion–controlled schemes). Clearly, the models are more sensitive to changes of γ, due to the exponential dependency (eq. 2.1), than to the proportional dependency of $\beta'\beta \cdot \rho_\infty$ or $D \cdot \beta' \cdot \rho_\infty$. Therefore, to estimate these parameters for the four schemes, an iterative process was applied in which $r(t)$ is calculated for varying values of $\beta'\beta \cdot \rho_\infty$ or $D \cdot \beta' \cdot \rho_\infty$ for a fixed value of γ. The calculations were

repeated with other values of γ, close to the surface energy of Pt (γ = 2.1 J/m^2 [139]), until the best fit to the data in figure 5.2b was obtained. The calculations showed that the models are indeed very sensitive to γ and that the models only come close to the observations in figure 5.2b for γ = 0.5-0.6 J/m^2. The lower surface energy of the Pt nanoparticles compared to metallic Pt is expected as the Pt nanoparticles should be covered with oxygen [69,70,72]. DFT calculations suggest that the surface O-terminated Pt sites is ca. 0.4-1.2 J/m^2 [63]. Moreover, the best fit to the radii of particles 1-9 is obtained with the following parameters: For interface-controlled ripening model (a) γ = 0.5 J/m^2, $\beta'\beta \cdot \rho_\infty$ = 2.7 s^{-1}·nm^{-2} with Voronoi weighting and (b) γ = 0.6 J/m^2, $\beta'\beta \cdot \rho_\infty$ = 4.1 s^{-1}·nm^{-2} with size dependent weighting. For diffusion-controlled ripening model (c) γ = 0.5 J/m^2, $D \cdot \beta' \cdot \rho_\infty$ = 1.4 s^{-1} with Voronoi weighting and (d) γ = 0.55 J/m^2, $D \cdot \beta' \cdot \rho_\infty$ = 1.6 s^{-1} size-dependent weighting. Figure 5.4a-d presents the calculated time-evolution of the particle radii for particles 1-9 of figure 5.2. The model parameters were found to give a good description of the growth and decay trends of 9 additional particles at a different region of the model catalyst, which confirms the robustness of the fitting procedure.

Figure 5.4 shows that all four schemes for locally correlated ripening capture the growth of the particles 1-3 as depicted in figure 5.2b. However, the schemes differ in the description of the decay and disappearance of particles 4-9. For the interface-controlled model weighted by the Voronoi opening angle, figure 5.4a shows that only particles 5 and 7 disappear whereas particles 4, 6, 8 and 9 remain without significant change during the observation period. The interface-controlled model weighted by the size-dependent weighting method instead predicts that all particles decay and vanish (fig. 5.4b), as observed (fig. 5.2b). In fact, the calculated decay for the particles 4, 6, 7 and 8 match the observations quantitatively well. However, some deviations are also apparent: Particle 9 decayed faster in the experiment than according to the calculations and the decay of particle 5 is better described by the Voronoi weighting scheme. For the diffusion-controlled model, as calculated using the Voronoi opening angle or the size dependent weighting method, the trends for the decaying particles in figure 5.4c-d are similar to the calculated decay using the interface-controlled model in figure 5.4a-b.

For the present experimental conditions, the description of the time-evolution of the individual particles by the interface- and the diffusion-controlled ripening models, including either weighting scheme, are similar and can thus not be distinguished. However, the local correlations are shown to strongly affect the particle decay and the calculated decay is strongly dependent on the weighting method. Specifically, the models, including the proposed size-dependent weighting method, match better most of the observed particle decays in figure 5.2b than the mean-field models, although deviations are apparent for the particles 5 and 9: A close inspection of the TEM images reveals that particle 5 was more distantly situated from smaller neighbor particles, which may explain why the Voronoi scheme gives a better description, and that particle 9 had one close and larger neighbor particle, which may explain why the size dependent weighting method described the decay of this particle better. These considerations may suggest that the optimal weighting method for describing local correlation effects depends on the detailed size and location of neighboring particles. Modeling the particle growth or decay may therefore intimately depend on the local conformation of the particle ensemble, and the lack of a generally applicable weighting scheme thus seems to complicate the detailed description of local correlation effects in ripening.

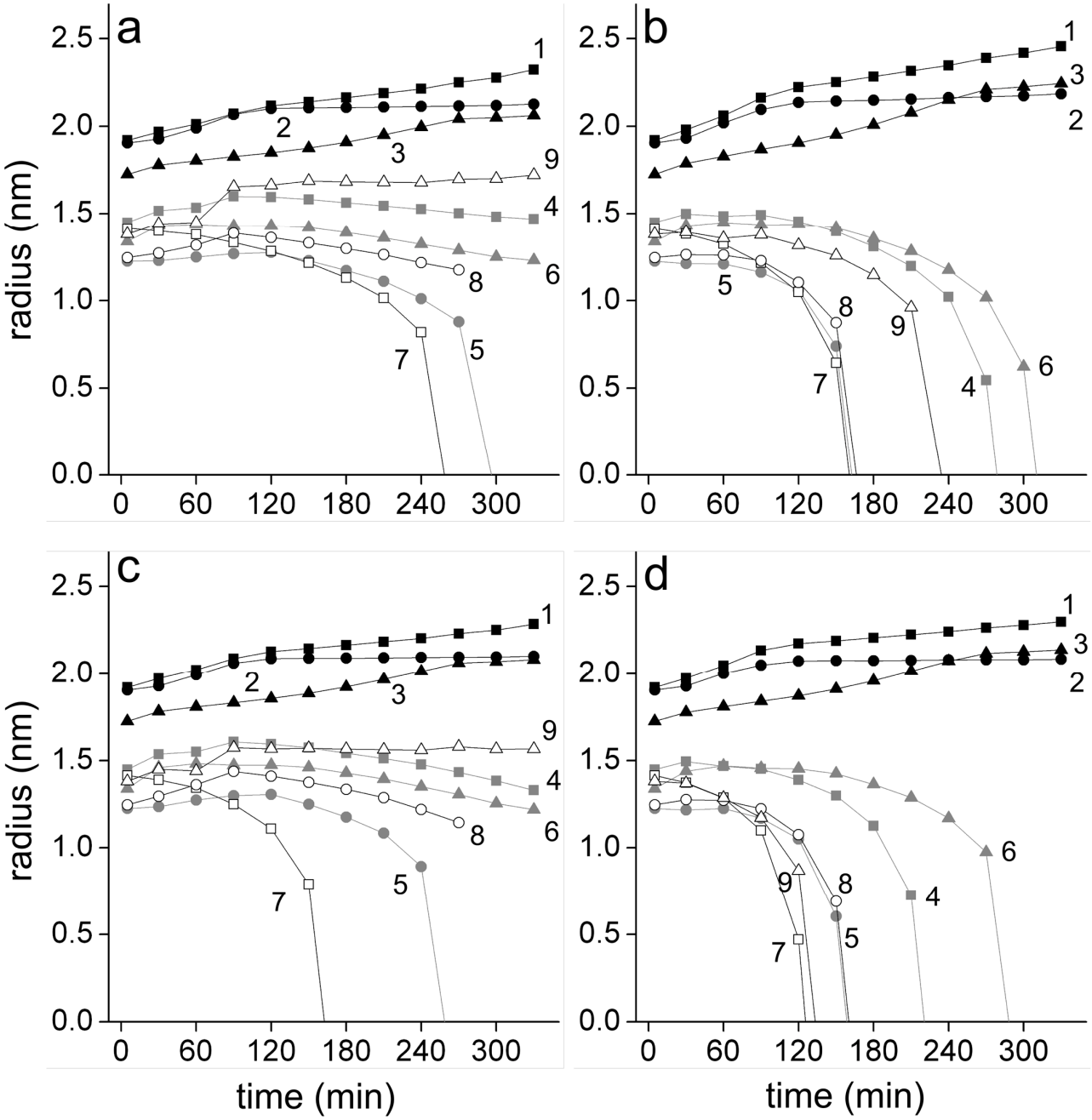

Fig. 5.4: Calculated particle radii as a function of time. The calculations are based on (a-b) the interface-controlled and (c-d) the diffusion-controlled ripening model including local correlations in the atom-exchange process. The local correlations are included by (a,c) the Voronoi and (b,d) the size-dependent weighting methods.

5.5. Limitations of the present analysis

Although the behavior of the individual nanoparticles exposed a deviation from the mean-field ripening model, an ensemble property such as the PSD is well described in that framework (section 4.1.5). Due to the initial uniform particle density and highly monodispersed size of the Pt nanoparticles, it is possible that the ensemble properties average over a sufficiently large ensemble

of different local configurations of nanoparticles to blur the distinct effect of the local correlations. Thus, for catalysts containing a more inhomogeneous nanoparticle ensemble, local correlations in ripening may be speculated to have a more distinct effect on the time-dependency of ensemble properties. The detailed relationship between the individual nanoparticle behavior and the ensemble properties could in principle be examined for the present model catalyst by integrating the results of an extended analysis similar to that presented in figure 5.1. Here, the discussion is limited to a basic description of local correlation effects in interface and diffusion controlled ripening.

The deviations between the mean-field ripening model and the experimental observations were proposed to reflect that local correlations between the nanoparticles influence the ripening process. However, as discussed in section 4.4, deviations could also result from other causes. Furthermore, the ripening models were applied irrespective of the nanoparticle sizes in the present analysis. As Pt nanoparticles with a radius below 0.5 nm contain less than 30 atoms, the geometrical surface curvature is not a well-defined parameter. In this size-regime, the Gibbs-Thomson relation (eq. 2.1), being a continuum model, breaks down per definition. Thus, although the size-dependence reflected by eq. 2.1 is generally accepted to be valid for larger particles, it is likely insufficient for the smallest particle sizes [43,131,136,140]. The size-dependent ripening of the smallest particles has been subject to debate: Houk et al. emphasized that, even within the Gibbs-Thomson model, eqs. 2.13 and 2.14 are imprecise for small particles because the equations rely on a first order Taylor expansion of eq. 2.1 [43]. The models, expressed by eqs. 5.1 and 5.4, apply eq. 2.1 directly and should thus better describe the smaller particles. For a particle sufficiently smaller than r^*, Yang et al. suggested that dr/dt is determined by the particle's own chemical potential and is thus less dependent on the neighbor particle configuration resulting in an accelerated decay trend of the smallest particles described by the exponential Gibbs-Thomson relation (eq. 2.1) [136]. A faster decay of small particles will also happen if the surface energy increases with decreasing particle size as suggested by Campbell et al. [131,140]. For the present study, a portion of the smallest particles revealed an almost linear decay of the particle radius with time, e.g. particle 7 and 9 in figure 5.2b, contrary to the accelerated decay rate predicted by the ripening models due to the exponential term in eq. 2.1 (fig. 5.2c and fig. 5.4a-d). For 50 additional particles with a radius below ca. 1 nm, a similar linear decay was observed for about half of these particles in the present experiment. It remains to be addressed if this observed linear particle decay can be accounted for by a size-dependent surface energy of the nanoparticles. Modeling the surface energy is further complicated by the size-dependent surface oxidation of the Pt nanoparticles [69,70,72].

5.6. Chapter summary

Although the analysis in chapter 4 showed that the time-dependency of the nanoparticle sizes overall is well-described by the mean-field ripening models, the analysis in the present chapter shows that deviations are revealed at the individual nanoparticle level (fig. 5.1, fig. 5.2). The deviations were proposed to reflect that the atom-exchange in the growth or decay of the individual nanoparticles was influenced by the size and location of the neighboring nanoparticles due to the high particle density in the present model catalyst. Including such local correlations between the neighboring particles in the kinetic ripening models gives a more satisfactory description of the evolution in the individual nanoparticle sizes (fig. 5.2, fig. 5.4). Such local correlations can be expected also to influence ripening in industrial catalysts with a high or inhomogeneous metal loading.

6. Effects of particle shape on Ostwald ripening

The analysis of the Ostwald ripening of Pt/Al_2O_3 and Pt/SiO_2 in chapter 4 was based on TEM images which revealed time- or temperature-resolved information of the projected particle shapes, sizes and positions. In other words, the analysis was limited to information in two dimensions, since information of the three-dimensional particle shapes was not available. The present chapter addresses the three-dimensional particle shapes for the oxide-supported Pt nanoparticles after sintering. To extract three-dimensional information from the particles, STEM was carried out on the Pt/Al_2O_3 and the Pt/SiO_2 model catalysts, and in addition AFM was carried out on the Pt/Al_2O_3 sample. As will be presented, the characterization suggests that the shape of the oxide supported Pt nanoparticles is related to the particle size. The chapter therefore ends with a discussion of the effect on the sintering of the size-dependency of the particle shape. The experimental observations for Pt/Al_2O_3 are compared with computer simulations which integrate the observed size-dependency of the particle shapes. Parts of these results are described in paper III (See List of included publications)

6.1. Size-dependent particle shapes according to STEM

As the TEM images only provide information about the size and shape of the nanoparticles normal to the electron beam, STEM images were acquired to evaluate the three-dimensional shapes of the Pt nanoparticles. STEM was performed on the Pt/Al_2O_3 and Pt/SiO_2 model catalysts after thermal aging in the tube furnace at 650°C (section 3.2.2). Figure 6.1 presents representative STEM images of the Pt/Al_2O_3 (fig. 6.1a) and Pt/SiO_2 (fig. 6.1b) sample, where the particles can be identified as bright area projections and the oxide support corresponds to the black area.

From the STEM images, the particle diameters were measured automatically (section 3.3.1). By using the software Image-Pro Plus, the STEM signal intensity was integrated over the projected area corresponding to each particle and the signal contribution from the background generated by the support material was subtracted. Since the integrated STEM signal intensity from a particle corresponds to the particle volume [141], any size-dependent variation in the shape of the supported Pt nanoparticles can be revealed from an intensity vs. particle diameter plot. Figure 6.1 presents the integrated STEM signal intensity plotted in arbitrary units as a function of the particle diameter for Pt/Al_2O_3 (c) and Pt/SiO_2 (d).

The relation between the particle volume and diameter depends on the exact three-dimensional particle shape, which can be described by models of multiple parameters depending on the known information of the shape. Since the three-dimensional shape of the oxide-supported Pt nanoparticles is not known a priori, a spherical cap (as defined in figure 2.2) is here used as a tentative approximation. The volume of a spherical cap with a constant height-diameter ratio as a function of the particle size is fitted to the experimental observations in figure 6.1c-d (dashed black) resulting in $R^2 = 0.95$ and $R^2 = 0.92$ for Pt/Al_2O_3 and Pt/SiO_2, respectively. According to the figure, the volume for a spherical cap with a constant shape increases faster with the diameter than the volume of the observed Pt nanoparticles. The shape of the observed particles is therefore not fully consistent with a spherical cap with a constant height-diameter ratio for all particle sizes and the height-diameter

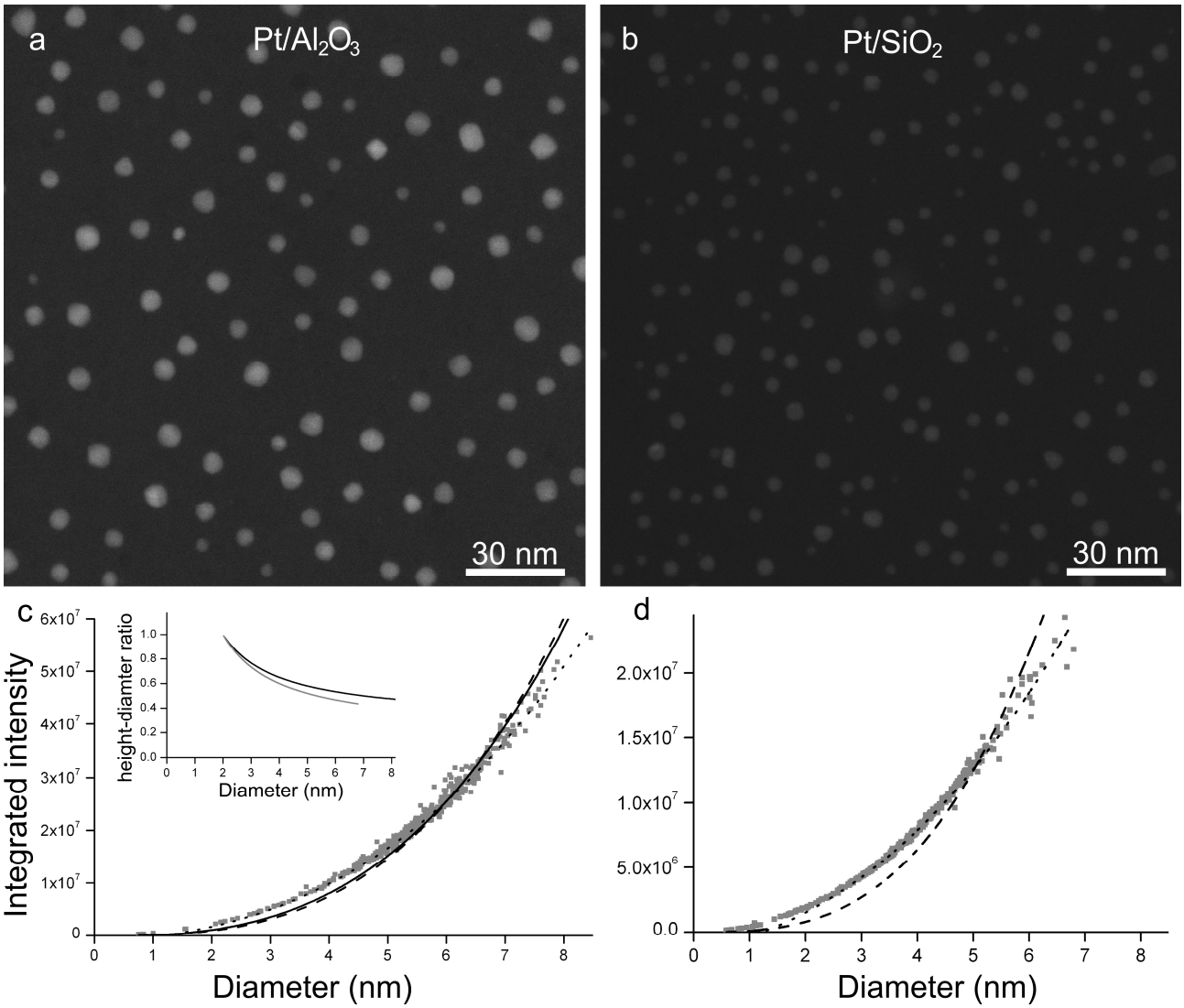

Fig. 6.1: Representative STEM images of (a) the Pt/Al_2O_3 and (b) the Pt/SiO_2 model catalyst after aging in a tube furnace in 1 bar 0.2 % O_2 in N_2 for 3 hours at 650℃. (c-d) The STEM signal intensity for (c) Pt/Al_2O_3 and (d) Pt/SiO_2 integrated over the projected area of the particles presented in arbitrary units against the particle diameter (grey). The volume of a spherical cap, $V(d) = C \cdot [1/2 - 3/4\cos(\theta) + 1/4\cos^3(\theta)] \cdot 1/6\pi d^3$ is fitted to the data with Pt/Al_2O_3: R^2 = 0.95 and Pt/SiO_2: R^2 = 0.92 (dashed lines). Here C is the calibration factor for converting particle volumes to the STEM signal intensities and θ is the metal-oxide contact angle, which is kept constant for all particle sizes. In addition, $V(d)$ with a size-dependent θ is fitted to the STEM data by assuming linear relation between the particle height and diameter and that particles for which d = 2 are spherical, resulting in Pt/Al_2O_3: R^2 = 0.98 and Pt/SiO_2: R^2 = 0.99 (dotted lines). The insert presents the size-dependent height-diameter ratio for Pt/Al_2O_3 (black) and Pt/SiO_2 (grey) calculated from the dotted lines. Finally, for Pt/Al_2O_3 $V(d)$ is plotted with a size-dependent θ corresponding to the size-dependent height-diameter ratio presented in figure 6.3d, resulting in R^2 = 0.97 (full line).

ratio for the observed particles must decrease for increasing diameters. A volume for a spherical cap with a size-dependent height-diameter ratio can be fitted to the STEM data based on information on the specific relation between the height and the diameter. To illustrate this, a close fit to the STEM data (Pt/Al_2O_3: R^2 = 0.98, Pt/SiO_2: 0.99) was obtained by assuming a simple linear relation between the height and the diameter and that the smallest particles are spherical i.e. h/d = 1 for d = 2 nm (fig. 6.1c,d, dotted black). A calculating of the size-dependent height-diameter ratio from the fitted lines show that the size-dependence of the height-diameter ratio is approximately similar for Pt/Al_2O_3

and Pt/SiO_2 (fig. 6.1, insert) i.e. if the small particles are spherical, the largest are approximately hemispherical.

For Pt/Al_2O_3 aged in oxygen, it was not possible to find previously reported three-dimensional particle shapes to compare these estimates with. For Pt/SiO_2 the three-dimensional particles shape was both reported as spherical when aged in oxygen (particle diameters = ca. 2 – 5 nm) [71] or vacuum (particles diameters = ca. 30 – 40 nm) [26], and hemispherical (particle diameters > ca. 4 nm) when aged in wet air or wet N_2 [53]. It is therefore not possible to determine whether the estimates from STEM are consistent with previous results, and it should be emphasized that this estimate was based on the arbitrary assumption of a spherical shape for the small particle sizes. Also, since the calibration constant, *C* (fig. 6.1, figure caption) relating the particle volume to the STEM signal intensity is unknown, the true relation between the particle heights and diameters cannot be determined from figure 6.1 alone.

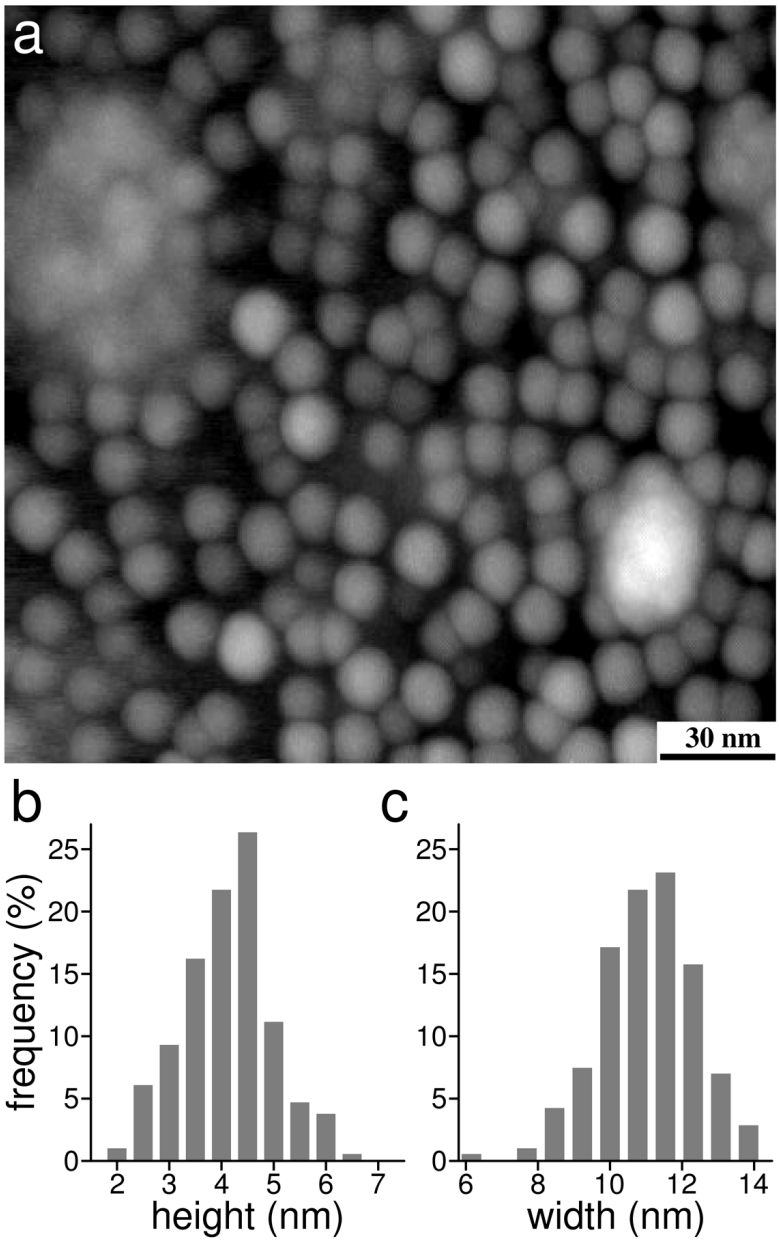

Fig. 6.2: (a) AFM image of the Pt/Al_2O_3 sample after aging in a tube furnace in 1 bar 0.2 % O_2 in N_2 for 3 hours at 650℃. (b) Particle height distribution an d (c) PSD. The number of measured particles is 217.

6.2. Size-dependent particle shapes of Pt/Al_2O_3 according to AFM

To obtain information about the absolute heights of the nanoparticles, AFM measurements was performed. Specifically, AFM images were recorded of the Pt/Al_2O_3 sample after thermal aging at 650°C (section 3.2.2). A representative AFM image is presented in figure 6.2a. In the image, the height of the AFM tip relative to the oxide support is depicted by a grey scale, from which Pt nanoparticles can be identified as brighter protrusions and the darker background can be linked to the oxide support. The larger (> 20 nm), bright features represent impurities on the surface, possibly induced during sample transfer to the UHV AFM. Pt nanoparticles at or in close vicinity of such regions were avoided in the data analysis. Figure 6.2b-c presents a particle height distribution (PHD) (b) and a PSD (c) based on measurements from the AFM images.

The particle diameters measured by AFM (figure 6.2c) are generally larger relative to the diameters as measured by TEM (fig. 4.8j), which can be attributed to the well-known effect of tip broadening in AFM for objects with a size comparable to the tip apex dimensions. Therefore, in order to obtain a direct correlation plot of the nanoparticle heights vs. the diameters, the PSD measured by AFM were aligned with the analogous PSD from TEM. The best fit, presented in figure 6.3a, was obtained when the width and the peak centre of the PSD from AFM were adjusted by multiplication and subtraction respectively, and the optimal multiplication (= 0.7) and subtraction values (= 2.4 nm) were determined by minimization of the total squared difference between the column heights in the PSDs from AFM and TEM. The effect of AFM tip broadening is graphically illustrated in figure 6.3b, by superimposing circles on the particle positions. Figure 6.3b serves to illustrate that the broadening is sufficiently small to allow the detection of small particles in the vicinity of larger ones. Figure 6.3c presents a plot of the particle height as a function of the nanoparticle diameters corrected for tip broadening. Interestingly, the majority of the data points lie in the region between the lines corresponding to a spherical (full grey) and a hemispherical (dashed grey) particle shape (fig. 6.3c). The Al_2O_3-supported Pt nanoparticles are therefore generally flatter than spheres, but higher than hemispheres. Assuming a linear relation between the height and diameter, two straight lines are fitted to the data: one which is unforced (full black) for which R^2 = 0.48 and one which is forced through the origin (dashed black) for which R^2 = 0.46. From the fitted lines in figure 6.3c, the size dependent height-diameter ratio was calculated, and the result is presented in figure 6.3d (full black and dashed black). The unforced line corresponds to a height-diameter ratio that indeed decreases as a function of particle size, reflecting a size-dependent cluster morphology for Pt on Al_2O_3. The AFM data does not describe the height-diameter ratio for particle sizes below 2 nm (fig. 6.3c-d), and simply extending the unforced fit in figure 6.3c below the limit of 2 nm, will result in a $h/d > 1$ for $d < 2$ nm, which seems unreasonable. It is therefore more likely that the height-diameter ratio is constant for the smallest particle sizes. On the contrary to the forced line corresponds to a constant height-diameter ratio for all particle sizes. Since the unforced line only fits the data slightly better than the forced line, the AFM data alone only weakly suggests a size-dependency of the height-diameter ratio. For comparison with the STEM data, the volume of the spherical cap including the size-dependent height-diameter ratio corresponding to the unforced line in figure 6.3d is fitted to figure 6.1c (full black) resulting in R^2 = 0.97. The particle volume including the size-dependent height-diameter ratio fits the STEM data slightly better than the fitted volume corresponding to the constant particle shape (dashed black, R^2 = 0.95). The difference between the two fits based on the AFM data is relatively small, compared to the trend of the STEM data which indicate a stronger size-dependence of the particle shape. The stronger size-dependency of the height-diameter relation according to the STEM data can be appreciated by re-plotting the black dotted line from figure 6.1c in figure 6.3d (black dotted line). In summary, the STEM and AFM data in combination suggest that the Al_2O_3-supported Pt nanoparticles generally are flatter

than spheres and that the height-diameter ratio decreases with the particle size, although there is not full consistence between the two dataset on the degree of the size-dependence of the height-diameter ratio.

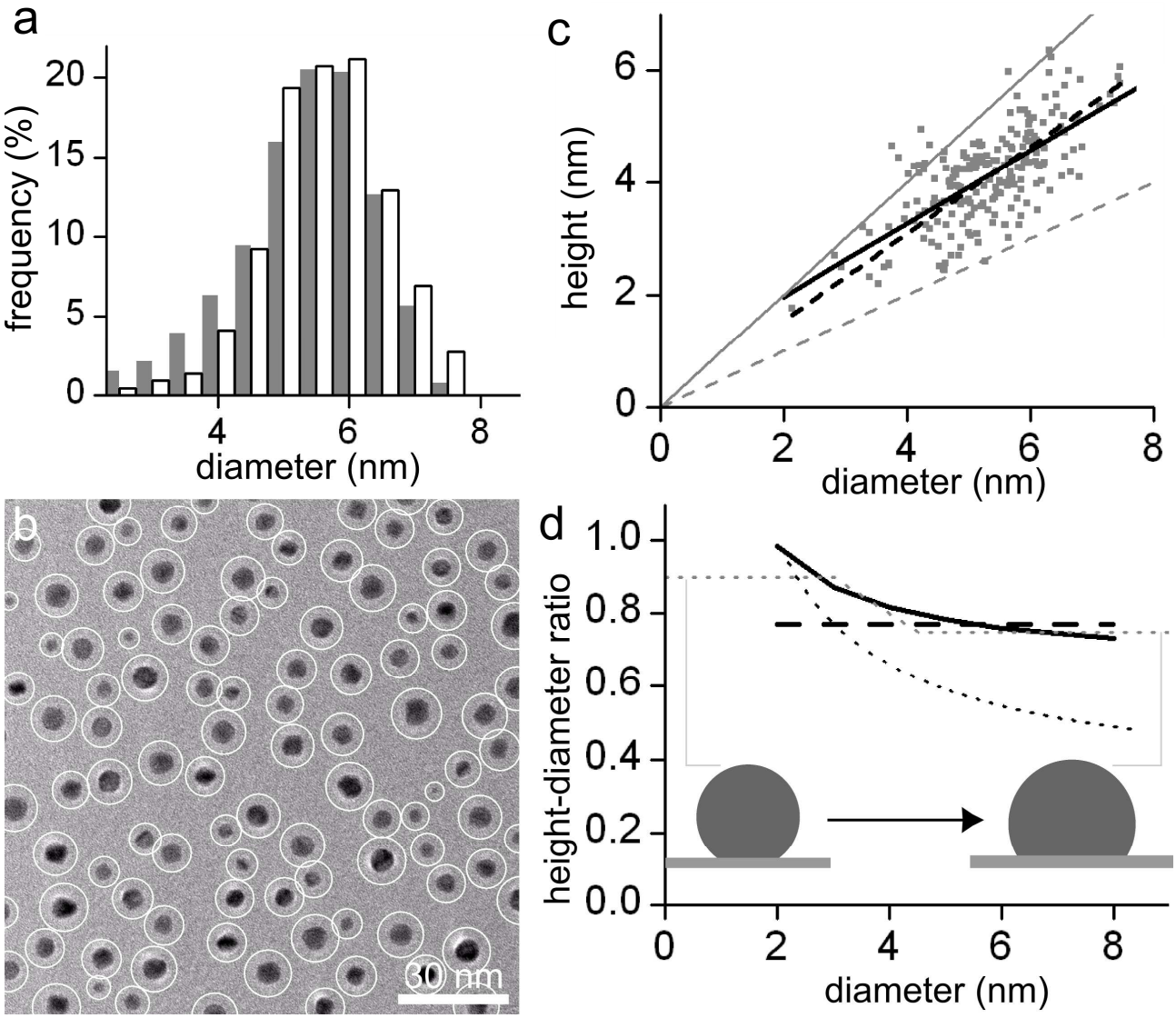

Fig. 6.3: (a) PSDs from the calibrated AFM measurements (white) and TEM measurements (grey). (b) TEM image of the Pt/Al_2O_3 sample after ageing at 650℃. The circles indicate the none-calibrated AFM diameters. (c) The nanoparticle height presented as a function of the calibrated nanoparticle diameter. Two straight lines are fitted to the dataset: One unforced (full black) and one forced through the origin (dashed black). For comparison, lines corresponding to a spherical (full grey) and a hemispherical (dashed grey) particle shape are indicated. (d) The height-to-diameter ratio is presented as a function of nanoparticle size based on the unforced (full black) and on the forced (dashed black) fitted lines in (c). The black dotted line corresponds to the black dotted line in figure 6.1c and represents the best fit to the STEM data. The height-diameter ratio values used in the simulation is indicated (dotted grey) and the nanoparticle shapes corresponding to the highest and lowest values of the height-diameter ratio are illustrated.

6.3. The effect on ripening of the size-dependent shapes according to computer simulations

To address the effect on the sintering of a size-dependence of the particle shapes, computer simulations based on a kinetic mean-field model for ripening in which the size-dependence of the particle shapes are integrated is compared with the experimental results for the sintering of the model catalysts presented in chapter 4.

Based on eq. 2.13, computer simulations of PSDs were performed following the procedure described in section 4.1.5. The PSDs of the as prepared model catalysts (fig 4.8a,f) were used as the initial PSDs. For both the simulation of Pt/Al_2O_3 and Pt/SiO_2 α_i in eq. 2.13 was based on the continuous height-diameter-trace given by the grey dotted line in figure 4.3d, to capture just the main trends of the size-dependence of the height-diameter ratios according to the unforced linear fit to the AFM data. This trace, which resembles the AFM data rather than the STEM data, was chosen to examine the effect of the least size-dependent variations in the height-to-diameter ratio. To fixate the time-scale in simulations, α_i' in eq. 2.13 is adopted so the final mean particle diameter corresponds to that observed after 3h ageing at 650°C. The simulations adopted time steps corresponding to units of $\alpha_i'^{-1} \cdot nm^3$, so time couples to α_i'. That is, a long simulated aging time (many calculation steps) at low temperature therefore corresponds to a short aging time (few calculation steps) at a higher temperature.

Figure 6.4a-d presents the initial and simulated PSDs for Pt/Al_2O_3. The simulation shows that the initial PSD evolves into a shape with a shoulder to the large particle side of the main peak over a bimodal PSD and further into a shape with a main peak shifted toward the large particle sizes and with a tail towards the small sizes (fig. 6.4a-d). It is intriguing that the simulated time-evolution of the PSD shape matches the experimental observations of the time-evolution as presented in figure 4.5a-f. Since time and temperature are linked in the simulations, i.e. the effect of temperature can be compensated with time, the simulated time-evolution also matches the PSD shape evolution in temperature (fig. 4.8f-j). According to figure 6.4a-d, the shoulder to the right side of the main peak develops for the PSDs during thermal aging of the supported nanoparticles where the height-diameter ratio is size dependent, while the shoulder or the bimodality was not observed for supported nanoparticles with constant shape (fig. 4.5, red or blue line).

Figure 6.4e-h presents the initial and simulated PSDs for Pt/SiO_2. As could be expected, the trends observed for Pt/Al_2O_3 can also be identified in the simulation for Pt/SiO_2, but the shoulder and the bimodality are much less pronounced for this sample, almost disappearing in the random noise. Figure 6.4 therefore shows that the transition shapes of the PSDs are highly dependent on the initial PSD, i.e. the PSD shape variations resulting from the size-dependent particle shapes are more pronounced for a narrow initial PSD compared with a wider one.

Because of the low degree of sintering during the in situ experiment for the Pt/SiO_2 due to the effect of the low N_2 partial pressure (section 4.3.1), only a shift in peak position and a broadening, but no characteristic shape changes in the PSD shape is observed for time-dependent PSDs (fig. 4.6). This complicates a comparison of the time-resolved experimental observations with the computer simulations presented in figure 6.4. Since time and temperature are linked in the simulations the simulations can, however be compared with the observed temperature-dependent PSDs (fig. 4.8a-e). From the experimental observations a shoulder to the right of the main peak is not clearly observed at any temperature (fig. 4.8a-e), although a shoulder may be weakly indicated to the right of the main peak in figure 4.8d. Bimodality is not observed for any temperature in figure

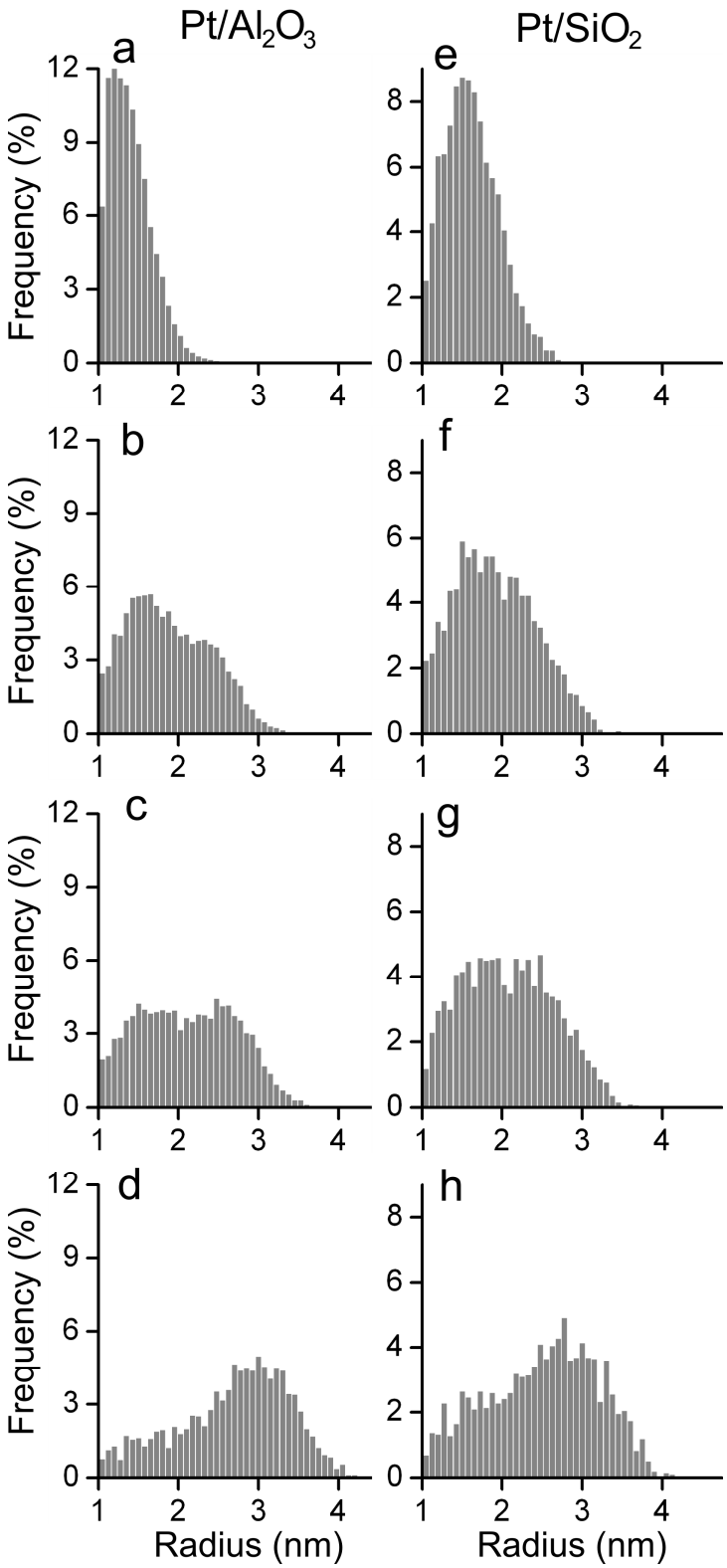

Fig. 6.4: Simulated PSDs for particles with decreasing height-diameter ratio. The contact angle, θ (eq. 2.13) used in the simulations is calculated from the height-diameter ratio indicated by the dotted line in figure 6.3d. The number of calculation steps for each simulation, corresponding to the sintering time in arbitrary time units, is (a,e) 0, (b,f) 20 (c,g) 30 and (d,h) 60. The initial distributions are identical to (a) fig 4.8f corresponding to the as-prepared Pt/Al_2O_3 sample and (b) fig 4.8a corresponding to the as-prepared Pt/SiO_2 sample. The number of particles in each distribution is (a) 14243 (b) 6651, (c) 5220, (d) 2807, (e) 6387, (f) 3431, (g) 2899 and (h) 2202. α' in eq. 2.13 is 0.11 $nm^{-1} \cdot min^{-1}$ for Pt/Al_2O_3 and 0.047 $nm^{-1} \cdot min^{-1}$ for Pt/SiO_2.

4.8a-e. These observations are consistent with the simulations from which a shoulder or bimodality are only weakly indicated (fig. 6.4e-h). The tails to the large particle side of the main peaks observed for the temperatures 550°C – 600°C (fig. 4.8c-d) that were associated with local particle correlations (section 4.2.1), are obviously not produced by the simulations since these do not include local ripening effects. Figure 6.4d,h shows that the simulated PSD for Pt/SiO_2 at 650°C is more symmetric than the PSD for Pt/Al_2O_3. A higher symmetry for the PSD of Pt/SiO_2 was also observed experimentally (fig. 4.8e), and was partly (but not fully) explained by the local particle correlations (fig. 4.8e, dotted line). Figure 6.4 offers an additional explanation for the higher symmetry, and it is therefore suggested that the more symmetric PSD for Pt/SiO_2 relative to Pt/Al_2O_3 after thermal aging at 650°C is a combined effect of the local particle correlations and a wider initial PSD.

6.4. Chapter summary

After sintering in an oxidizing environment, size-dependent shapes of Pt nanoparticles on the oxide supports was shown to be consistent with STEM measurements for both model catalysts and also with AFM measurements for the Pt/Al_2O_3 model catalyst. Specifically, the particles are generally flatter for the larger particle sizes. For the Pt/Al_2O_3 sample the absolute particle heights were determined by using AFM, and according to this the smallest particles are approximately spherical, the height-diameter ratio decreases to ca. 0.7 for the largest particles. Computer simulations show that the PSDs during ripening are influenced by the size-dependent shape of the supported nanoparticles. The observed size-dependence of the three-dimensional shape of the supported nanoparticles therefore offers a possible explanation for the transition shapes of the PSDs for Pt/Al_2O_3 presented in chapter 4. Also for Pt/SiO_2 the size-dependence of the particle shapes was found to be consistent with the experimental observations.

7. Effects of the initial particle density and size distribution on Ostwald ripening

In addition to the influence of the catalyst materials and the aging conditions, the sintering process can also be influenced by the detailed characteristics of the supported metal nanoparticles, such as the particle density [15,58] and the initial PSD [49] as indicated by the PSD simulations in chapter 6. This chapter presents a further analysis of how the Ostwald ripening of a Pt/SiO_2 model catalyst is influenced by the characteristics of the initial PSD as well as the initial particle density.

7.1. Pt/SiO_2 model catalysts from the cluster source

In an early theoretical study, Flynn and Wanke found that the sintering rate increases with an increasing width of the initial PSD [49]. This finding might also be concluded from the apparent correlation of the sintering rate with the particle size spread according to figure 4.3a,c and figure 4.9a,c. In a related experimental study, Flynn and Wanke observed a substantially increased sintering rate for an industrial type Pt/Al_2O_3 catalyst in oxygen at 575ºC when a portion of a pre-sintered catalyst with large particles was mixed with the catalyst. The observed higher degree of sintering was attributed to additional large particles acting as "sinks" for the transported metal [58]. To monitor the effect of additional large particles on the ripening of Pt nanoparticles directly, in situ TEM experiments were carried out on Pt/SiO_2 model catalysts with initial bimodal PSDs prepared by using a cluster source (section 3.1.2). By combining PVD with the preparation with the cluster source, four different Pt/SiO_2 model catalysts were prepared with varying particle density, with or without additional large particles (table 7.1). The capital letters *A* - *D* will be used as identifiers for model catalysts in this chapter according to table 7.1. It should be noticed that *A* is identical to the Pt/SiO_2 samples presented in chapter 4 - 6. The particle density of B and D is reduced to ca. 40 % of the particle density of A and C. The reduction in density corresponds to an approximate increase in the mean particle distance by a factor of 2.

	A	*B*	*C*	*D*
Particle density	High	Low	High	Low
Additional large particles	No	No	Yes	Yes
Preparation technique	PVD	Cluster source	PVD + Cluster source	Cluster source

Table 7.1: Overview of the characteristics and preparation techniques for the Pt/SiO_2 model catalysts.

7.2. In situ TEM results

The sintering of the nanoparticles of the Pt/SiO_2 model catalysts were activated by heating the samples by 30°C/min. up to 650°C in an atmosphere of 10 mbar air, similar to the in situ experiment described in chapter 4 (section 3.2.1.1). The electron beam effects were not estimated specifically for the samples prepared with the cluster source (*B* - *D*, table 7.1). Instead, it was assumed that the electron beam effects were comparable to that of the Pt/SiO_2 prepared by PVD (*A*, table 7.1), and the electron beam effects were minimized accordingly (section 3.2.1.3).

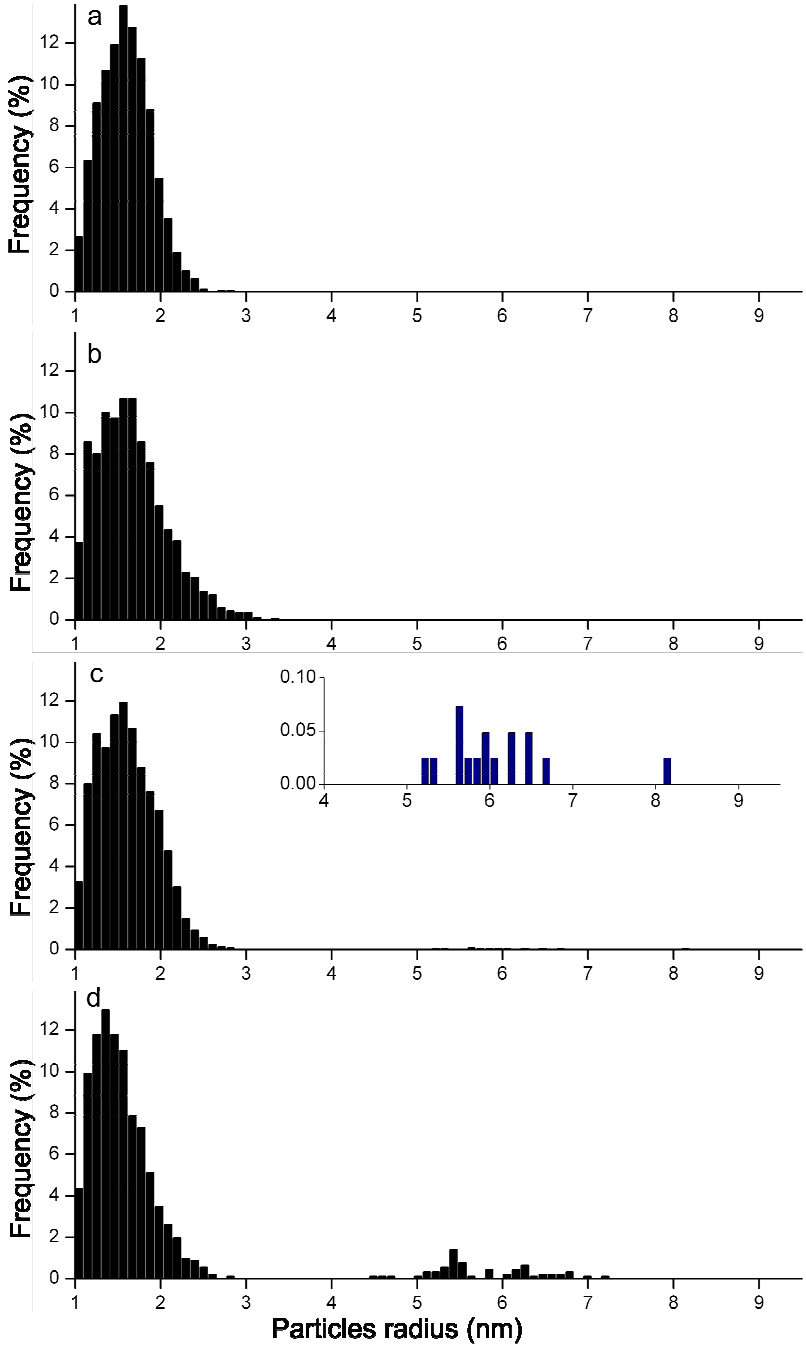

Fig. 7.1: PSDs from the four as-prepared Pt/SiO_2 samples (a) *A*, (b) *B*, (c) *C* and (d) *D*.

Initial PSDs

To determine the similarities and differences between the PSDs of the four samples, the particle sizes were measured automatically (section 3.3.1) from the TEM images acquired during the in situ experiments at regions on the sample *A*, *B*, *C* and *D* that were previously un-exposed to the electron beam. The PSDs corresponding to 5 min aging time is presented in figure 7.1 for sample *A* (a), *B* (b), *C* (c) and *D* (d). The initial (= after 5 min aging) mean radius of the small particles is ca. 1.5 nm (*A*: 1.54 nm, *B*: 1.61 nm, *C*: 1.55 nm, *D*: 1.47) and the radii are generally below ca. 2.5 for sample *A*, *C* and *D*, while the PSD for the small particles of sample *B* is wider with particle radii generally below ca. 3 nm. The sizes of the additional large particles in the samples *C* and *D* are ca. 5 – 7 nm in radius (one particle in sample *C* had a radius = ca. 8 nm). Because of the high density of the small particles in sample *C*, the measured frequencies of the additional large particles are relatively low and best observed from the inserted plot in figure 7.1c.

Analysis of the growth or shrinkage of individual nanoparticles

Figure 7.2 presents time-resolved TEM images recorded in situ of the same region of the samples (a-d) *B*, (e-g) *C* and (h-k) *D*. Similar time-resolved TEM images are presented for sample *A* in figure 4.2. In order to monitor several large particles within a single TEM image, a lower magnification is used for the TEM images presented in figure 7.2 relative to the images presented in figure 4.2, which should be kept in mind when comparing the results of sample *B*, *C* and *D* with *A*. The large white spots observed in figure 7.2e-k results from diffraction contrast from the additional large particles. The different positions of the white spots reflect variations in the focus settings. The in situ experiment for sample *C* was terminated after 240 min due to a shortcut of a heater wire in the heating holder (fig. 7.2e-g).

For all four samples (*A* – *D*), the nanoparticles remained immobile during the experiment and the projected area of the particles either increased or decreased. Hence, the sintering for all samples was governed by Ostwald ripening. Also, inspection of the TEM images for all samples reveals that the particle density decreases and the mean particle radius increases as a function of time. At first sight, the effect of the large particles on the Ostwald ripening is not obvious (fig. 7.2e-k).

To get at deeper insight into the ripening, the growth rates, *dr/dt*, of individual particles were measured manually (section 3.3.1) from the TEM images of sample *C* for the particles in the vicinity of one of the additional large particles (the large particle in the lower left corner in figure 7.2e-g). Figure 7.3 presents *dr/dt* as a function of the distance to the center of the large particle (radius ca. 5 nm). Both positive and negative growth rates are observed, except for particles within a distance of ca. 8 - 10 nm of the edge of the large particle, where only negative growth rates are observed. This tentative analysis therefore reveals reduced growth rates for the small particles in the vicinity of a much larger particle. Thus it appears that the large particles act to lower the density of the diffusion species in their local environment, consistent with the “sink”-effect of large particles suggested by Flynn and Wankes experiment [58] and with the analysis of local particle correlations in chapter 5.

Analysis of the ensemble averaged growth

To determine how the differences of the initial PSDs and particle density generally influence the sintering rate, the mean particle radii are compared pair wise as a function of time for the samples *A*, *B*, *C* and *D* in figure 7.4. In figure 7.4a the sintering of the Pt/SiO_2 model catalyst is compared for the high (*A*) and low (*B*) particle density, and according to the figure the mean particle radius increases faster for sample *B* with the lowest particle density. At first sight, this is surprising since previous studies have reported that the sintering rate increases with the metal loading, contrary to

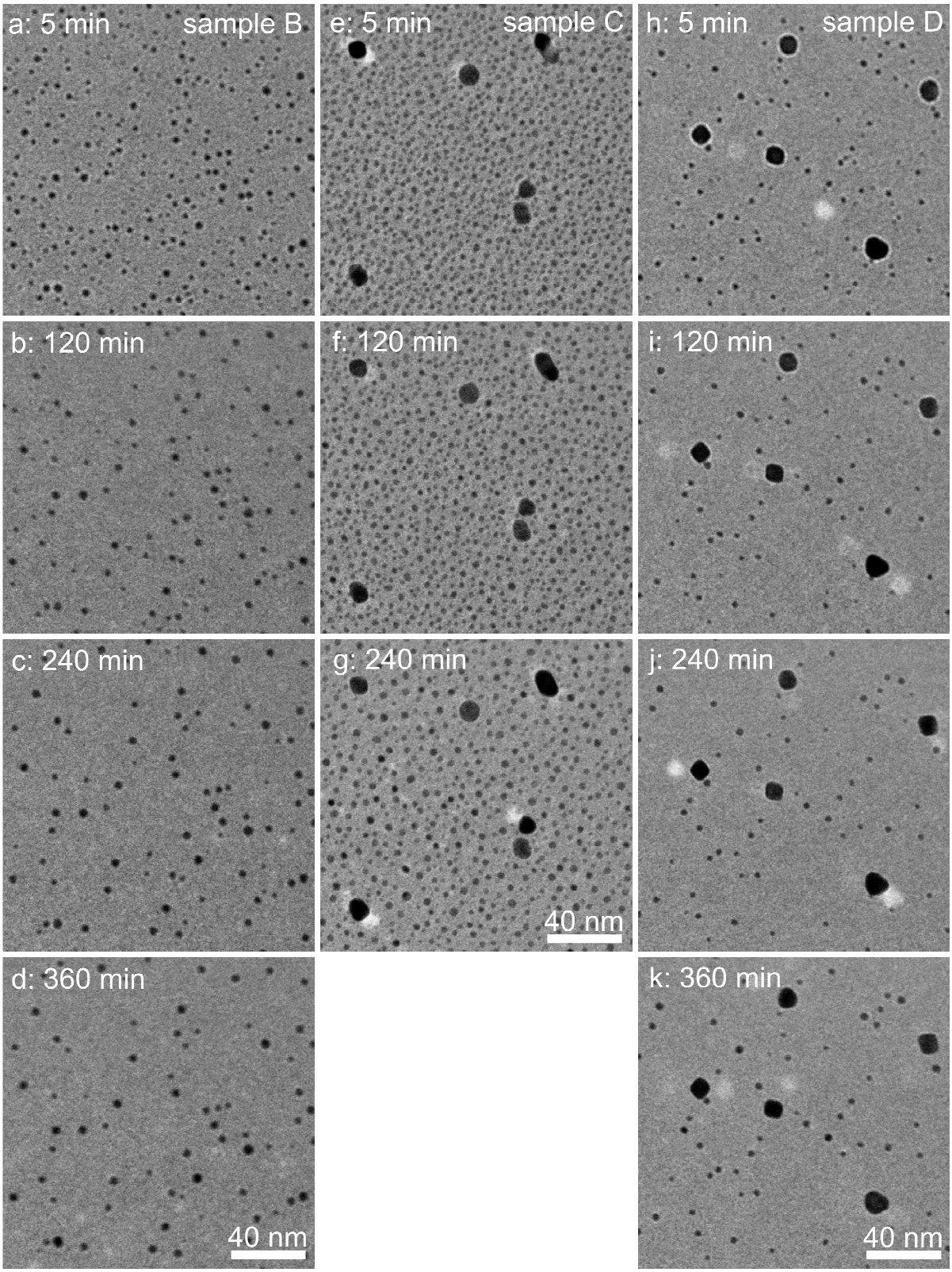

Fig. 7.2: Time-resolved TEM images recorded in situ at the same region of each Pt/SiO_2 model catalyst during exposure to 10 mbar air at 650ºC. The denoted times are relative to the time at which the temperature reached 650ºC. The as-prepared state of the present Pt/SiO_2 model catalysts deviates from as-prepared state of the Pt/SiO_2 model catalyst presented in chapter 4 (fig. 4.2) by having (a-d) a lower particle density (sample *B*), (e-g) additional large Pt particles while maintaining a similar high particle density (sample *C*) and (h-k) a lower particle density and additional large Pt particles (sample *D*).

the present result [15,58]. It should, however, be recalled that the initial PSD of the low density sample (*B*) is wider than the initial PSD of the high density sample (*A*) (fig. 7.1a,b). Figure 7.1 and figure 7.4 therefore do not necessarily show that the degree of sintering reduces with increasing particle density, but rather indicate that the sintering rate increases with the width of the initial PSD as previously suggested by Flynn and Wanke [49], and by figure 4.3a,c and 4.9a,c. Figure 7.2 and figure 7.4 also indicate, that an increase of the mean distance between the particles by a factor of ca. 2, does not reduce the sintering rate significantly.

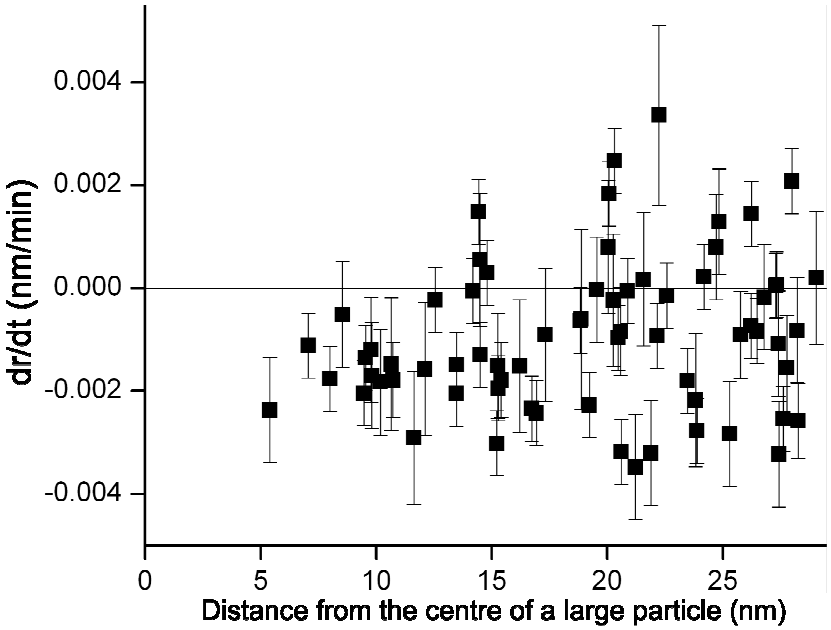

Fig. 7.3: The growth rate, *dr/dt*, for individual Pt nanoparticles presented as a function of the distance to the center of a large particle. The number of measurements is 86. The error bars indicate the propagated measurement errors from $\delta x_{manual\_measure}$ (section 3.3.3). The length of the error bars varies because *dr/dt* is measured over different time intervals.

The sintering of the Pt/SiO_2 model catalyst is compared in figure 7.4b for the high (*C*) and low (*D*) particle density including the additional large particles. In this case it is more complicated to objectively determine the widths of the corresponding PSD from figure 7.1. The width of the initial PSD for small particles alone is wider for sample *C* than for sample *D* (fig. 7.1c,d), while the width is considerably larger for sample *D* when calculated as the radius standard deviation by including the additional large particles. According to figure 7.4b, the increase in the mean particle radius is similar for sample *C* and *D* including (filled symbols) or excluding (open symbols) the additional large particles. Both figure 7.4a and figure 7.4b therefore show that the sintering rate is not significantly reduced by increasing the distances between the particles. This could suggest that the diffusion on the support is a rapid process, and that the Ostwald ripening is limited by interface processes rather than by diffusion of the atomic Pt-species at the support between the particles. For comparison, an analysis similar to the one presented in figure 5.1, was tentatively carried out based on automatic measurements on the TEM images of sample *B*. The model assuming interface control (R^2 = 0.24) did, however, not fit the data significantly better than the model assuming diffusion control (R^2 = 0.23).

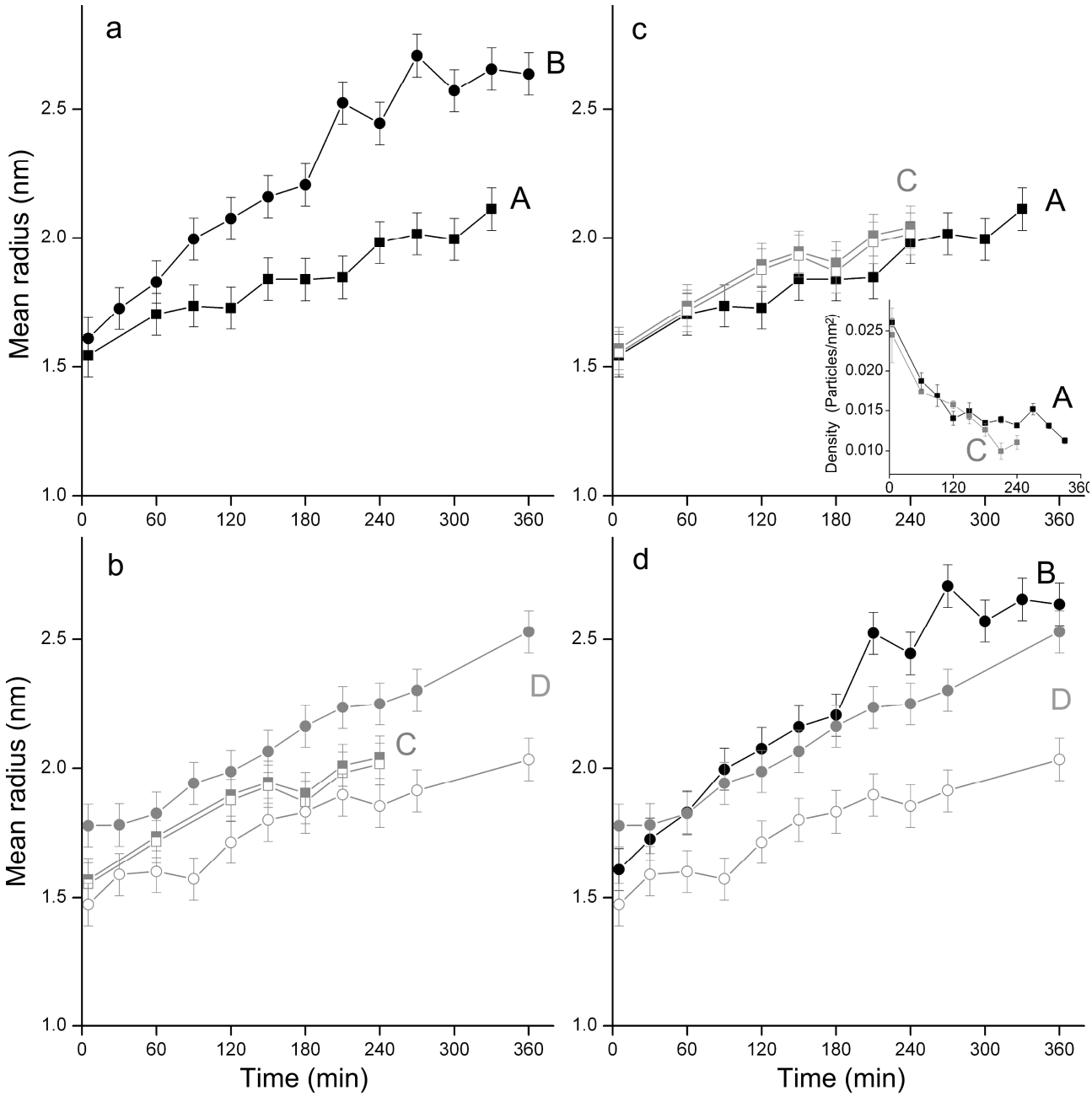

Fig. 7.4: The mean particle radius is presented as a function of time for the four different Pt/SiO_2 model catalysts *A* (black filled squares), *B* (black filled circles), *C* (grey filled squares) and *D* (grey filled circles). The four plots compare (a) *A* with *B*, in (b) *C* with *D*, (c) *A* with *C* and (d) *B* with *D*. For comparison, the mean particle radius calculated for *C* (grey open squares) and *D* (grey open symbols) without including the large particles is presented. The inserted graph in (c) presents the time-resolved particle density for sample A and C. Error bars: See Appendix B.

From figure 7.4c it can be observed that the mean radius for the high density samples, *A* closely follows the mean radius for the high density sample with additional large particles, *C* both calculated by including (filled symbols) or excluding (open symbols) the additional large particles. This result could suggest that the "sink"-effect of the additional large particles observed from figure 7.3 is insignificant in relation to the ensemble averaged growth rate. However, the presence of the large particles may influence the ripening process on a short time scale in a more subtle way than by simply increasing the mean particle radius. Figure 7.3 indicates that the "sink"-effect acts to reduce

the growth of a group of small particles. To determine the influence on the particle ensemble of the additional large particles, the time-resolved particle density, which is a more sensitive ensemble averaged parameter, is presented for sample *A* and *C* in insert in figure 7.4c. The particle density decrease more for the sample with the additional large particles, *C* relative to the sample without additional large particles, *A*, consistent with the indicated "sink"-effect by figure 7.3.

The time-resolved mean particle radii are compared in figure 7.4d for the low density sample with (*D*) and without (*B*) the additional large particles, calculated by including (filled symbols) or excluding (open symbols) the additional large particles. The increase in the mean radius for the low density sample, *B* is similar to the increase in the mean radius for the low density sample with additional large particles, *D*. Because of a significant variation in the initial particle density for the sample *B* and *D* (fig. 7.2a,h), it is not possible to compare the time-resolved particle density directly as was done for the samples *A* and *C* (fig. 7.4c, insert).

7.3. Limitations of the analysis

It should be emphasized that the results in this chapter only represent a tentative analysis, and there are a number of limitations. Firstly, the analysis depends on the assumption that the sintering rates for nanoparticles of the same size and similar local environment are independent of the preparation method, which according to previous studies is not always true [12,21,60]. To validate this assumption in further investigations, it is necessary to produce samples with identical statistical characteristics for the particles with both preparation techniques. This is a challenge because low particle densities are difficult to obtain by PVD, while when preparing the samples with the cluster source the probability of particles directly landing onto other particles increases with the particle density, leading to increasing PSD widths for increasing particle densities. Secondly, because of the un-intended variations in the widths of the initial PSDs, both the PSD width and the particle density varies, which makes it difficult to separate the influence of each parameter in the analysis. Finally, as mentioned in the previous chapters, local variations in the interactions between the metal and support may influence the results. Such an effect could possibly explain the existence of small particles in close vicinity to the additional large particles by the end of the experiments (fig. 7.2g,k) in spite of the suggested "sink"-effect.

7.4. Chapter summary

The sintering was compared for Pt/SiO_2 model catalysts with high and low particle density and for bimodal and monomodal initial PSDs. According to the preliminary analysis, the sintering rate is not directly related to the particle density, which could indicate that the Ostwald ripening is interface controlled, consistent with the results in chapter 4. Additionally, the sintering rate was found to increase for an increasing width of the initial PSD, consistent with both the results in chapter 4 and with an early theoretical study [49]. The influence of the bimodality of the initial PSD was analyzed by measuring the growth rates of individual nanoparticles in the vicinity of a large particle, and by measuring the time-dependent particle density. Both measurements showed that the additional large particles influence the growth rate of the smaller particles indicating that large particles acts to lower the density of the diffusion species in their local environment, thus locally

enhancing the sintering rate. This effect could be an explanation for the dependence of the overall sintering rate on the spread of the particle sizes. It should be emphasized that the present chapter only presents preliminary results, and further investigations will be needed to confirm, and expand on these tentative results.

8. Ostwald ripening of bimetallic Pt-Pd/Al_2O_3

The addition of Pd to the Pt-based oxidation catalysts has been reported to reduce the sintering of the oxide supported Pt nanoparticles in oxygen [16,73,74]. To address the influence of Pd on the sintering for such a bimetallic system, in situ TEM experiments were carried out with a bimetallic Pt-Pd/Al_2O_3 model catalyst as well as a monometallic Pd/Al_2O_3. STEM-EDS elemental mapping was applied to determine the distribution of the two metals in the bimetallic model catalyst before and after thermal aging. This chapter presents preliminary results from these experiments.

8.1. In situ TEM results for the bimetallic catalyst

Sintering of the nanoparticles of the bimetallic Pt-Pd/Al_2O_3 model catalysts was activated by heating the samples at 30^{o}C/min. up to 650°C, in an atmosphere of 10 mbar air similar to the in situ experiment for the model catalysts with pure Pt particles (chapter 4, section 3.2.11). It was estimated that the electron beam effects were negligible as described in section 3.2.1.3.

Figure 8.1 presents time-resolved TEM images recorded in situ from the same region of the sample. The Pt-Pd nanoparticles remained immobile during the experiment and the projected areas of the particles either increased or decreased (an example of each is indicated by arrows to guide the eye). Hence, the observations demonstrate that the sintering was governed by Ostwald ripening.

In addition to the TEM images of the sample region followed over time, TEM images were acquired during the in situ experiment, from regions on the sample that were previously un-exposed to the electron beam. Time-resolved PSDs extracted from the additional TEM images by automatic measurements (section 3.3.1) are presented in figure 8.2. As described in detail in chapter 4, basing the PSDs on the additional images offer better counting statistics than could be obtained from measurements on the TEM images in figure 8.1. Also, this approach eliminates the minor electron beam effects, which still may influence the data extracted from the region followed over time, even after the careful minimization of the beam effect described in section 3.2.1.3. According to figure 8.2, the PSD broadens over time, develops a shoulder to the large particle side of the main peak (fig. 8.2c-d), becomes more symmetric (fig. 8.2e) and finally becomes asymmetric with a tail to the small particle side of the main peak (fig. 8.2f). Comparison with fig. 4.5 shows that the evolution in PSD shape for the bimetallic Pt-Pd/Al_2O_3 is similar to that of Pt/Al_2O_3. A difference between the sintering of the bimetallic and the monometallic model catalysts is that the degree of sintering is slightly lower for the Pt-Pd/Al_2O_3 (mean radius = 3 nm at t = 360 min) than for Pt/Al_2O_3 (mean radius = 4 nm at t = 360 min), consistent with a previous study of the thermal aging of alumina-supported Pt or Pt-Pd nanoparticles in air [74].

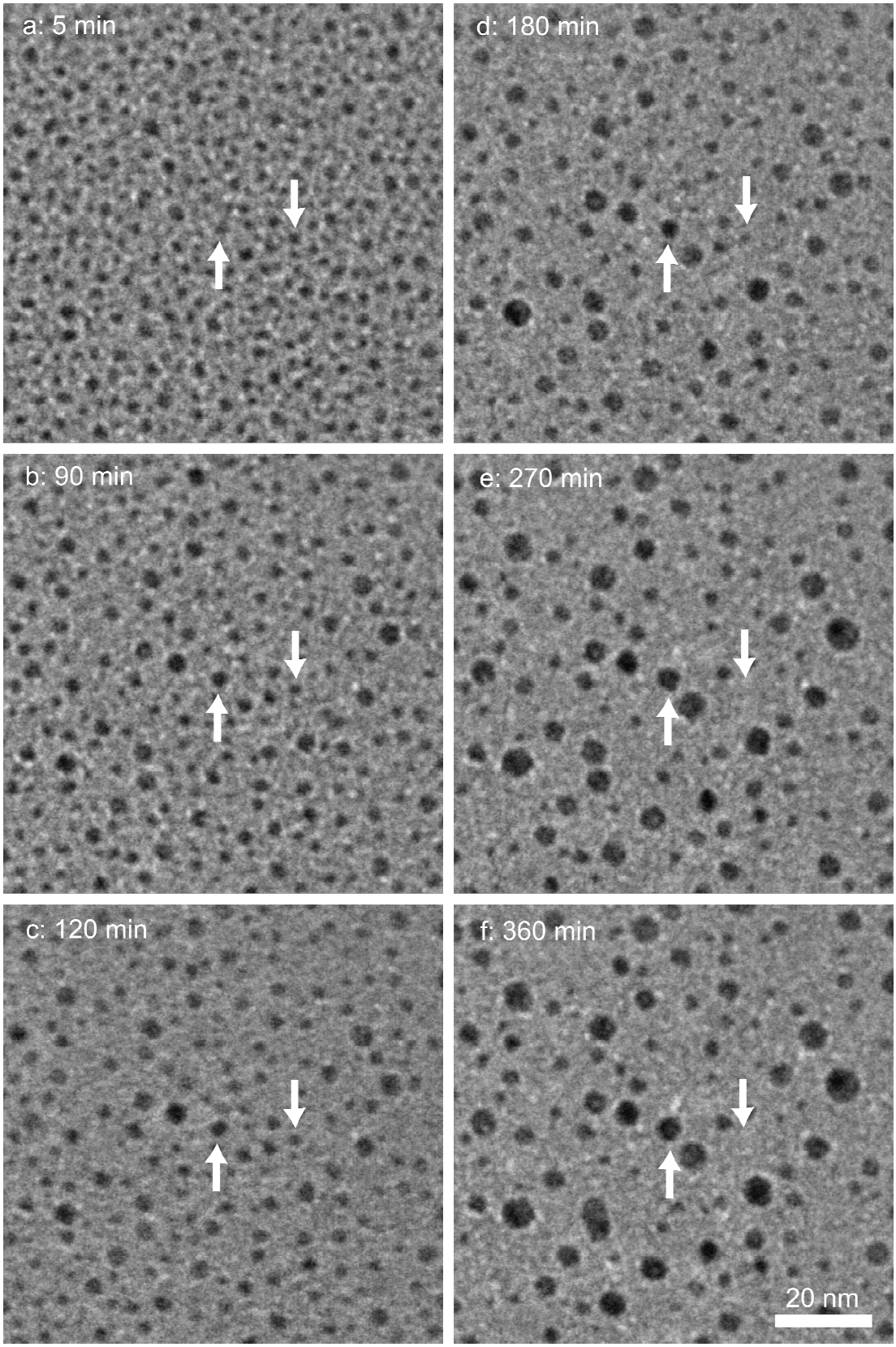

Fig. 8.1: (a-f) Time-resolved TEM images recorded in situ at the same region of a Pt-Pd/Al_2O_3 model catalyst during exposure to 10 mbar air at 650ºC. The denoted times are relative to the time at which the temperature reached 650ºC. To guide the eye, arrows indicate examples of a growing and of a decaying particle.

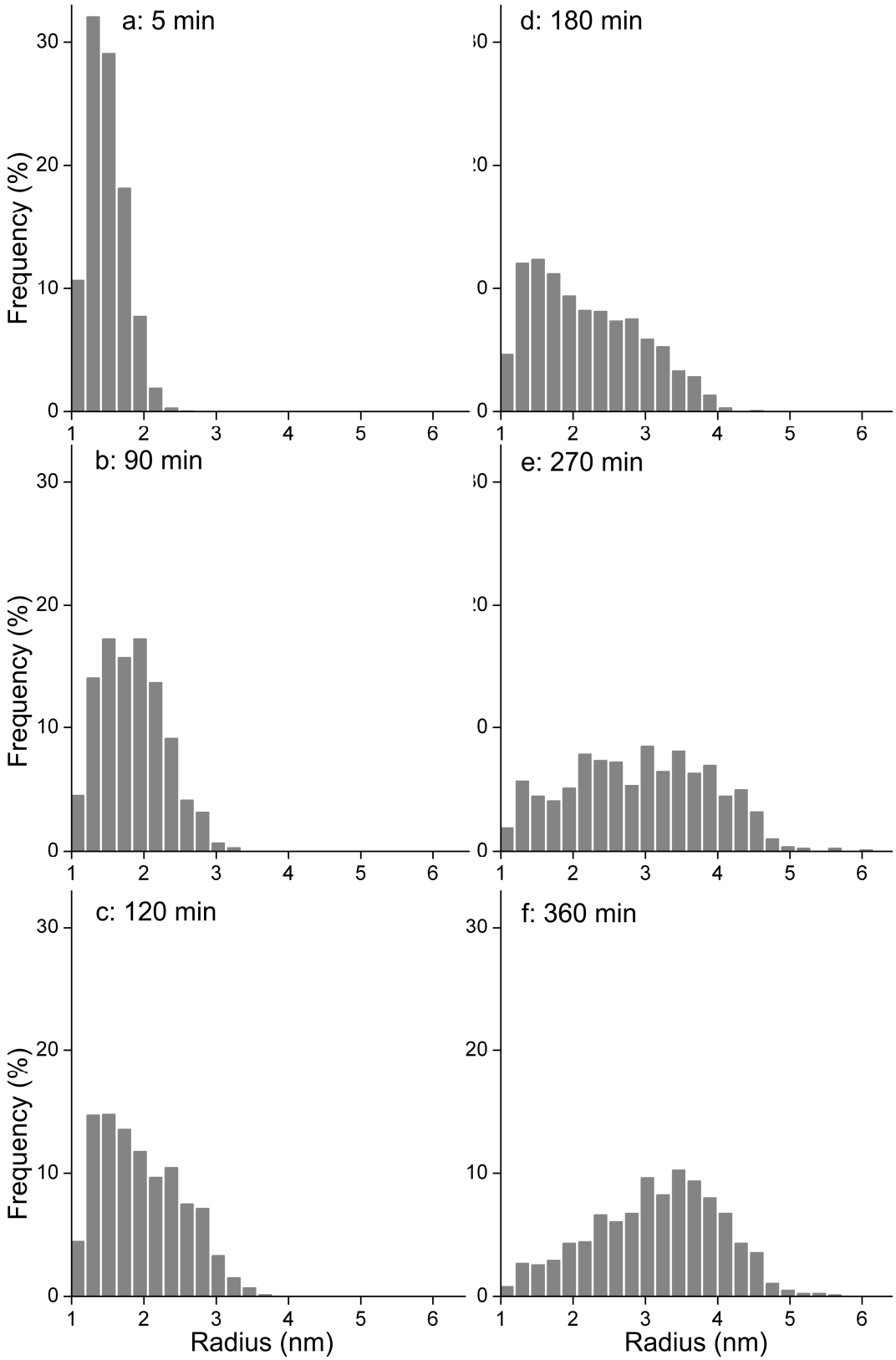

Fig. 8.2: PSDs from Pt-Pd/Al_2O_3 based on TEM images of regions previously unexposed to the electron beam recorded during exposure to 10 mbar air at 650ºC. The indicated aging times correspond to the aging times in figure 8.1. The number of measured particles included in each distribution is (a) 2069, (b) 1335, (c) 1405, (d) 1289, (e) 788 and (f) 809.

8.2. In situ TEM results for Pd/Al_2O_3

To address the influence of the presence of Pd on the sintering of the bimetallic $Pt\text{-}Pd/Al_2O_3$, another in situ experiment was performed, but with a monometallic Pd/Al_2O_3 model catalyst. Again, the sintering was activated by heating the samples by 30°C/min. up to 650°C in an atmosphere of 10 mbar air (section 3.2.1.1), and the electron beam effects were minimized as previously described (section 3.2.1.3).

Figure 8.3 presents the time-resolved TEM images recorded in situ from a single region of the sample. The time needed for stabilization of drift of the TEM holder, was a few minutes more than for the previous experiments, and the first recorded images corresponds to a thermal aging time of 10 min (fig. 8.3a) instead of 5 min as for the previous in situ experiments (fig. 4.1a, fig. 4.2a, fig. 8.1a). The Al_2O_3-supported Pd nanoparticles remained immobile during the experiment, and the projected area of the particles either increased or decreased (fig. 8.3, an example of each is indicated by arrows), which shows that the sintering of Pd/Al_2O_3 in an oxidizing environment is dominated by Ostwald ripening. The result is consistent with a previous in situ TEM study which showed that Ostwald ripening dominated the sintering of Pd/Al_2O_3, while coalescence events were only observed for particles closely neighbored to other particles [30].

Figure 8.4 presents time-resolved PSDs extracted from the additional TEM images by manual measurements (section 3.3.1). An asymmetric PSD shape with a tail to the large particle side of the main peak develops with time according to the figure and this observation is consistent with results previously reported for Pd/Al_2O_3 catalysts when heated in an oxidizing environment [142].

There are significant differences between the Ostwald ripening of the Pt-based model catalysts (fig. 4.1, fig. 4.2, fig. 4.5, fig. 4.6) and the sintering of the Pd/Al_2O_3 model catalyst that can be observed from both the time-resolved images (fig. 8.3) and PSDs (fig. 8.4). Firstly, most of the supported Pd nanoparticles seem not to grow or shrink in radius, but remain stable both with respect to position and size, consistent with a reported low degree of sintering for Pd/Al_2O_3 catalysts from previous in situ TEM [28] and post mortem [74] studies. Secondly, for Pd/Al_2O_3 a few large particles grew rapidly, and they grew to larger particle sizes than observed for any particles of the Pt-based model catalysts (fig. 4.5, fig. 8.4). Thirdly, for Pd/Al_2O_3 contrast variations can be observed in the projections of some of the largest particles (for example the particle marked with an upward arrow in figure 8.3c-f). Specifically, a region with a relatively darker contrast can be observed within the full projected area, and the position and size of the dark region is identical to the position and size of the initial particle (t = 10 min). In terms of mass-thickness contrast (section 2.2.2), this suggests either a) abrupt changes in the thickness of the particle, such as a relatively thin layer of Pd growing from the initial particle which is thicker than the growing layer, b) that the growing layer is a material with a lower density, such as PdO or c) a combination of a) and b).

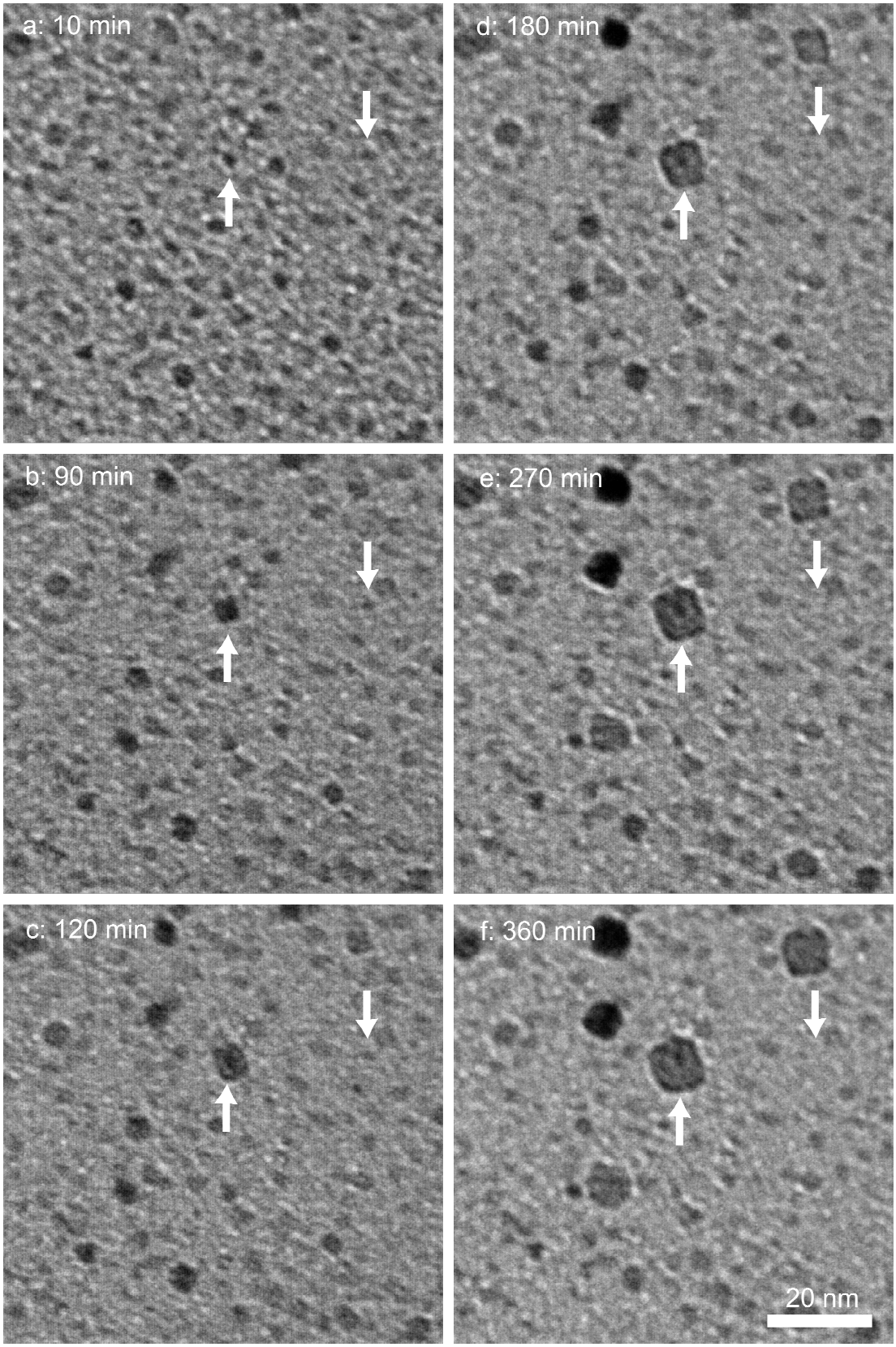

Fig. 8.3: Time-resolved TEM images recorded in situ at the same region of a Pd/Al_2O_3 model catalyst during exposure to 10 mbar air at 650ºC. The denoted times are relative to the time at which the temperature reached 650ºC. To guide the eye, arrows indicate examples of a growing and of a decaying particle.

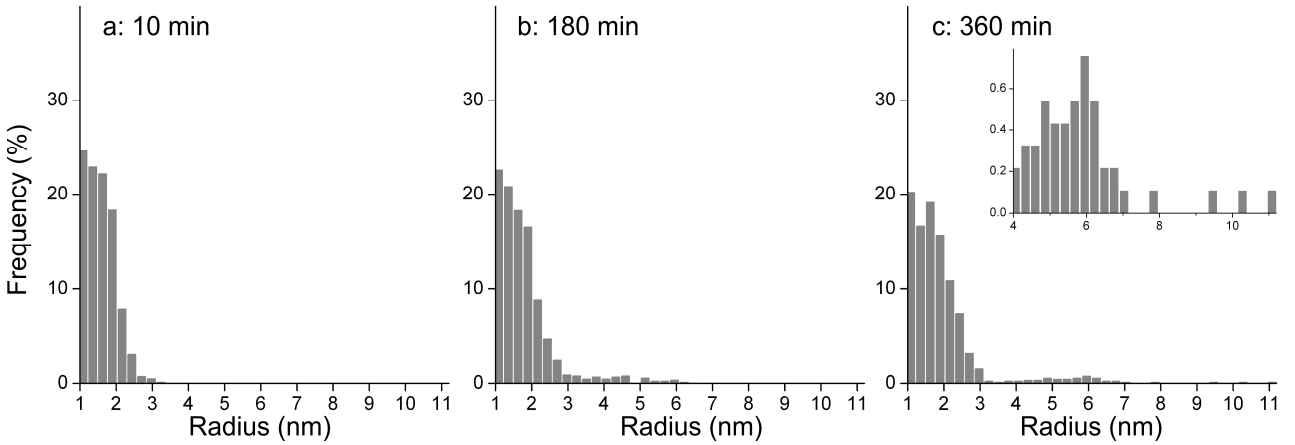

Fig. 8.4: PSDs from Pd/Al_2O_3 based on TEM images of regions previously unexposed to the electron beam recorded during the exposure to 10 mbar air at 650ºC. The indicated aging times correspond to the aging times in figure 8.3. The number of measured particles included in each distribution is (a) 835, (b) 918 and (c) 931. The manual particle measurement procedure (section 3.3.1) was applied due a relatively low contrast in the images.

8.3. The metal distribution in the bimetallic catalyst

A priori it is not known whether the particles in the $Pt\text{-}Pd/Al_2O_3$ model catalyst are present as alloys or as separated Pt and Pd particles. An estimate based on eq. 2.22, shows that the contrast of particles of pure Pt and Pd with radii in the range of 1.5 – 3 nm would only differ in contrast by 3 – 4 % in spite of a relatively large difference in the atomic number, *Z* of the two metals. From figure 8.1 it would therefore be difficult to distinguish particles of Pt from particles of Pd even if these were separated as monometallic particles.

To determine the relative distribution of the two metals, elemental maps were recorded of the $Pt\text{-}Pd/Al_2O_3$ model catalyst with STEM-EDS (section 3.2.2). Figure 8.5a presents representative results for the elemental mapping of an as-prepared sample. Specifically, the figure presents a STEM image of the sample before (Before scan) and after (After scan) the scan for the elemental map together with the detected electrons during the scan for the elemental map (Scan) and the elemental maps representing Pt (Pt) and Pd (Pd). In the "Before scan"-image, the region intended for the scan is indicated. In the "After scan"-image the region that was actually scanned is estimated by inspection of the "Scan"-image and by the beam induced changes observed from the "After scan"-image. According to figure 8.5a, most of the particles from the as-prepared sample consist of both Pt and Pd. In the scanned region, one particle (indicated by an arrow) apparently consists of only Pd. As described in detail in section 3.1.2, Pd was evaporated onto the sample after Pt during the sample preparation and therefore some Pd must be evaporated directly onto the Pt particles. The Pd evaporated directly onto the Al_2O_3-support could either have diffused to and attached to the Pt particles or could have formed new particles of pure Pd. It is therefore not surprising to see that most particles consist of both metals, while a few consists of pure Pd according to figure 8.5a. A quantitative analysis of an EDS spectrum (not presented) recorded over a larger area (90 x 90 nm^2) showed that the atomic Pt/Pd ratio was ca. 1.1.

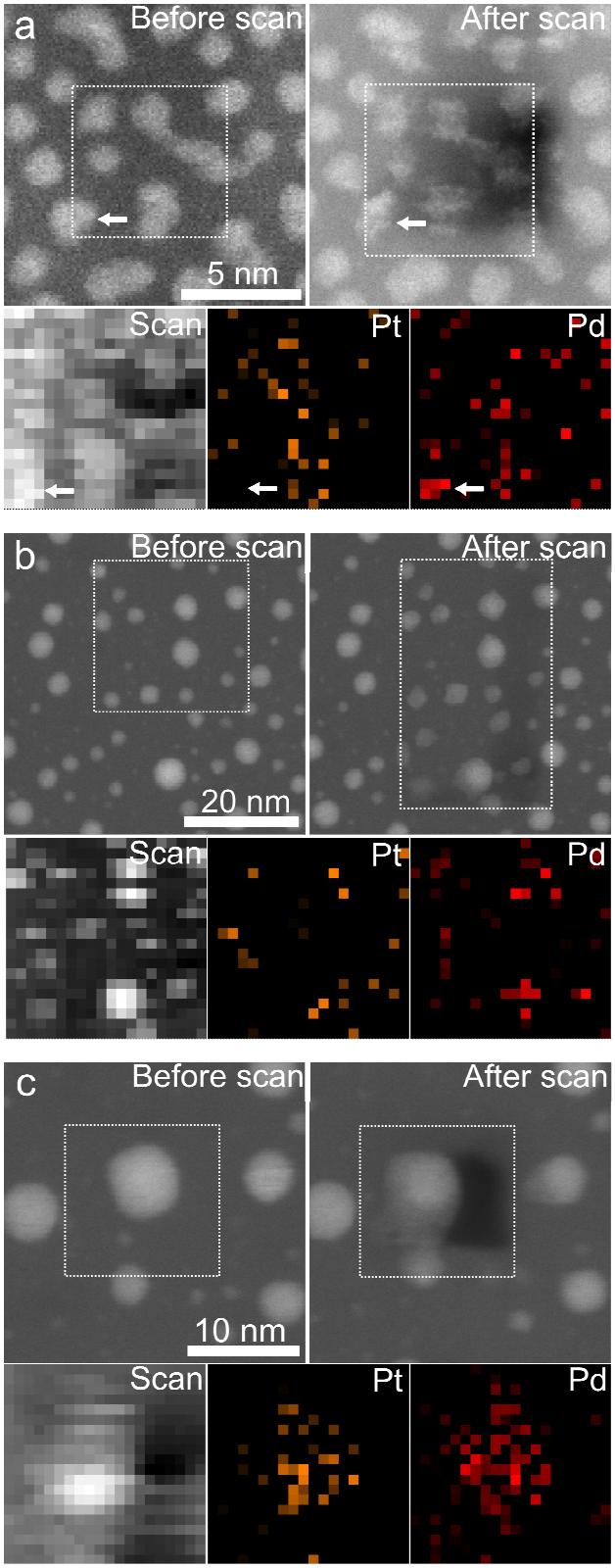

Fig. 8.5: (a) STEM images of the fresh Pt-Pd/Al_2O_3 sample before and after the scan for the elemental map is presented together with the detected electrons during the scan for the elemental map (Scan) and the elemental maps representing Pt and Pd respectively. In the “Before scan”-image, the region intended for the scan is indicated. In the “After scan”-image the region that was actually scanned is estimated by inspection of the “Scan”-image and by the beam induced changes observed from the “After scan”-image. (b-c): Similar to (a), but for the sample after the in situ sintering experiment.

Figure 8.5b presents representative results for the elemental mapping of the Pt-Pd/Al_2O_3 model catalyst after the in situ experiment. The elemental maps show that the sintered particles consist of both Pt and Pd (fig. 8.5b). Particles consisting of only one metal were not observed, but the possibility of pure Pt or Pd particles can not be excluded due to the relatively low counting statistics of both particles and EDS-signal.

To determine the metallic distribution within the particles after sintering, additional scans were performed on the sintered sample at regions with relatively large particles. Figure 8.5c presents such a scan. The elemental maps do not show structural differences between the two metals, such as a core-shell structure. According to figure 8.5c the Pt and Pd are apparently distributed evenly in the particle, but due to the low EDS counting statistics structural differences in the distribution can not be ruled out.

It should be emphasized that is was generally, and particularly for the as-prepared sample, difficult to obtain high EDS counting statistics without inducing severe damage to the sample by the strong intensity of the electron beam, as can be seen in the "After scan"-images (fig. 8.5a-c). For future work STEM-EDS mapping could be repeated at a lower electron voltage to reduce this effect. Also, the drift of the samples was problematic for the analysis, as the scanned region often differed from the region chosen for the scan, which is particularly obvious from figure 8.5b.

Together, the figures 8.1 and 8.5 show that the bimetallic Pt-Pd/Al_2O_3 model catalyst mainly consists of alloyed Pt-Pd (ca. 50%/50%) nanoparticles which sinter via Ostwald ripening. For the present experimental conditions, both metals are mobile as diffusing atomic Pt- or Pd-species which was observed from fig. 4.1 and from fig. 8.3. This is also consistent with the elemental map presented in figure 8.5c, since a quantitative analysis of the EDS spectra for the relatively large particle observed in this figure (volume = ca. 270 nm^3 compared to the volume = ca. 14 nm^3 for the mean particle size in the as-prepared sample, assuming a spherical shape for both particle sizes) shows that the Pt/Pd ratio is ca. 1.3. The large particle in figure 8.5c therefore mainly consists of atoms of both metals that have been transported during the sintering process.

8.4. Discussion

According to previous studies, oxide supported Pd or Pt-Pd nanoparticles can be prepared in either metal or oxide forms [73]. For similar Pd/SiO_2 and Pt-Pd/SiO_2 model catalysts, the metallic phase was observed in the as-prepared state, while PdO appeared after heating in air to 300°C - 400°C [73]. At higher temperatures, the PdO decomposes to Pd. Al_2O_3-supported palladium nanoparticles decompose from PdO to Pd at ca. 800°C [143], but the exact decomposition temperature depends on the partial pressure of oxygen [73], the support material [28,143] and the metal loading [28]. In the intermediate temperature range, Pd and PdO may coexist in an oxidizing environment [28,73]. For the present in situ experiments (fig. 8.1, fig. 8.3), it is therefore likely, that both the Pd and the PdO phases are present. For both Pd/Al_2O_3 and Pt-Pd/SiO_2, wetting and spreading has been observed during the transition from Pd to PdO [28,144], and the PdO phase has been associated with growing irregular shaped, low contrast areas [73,144] in contact with the metal crystallites [73]. Accordingly, the growing, low contrast areas observed for the Pd/Al_2O_3 model catalyst (fig. 8.3) are likely to represent thin layers of the PdO phase. According to a previous post mortem TEM study, the aging of Pd/α-alumina in N_2 at 900°C did only result in a shift of the main peak of the PSD, but not in an asymmetric PSD shape with a tail to the large particle side [145]. This observation supports the interpretation that the large particles represented by the tail to the large

particle side of the main peak of the PSDs in figure 8.4, corresponds to the oxidized phase of palladium while the main peak may correspond to Pd, PdO or Pd/PdO mixtures. For the bimetallic Pt-Pd/Al_2O_3 catalyst, growing low contrast areas are not clearly observed (fig. 8.1). This suggests that the PdO phase either stays at, in, or below the particles.

As described in section 2.1.2, the Pt is most probably transported in the form of volatile PtO_2 species [12,15,19,56,65], while PdO is considered to be less volatile [73,74] which may be related to a higher a melting point (PtO_2: 450°C, PdO: 870°C, Pt: 1768°C, Pd: 1555°C) [74]. This could suggest that the lower degree of sintering observed for Pd/Al_2O_3 (fig. 8.3, fig. 8.4) relative to Pt/Al_2O_3 (fig. 4.1, fig. 4.5) can be explained by a lower concentration of diffusing PdO species in Pd/Al_2O_3 relative to the concentration of diffusing PtO_2 species in Pt/Al_2O_3 for the same experimental conditions. The observation in figure 8.3 of the apparently rapid growing areas which likely represent PdO, is consistent with a relatively low concentration of diffusion species, if the modest thickness of the growing layers is taken into account.

For the bimetallic Pt-Pd/Al_2O_3 model catalyst (fig. 8.1), it can be speculated that the stabilizing effect on the sintering of Pt results from the presence of the relatively stable PdO phase. One suggestion is that formation of the PdO phase at the surface of the alloyed Pt-Pd particles lowers the surface density of Pt [73,74,144]. A skin of microcrystalline PdO on a few particles has been indicated from dark field TEM imaging of Pt-Pd/SiO_2 in oxygen [73]. Another possible explanation for the stabilizing effect is based on the fact that the interactions between the oxides are stronger than between metals and oxides [73,146,147]. It has been suggested that strong interactions between PdO and the support can lead to inter-diffusion between the oxide phases [148]. Consistent with this suggestion, the local structure of PdO supported on γ-alumina has been reported to be significantly different from that of bulk PdO [28]. As previously suggested [73,74], it can therefore be speculated that the strong PdO-oxide interaction results in stabilized layers of PdO which could act as traps for diffusing species. The present STEM-EDS analysis shows that the particles consist of both platinum and palladium, while particles of pure Pd were not found after sintering. This is consistent with the suggestion that diffusing Pt-species will bind to PdO.

It is interesting to notice that the degree of sintering of the bimetallic Pt-Pd/Al_2O_3 system is higher than for the monometallic Pd/Al_2O_3 system. The line of thought could therefore be reversed, so that it is concluded that the presence of Pt in a Pd-based catalyst increases the sintering, i.e. Pt increases the mobility of Pd. This could indicate that the formation of Pt-Pd alloys results in a weakening of the interaction between the PdO and the oxide support.

The present analysis has certain limitations, and future investigations are needed to settle the speculations related to the stabilizing effect of Pd on the Pt-based catalysts. Firstly, the interpretation of the growing low contrast areas in figure 8.3 was based on previously reported results, but was not determined independently from the present experiments. Diffraction and dark field imaging could help to verify the presence and the location of the PdO phase. Secondly, the statistics of the elemental mapping is poor, which weakens the statement that no particles of pure Pd were found after sintering. An extended STEM-EDS analysis could improve this point. Thirdly, a core-shell structure is difficult to observe for even the largest nanoparticles in the present bimetallic model catalyst. Extended sintering (longer aging times or higher oxygen partial pressure) could be applied for obtaining larger particles for which the presence of a core-shell structure would be easier to determine.

8.5. Chapter summary

In summary, the preliminary results for the monometallic Pd/Al_2O_3 and the bimetallic $Pt\text{-}Pd/Al_2O_3$ show that both model catalysts sintered via Ostwald ripening in 10 mbar O_2 at 650ºC. The bimetallic model catalyst consists of mainly alloyed Pt-Pd nanoparticles and the mass-transport was mediated by diffusing Pt- or Pd-species, resulting in a system with larger alloyed particles in which the two metals apparently are evenly distributed. Localized differences in the concentration, such as a core-shell structure can however not be ruled out based on the present preliminary analysis. Time-resolved PSDs for the bimetallic $Pt\text{-}Pd/Al_2O_3$ are qualitatively similar to those for monometallic Pt/Al_2O_3 and the PSDs quantitatively show that the degree of sintering is lower for the bimetallic system, consistent with previous studies. The stabilizing effect of Pd could possibly be explained by strong interactions between the present PdO phase and the oxide support or by a reduced surface density of PtO_2 species.

9. Conclusions and Outlook

This thesis addressed the sintering of noble metal nanoparticles with relevance to the diesel oxidation catalyst. The sintering of model catalysts composed of Pt and Pd nanoparticles on planar, homogeneous oxide support materials was studied in an oxidizing environment by using in situ and post mortem TEM. The main results were presented by time-resolved in situ TEM images which demonstrated that the sintering of the Pt, Pd and bimetallic Pt-Pd nanoparticles was governed by the Ostwald ripening mechanism (chapters 4 and 8). For Pt, this was shown for both an Al_2O_3 and a SiO_2 support material. The Ostwald ripening was enhanced by the oxygen atmosphere, which suggested that the mass-transport was mediated by diffusing Pt-oxygen species and it was furthermore found that at temperatures up to 750ºC the diffusion mainly takes place at the oxide support. Unexpectedly, the results showed that the sintering of Pt/SiO_2 depends on the partial pressure of N_2 at temperatures below 750ºC.

The sintering process was presented statistically as a function of time or temperature by PSDs extracted from the in situ or post mortem TEM images. The statistical representations were analyzed by comparison with theoretical models for Ostwald ripening, either by directly fitting the so-called LSW model to the experimental data or via computer simulated PSDs. The PSDs appearing at the end of the in situ experiment or after sintering at the highest temperature from the ex situ results could be fitted with the LSW model, consistent with the theory for Ostwald ripening (chapter 4). Particularly for Pt/Al_2O_3, the fit of the LSW model closely matched the observations. Unexpected PSD shapes did also appear as a function of time or temperature for both the Pt/Al_2O_3 and Pt/SiO_2 model catalysts. It was found that the Pt nanoparticles tended to adopt size-dependent three-dimensional shapes during sintering. Specifically, the particles were generally flatter for the larger particle sizes. Computer simulations based on a simple model for Ostwald ripening showed that the PSDs were influenced by the size-dependence of the shape of the supported nanoparticles, and that the otherwise unexpected transition shapes of the PSDs could be simulated when the size-dependence was integrated in the kinetic ripening model (chapter 6). For Pt/SiO_2, the unexpected PSD shapes could only partly be attributed to the effect of size-dependent particle shapes. In addition it was found that the sintering of Pt/SiO_2 was influenced by local correlations between the nanoparticles which influence the PSD shape. A detailed analysis of the local correlations showed that the growth or decay of the individual nanoparticles was influenced by the size and location of the neighboring nanoparticles and that a more satisfactory description of the evolution of the individual nanoparticle sizes could be obtained by including the local correlations in the kinetic models (chapter 5). The local ripening effect was also determined for a Pt/SiO_2 model catalyst with a bimodal initial PSD, by measuring the growth rates of the individual nanoparticles in the vicinity of a relatively large particle and by comparing the time-dependent particle density for Pt/SiO_2 model catalysts with and without additional large particles. It appears that the larger particles act to lower the density of the diffusion species in their local environment and thereby locally enhance the sintering rate. Consistently, the results indicated that the overall sintering rate scales with the spread of the particle sizes, based both on an observed similarity between the time-dependence of the mean radius and the particle size spread and on a tentative analysis of the sintering of Pt/SiO_2 model catalysts with different initial particle size spreads (chapter 7).

Finally, a preliminary analysis showed that the bimetallic $Pt\text{-}Pd/Al_2O_3$ model catalysts mainly consists of alloyed Pt-Pd nanoparticles and that the mass-transport was mediated both by diffusing Pt- and Pd-species, resulting in a system with larger alloyed particles. The degree of sintering was lower for the bimetallic $Pt\text{-}Pd/Al_2O_3$ model catalyst than for Pt/Al_2O_3, which means that Pd has a

stabilizing effect on the Pt-based catalysts. The stabilizing effect of Pd could possibly be explained by strong interactions between the present PdO phase and the oxide support or by a reduced surface density of PtO_2 species (chapter 8).

The conclusion that the sintering is entirely dominated by Ostwald ripening at the oxide support may help to focus the future development of more stable diesel oxidation catalysts on the relevant sintering mechanism. Specific strategies for the development of more stable catalysts could be inspired by the coupling between low sintering rates and a low spread in the particle sizes. A route to slow down the deactivation could be to aim for a very low initial spread in the particle sizes. This may prolong the meta-stable initial state and result in higher total activity. Another strategy could be to further develop the bimetallic Pt-Pd/oxide system, for example by creating anchor points for PdO at the oxide support. Finally, the high degree of consistency between of the theoretical models (the LSW model and eq. 2.12) and the experimental observations shows that the theoretical models are applicable for predicting the sintering of simple catalyst systems of oxide supported nanoparticles in a oxidizing environment. The present results could thereby become bases for further developments on the theoretical models which could lead to new insight into the sintering of more complex systems.

The sintering of model catalysts in the relatively low oxygen partial pressures could deviate relative to the sintering of real diesel oxidation catalysts. An obvious aim for future work would therefore be to try to bridge the gab between the model and realistic catalyst systems. Since high pressure in situ TEM sample holders are now available [149], the in situ experiments could in principle be reproduced at a realistic gas pressure and composition. Also the planar model catalyst could be gradually modified towards the characteristics of a realistic catalyst, for example by using a crystalline oxide or by fabricating well-defined structures in the support via e-beam lithography to address to influence of the support structure on the sintering. The results from sintering experiments with such model catalysts could finally be compared with similar results from the realistic diesel oxidation catalysts.

Appendix A: List of abbreviations

AFM	Atomic force microscopy
CB	Carbon black
CNT	Carbon nanotube
CTF	Contrast transfer function
DOC	Diesel oxidation catalyst
EDS	Energy dispersive spectroscopy
ESEM	Environmental scanning electron microscopy
ETEM	Environmental transmission electron microscopy
FEG	Field emission gun
HAADF	High angle annular dark field
LSW	Model for Ostwald ripening by Lifshitz, Slyozov and Wagner
PHD	Particle height distribution
PSD	Particle size distribution
PVD	Physical vapor deposition
SEM	Scanning electron microscopy
SNR	Signal-to-noise ratio
STEM	Scanning transmission electron microscopy
TEM	Transmission electron microscopy
UHV	Ultra high vacuum
XPS	X-ray photoelectron spectroscopy
WPO	Weak phase object

Appendix B: Deviations in the error calculations

The standard deviation, *SD* for a parameter, *x* is defined as [119],

$$SD = \sqrt{\frac{1}{N-1}\sum_{i}^{N}\left(x_i - x_{mean}\right)^2} \tag{B.1}$$

where *N* is the number of measurements and x_{mean} is the arithmetic mean of *x*. The standard deviation of the mean value, *SDOM* is defined as,

$$SDOM = \frac{SD}{\sqrt{N}} \tag{B.2}$$

Figure 4.3
(a,c) Since the analysis mainly focuses on the relative changes in the mean radius, the errors are calculated as the propagated error from $\delta x_{automatic\_measure}$ without taking δx_{TEM_cal} into account (section 3.3.3). However, when comparing the absolute values of the mean radius from Pt/Al_2O_3 and Pt/SiO_2 respectively, it should be noticed that the systematic error δx_{TEM_cal} may shift the plotted mean radii by 10 %. (b,d) The particle density and the metal volume per support area do not, or only to a minor extent, depend on the error on the particles sizes. The errors are therefore calculated as the standard deviation (eq. B.1) of the particle density and of the volume per support area, respectively, measured from different TEM images.

Figure 4.9
(a) The TEM image acquisition for the data presented by this figure was carried out over a time span of several months which means that the TEMs were calibrated between the measurements. Also, two different TEMs were used for the image acquisition as mentioned in section 3.2.2. For these reasons, the errors equal the systematic error, δx_{TEM_cal} (section 3.3.3). (b-d) To take the systematic error from δx_{TEM_cal} into account, the particle density, the standard deviation and the volume metal per support area was calculated two times; first where all measured distances were increased by 10 % and secondly where all measured distances were decreased by 10 %. The error of was estimated as the difference between these two measurements.

Figure 4.10
The estimated errors are 10 % of the measured value. For the value corresponding to 800ºC, 10 % of the measured value will result in a unreasonably low error below 1 % point. For this data point it is assumed that the error is of approximately the same size as for the other points. Hence for this data point an error of 0.5 % points is estimated.

Figure 7.4
In the in situ experiments with the Pt/SiO_2 sample with a bimodal PSD prepared with the cluster source (section 3.1.2) the focus settings varied significantly. To determine the error induced by the focus variation, an image series was recorded during the experimental conditions of the same region of the sample. In this image series the focus was varied corresponding to that of the in situ experiments as conservatively estimated from the thickness of the Fresnel fringes at the edges of the

particles. The mean particle sizes were obtained by automatic measurements of ca. 600 particles in TEM images from the focus series of the same region, resulting in a measured error of 0.16 nm on the mean diameter. Since this value is larger than the propagated measuring error as calculated with eq. 3.2, the error bars represent the errors induced by the focus variation. (c) The error bars in the insert represent the standard deviation of the particle density.

References

[1] B. A. A. L. van Setten, M. Makkee, and J. A. Moulijn, *Science and technology of catalytic diesel particulate filters*, Catal. Rev., 43 (2001) 489.

[2] M. V. Twigg, *Progress and future challenges in controlling automotive exhaust gas emissions*, Appl. Catal. B, 70 (2007) 2.

[3] M. V. Twigg, *Catalytic control of emissions from cars*, Catal. Today, 163 (2011) 33.

[4] R. M. Heck and R. J. Farrauto, *Automobile exhaust catalysts*, Appl. Catal. A, 221 (2001) 443.

[5] K. Herbst, G. Mogensen, F. Huber, M. Østberg, and M. S. Skjøth-Rasmussen, *Challenges in applied oxidation catalysis*, Catal. Today, 157 (2010) 297.

[6] F. Haass and H. Fuess, *Structural characterization of automotive catalysts*, Adv. Eng. Mater., 7 (2005) 899.

[7] M. K. Khair and W. A. Majewski, *Diesel Emissions and Their Control*, SAE International, Warrendale, PA 2006.

[8] H. Lueders, P. Stommel, and R. Backes, *Applications for the Regeneration of Diesel Particulate Traps by Combining Different Regeneration Systems*, SAE Technical paper, (1997) 970470.

[9] Jääskeläinen, H. Diesel Exhaust Gas. www.dieselnet.com. 2009.

[10] S. E. Wanke and P. C. Flynn, *The Sintering of Supported Metal Catalysts*, Catal. Rev. -Sci Eng., 12 (1975) 93.

[11] P. Wynblatt and N. A. Gjostein, *Supported metal crystallites*, in: J. O. McCaldin and G. A. Somorjai (Eds.), Progress in solid state Chemistry, Elsevier Science, Amsterdam, 1976, pp. 21-58.

[12] J. B. Butt and E. E. Petersen, Activation, *Deactivation, and Poisoning of Catalysts*, Academic Press Inc, San Diego 1988.

[13] R. T. K. Baker, C. H. Bartholomew, and D. B. Dadyburjor, *Sintering and redispersion: Mechanicsms and Kinetics*, in: Horsley.J.A. (Ed.), Stability of Supported Catalysts: Sintering and Redispersion, Catalytica inc, California, 1991, pp. 169-225.

[14] R. T. K. Baker, *Catalyst Deactivation*, C. H. Bartholomew and J. B. Butt (Eds.), Elsevier Science Publishers, 1991.

[15] C. H. Bartholomew, *Sintering kinetics of supported metals: New perspectives from a unifying GPLE treatment*, Appl. Catal. A, 107 (1993) 1.

[16] C. H. Bartholomew, *Catalysis - A Specialist Periodical Report, Catalysis - A Specialist Periodical report*, The Royal Society of Chemistry, Cambridge, 1993, pp. 41-82.

[17] C. H. Bartholomew, *Sintering and Redispersion of Supported Metals: Perspectives from the Litterature of the Past Decade*, Stud. Surf. Sci. Catal., 111 (1997) 585.

[18] G. A. Fuentes and E. Salinas-Rodriguez, *Catalyst Deactivation*, C. H. Bartholomew and G. A. Fuentes (Eds.), Elsevier Science B. V., Amsterdam, 1999, pp. 573-584.

[19] P. Lööf, B. Stenbom, H. Nordén, and B. Kasemo, *Rapid Sintering in NO of Nanometre-Sized Pt Particles on γ-Al_2O_3 Observed by CO Temperature-Programmed Desorption and Transmission Electron Microscopy*, J. Catal., 144 (1993) 60.

[20] R. T. K. Baker, P. S. Harris, and R. B. Thomas, *Direct observation of particle mobility on a surface in a gaseous environment*, Surf. Sci., 46 (1974) 311.

[21] R. T. K. Baker, C. Thomas, and R. B. Thomas, *Continouus Observation of the Particle Size Behavior of Platinum an Alumina*, J. Catal., 38 (1975) 510.

[22] K. Heinemann and H. Poppa, *Direct observation of small cluster mobility and ripening*, Thin Solid Films, 33 (1976) 237.

[23] G. B. McVicker, R. L. Garten, and R. T. K. Baker, *Surface Area Stabilization of Ir/Al_2O_3 Catalysts by CaO, SrO, and BaO Under Oxygen Atmospheres: Implications on the Mechanism of Catalyst Sintering and Redispersion*, J. Catal., 54 (1978) 129.

[24] R. T. K. Baker, *In situ Electron Microscopy Studies of Catalyst Particle Behavior*, Catal. Rev. -Sci Eng., 19 (1979) 161.

[25] R. T. K. Baker, *The Relationship between Particle Motion on a Graphite Surface and Tamman Temperature*, J. Catal., 78 (1982) 473.

[26] M. Arai, T. Ishikawa, T. Nakayama, and Y. Nishiyama, *Effects of metal-support interaction and temperature on the sintering of Pt and Ag particles supported on inorganic solids*, J. Col. Interf. Sci., 97 (1984) 254.

[27] R. T. K. Baker, *A review of In-Situ Electron Microscopy Studies of Metal/Metal Oxide-Graphite Interactions*, J. Adhesion, 52 (1995) 13.

[28] N. M. Rodriguez, S. G. Oh, R. A. Dalla-Betta, and R. T. K. Baker, *In Situ Electron Microscopy Studies of Palladium Supported on Al_2O_3, SiO_2 and ZrO_2 in Oxygen*, J. Catal., 157 (1995) 676.

[29] R. Anton and P. Kreutzer, *In situ TEM evaluation of the growth kinetics of Au particles on highly oriented pyrolithic graphite at elevated temperatures*, Phys. Rev. B, 61 (2000) 16077.

[30] R. J. Liu, P. A. Crozier, C. M. Smith, Hucul.D.A., J. Blackson, and G. Salaita, *Metal sintering mechanisms and regeneration of palladium/alumina hydrogenation catalysts*, Appl. Catal. A, 282 (2005) 111.

[31] R. Sharma and P. A. Crozier, *Handbook of microscopy for nanotechnology*, N. Yao and Z. L. Wang (Eds.), Kluwer Academic Publishers, 2005, pp. 531-565.

[32] J. Sehested, *Four challenges for nickel steam-reforming catalysts*, Catal. Today, 111 (2006) 103.

[33] K. Kishita, T. Kamino, A. Watabe, K. Kuroda, and H. Saka, *In situ TEM observation of solid-gas reactions*, J. Phys. Conf. Ser., 126 (2008) 012085.

[34] H. Zheng, R. K. Smith, Y.-W. Jun, C. Kisielowski, U. Dahmen, and P. A. Alivisatos, *Observation of Single Colloidal Platinum Nanocrystal Growth Trajectories*, Science, 324 (2009) 1309.

[35] A. B. Laursen, K. T. Højholt, L. F. Lundegaard, S. B. Simonsen, S. Helveg, F. Schüth, M. Paul, J.-D. Grundwaldt, S. Kegnæs, C. H. Christensen, and K. Egeblad, *Substrate Size-Selective Catalysis with Zeolite-Encapsulated Gold Nanoparticles*, Angew. Chem. Int. Ed., 49 (2010) 3504.

[36] K. Ida, Y. Sugiyama, Y. Chujyo, M. Tomonari, T. Tokunaga, K. Sasaki, and K. Kuroda, *In-situ TEM studies of the sintering behavior of copper nanoparticles covered by biopolymer nanoskin*, Journal of Electron Microscopy, 59 (2010) S75.

[37] S. Janbroers, P. A. Crozier, H. W. Zandbergen, and P. J. Kooyman, *A model study on the carburization process of iron-based Fischer-Tropsch catalysts using in situ TEM-EELS*, Appl. Catal. B, 102 (2011) 521.

[38] H. Hirata, K. Kishita, Y. Nagai, K. Dohmae, H. Shinjoh, and S. Matsumoto, *Characterization and dynamic behavior of precious metals in automotive exhaust gas purification catalysts*, Catal. Today, 164 (2011) 467.

[39] E. Ruckenstein and B. Pulvermacher, *Growth Kinetics and the Size Distributions of Supported Metal Crystallites*, J. Catal., 29 (1973) 224.

[40] B. K. Chakraverty, *Grain size distribution in thin films - 1. conservative systems*, J. Phys. Chem. Solids., 28 (1967) 2401.

[41] P. C. Flynn and S. E. Wanke, *A Model of Supported Metal Catalyst Sintering - I Development of Model*, J. Catal., 34 (1974) 390.

[42] R. Finsy, *On the Critical Radius in Ostwald Ripening*, Langmuir, 20 (2004) 2975.

[43] L. R. Houk, S. R. Challa, B. Grayson, P. Fanson, and A. K. Datye, *The definition of "critical radius" for a collection of nanoparticles undergoing Ostwald ripening*, Langmuir, 25 (2009) 11225.

[44] I. M. Lifshitz and V. V. Slyozov, *The kinetics of precipitation from supersaturated solid solutions*, J. Phys. Chem. Solids., 19 (1961) 35.

[45] C. Z. Wagner, *Theorie der alterung von niederschlagen durch umlosen (Ostwald-reifung)*, Electrochemie, 65 (1961) 581.

[46] C. G. Granqvist and R. A. Buhrman, *Size Distributions for Supported Metal Catalysts*, J. Catal., 42 (1976) 477.

[47] A. K. Datye, Q. Xu, K. C. Kharas, and J. M. McCarty, *Particle size distributions in heterogeneous catalysts: What do they tell us about the sintering mechanism?*, Catal. Today, 111 (2006) 59.

[48] G. A. Fuentes and E. Salinas-Rodriguez, *Realistic particle size distributions during sintering by Ostwald ripening*, in: J.J. Spivey, G.W. Roberts, B.H. Davis (Eds.), Studies in Surface Science and Catalysis, Elsevier Science, Amsterdam, Vol. 139, (2001) 503-510.

[49] P. C. Flynn and S. E. Wanke, *A Model of Supported Metal Catalyst Sintering II*, J. Catal., 34 (1974) 400.

[50] S. E. Wanke, *Commentes on the Sintering Mechanism of Supported Metal Catalysts*, J. Catal., 46 (1977) 234.

[51] C. G. Granqvist and R. A. Buhrman, *Reply to "Comments on the Sintering Mechanism of Supported Metal Catalysts"*, J. Catal., 46 (1977) 238.

[52] G. Comsa, *Remarks on the size distribution function of ultrafine metal particles*, J. Phys-Paris, 38 (1977) C2-185.

[53] M. Chen and L. D. Schmidt, *Morphology and sintering of Pt crystallites on amorphous SiO_2*, J. Catal., 55 (1978) 348.

[54] S. D. Coughlan and M. A. Fortes, *Selfsimilar size distributions in particle coarsening*, Scripta Metall. Mater., 28 (1993) 1471.

[55] Y. D. Smet, L. Deriemaeker, and R. Finsy, *A simple Computer Simulation of Ostwald Ripening*, Langmuir, 13 (1997) 6884.

[56] P. J. F. Harris, *Growth and structure of supported metal catalyst particles*, Int. Mater. Rev., 40 (1995) 97.

[57] E. Ruckenstein and B. Pulvermacher, *Kinetics of Crystallite Sintering During Heat Treatment of Supported Metal Catalysts*, AlChE, 19 (1973) 356.

[58] P. C. Flynn and S. E. Wanke, *Experimental Studies of Sintering of Supported Platinum Catalysts*, J. Catal., 37 (1975) 432.

[59] T. J. Lee and Y. G. Kim, *Redispersion of Supported Platinum Catalysts*, J. Catal., 90 (1984) 279.

[60] E. Ruckenstein and Y. F. Chu, *Redispersion of platinum crystallites supported on alumina-Role of wetting*, J. Catal., 59 (1979) 109.

[61] J. M. Rickard, L. Genovese, A. Moata, and S. Nitsche, *Redispersion of platinum on Pt/Al_2O_3 model catalyst in oxygen studied by transmission electron microscopy*, J. Catal., 121 (1990) 141.

[62] Rosner, G. *Diesel fuel and exhaust emissions*. 1996. Genova, WHO Report.

[63] N. Seriani, W. Pompe, and L. C. Ciacchi, *Catalytic Oxidation Activity of Pt_3O_4 Surfaces and Thin films*, J. Phys. Chem. B., 110 (2006) 14860.

[64] P. L. Hansen, J. B. Wagner, S. Helveg, J. R. Rostrup-Nielsen, B. S. Clausen, and H. Topsøe, *Atom-resolved imaging of dynamic shape changes in supported copper nanocrystals*, Science, 295 (2002) 2053.

[65] H. C. Yao, M. Sieg, and H. K. Plummer, *Surface Interactions in the Pt/γ-Al_2O_3 system*, J. Catal., 59 (1979) 365.

[66] R. T. K. Baker, *Effect of Wetting on the Morphology of Supported Platinum Crystallites*, J. Catal., 63 (1980) 523.

[67] S. Horch, H. T. Lorensen, S. Helveg, E. Lægsgaard, I. Stensgaard, K. W. Jacobsen, J. K. Nørskov, and F. Besenbacher, *Enhancement of surface self-diffusion of platinum atoms by adsorbed hydrogen*, Nature, 398 (1999) 134.

[68] R. J. Berry, *Study of multilayer surface oxidation of platinum by electrical resistance technique*, Surf. Sci., 76 (1978) 415.

[69] R. W. McCabe, C. Wong, and H. S. Woo, *The Passivating Oxidation of Platinum*, J. Catal., 114 (1988) 354.

[70] C.-B. Wang, H.-K. Lin, S.-N. Hsu, T.-H. Huang, and H.-C. Chiu, *Enthalpies of reduction-oxidation of alumina-supported platinum*, J. Mol. Catal. A, 188 (2002) 201.

[71] L. K. Ono, B. Yuan, H. Heinrich, and B. Roldan Cuenya, *Formation and thermal stability of platinum oxides on size-selected platinum nanoparticles: Support effects*, J. Phys. Chem. C, 114 (2010) 22119.

[72] P. Lööf, B. Kasemo, L. Björnkvist, S. Andersson, and A. Frestad, *Studies on Surface Science and Catalysis*, A. Crucq (Ed.), Elsevier, Amsterdam, 1991, p. 253.

[73] M. Chen and L. D. Schmidt, *Morphology and Composition of Pt-Pd Alloy Crystallites on SiO_2 in Reactive Atmospheres*, J. Catal., 56 (1979) 198.

[74] M. Kaneeda, H. Iizuka, T. Hiratsuka, N. Shinotsuka, and M. Arai, *Improvement of thermal stability of NO oxidation Pt/Al_2O_3 catalyst by addition of Pd*, Appl. Catal. B, 90 (2009) 564.

[75] J. Zhang, K. Sasaki, E. Sutter, and R. R. Adzic, *Stabilization of Platinum Oxygen-Reduction Electroncatalysts Using Gold Clusters*, Science, 315 (2007) 220.

[76] W. Zou and R. D. Gonzalez, *Stabilization and sintering of porous Pt/SiO_2: a new approach,* Appl. Catal. A, 102 (1993) 181.

[77] S. E. Wanke, *Progress in Catalyst Deactivation*, J. L. Figueiredo (Ed.), M. Nijhoff, Boston, 1982, pp. 315-328.

[78] J. P. Franck and G. Martino, *Progress in Catalyst Deactivation*, J. L. Figueiredo (Ed.), M. Nijhoff, Boston, 1982, pp. 355-397.

[79] T. Tanabe, Y. Nagai, K. Dohmae, H. Sobukawa, and H. Shinjoh, *Sintering and redispersion behavior of Pt on Pt/MgO*, J. Catal., 257 (2008) 117.

[80] M. Casapu, J. D. Grunwaldt, M. Maciejewski, A. Baiker, S. Eckhoff, U. Göbel, and M. Wittrock, *The fate of platinum in Pt/Ba/CeO_2 and Pt/Ba/Al_2O_3 catalysts during thermal aging*, J. Catal., 251 (2007) 28.

[81] T. Tanabe, Y. Nagai, K. Dohmae, M. Hatanaka, N. Takahashi, N. Takagi, Y. Ikeda, N. Hara, S. Pascarelli, G. Guilera, M. Newton, H. Shinjoh, and S. Matsumoto, *In situ real time observations and anchor site model of platinum sintering on ceria based oxide surface*, The 14th international Congress on Catalysis, 2009.

[82] J. Fan, X. Wu, X. Wu, Q. Liang, R. Ran, and D. Weng, *Thermal ageing of Pt on low-surface-area CeO_2-ZrO_2-La_2O_3 mixed oxides: Effect on the OSC performance*, Appl. Catal. B, 81 (2008) 38.

[83] T. Kanazawa, *MFI zeolite as a support for automotive catalysts with reduced Pt sintering*, Appl. Catal. B, 65 (2006) 185.

[84] I. Sushumna and E. Ruckenstein, *Events observed and evidence for crystallite migration in Pt/Al_2O_3 catalysts*, J. Catal., 109 (1988) 433.

[85] P. J. F. Harris, E. D. Boyes, and J. A. Cairns, *The Sintering of an Alumina-Supported Platinum Catalytist Studied by Transmission Electron Microscopy*, J. Catal., 82 (1983) 127.

[86] P. J. F. Harris, *The Sintering of Platinum Particles in an Alunina-Supported Catalyst: Further Transmission Electron Microscopy Studies*, J. Catal., 97 (1986) 527.

[87] J. Singh and D. E. Wolfe, *Review Nano and macro-structured component fabrication by electron beam-physical vapor deposition (EB-PVD)*, J. Mater. Sci., 40 (2005) 1.

[88] H. Haberland, M. Karrais, M. Mall, and Y. Thurner, *Thin-films from energetic cluster impact - a feasibility study*, J. Vac. Sci. Technol. A, 10 (1992) 3266.

[89] P. H. Dawson, W. E. Austin, A. E. Holme, J. H. Leck, R. F. Herzog, J. F. J. Todd, G. Lawson, R. F. Bonner, J. P. Carrico, G. R. Carignan, and M. S. Story, *Quadrupole Mass Spectrometry and its applications*, Elsevier Scientific Publishing Company, 1976.

[90] P. J. Goodhew, J. Humphreys, and R. Beanland, *Electron Microscopy and Analysis*, Taylor and Francis Inc, London - New York 2001.

[91] D. B. Williams and C. B. Carter, *Transmission Electron Microscopy*, Springer Science+Business Media Inc., New York 1996.

[92] L. Reimer, *Transmission Electron Microscopy*, Springer, Berlin 1997.

[93] E. M. James and N. D. Browning, *Practical aspects of atomic resolution imaging and analysis in STEM*, Ultramicroscopy, 78 (1999) 125.

[94] I. Chorkendorff and J. W. Niemantsverdriet, *Concepts of Modern Catalysis and Kinetics*, Wiley-VCH Verlag GmbH & Co. KGaA, Weinheim 2007.

[95] I. Chorkendorff, *Experimental Surface Physics*, CINF - Technical University of Denmark, Kgs. Lyngby 2009.

[96] H. G. Tompkins and E. A. Irene, *Handbook of Ellipsometry*, William Andrew Publishing - Springer-Verlag GmbH & Co. KG, Norwich, NY - Heidelberg 2005.

[97] C. D. Wagner, W. M. Riggs, L. E. Davis, and J. F. Moulder, *Handbook of X-ray Photoelectron Spectroscopy*, Perkin-Elmer Corporation, Minnesota 1979.

[98] R. F. Egerton, *Physical Principles of Electron Microscopy - An Introduction to TEM, SEM and AEM*, Springer Science+Business Inc., New York 2005.

[99] R. D. Heidenreich, *Fundamentals of Transmission Electron Microscopy*, Interscience Publichers, 1964.

[100] M. T. Otten, *Philips Electron Optics*, Philips Application Laboratory, 1993.

[101] H. Saka, T. Kamino, S. Arai, and K. Sasaki, *In Situ Heating Transmission Electron Microscopy*, MRS Bull, 33 (2008) 93.

[102] J. Cumings, E. Olsson, A. K. Petford-Long, and Y. Zhu, *Electric and magnetic phenomena studied by in situ transmission electron microscopy*, MRS Bull, 33 (2008) 101.

[103] R. T. K. Baker, E. B. Prestridge, and R. L. Garten, *Electron Microscopy of Supported Metal Particles*, J. Catal., 56 (1979) 390.

[104] A. K. Datye, *Electron microscopy of catalysts: recent achievements and future prospects*, J. Catal., 216 (2003) 144.

[105] P. L. Hansen, S. Helveg, and A. K. Datye, *Atomic-Scale Imaging of Supported Metal Nanocluster Catalysts in the Working State*, Adv. Catal., 50 (2006) 77.

[106] T. W. Hansen, J. B. Wagner, and R. E. Dunin-Borkowski, *Aberration corrected and monochromated environmental transmission electron microscopy: Challenges and prospects for materials science*, Mater. Sci. Technol., 26 (2010) 1338.

[107] A. W. Grant and B. Kasemo, *Transmission electron microscopy 'windows' for nanofabricated structures*, Nanotechnology, 15 (2004) 1175.

[108] E. P. DeGarmo, J. T. Black, and R. A. Kohser, *Materials and Processes in Manufacturing*, Wiley, 2003.

[109] S. B. Simonsen, S. Dahl, E. Johnson, and S. Helveg, *Ceria-catalyzed soot oxidation studied by environmental transmission electron microscopy*, J. Catal., 255 (2008) 1.

[110] Simonsen, S. B. *In situ studies of CeO_2-catalyzed soot oxidation by means of Environmental Transmission Electron Microscopy*. Master Thesis, 2008. University of Copenhagen - Haldor Topsøe A/S.

[111] H. G. Wagner, *Particulate Carbon*, D. C. Siegla and G. W. Smith (Eds.), Plenum Press, New York-London, 1981, pp. 1-29.

[112] J. P. A. Neeft, T. X. Nijhuis, E. Smakman, M. Makkee, and J. A. Moulijn, *Kinetics of the oxidation of diesel soot*, Fuel, 76 (1997) 1129.

[113] M. N. Bokova, C. Dercarne, E. Bi-Aad, A. N. Pryakhin, V. V. Lunin, and A. Aboukais, *Kinetics of catalytic carbon black oxidation*, Thermochim. Acta, 428 (2005) 165.

[114] W. C. Yang, M. Zeman, H. Ade, and R. J. Nemanich, *Attractive Migration and Coalescence: A Significant Process in the Coarsening of TiO_2 Islands on the Si(111)*, J. Phys. Rev. Lett., 90 (2003) 136102.

[115] G. H. Enevoldsen, A. S. Foster, M. C. Christensen, J. V. Lauritsen, and F. Besenbacher, *Noncontact atomic force microscopy studies of vacancies and hydroxyls of TiO_2(110) : Experiments and atomistic simulations*, Phys. Rev. B, 76 (2007) 205415.

[116] S. Gritschneder, Y. Namai, Y. Ywasawa, and M. Reichling, *Structural features of CeO_2(111) revealed by dynamic SFM*, Nanotechnology, 16 (2005) s41.

[117] V. Barwich, M. Bammerlin, A. Baratoff, R. Bennewitz, M. Guggisberg, C. Loppacher, O. Pfeiffer, E. Meyer, H.-J. Günterodt, J.-P. Salvetat, J.-M. Bonard, and L. Forró, *Carbon nanotuge tips in non-contact SFM*, Appl. Surf. Sci., 157 (2000) 269.

[118] D. Freedman and P. Z. Diaconis, *On the Histogram as a Density Estimator: L_2 Theory*, Wahrscheinlichkeit, 57 (1981) 453.

[119] J. R. Taylor, *An Introduction to Error Analysis*, University Science Books, Sausalito 1997.

[120] T. M. Rogers and R. C. Desai, *Numerical study of late-stage coarsening for off-critical quenches in the Cahn-Hilliard equation of phase separation*, Phys. Rev. B., 39 (1989) 11956-11964.

[121] N. C. Bartelt, W. Teis, and R. M. Tromp, *Ostwald ripening of two-dimensional islands on Si(001)*, Phys. Rev. B, 54 (1996) 11741.

[122] A. J. Ardell, *Late-stage two-dimensional coarsening of circular clusters*, Phys. Rev. B., 41 (1990) 2554.

[123] P. W. Voorhees, *The Theory of Ostwald Ripening*, J. Stat. Phys., 38 (1985) 231.

[124] M. Marder, *Correlations and Ostwald ripening*, Phys. Rev. A, 36 (1987) 858.

[125] A. Chakrabarti, R. Toral, and J. D. Gunton, *Late-stage coarsening for off-critical quenches: Scaling functions and the growth law*, Phys. Rev. E, 47 (1993) 3025.

[126] J. H. Yao, K. R. Elder, H. Guo, and M. Grant, *Theory and simulation of Ostwald ripening*, Phys. Rev. B., 47 (1993) 14110.

[127] O. Krichevsky and J. Stavans, *Correlated Ostwald Ripening in Two Dimensions*, Phys. Rev. Lett., 70 (1993) 1473.

[128] J. H. Yao, K. R. Elder, H. Guo, and M. Grant, *Late stage droplet growth*, Physica A, 204 (1994) 770.

[129] R. Toral, A. Chakrabarti, and J. D. Gunton, *Large scale simulations of the two-dimensional Cahn-Hilliard model*, Physica A, 213 (1995) 41.

[130] N. Akaiwa and D. I. Meiron, *Numerical simulation of two-dimensional late-stage coarsening for nucleation and growth*, Phys. Rev. E, 51 (1995) 5408.

[131] C. T. Campbell, S. C. Parker, and D. E. Starr, *The effect of size-dependent nanoparticle energetics on catalyst sintering*, Science, 298 (2002) 811.

[132] E. Ruckenstein and D. B. Dadyburjor, Mechanisms of Aging of Supported Metal Catalysts, J. Catal., 48 (1977) 73.

[133] D. B. Dadyburjor, S. P. Marsh, and M. E. Glicksman, *The Role of Multiparticle-Adatom Interactions on the Sintering of Supported Metal Catalysts*, J. Catal., 99 (1986) 358.

[134] W. Theis, R. M. Bartelt, and R. M. Tromp, *Chemical Potential Maps and Spatial Correlations in 2D-Island Ripening on Si(001)*, Phys. Rev. Lett., 75 (1995) 3328.

[135] K. Morgenstern, G. Rosenfeld, and G. Comsa, *Local correlation during Ostwald ripening of two-dimensional islands on Ag(111)*, Surf. Sci., 441 (1999) 289.

[136] F. Yang, M. S. Chen, and D. W. Goodman, *Sintering of Au particles supported on TiO_2(110) during CO oxidation*, J. Phys. Chem. C, 113 (2009) 254.

[137] X. Zheng and B. Bigot, *Ostwald ripening on a substrate: modeling local interparticle diffusion*, J. Phys. II France, 4 (1994) 743.

[138] G. Voronoi and J. Reine, *Nouvelles applications des paramètres continus à la théorie des formes quadratiques*, Angew. Math., 134 (1980) 556.

[139] M. McLean and J. Hondros, *A study of grain-boundary grooving at the platinum/alumina interface*, J. Mater. Sci., 6 (1971) 19.

[140] S. C. Parker and C. T. Campbell, *Kinetic model for sintering of supported metal particles with improved size-dependent energetics and applications to Au on TiO_2(110)*, Phys. Rev. B., 75 (2007) 035430.

[141] A. Carlsson, A. Puig-Molina, and T. V. W. Janssens, *New Method for Analysis of Nanoparticle Geometry in Supported fcc Metal Catalysts with Scanning Transmission Electron Microscopy*, J. Phys. Chem. B., 110 (2006) 5286.

[142] J. G. McCarty, G. Malukhin, D. M. Poojary, A. K. Datye, and Q. Xu, *Thermal Coarsening of Supported Palladium Combustion Catalysts*, J. Phys. Chem. B, 109 (2005) 2387.

[143] R. J. Farrauto, J. K. Lampert, M. C. Hobson, and E. M. Waterman, *Thermal decomposition and reformation of PdO catalysts; support effects*, Appl. Catal. B, 6 (1995) 263.

[144] J. J. Chen and E. Ruckenstein, *Role of Interfacacial Phenomena in the Behavior of Alumina-Supported Palladium Crystallites in Oxygen*, J. Phys. Chem., 85 (1981) 1606.

[145] R. S. Goeke and A. K. Datye, *Model oxide supports for studies of catalyst sintering at elevated temperatures*, Top. Catal., 46 (2007) 3.

[146] M. Heemeier, S. Stempel, Sh. K. Shaikhutdinov, J. Libuda, M. Bäumer, R. J. Oldman, S. D. Jackson, and H.-J. Freund, *On the thermal stability of metal particles supported on a thin alumina film*, Surf. Sci., 523 (2003) 103.

[147] J.-L. Lu, J. Weissenrieder, S. Kaya, H.-J. Gao, S. Shaikhutdinov, and H.-J. Freund, *Structure, thermal stability, and CO adsorption properties of Pd nanoparticles supported on an ultra-thin SiO_2 film*, Surf. Rev. Lett., 14 (2007) 927.

[148] I. Davoli, S. Stizza, A. Bianconi, M. Benfatto, C. Furlani, and V. Sessa, *The local electronic structure of PdO crystal and PdO catalyst supported on SiO_2 and γ-Al_2O_3 from L_3 and L_1 x-ray absorption Pd edge in XANES spectra*, Solid State Commun., 48 (1983) 475.

[149] J. F. Creemer, S. Helveg, G. H. Hoveling, S. Ullmann, A. M. Molenbroek, P. M. Sarro, and H. W. Zandbergen, *Atomic-scale electron microscopy at ambient pressure*, Ultramicroscopy, 108 (2008) 993.

Paper I

J|A|C|S ARTICLES

Published on Web 05/19/2010

Direct Observations of Oxygen-induced Platinum Nanoparticle Ripening Studied by In Situ TEM

Søren B. Simonsen,[†,‡] Ib Chorkendorff,[‡] Søren Dahl,[‡] Magnus Skoglundh,[§] Jens Sehested,[†] and Stig Helveg*[,†]

Haldor Topsøe A/S, Nymøllevej 55, DK-2800 Kgs. Lyngby, Denmark, CINF, Department of Physics, Technical University of Denmark, DK-2800 Kgs. Lyngby, Denmark, and Competence Centre for Catalysis (KCK), Chalmers University of Technology, SE-41296, Göteborg, Sweden

Received December 3, 2009; E-mail: sth@topsoe.dk

Abstract: This study addresses the sintering mechanism of Pt nanoparticles dispersed on a planar, amorphous Al_2O_3 support as a model system for a catalyst for automotive exhaust abatement. By means of *in situ* transmission electron microscopy (TEM), the model catalyst was monitored during the exposure to 10 mbar air at 650 °C. Time-resolved image series unequivocally reveal that the sintering of Pt nanoparticles was mediated by an Ostwald ripening process. A statistical analysis of an ensemble of Pt nanoparticles shows that the particle size distributions change shape from an initial Gaussian distribution via a log-normal distribution to a Lifshitz−Slyozov−Wagner (LSW) distribution. Furthermore, the time-dependency of the ensemble-averaged particle size and particle density is determined. A mean field kinetic description captures the main trends in the observed behavior. However, at the individual nanoparticle level, deviations from the model are observed suggesting in part that the local environment influences the atom exchange process.

Introduction

The size and shape of nanoscale structures often play a crucial role for the physiochemical properties of a nanomaterial.[1,2] Although a variety of size-selected nanoparticle synthesis methods are available, the stability of the nanoscale structures is by no means guaranteed. Due to their excess surface free energy, nanoscale structures present a metastable solid state and will inevitably tend to aggregate into larger structures.[3−6] The stability of metal nanoparticles dispersed on for example an oxide support is important for their extensive use as efficient catalysts in environmental technologies and in the production of fuels and chemicals.[1,2] The high temperature and reactive gas conditions encountered during catalysis often accelerate the sintering, which results in a loss of active surface area of the nanoparticles, causing an undesired catalyst deactivation. To further advance the synthesis and application of stable catalysts, and nanostructures in general, a detailed understanding of the mechanisms and kinetics governing their stability is of utmost importance.

The sintering of supported nanoparticles is typically attributed to mass-transport mechanisms involving crystallite or atomic migration. The crystallite migration mechanism refers to sintering mediated by the migration of the nanoparticles and, subsequent, the coalescence with neighboring nanoparticles.[3] The atom migration mechanism refers to the Ostwald ripening process in which sintering occurs by diffusion of atoms or atomic species between immobile nanoparticles either on the surface of the support or through the gas phase.[3,7] For both mechanisms, kinetic models for the sintering of the supported nanoparticles have been established.[3,7] Specifically, the Ostwald ripening process is influenced by the so-called Gibbs−Thompson effect relating surface coverage of diffusing atomic species to the nanoparticle size. The result is that the concentration of atomic species is higher in the vicinity of small particles than of large particles. The concentration gradient leads to a net flux of atomic species from the smaller particles toward the larger ones, so the larger particles eventually grow at the expense of the smaller ones. A mean-field model for Ostwald ripening kinetics, relevant for the present Pt catalyst described below,[8] describes the so-called interface-controlled rate of nanoparticle radius changes, dR/dt, by[3,9]

$$\frac{dR}{dt} = \frac{\alpha}{R^2}\left(\frac{R}{R^*} - 1\right) \quad (1)$$

where α is a system-dependent parameter, R is the particle size and R^* is the critical radius. The critical radius corresponds to the particle size which neither shrinks nor grows and which is in equilibrium with a constant concentration of atomic species in the area between the particles (also referred to as the mean-

[†] Haldor Topsøe A/S.
[‡] Technical University of Denmark.
[§] Chalmers University of Technology.

(1) Somorjai, G. A.; Frei, H.; Park, J. Y. *J. Am. Chem. Soc.* **2009**, *131*, 16589.
(2) Bell, A. T. *Science* **2003**, *299*, 1688.
(3) Wynblatt, P.; Gjostein, N. A. *Prog. Solid State Chem.* **1976**, *9*, 21.
(4) Bartholomew, C. H. *Stud. Surf. Sci. Catal.* **1997**, *111*, 585.
(5) Fuentes, G. A.; Salinas-Rodriguez, E. In *Catalyst Deactivation*; Bartholomew, C. H., Fuentes, G. A., Eds.; Elsevier Science B.V.: Amsterdam, 1999; pp 573−584.
(6) Campbell, C. T. *Surf. Sci. Rep.* **1997**, *227*, 1.
(7) Chakraverty, B. K. *J. Phys. Chem. Solids* **1967**, *28*, 2401.
(8) Flynn, P. C.; Wanke, S. E. *J. Catal.* **1974**, *34*, 400.
(9) Coughlan, S. D.; Fortes, M. A. *Scr. Metall. Mater.* **1993**, *28*, 1471.

 10.1021/ja910094r

field) at the given time. R^* will increase with time as sintering proceeds, and R^* equals the mean particle radius.[10]

In the past, the sintering models were mainly evaluated by comparing with experimental observations of ensemble averages or distributions of particle sizes obtained by post-mortem characterization.[3,8,11−17] Although this approach has provided significant insight into sintering, deviations of the experimental observations from the model predictions have spurred much debate on the use of indirect observations to unambiguously obtain mechanistic insight.[12,16,17] In this respect, the ensemble-averaged measurements may be beneficially complemented by time-resolved microscopy of the individual nanoparticles using e.g. scanning tunneling microscopy (STM),[18−21] low energy electron microscopy (LEEM),[22] or transmission electron microscopy (TEM).[23−32] Specifically, TEM of oxide-supported nanoparticle catalysts may be performed by a quasi *in situ* method, in which different or the same areas of a catalyst are monitored repeatedly between successive aging treatments in catalytic reactors,[3,13,29−32] or by an *in situ* method, in which a specific catalyst area is monitored while the aging treatment is performed inside the microscope.[23−28]

In the following, we focus on Pt nanoparticles dispersed on an Al_2O_3 support. The Pt/Al_2O_3 system represents catalysts for e.g. oxidation reactions in diesel and lean-burn engine exhaust abatement. A net-oxidizing (lean) exhaust composition is characteristic for this type of automotive exhausts.[33] Previous studies suggest that sintering of Pt nanoparticles dispersed on either planar model or porous technical-relevant alumina supports is strongly promoted by the exposure to oxygen at temperatures above ca. 500 °C,[3,34] but other components of the diesel exhaust, such as nitrogen oxides and CO, may also affect the catalyst stability.[35] Indirect measurements have been pursued to reveal the dominating oxygen-induced sintering mechanism. For a range of Pt/Al_2O_3 catalyst structures and oxidizing reaction conditions, it is suggested that the Ostwald ripening mechanism dominates[31,36,37] whereas, for Pt particle sizes below 4−5 nm, the particle migration and coalescence mechanism is suggested to dominate.[3,30] However, based on *in situ* TEM observations, Baker et al. found that Pt particles, larger than 2.5 nm, remain stationary during exposure to 2 mbar O_2 at temperatures up to 900 °C and that ripening is the dominating sintering mechanism.[24] Following the approach by Baker et al., we here present *in situ* TEM observations of Pt nanoparticles dispersed on a planar Al_2O_3 support during exposure to air at elevated temperatures to mimic lean-burn conditions. Time-resolved TEM images of the individual nanoparticles unequivocally reveal severe sintering governed by Ostwald ripening. Based on the *in situ* observations, we present a direct examination of the applicability of eq 1 for predicting the temporal evolution of the particle size distributions and ensemble averages.

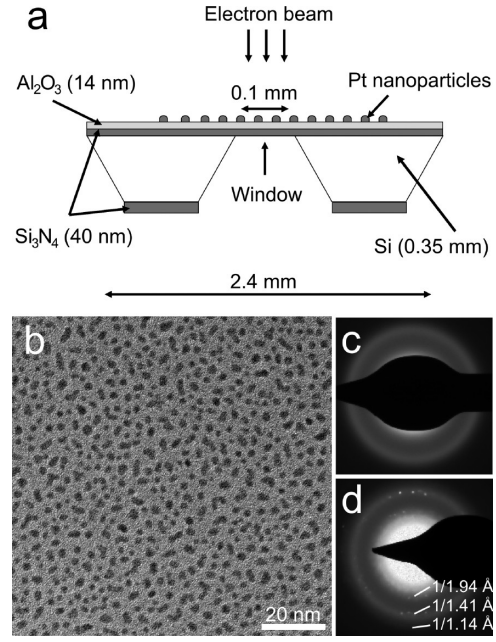

Figure 1. (a) Schematic side view of the Pt/Al_2O_3 model catalyst. (b) TEM image of the as-prepared Pt/Al_2O_3 model catalyst. (c) Electron diffraction pattern of the bare Si_3N_4-supported alumina film. (d) Electron diffraction pattern of the model catalyst. Diffraction spots corresponding to the Pt (111), (200), and (220) lattice planes are indicated.

Experimental Details

The model catalysts consisting of Pt nanoparticles dispersed on a flat, amorphous Al_2O_3 support were prepared on 40 nm thick, amorphous Si_3N_4 windows, supported on 0.35 mm thick Si wafers, to enhance electron transparency (Figure 1a). The flat, amorphous alumina support matches closely a homogeneous medium, which is one of the assumptions of eq 1. Moreover, the uniform support further excludes the inhomogeneous and porous structure of technical support materials that may influence the sintering dynamics in ways that are difficult to predict.[3,34,38]

Following the Si_3N_4 window preparation,[39] the specimens were cleaned by oxidation using a microwave plasma processor (TePla 300PC) operated at 250 W for 2 min in 1 mbar O_2. The Al_2O_3 support was formed by physical vapor deposition from an Al_2O_3 target of 99.99% nominal purity (Kurt J. Lesker Company) using

(10) Finsy, R. *Langmuir* **2004**, *20*, 2975.
(11) Ruckenstein, E.; Pulvermacher, B. *J. Catal.* **1973**, *29*, 224.
(12) Granqvist, C. G.; Buhrman, R. A. *J. Catal.* **1976**, *42*, 477.
(13) Harris, P. J. F. *Int. Mater. Rev.* **1995**, *40*, 97.
(14) Campbell, C. T.; Parker, S. C.; Starr, D. E. *Science* **2002**, *298*, 811.
(15) Sehested, J.; Gelten, J. A. P.; Remediakis, I. N.; Bengaard, H.; Nørskov, J. K. *J. Catal.* **2004**, *223*, 432.
(16) Datye, A. K.; Xu, Q.; Kharas, K. C.; McCarty, J. M. *Catal. Today* **2006**, *111*, 59.
(17) Wanke, S. E. *J. Catal.* **1977**, *46*, 234.
(18) Morgenstern, K.; Rosenfeld, G.; Comsa, G. *Surf. Sci.* **1999**, *441*, 289.
(19) Linderoth, T. R.; Horch, S.; Petersen, L.; Helveg, S.; Lægsgaard, E.; Steensgaard, I.; Besenbacher, F. *Phys. Rev. Lett.* **1999**, *82*, 1494.
(20) Jak, M. J. J.; Konstapel, C.; Kreuningen, A. van; Verhoeven, J.; Frenken, J. W. M. *Surf. Sci.* **2000**, *457*, 295.
(21) Yang, F.; Chen, M. S.; Goodman, D. W. *J. Phys. Chem. C* **2009**, *113*, 254.
(22) Theis, W.; Bartelt, N. C.; Tromp, R. M. *Phys. Rev. Lett.* **1995**, *75*, 3328.
(23) Baker, R. T. K.; Harris, P. S.; Thomas, P. B. *Surf. Sci.* **1974**, *46*, 311.
(24) Baker, R. T. K.; Thomas, C.; Thomas, R. B. *J. Catal.* **1975**, *38*, 510.
(25) Heinemann, K.; Poppa, H. *Thin Solid Films* **1976**, *33*, 237.
(26) Anton, R.; Kreutzer, P. *Phys. Rev. B* **2000**, *61*, 16077.
(27) Liu, R. J.; Crozier, P. A.; Smith, C. M.; Hucul, D. A.; Blackson, J.; Salaita, G. *Appl. Catal. B* **2005**, *282*, 111.
(28) Hannon, J. B.; Kodambaka, S.; Ross, F. M.; Tromp, R. M. *Nature* **2006**, *440*, 69.
(29) Sushumna, I.; Ruckenstein, E. *J. Catal.* **1988**, *109*, 433.
(30) Harris, P. J. F.; Boyes, E. D.; Cairns, J. A. *J. Catal.* **1983**, *82*, 127.
(31) Bartholemew, C. H. *Catalysis - A Specialist Periodical Report, volume 10*; The Royal Society of Chemistry: Cambridge, 1993; 41−82.
(32) Bellare, A.; Dadyburjor, D. B.; Kelly, M. J. *J. Catal.* **1989**, *117*, 78.
(33) Twigg, M. V. *Appl. Catal. B* **2007**, *70*, 2.
(34) Wanke, S. E.; Flynn, P. C. *Catal. Rev. Sci. Eng.* **1975**, *12*, 93.
(35) Lööf, P.; Stenbom, B.; Nordén, H.; Kasemo, B. *J. Catal.* **1993**, *144*, 60.
(36) Lee, T. J.; Kim, Y. G. *J. Catal.* **1984**, *90*, 279.
(37) Rickard, J. M.; Genovese, L.; Moata, A.; Nitsche, S. *J. Catal.* **1990**, *121*, 141.
(38) Ahn, T. M.; Tien, J. K.; Wynblatt, P. *J. Catal.* **1980**, *66*, 335.
(39) Grant, A. W.; Hu, Q.-H.; Kasemo, B. *Nanotechnology* **2004**, *15*, 1175.

an electron beam evaporator (AVAC HVC600) operated with a base vacuum pressure of 4×10^{-6} mbar and a deposition rate of 0.05 nm/s. The resulting Al_2O_3 layer had a thickness of ca. 14 nm measured using ellipsometry and a root-mean-square roughness below 0.4 nm over a 100 μm^2 area determined by atomic force microscopy. X-ray photoelectron spectroscopy reveals a characteristic peak at 74.6 eV which corresponds to the table value for the Al $2p_{3/2}$ peak in pure Al_2O_3 (74.7 eV). Furthermore, an electron diffraction pattern of the Si_3N_4-supported alumina layers, obtained using a Titan 80-300 transmission electron microscope (FEI Company), demonstrates only broad and diffuse bands of diffracted electrons consistent with an amorphous structure (Figure 1c). In a final preparation step, platinum was deposited onto the Al_2O_3 support layer using the electron beam evaporator (AVAC HVC600) operated with a base vacuum pressure of 4×10^{-6} mbar. Deposition was done using a Pt target of 99.99% nominal purity (Nordic High Vacuum AB) with a deposition rate of 0.05 nm/s for a nominal Pt thickness of 0.5 nm. The as-deposited Pt was present as irregularly shaped and crystalline islands with a width of ca. 3 nm (Figures 1b, d).

X-ray photoelectron spectroscopy reveals a ca. 10% atomic concentration of carbon contamination on the as-prepared model catalyst. Based on a previous study of noncatalytic carbon black oxidation,[40] it is most likely that the carbon contamination on the Pt/Al_2O_3 sample desorbed or reacted off during heating or during the first few minutes at constant temperature in which the sample position stabilized from thermal drift.

The *in situ* TEM experiments were performed using a CM300 FEG-ST (Philips/FEI Company) electron microscope equipped with a differentially pumped environmental cell.[41] The microscope was operated with a primary electron energy of 300 keV and an ultimate information limit down to ca. 0.14 nm, depending on the *in situ* conditions. The instrument permitted TEM images and time-lapsed TEM image series to be acquired *in situ* of samples during the exposure to reactive gases (up to ca. 15 mbar) and elevated temperatures (up to ca. 900 °C). TEM imaging was performed *in situ* using a 1k × 1k Tietz Fastscan F-114 CCD camera, an objective aperture (scattering semiangle of 7.5 mrad) and a magnification such that the resulting pixel resolution was 0.26 nm. In the electron microscope, the specimens were exposed to 10 mbar technical air composed of 21% O_2 and 79% N_2 (class 2 from Air Liquide). Each specimen exposed to this environment was mounted with the Pt/Al_2O_3 side facing the bottom of the Inconel furnace of a Gatan heating holder (model 628). The holder facilitated the heating of the specimens in the gas environment at a rate of 30 °C/min to a temperature in the range 200−650 °C, where the temperature was kept constant within ca. 3 °C for up to 6 h. The temperature was measured using a Pt−Pt/Rh (13%) thermocouple spot-welded on the side of the furnace. For temperature calibration, as-prepared specimens were aged either in the microscope or in a thermally equilibrated external tube reactor in 10 mbar technical air at 740 °C for 3 h. Because the average Pt particle size after the heat treatment only differed by 0.5% for the specimens, the temperature measured on the furnace is concluded to be representative for the specimen temperature in the present experiments.

From the acquired TEM images, Pt particle sizes were measured by manually or automatically outlining the particle perimeters, using the software ImageJ, and the corresponding projected areas of the particles were converted to particle diameters using a circular approximation. To check the consistency of the automatic approach, images with 1000 particles were automatically and manually analyzed. The best agreement was obtained for an automatic analysis of the images processed by a Gaussian blur filter (sigma = 3.0) and, subsequently, by a minimum filter (radius = 2.0 pixels). For particles with diameters larger than 2 nm, the error of the particle diameter determined by the automated measurements is approximately ±0.5 nm. A disadvantage of the filter combination is that the sizes of the very small particles (diameter less than 2 nm) are overestimated. To circumvent this problem, particles with a diameter smaller than 2 nm were omitted in the present analysis. In two cases, it was necessary to measure diameters below the limit of 2 nm, and in these cases manual measurements were applied (Figures 2 and 4). The automatically measured diameters are presented in the form of time-lapsed particle size distributions (PSDs) with an optimum bin-size calculated according to ref 42. Due to sintering, the optimum bin-size changes during the experiment and, as a compromise, the bin-size is therefore calculated using the particle size measurements after 3 h in the *in situ* experiment.

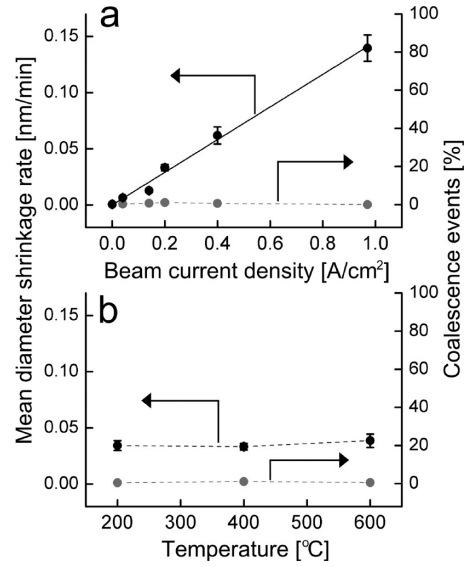

Figure 2. The mean particle diameter shrinkage rate and the number of coalescence events of the Pt/Al_2O_3 catalyst during exposure to 10 mbar air presented (a) as a function of beam current density at constant temperature (400 °C) and (b) as a function of temperature at constant beam current density (0.21 A/cm^2). For each data point, the mean diameter shrinkage rate is based on measurements on 30 particles and the percentage of coalescence events is calculated from more than 400 particles. Error bars refer to the standard deviation of the mean diameter.

Before performing the actual experiments, it is mandatory to understand and control artifacts that may be induced by the electron beam so that they can be eliminated. The electron beam effects were examined by observing the Pt/Al_2O_3 model catalyst during the exposure to 10 mbar technical air at a temperature of 400 °C. Under these conditions, different regions on the specimen were observed, each at a different beam current density below 1 A/cm^2. The regions were initially unexposed to the electron beam and were subsequently imaged with a frame rate of 1.4 frames/s (exposure time = 0.5 s) for 30 min. The image series reveal two main effects of the electron beam: the shrinkage of the projected Pt nanoparticle areas and the coalescence of neighboring Pt nanoparticles.

To address the shrinkage, the diameters of 30 Pt nanoparticles were manually measured in the first and last frame of the image series. For particles that eventually disappeared during the 30 min of exposure to the electron beam, the final diameter measurement was obtained from the last frame, where the particles were clearly visible, and the shorter beam exposure time was taken into account.

Figure 2a shows a plot of the mean Pt nanoparticle diameter shrinkage rate versus the electron beam current density and reveals a linear increase in the diameter shrinkage rate of the Pt nanoparticles with beam current densities increasing up to 1 A/cm^2. The diameter shrinkage was absent in similar experiments conducted in high vacuum (10^{-7} mbar) or 10 mbar N_2 as well as in the

(40) Simonsen, S. B.; Dahl, S.; Johnson, E.; Helveg, S. *J. Catal.* **2008**, *255*, 1.
(41) Hansen, P. L.; Datye, A. K.; Helveg, S. *Adv. Catal.* **2006**, *50*, 77.
(42) Freedman, D.; Diaconis, P. *Z. Wahrscheinlichkeit* **1981**, *57*, 453.

experiments with technical air, but with the electron beam blinded off between the first and last frame (corresponding to a beam current density of 0 A/cm^2 in Figure 2a). Hence, the diameter shrinkage is therefore a combined effect of the electron beam and the oxidizing gas environment.

To address the mechanisms for the apparent loss of Pt, the experiment at 400 °C and 0.21 A/cm^2 was repeated with a new specimen for a prolonged period of 2 h. Energy dispersive spectroscopy of the same area on a specimen in its as-prepared state and after the 2 h exposure to the electron beam reveal a loss of Pt as seen from a reduction in the Pt L and M peak intensity. The Pt is probably removed as volatile Pt-oxygen species by the electron beam.

The study of the electron beam effects was repeated to address the influence of temperature variations by using a new specimen exposed to the oxidizing conditions at a temperature of 200 and 600 °C. Figure 2b shows that the shrinkage was independent of temperature in this interval.

Finally, concerning the coalescence of neighboring Pt particles, only a minor fraction of ca. 1% of the total number of nanoparticles apparently coalesced in the oxidizing gas environment irrespective of the electron beam current density and temperature (Figures 2a−b). Specifically, the coalescence events involved only particles located in close vicinity with their center of mass separated by ca. 3 nm and did not involve migration of particles over longer distances. The events could be coalescence events or rapid localized ripening events in accordance with ref 43. Coalescence events of the type described above were also observed at RT in the high vacuum of 10^{-7} mbar in the electron microscope.

The present series of experiments demonstrates the importance of minimizing the electron dose on the specimen to quantitatively compare the changes in the ensemble of supported Pt nanoparticles with sintering models. Hence, *in situ* TEM was performed using a low electron beam current density of 0.07 A/cm^2 to minimize the effect of the electron beam. Due to the low electron beam current density, the noise level increases in the TEM images. To improve the signal-to-noise ratio as well as to reduce the effect of thermal drift of the specimen in the TEM images, each TEM image presented in the following represents the average of six aligned TEM images recorded successively with an exposure time of 0.5 s and a frame rate of 1.4 frames/s. For sample regions monitored over the prolonged periods of the *in situ* experiment, TEM imaging was performed in this way and repeated every 30 min for 6 h. In the intervening period, the electron beam was removed from the region. Including time needed for focusing and imaging, the sample regions used in the present analyses were exposed to the electron beam for ca. 1.3 min per image giving a total exposure time of ca. 17 min. Combined with the measured shrinkage rates (Figure 2), the total Pt particle diameter shrinkage caused by the electron beam can therefore be estimated to 0.2 nm, which is negligible compared to the particle sizes.

Results and Discussion

Sintering of the Pt nanoparticles was activated by heating the model catalyst by 30 °C/min up to 650 °C in an atmosphere of 10 mbar technical air. TEM images were acquired after the establishment of isothermal conditions (corresponding to time $t = 0$ min) and the stabilization of sample drift. In terms of mass−thickness contrast, the Pt nanoparticles are identified in the TEM images as the darker contrast features, which are superimposed at the brighter background that corresponds to the amorphous Al_2O_3 support. TEM images acquired 5 min after the establishment of isothermal conditions show that the Pt nanoparticles were very similar with respect to size and shape (Figure 3a). Specifically, the treatment resulted in a transformation of the irregular shapes of the as-prepared Pt nanoparticles (Figure 1b) to predominantly circular projected shapes (Figure 3a). A circular projected shape reflects a compact three-dimensional shape consistent with surface energy minimization for a metal nanoparticle. The corresponding distribution of particle diameters (Figure 3f) has an arithmetic mean value of ca. 3 nm with full-width at half-maximum of only 1.4 nm. Moreover, in this initial state, the particle density was 0.04 particles/nm^2 corresponding to a mean particle−particle separation of ca. 5 nm. The uniform ensemble of Pt nanoparticles prevailed over the entire specimen.

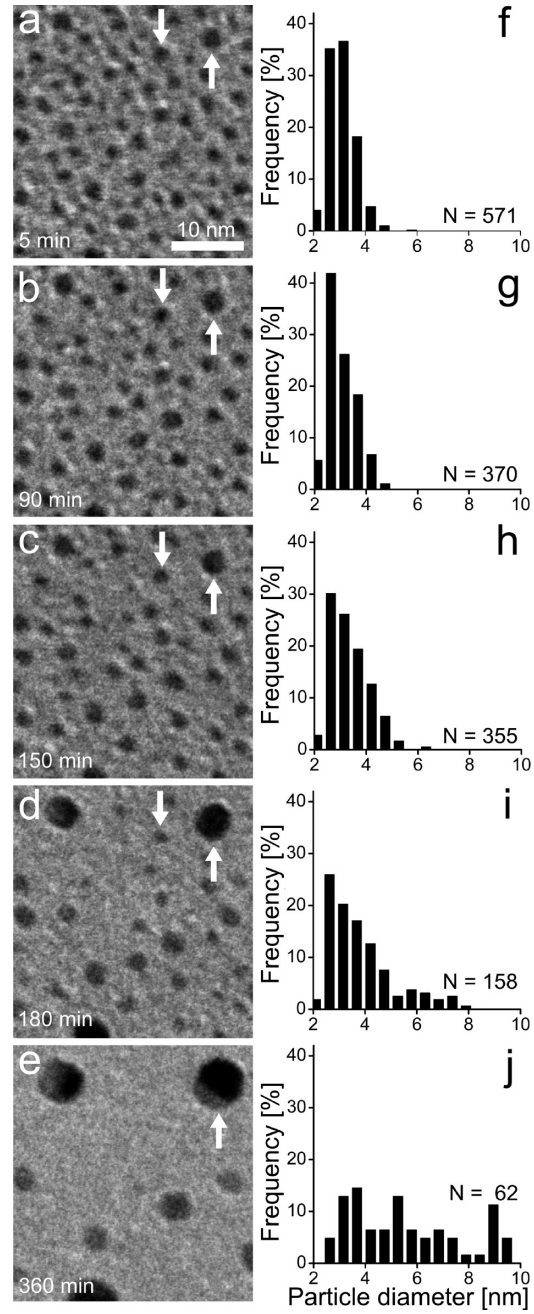

Figure 3. (a−e) Time-lapsed TEM images recorded *in situ* of the same area of a Pt/Al_2O_3 model catalyst during exposure to 10 mbar air at 650 °C. The images are 40 × 40 nm^2 sections of TEM images with a full area of 130 × 130 nm^2. To guide the eye an example of a growing and a shrinking particle is indicated with arrows. (f−j) Particles size distributions based on measurements from the full TEM images. *N* indicates the number of particles included in each particle size distribution.

(43) Yang, W. C.; Zeman, M.; Ade, H.; Nemanich, R. J. *Phys. Rev. Lett.* **2003**, *90*, 136102.

To monitor dynamical changes of the Pt nanoparticles over the course of time, consecutive TEM images were recorded *in situ* of the same area of the specimen and played back in the form of a movie (Figures 3a−e, Movie S1). The image series directly reveals that the Pt particles remained immobile during the experiment and that the projected area of the Pt particles either increased or decreased. The observations cannot be due to a morphological transformation of the Pt particles, such as a wetting/nonwetting transformation,[44] because the smaller particles eventually disappeared and the larger particles obtained a more pronounced dark contrast, consistent with an increased particle height along the electron beam direction. Hence, the observations directly suggest that the sintering of the Pt nanoparticles was governed by an Ostwald ripening mechanism, in agreement with ref 24. The corresponding mass-transport is possibly mediated by Pt atoms, or more likely Pt-oxygen species, since previous studies suggest that the sintering rate of supported Pt nanoparticles in oxidizing environments is accelerated due to the formation of volatile Pt−oxygen species.[3,35,45] The Pt−oxygen species are too small or too fast to be directly detected with the present settings. A similar effect of gas−metal species with enhanced rate of formation or transport has also been observed in other systems including H−Pt,[46] S−Cu,[47,48] or OH−Ni_2.[49]

The time-resolved image series provides further insight into the local ripening dynamics of the individual nanoparticles. Figure 4 shows the projected particle diameters in a TEM image series for a selection of Pt nanoparticles. In general, the nanoparticles with a large initial diameter tended to grow, while particles with smaller initial diameters tended to shrink over the course of time. Hence the overall dynamics followed the expectation for the Ostwald ripening process.[8] According to mean-field models, such as eq 1, particles with the same size should grow or decay at the same rate. However, a detailed examination of the *in situ* TEM data reveals discrepancies from the mean-field model. For instance, Figure 4 shows that while the diameter increases of particles 1 and 2 are similar, the diameters of particles 6−8 decay at different rates although the initial diameters are the same. The differences in growth rate are also obvious for particles 3−5.

Similar deviations were previously reported for metal systems under ultra-high vacuum and for Au/TiO_2 under CO oxidation reaction.[18,21] In accordance with these findings, the present observations (Figure 4) may be attributed to a local effect. That is, the exchange rate of diffusing species for a Pt nanoparticle depends on the size of and the distance to the neighboring nanoparticles rather than on the mean-field concentration established by all nanoparticles. Figure 4 also shows surprisingly that the diameters of most particles were almost stable during the initial stage of the sintering process and that this initial period lasted for up to 2 h of the experiment. During the initial stage, a change in diameter is, however, observed for the smallest particles (Figure 4).

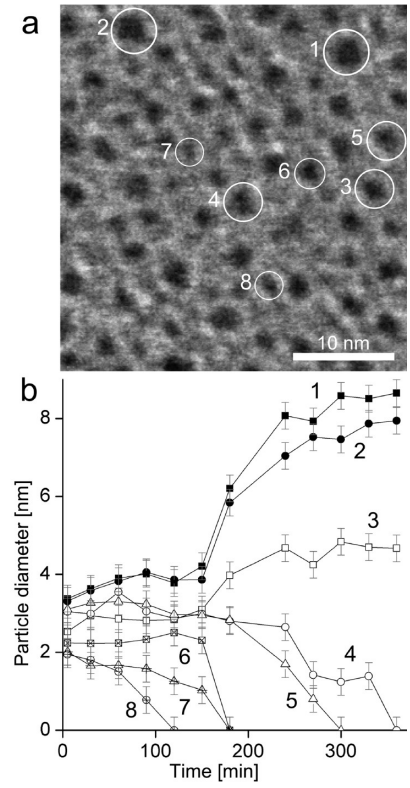

Figure 4. (a) Selection of eight particles in Figure 3a (white circles) for time-resolved analysis. (b) The diameters of the selected particles presented as a function of time. The error bars indicate estimated measuring errors from the manual outlining of the particles.

Based on eq 1, it is expected that the rate of diameter change will be highest for the smallest particles.

The apparent local effects on ripening raise the question whether the mean-field model is applicable for describing the ripening kinetics for an entire ensemble of Pt nanoparticles. Figures 3f−j present PSDs derived from particle measurements in the area followed through the experiment (corresponding to Figures 3a−e). Interestingly, the initial Gaussian shape transforms into a skew form as a tail of larger particles emerges on the right side of the mean value and consequently the distribution broadens as a function of time. However, the number of particles in the fixed field of view drops with time. To circumvent the reduced counting statistics, the observations are complemented by a more thorough statistical analysis. This analysis is based on a larger number of TEM images that were acquired during the *in situ* experiment. At each aging stage (corresponding to the stages of Figure 3), several TEM images were acquired at areas on the specimen that were previously not exposed to the electron beam. Figures 5a−e present examples of TEM images of such different areas, and Figures 5f−j present the PSDs from all the TEM images obtained at a given stage. Qualitatively, Figure 5 reveals changes in the Pt nanoparticle sizes similar to Figure 3. The improved statistical material, however, results in more well-defined PSD shapes. Specifically the initial shape is approximately Gaussian (Figure 5f). At later stages, the PSD is fitted better with a log-normal distribution (Figure 5g) as larger particles formed at the expense of the smaller particles. Eventually the distribution peaks to the left of its mean value (Figure 5j), and at this stage the distribution is fitted well with

(44) Hansen, P. L.; Wagner, J. B.; Helveg, S.; Rostrup-Nielsen, J. R.; Clausen, B. S.; Topsøe, H. *Science* **2002**, *295*, 2053.
(45) Chaston, J. C. *Platinum Metals Rev.* **1966**, *10*, 91.
(46) Horch, S.; Lorensen, H. T.; Helveg, S.; Lægsgaard, E.; Stensgaard, I.; Jacobsen, K. W.; Nørskov, J. K.; Besenbacher, F. *Nature* **1999**, *398*, 134.
(47) Feibelman, P. J. *Phys. Rev. Lett.* **2000**, *85*, 606.
(48) Ling, W. L.; Bartelt, N. C.; Pohl, K.; Figuera, J.; Hwang, R. Q.; McCarty, K. F. *Phys. Rev. Lett.* **2004**, *93*, 166101.
(49) Sehested, J. *J. Catal.* **2003**, *217*, 417.

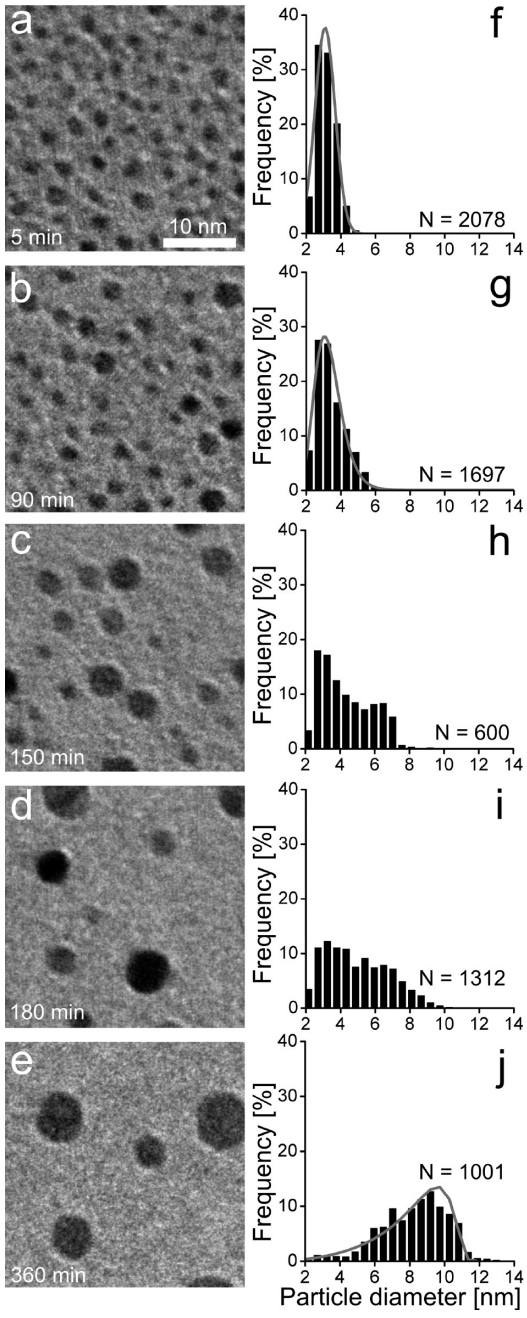

Figure 5. (a−e) TEM images of different randomly chosen areas of a Pt/Al_2O_3 model catalyst during exposure to 10 mbar air at 650 °C. The images are 40 × 40 nm^2 sections of TEM images with a full area of 130 × 130 nm^2. (f−j) PSDs based on measurements from a number of TEM images of areas previously unexposed to the electron beam. A (f) Gaussian, (g) log-normal, and (j) two-dimensional LSW distribution are fitted to the data.[52] *N* indicates the number of particles included in each particle size distribution.

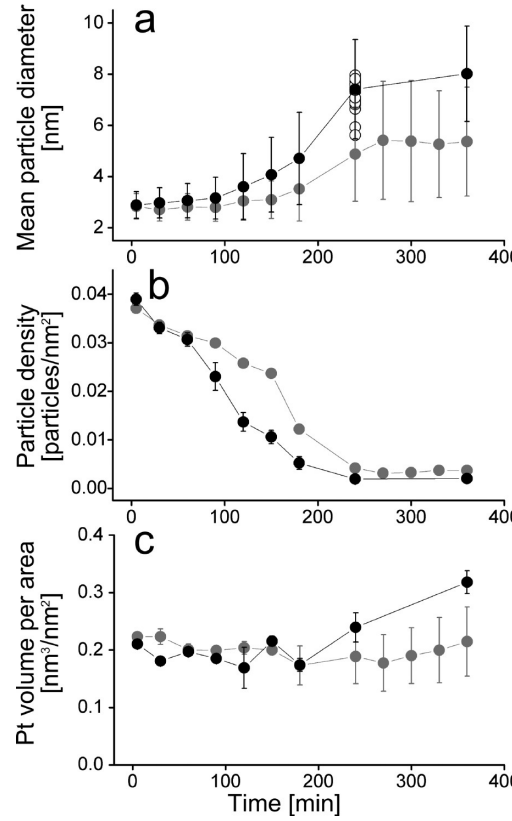

Figure 6. (a) Mean particle diameter, (b) particle density, and (c) Pt volume per support area as a function of aging time for particles in an area followed over time, corresponding to Figure 3 (gray), and for areas previously unexposed to the electron beam, corresponding to Figure 5 (black). In (a−b) error bars refer to the standard deviation of the particle diameters and density respectively. In (c) error bars refer to the propagated measuring error. In (a), an example of the statistical spread in mean particle diameter for different areas on the specimen is presented with open circles at 240 min.

the so-called Lifshitz−Slyozov−Wagner (LSW) model[50,51] modified to represent a two-dimensional system.[52]

The LSW model was previously established to describe Ostwald ripening mediated sintering,[50,51] but the distinct LSW shaped PSD has not previously been reported on technical catalysts. Even after severe aging in oxygen at ambient pressures, log-normal like shapes are typical for PSDs of technical catalysts.[16] It has been discussed that the sintering mechanism may be deduced from the specific shapes of the particle size distributions.[3,8,11,12] However, Datye et al. argued recently, based on indirect post-mortem examinations of technical relevant catalysts, that it indeed is difficult to infer the mechanism from the particle size distributions.[16] In line with this work, the present findings reveal that such attempts are not straightforward, because the PSD may expose a time-dependency, and that a transitional period may exist, in which one specific sintering mechanism results in several different shapes of the PSD. A possible explanation for why the LSW shape is found in this study in contrast to studies on technical catalysts is that the present uniform support and homogeneous initial distribution of the Pt nanoparticles resemble the assumptions underlying the LSW model closer than the inhomogeneous support structure and nanoparticle distribution of technical catalysts.

Based on the PSDs, the temporal evolution of ensemble-averaged properties, such as the number-averaged mean particle diameter and particle density, is determined (Figures 6a−b). Figure 6a shows that the overall trend of change in the mean diameter with aging time is similar for the limited area (corresponding to Figure 3) and the additional areas (corresponding to Figure 5). The mean diameter remains almost stable during the initial period, but suddenly it increases rapidly, and

(50) Lifshitz, I. M.; Slyozov, V. V. *J. Phys. Chem. Solids* **1961**, *19*, 35.
(51) Wagner, C. *Z. Elektrochemie* **1961**, *65*, 581.
(52) Rogers, T. M.; Desai, R. C. *Phys. Rev. B* **1989**, *39*, 11956.

subsequently it becomes roughly constant with time. Figure 6a also shows how the standard deviation of the particle sizes changes with time as well. Initially, the standard deviation is small reflecting a narrow initial PSD. The spread in particle sizes increases at the onset of the fast increase in the mean particle diameter. Finally both the mean diameter and the particle spread remain almost constant. Figure 6b shows that the particle density is high during the initial stage and is reduced with time, until it stabilizes when the mean diameter stabilizes (Figures 6a−b). Hence, Figures 6a and b show that the sintering rate slows down in the final sintering stage. That the mean diameter is almost stable in the initial stage (Figure 6a) could indicate that no sintering took place at this stage. However, the decrease in density shows that particles decayed and that a slow sintering process indeed proceeded (Figure 6b). This is also consistent with Figure 4b which shows that the smallest particles appeared to shrink over time.

Although the data sets (Figures 6a−b) reflect the same overall trend, differences are also apparent. Based on the consideration of electron-beam-induced shrinkage (Figure 2), the difference is likely not dominated by such effects. It cannot be ruled out that the difference partly resulted from removal of free diffusing Pt−oxygen species from the specimen by the electron beam. However, the volume of Pt in the nanoparticles can be estimated using a hemispherical shape approximation to the projected Pt particles outlined in the TEM images. Figure 6c shows that the Pt volume is stable throughout most of the experiment and does not reflect a significant loss of Pt, but rather a slight increase in the end. Because Pt was not added to the sample, the apparent volume increase indicates that the particle shape changed to obtain a slightly larger projected area and that the hemispherical shape assumption is too simple. Hence the results (Figure 6c) can only be taken as indicative. It is noted that the mean particle diameter obtained from single TEM images of different areas indeed varies as indicated (Figure 6a, open circles) and this intrinsic spread is likely the reason for the discrepancy between the particle size averaged over a single area and multiple areas.

To address the question whether the observed temporal evolution of the PSDs, as well as the mean particle diameter and particle density, reflects the Ostwald ripening characteristics, the observations are compared to simulations based on eq 1. The simulations followed the procedure of Smet et al.[53] with discrete time steps of 0.5 min and using an initial Gaussian particle size distribution with a particle number and a particle density corresponding to the PSD in Figure 5f. The simulations were performed in an iterative way by varying a constant corresponding to α of eq 1 until the particle density of the simulated distribution fitted the observed particle density of Figure 5 best for all times. These simulations produced the PSDs presented in Figure 7a, the mean particle diameter (black line) presented in Figure 7b, and the particle density (black line) presented in Figure 7c. In another simulation run, the simulation constant was tuned to obtain the best match with the mean particle diameter of Figure 5. The simulated mean particle diameter and corresponding density are shown as the gray curves in Figures 7b, c.

The simulated PSDs as a function of time show that the initial Gaussian shape transforms into an LSW shape over time. The simulated end distribution matches the experimentally observed PSD (Figure 5j). However, while the simulations indicate a gradual change of the initial Gaussian distribution into the LSW

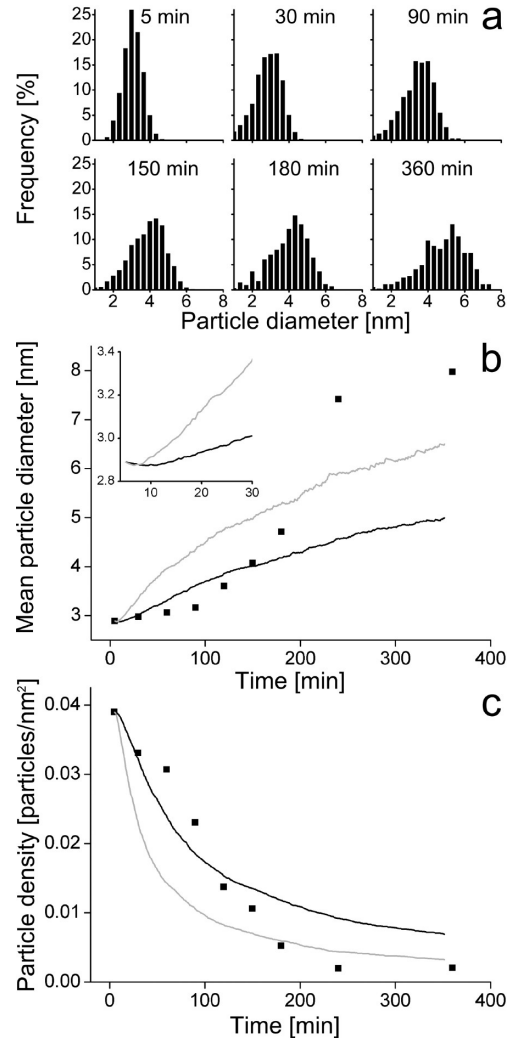

Figure 7. Simulations of the time-evolved particle size distribution (a), mean particle diameter (b), and particle density (c) following ref 53. The initial particle size distribution used for the simulation is a Gaussian distribution with mean and width corresponding to the distribution in Figure 5f. Experimental measurements of the mean particle diameter and density corresponding to Figures 6a−b are included (squares). For (b) and (c), the parameters of the simulation are set to obtain the best possible agreement with the observed mean diameter (gray) or particle density (black). To guide the eye a zoom on the first 30 min is inserted in (b).

shape, the experimentally observed distributions show transitional shapes with a tendency for a tail to the right of their maximum until the LSW shape emerges. The difference may reflect inherent scattering of the experimental data or the shortcomings of the model as discussed below.

The simulated mean particle diameter evolves in time with an initial almost stationary period, followed by a rapid increase and, subsequently, by a period of slower growth (Figure 7b). The simulated particle density evolves with an initial fast decrease which subsequently slows down. The trends in the time-evolution of the mean particle diameter have previously been reported for simulations based on narrow Gaussian initial PSDs.[8,53] There appears to be overall qualitatively agreement between the simulated and the experimental data for time-dependency of the mean particle diameter and particle density whereas quantitative differences are apparent. Specifically, both the simulations and the experiment show interestingly that the initial stage with slow sintering is correlated with a narrow PSD. One explanation for the coupling of slow sintering with a narrow

(53) Smet, Y. D.; Deriemaeker, L.; Finsy, R. *Langmuir* **1997**, *13*, 6884.

PSD is that even though a concentration of atomic species is believed to be generated from the initially small particles, larger particles are needed to take up the atomic species according to the Gibbs−Thompson effect. This, in turn, means that a broadening of the PSD will increase the sintering rate. This result also suggests that one route to suppress the deactivation of industrial catalysts through sintering could be to aim for very narrow initial PSDs. This will not be a route for stabilizing the catalysts, but may be a route for prolonging the metastable initial state resulting in higher total activity. In comparison, a slow onset for S induced ripening of Cu is also previously reported but attributed to a shift in S concentration.[48]

The differences between the simulated and observed time-dependencies of the mean particle diameter and particle density may include several effects. First, the initial period with a stationary mean particle size and narrow particle size distribution is considerably shorter for the simulated (ca. 10 min) than for the experimental data (ca. 2 h). The longer stationary period in the experiment could possibly be an additional kinetic effect related to the establishment of the concentration of Pt−oxide complexes on the support. Second, the experimental observations show final mean particle sizes and particle densities that are larger and smaller, respectively, as compared to the simulated parameters. It should also be noted that although the present model systems were generated to closely match the assumptions underlying the model (eq 1), the experimental situation still may deviate from the model assumptions. Because the particles are imaged in a projection orthogonal to the support surface, the projected particle diameter represents only a simple measure for the Pt morphology. The particle shape is determined by the surface free energies of the exposed Pt surface sites and by the Pt−alumina interface energy. As the nature of the surface sites may change with size[54] and oxygen adsorption is site-dependent,[55,56] the oxygen atmosphere may affect the surface free energy and hence the particle shapes in a size-dependent manner. Moreover, as surface defects could act as anchor sites (as suggested for Pt on gamma-alumina[57]), the interface energy may also be speculated to be partly inhomogeneous. In such a case the adhesion of the Pt particles with different sizes could vary and thus also affect the Pt morphology. Furthermore, it is noted that the used model assumes that the concentration of atomic species around the particles is described by the Gibbs−Thompson equation and that the concentration increases to the mean-field value, which pertains to the area between the immobile particles.[3] However, the high initial fractional Pt coverage and a small mean Pt particle separation of ca. 5 nm may cause a breakdown of the mean-field approximation because of overlap in concentration gradients of the atomic species surrounding the particles. The particles may therefore directly affect their neighbor's growth rates rather than indirectly through the mean-field concentration of mass-transporting species. The direct interaction with neighbor particles could explain the local deviations from the mean-field model (Figure 4). Moreover, a local overlap of the concentration gradient can be imagined to affect the time-dependency of the changes in the whole ensemble of Pt nanoparticles, as addressed by Dadyburjor et al.,[58] and hence cause deviations in particle size distributions, average particle size, and particle density from the mean-field model predictions as reflected in Figure 7.

Conclusion

In situ TEM was used to monitor Pt nanoparticles dispersed on a planar, amorphous Al_2O_3 support during exposure to 10 mbar of synthetic air at 650 °C. Time-resolved image series unequivocally reveal that Pt nanoparticle sintering was mediated by an Ostwald ripening process and allow for a direct comparison to the mean-field model for Ostwald ripening. A statistical analysis of an ensemble of Pt nanoparticles shows that the particle size distributions change shape as a function of time. Specifically, the particle size distribution changes from an initial Gaussian distribution via a log-normal type distribution to an LSW distribution under the present sintering conditions. Furthermore, the overall trends of the time-dependency of the ensemble-averaged particle size and the particle density agree with the mean-field expectations. However, at the individual nanoparticle level discrepancies are observed suggesting that the local environment influences the atom exchange process.

Acknowledgment. We gratefully acknowledge Bengt Kasemo, Jonas Andersson, Elin Larsson, and Laurent Feuz (Chemical Physics Group) as well as Eva Olsson (Microscopy and Microanalysis Group) at Chalmers University of Technology for contributing to sample preparations. We thank the MC2-Access project for financial support. We acknowledge the participation of the CTCI Foundation, Taiwan, in the establishment of the *in situ* TEM facility at Haldor Topsøe A/S. CINF is funded by The Danish National Research Foundation.

Supporting Information Available: Movie S1 shows the time-lapsed *in situ* TEM images of the Pt/Al_2O_3 model catalyst during exposure to 10 mbar air at 650 °C. The acquisition time relative to the time of reaching the temperature 650 °C is given for each frame. S1 shows the full 130 × 130 nm^2 area corresponding to Figures 3a−e. This material is available free of charge via the Internet at http://pubs.acs.org.

JA910094R

(54) Hardeveld, R.; Hartog, F. *Surf. Sci.* **1969**, *15*, 189.
(55) Wand, L.; Roudgar, A.; Eikerling, M. *J. Phys. Chem. C* **2009**, *113*, 17989.
(56) Sljivancanin, Z.; Hammer, B. *Surf. Sci.* **2002**, *515*, 235.
(57) Kwak, J. H.; Hu, J.; Mei, D.; Yi, C.-W.; Kim, D. H.; Peden, C. H. F.; Allard, L. F.; Szanyi, J. *Science* **2009**, *325*, 1670.
(58) Dadyburjor, D. B.; Marsh, S. P.; Glicksman, M. E. *J. Catal.* **1986**, *99*, 358.

Paper II

Journal of Catalysis 281 (2011) 147–155

Contents lists available at ScienceDirect

Journal of Catalysis

journal homepage: www.elsevier.com/locate/jcat

Ostwald ripening in a Pt/SiO_2 model catalyst studied by *in situ* TEM

Søren Bredmose Simonsen [a,b], Ib Chorkendorff [b], Søren Dahl [b], Magnus Skoglundh [c], Jens Sehested [a], Stig Helveg [a,*]

[a] Haldor Topsøe A/S, Nymøllevej 55, DK-2800 Kgs. Lyngby, Denmark
[b] CINF, Department of Physics, Technical University of Denmark, DK-2800 Kgs. Lyngby, Denmark
[c] Competence Centre for Catalysis (KCK), Chalmers University of Technology, SE-41296, Göteborg, Sweden

ARTICLE INFO

Article history:
Received 21 February 2011
Revised 17 April 2011
Accepted 18 April 2011
Available online 26 May 2011

Keywords:
Catalyst deactivation
Sintering
Ostwald ripening
Nanoparticles
Pt
In situ TEM

ABSTRACT

Sintering of Pt nanoparticles dispersed on a planar SiO_2 support was studied by *in situ* transmission electron microscopy (TEM). A time-lapsed TEM image series of the Pt nanoparticles, acquired during the exposure to 10 mbar synthetic air at 650 °C, reveal that the sintering was governed by the Ostwald ripening mechanism. The *in situ* TEM images also provide information about the temporal evolution of the Pt particle size distribution and of the growth or decay of the individual nanoparticles. The observed Pt nanoparticle changes compare well with predictions made by mean-field kinetic models for ripening, but deviations are revealed for the time-evolution for the individual nanoparticles. A better description of the individual nanoparticle ripening is obtained by kinetic models that include local correlations between neighboring nanoparticles in the atom-exchange process.

1. Introduction

Metal nanoparticles dispersed on a porous support material are used as efficient heterogeneous catalysts for diverse applications in energy conversion, chemical supply, and environmental protection [1,2]. However, the high-surface area of the nanoparticles is associated with an excess surface energy, so the nanoparticles represent a meta-stable solid state. Given sufficient thermal activation, the nanoparticles will therefore sinter into larger particles and this coarsening causes an unwanted reduction in the metal surface area, which may affect the catalyst performance [3–5]. At the microscopic level, the sintering is attributed to the transport of atomic species (metal atoms or complexes consisting of metal atoms and gas derivatives) at the surface of the nanoparticle or the support material [4]. The specific transport pathways for the atomic species are often considered to reflect the following generic sintering mechanisms [4,6]: (i) particle migration, in which the nanoparticles diffuse over the support and eventually coalesce with other nanoparticles, and (ii) atom migration, in which atomic species are emitted from one nanoparticle, diffuse over the support and attach to another nanoparticle. The latter mechanism is often referred to as Ostwald ripening.

In Ostwald ripening, the transport of atomic species is explained by the Gibbs–Thomson relation [4,7], which describes the surface concentration of the diffusing species at support sites adjacent to the edge of a nanoparticle, ρ_r, by

$$\rho_r = \rho_\infty \exp\left(\frac{2\gamma\Omega}{kTr}\right) \quad (1)$$

where r is the radius of the nanoparticle, ρ_∞ the surface concentration of atomic species in equilibrium with an infinitely large particle, γ the surface energy, Ω the atomic volume, k Boltzmann's constant, and T the temperature. According to Eq. (1), the concentration of atomic species is higher near small particles than near larger particles. As a result of the gradient in concentration, a net flux of atomic species will diffuse from smaller to larger particles, so the larger particles eventually grow at the expense of the smaller ones. The growth or decay of the nanoparticles is often described by kinetic models relying on the mean-field assumption of the concentration of atomic species. That is, the concentration of atomic species on the support is constant beyond the screening distance, L, from the edge of the particle, and this mean-field concentration is governing the atom-exchange for each particle in the ripening process [4,7]. Combined with the assumption of a flat and homogeneous catalyst support, expressions for the rate of particle size change can be derived. For an interface-controlled ripening process, in which the diffusion over the support is fast and the flux away from the particle edge is limiting, the rate by which the radius changes, dr/dt, can be expressed by [4]:

* Corresponding author.
E-mail address: sth@topsoe.dk (S. Helveg).

0021-9517/$ - see front matter © 2011 Elsevier Inc. All rights reserved.
doi:10.1016/j.jcat.2011.04.011

$$\frac{dr}{dt} = \frac{\alpha}{r^2}\left(\frac{r}{r^*} - 1\right) \quad (2)$$

For a diffusion-controlled ripening process, in which the diffusion on the support is limiting, the rate by which the radius changes can be expressed by [4]:

$$\frac{dr}{dt} = \frac{\alpha'}{r^3 \ln(L/r)}\left(\frac{r}{r^*} - 1\right) \quad (3)$$

In Eqs. (2) and (3), α and α' are system specific parameters, r the particle radius, and r^* the critical radius. At a given time in the sintering process, the critical radius corresponds to the particle size, which is in equilibrium with the mean-field concentration and therefore does not change. Moreover, Eqs. (2) and (3) are based on a first-order Taylor expansion of Eq. (1). In this approximation, r^* equals the arithmetic mean radius of the particle ensemble [8]. For sufficiently small particles, the Taylor expansion is inapplicable and r^* deviates from the mean radius [9].

The applicability of the kinetics models (Eqs. (2) and (3)) for describing ripening in heterogeneous catalysts has been subject to much debate [10–18]. For instance, as discussed by Voorhees [17] and Dadyburjor et al. [18], the mean-field assumption for the concentration of ripening–mediating species should be useful for catalysts with low metal loadings, because the metal particles are, on the average, sufficiently far apart on the support as compared with the screening distance (L). But, even for such catalysts, the actual preparation route may result in regions of high local particle density with a mean particle separation that is comparable with the particle size. As the particle separation approaches the screening distance (L), the particles will alter the concentration of atomic species in the vicinity of neighboring particles as compared with the uniform mean-field concentration. Hence, in such a nanoparticle ensemble, a nanoparticle should experience an effective concentration of atomic species, depending on the location and size of the neighboring nanoparticles, and so the nanoparticle ripening should correlate with the local conformation of nanoparticles. Previously, it was demonstrated that such local correlations in ripening are present in homoepitaxial systems, including Si-islands on Si(1 1 1) [19,20] and Ag-islands on Ag(1 1 1) [21]. These studies used time-resolved microscopy to monitor the ripening of two-dimensional islands with radii larger than ca. 5 nm under ultrahigh vacuum conditions and revealed a size-dependency of the island ripening, which is not well described by mean-field kinetic models but better described by kinetic models incorporating local correlations. Recently, *in situ* microscopy of model catalyst systems, including three-dimensional Au nanoparticles on TiO_2 during the CO oxidation [22] and Pt nanoparticles on Al_2O_3 during oxidizing conditions [23], revealed that local correlations between the metal nanoparticles may also affect ripening processes in heterogeneous catalysts. However, a detailed description of the correlated ripening effect was not pursued for those model catalysts.

In the present study, we address the issue of local correlations in ripening for a Pt/SiO_2 catalyst. The Pt/SiO_2 catalyst system is representative for, e.g., oxidation catalysts in diesel or lean-burn engine exhaust treatment. Our study focuses on a catalyst system consisting initially of highly monodisperse Pt nanoparticles (radius of ca 1.5 nm) with a high, uniform density (ca. 0.03 particles/nm^2) on a planar, amorphous SiO_2 support. This is an ideal model system because Pt is expected to sinter via ripening under oxidizing conditions [24], and because the high density of the Pt nanoparticles, corresponding to a short particle interspacing of ca. 3 nm, should enhance the effect of local correlations in the nanoparticle ripening. Specifically, by means of *in situ* transmission electron microscopy (TEM), the model catalyst was monitored during exposure of the sample to 10 mbar of 21 % O_2 in N_2 at 650 °C. Time-resolved TEM images of the model catalyst confirm unambiguously that the Pt sintering was mediated by Ostwald ripening. The quantitative analysis of the growth and decay of the Pt nanoparticles is systematically compared with the predictions of the interface-controlled and diffusion-controlled ripening models including (i) a mean-field assumption and (ii) local correlations for the atom-exchange process, as described in the framework of [19,20,25]. The analysis shows that Pt nanoparticle ripening is well described by both interface- and diffusion-controlled ripening models under the present experimental conditions and that a kinetic description, including information of the local particle conformation, gives a better description of the temporal evolution of the individual nanoparticle sizes.

2. Materials and methods

The Pt/SiO_2 model catalyst was formed on a Si wafer with a 30 nm thick, amorphous and electron-transparent Si_3N_4 window (Fig. 1). Following the Si_3N_4 window preparation [26], a flat and amorphous SiO_2 support layer was formed by oxidizing the Si_3N_4 surface using a microwave plasma processor (TePla 300PC) operated at 1 kW with 1 mbar O_2 for 40 min. The resulting SiO_2 layer had a thickness of ca. 7 nm, measured by ellipsometry, and a root-mean-square roughness below 0.6 nm over a 100 μm^2 area, determined by atomic force microscopy. X-ray photoelectron spectroscopy (XPS) revealed a characteristic peak at 103.5 eV, corresponding to the reference value for the Si $2p_{3/2}$ peak in SiO_2 [27]. Diffraction patterns of the Si_3N_4-supported SiO_2 layer, obtained using a Titan 80–300 transmission electron microscope (FEI Company), demonstrate only broad and diffuse bands of diffracted electrons consistent with an amorphous structure. Thus, the SiO_2 support matched closely a homogeneous medium. Platinum was deposited onto the SiO_2 support using an electron beam evaporator (AVAC HVC600) with a base vacuum pressure of $4 \cdot 10^{-6}$ mbar. The evaporator was operated with a Pt target of 99.99 % nominal purity (Nordic High Vacuum AB) and with a deposition rate of 0.05 nm/s to form a Pt film with a nominal thickness of 0.5 nm. The as-deposited Pt was present as irregularly shaped particles with a mean radius of ca. 1.5 nm. The irregular, projected shapes transformed into a circular, projected shape of the Pt particles during the establishment of the aging conditions, in accordance with [23]. Moreover, XPS revealed a surface carbon contamination on the as-prepared samples of ca. 8 at.%. The carbon most likely reacted off or desorbed prior to the *in situ* TEM observations [23].

In situ TEM was performed using a CM300 FEG-ST (Philips/FEI Company) transmission electron microscope equipped with a differentially pumped environmental cell [28]. This microscope permits the acquisition of TEM images or time-lapsed image series of samples during the exposure to reactive gases (up to ca. 15 mbar) and elevated temperatures (up to ca. 900 °C). Specifically,

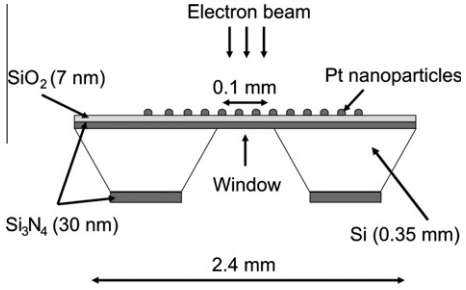

Fig. 1. Schematic side view of the Pt/SiO_2 model catalyst.

the microscope was operated with a primary electron energy of 300 keV and an ultimate information limit of ca. 0.14 nm, depending on the *in situ* conditions. For the present experiments, the specimen was imaged during the exposure to 10 mbar technical air composed of 21% O_2 and 79% N_2 (class 2 from Air Liquide). For heating, the specimen was mounted with the Pt/oxide side facing the bottom of the Inconel furnace of a Gatan single-tilt heating holder (model 628). The specimen was heated in the gas environment at a rate of 30 °C/min from room temperature up to 650 °C. The temperature was measured by a PtRh thermocouple spot-welded on the furnace. After the establishment of the isothermal conditions at 650 °C (corresponding to time $t = 0$ min), the temperature was kept constant within ca. 3 °C. The TEM imaging was performed after drift-stabilization of the sample holder.

The *in situ* TEM imaging was performed using a 1 k × 1 k Tietz Fastscan F-114 CCD camera, with an objective aperture (scattering semi-angle of 7.5 mrad) inserted and at a fixed magnification corresponding to an image pixel size of 0.13 nm. Moreover, the effective information limit was 0.21 nm, as confirmed by a Young fringe test performed with a separate sample in 10 mbar air at 500 °C. The *in situ* imaging of the supported Pt nanoparticles was carried out in two different modes: (i) A dynamic mode was applied in which a time-lapsed image series was acquired at the same area of the specimen. The image series consist of images, which were acquired at times relative to $t = 0$ min at intervals of 30 min. For each time step, the image was averaged over six consecutive, aligned TEM frames of 0.5 s. exposure. The image averaging was adopted to improve the signal-to-noise ratio in the images and to reduce the effect of residual thermal drift [23]. (ii) A static mode in which additional TEM images were acquired within 5 min of the time corresponding to each of the images of the time-lapsed image series. The static TEM images were acquired by shifting the beam to a distant area, which was prior unexposed to the electron beam. The static images were also averaged of six consecutive, aligned TEM frames of 0.5 s. exposure. Subsequently, the beam was blanked until acquisition of the following image in the image series.

To ensure a negligible effect of the electron beam on the present observations, the electron-illumination conditions were examined prior to the actual experiment, following the procedure in [23]. The present Pt/SiO_2 system was imaged during the exposure to 10 mbar technical air at 200–600 °C under varying electron beam current densities. The TEM images show that a minor fraction of ca. 1% of the particles coalesced with close neighbor particles and that the main effect of the electron beam was an induced Pt particle decay. The particle decay rate depended linearly on the beam current density and was higher than for the Pt/Al_2O_3 system in [23]. Consequently, in the present experiments, imaging was performed using a lower electron beam current density of 0.03 A/cm^2, corresponding to a particle radius decay rate of 0.01 nm/min. For the total exposure time of ca 9 min for the specific area in the time-lapsed image series, the beam-induced mean Pt particle radius decay was thus estimated to ca. 0.09 nm, which is negligible, compared with the Pt particle sizes and the estimated measuring error.

From the TEM images, Pt particle sizes (radii) were obtained from diameters, measured using a circular approximation to their projected area. The projected areas were measured manually or automatically, as described in [23]. Images from the static imaging mode were analyzed automatically for generating particle size distributions (PSD's) with a large data set. For the diameter measurements, the estimated error is 0.5 nm. Images from the dynamic imaging mode were analyzed manually for examining individual nanoparticles more precisely. For the manual diameter measurements, the estimated error equals the effective information limit of 0.21 nm.

3. Results

3.1. Sintering mechanism

To directly visualize structural transformations of the supported Pt nanoparticles, the time-lapsed TEM images were acquired of a specific specimen area *in situ* during exposure to the oxidizing gas environment (Fig. 2, Supplementary materials). Fig. 2 reveals that the Pt particles remained immobile and that the projected areas of the Pt particles either increased or decreased. Overall, the mean Pt particle size increased as the shrinking particles eventually disappeared. Hence, the observations unequivocally demonstrate that the Pt nanoparticles sintered and that the sintering was governed by the Ostwald ripening process. The finding is in accord with the previous work by Chen and Schmidt, who used *ex situ* TEM to monitor a specific area on a similar model catalyst after several aging treatments at temperatures from 600 °C to 685 °C in 1 atm. air [24]. Also, ripening-mediated sintering of Pt nanoparticles was reported in experiments with Pt/Al_2O_3 model catalysts [23,29]. In comparison, the relative importance of the atom and particle migration mechanisms for industrial Pt/SiO_2 catalysts has been debated [30–33]. The debate reflects in part that these studies are based on indirect and/or postmortem examinations, which may hamper an unambiguous determination of the prevailing sintering mechanism [10]. Previously, it was proposed that oxygen accelerates sintering of Pt nanoparticles through the formation of

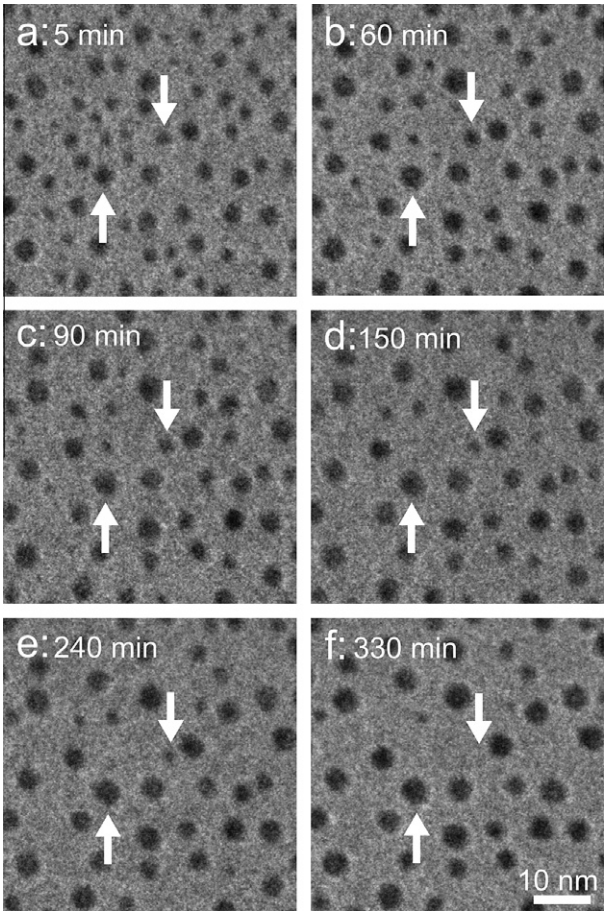

Fig. 2. (a–f) Time-lapsed TEM images recorded *in situ* at the same area of the Pt/SiO_2 model catalyst during exposure to 10 mbar air at 650 °C. The images are 50 × 50 nm^2 sections of the full TEM images of size 130 × 130 nm^2 (see Supplementary materials). The denoted times are relative to the time at which the temperature reached 650 °C. To guide the eye, arrows indicate examples of a growing and of a decaying particle.

volatile Pt-oxide species [4,24,34,35]. It is possible that such species also mediated sintering in the present *in situ* TEM experiments.

3.2. Particle size distributions

To complement the dynamic observations with more extended statistical information about the ensemble of Pt nanoparticles, TEM images were acquired in the static mode at independent and distant areas of the specimen during exposure to the oxidizing gas environment. From the additional images, the Pt particle size distribution (PSD) was extracted automatically as a function of time. Fig. 3 shows the PSDs with a main peak that gradually shifts toward larger particle size over time, consistent with the dynamic observations (Fig. 2). The initial mean particle radius is 1.5 nm with a standard deviation of 0.3 nm, and the mean radius is 2.1 nm with a standard deviation of 0.4 nm, at the end of the experiment (t = 330 min).

The observed time-evolution of the PSD can be compared with that predicted by the mean-field interface- and diffusion-controlled ripening models, as in other ripening studies [4,10,11,14,16,17,36]. By Eqs. (2) and (3), the time-evolution of the PSD was calculated numerically following the procedure described by Smet et al. [36]. Specifically, the PSD in Fig. 3a was used as the initial PSD and a discrete time step of 0.5 min was chosen. The simulations were made iteratively by systematically varying the constants α and $\alpha'/\ln(L/r)$ in Eqs. (2) and (3), respectively, until the mean particle radii of the calculated and measured PSD matched at the end of the experiment (t = 330 min). The iterative procedure resulted in $\alpha = 0.035\ \mathrm{nm^{-1}\ min^{-1}}$ and $\alpha'/\ln(L/r) = 0.067\ \mathrm{nm^{-1}\ min^{-1}}$ for the interface- and diffusion-controlled ripening models, respectively. In the present PSD simulations, the term $\ln(L/r)$ is considered constant for the following reasons: (a) The relation between r and L is not a priori known. (b) For a constant L, the relation $L > r$ must be satisfied at all times and for all particles, since otherwise $dr/dt \to \pm\infty$ for $r \to L$ (Eq. (3)). This leads to an inconsistency with the mean-field assumption, since the size of the largest particles ($r \approx 2.5$ nm at t = 5 min) exceeds the mean distance between the edges of the neighboring particles (ca. 1.5 nm at t = 5 min).

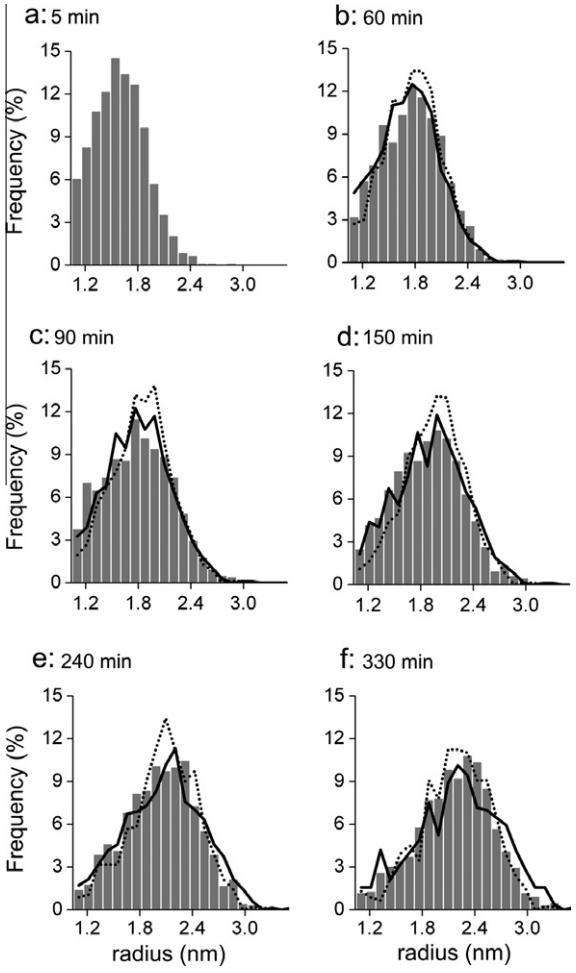

Fig. 3. (a–f) Time-lapsed particle size distributions obtained from the static TEM images. The static TEM images were recorded *in situ* of different areas of the Pt/SiO_2 model catalyst during the exposure to 10 mbar air at 650 °C. Prior to the static TEM image acquisition, the areas were unexposed to the electron beam. The number of measured particles included in each distribution is (a) 1593, (b) 2059, (c) 1101, (d) 1225, (e) 1095, and (f) 1134. The lines indicate histograms simulated based on the interface-controlled (solid) and diffusion-controlled (dotted) ripening models in Eqs. (2) and (3) with (a) as the initial distribution. The number of particles drops throughout the simulation to (b) 1224, (c) 1079, (d) 891, (e) 699, and (f) 573 for the interface-controlled model and (b) 1065, (c) 926, (d) 725, (e) 566, and (f) 463 for the diffusion-controlled model.

Fig. 3 includes the simulated PSDs for interface-controlled (solid line) and the diffusion-controlled (dotted line) ripening. The PSDs, based on the diffusion-controlled ripening model, seem slightly narrower than the PSDs, based on the interface-controlled model, as suggested in [4,20], but the difference is not significant. Thus, the comparison in Fig. 3 shows that the mean-field models describe the observed PSDs well. At first glance, an agreement is expected because the mean-field models are based on the assumption of a homogeneous support, which is approached by the planar and amorphous SiO_2 support in the present model catalyst. Moreover, the comparison shows that both the diffusion- and interface-controlled process may contribute to the ripening in the present experiments. However, the interface-controlled ripening would have been expected to dominate due to the relatively high metal loading and thus small diffusion distances between the nanoparticles in the present model catalysts [37]. The lack of a pronounced difference between the models may be due to the short aging times resulting only in a slight change of mean radius from 1.5 nm to 2.1 nm in the present experiment (Fig. 3).

3.3. Nanoparticle growth and decay rates

Although, the previous analysis shows that the mean-field models describe the observed PSDs well, it is noteworthy that the analysis is based on an ensemble of nanoparticles, which may tend to average out any effect of interactions between the nanoparticles. To address the possibility of such local dependencies, the dynamic changes of the individual nanoparticles may on the contrary be examined. Specifically, from the time-lapsed image series (Fig. 2, Supplementary information), the growth or decay rate of individual nanoparticles was obtained by manually measuring the change in radius over the time interval, t = 60–120 min, for each individual particle in the image. For normalization, the mean radius, r_{mean}, was calculated from the particle radii measured at t = 60 min. Fig. 4a shows the measured dr/dt as a function of the normalized radius, r/r_{mean}. For the majority of the nanoparticles, the growth or decay rates belong to the first or third quadrant, respectively, corresponding to a positive dr/dt for $r/r_{mean} > 1$ or a negative dr/dt for $r/r_{mean} < 1$. Thus, particles larger or smaller than the average particle size grew or shrank, respectively, as predicted by the mean-field ripening models. However, a minor fraction of the nanoparticles is associated with a rate of radius change in the second and fourth quadrant. As these rates are not accounted for by the estimated measurement error (indicated by the error bars), it seems that the mean-field models are not sufficient to fully account for the observed ripening.

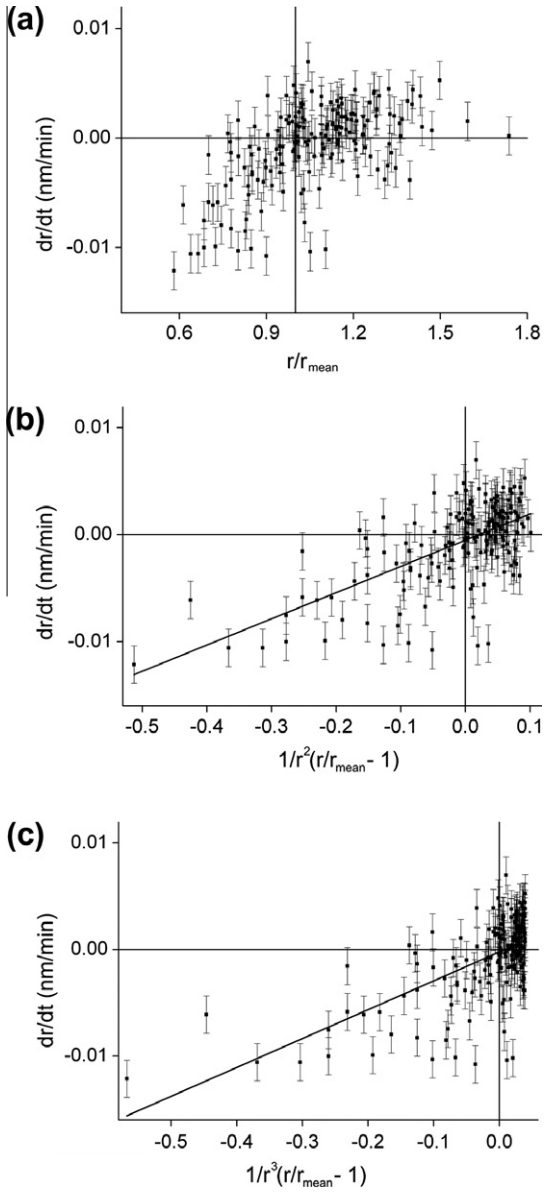

Fig. 4. The growth and decay rate, dr/dt, for individual Pt nanoparticles presented as a function of (a) normalized radius, r/r_{mean}, (b) $1/r^2(r/r_{mean} - 1)$, corresponding to Eq. (2), and (c) $1/r^3(r/r_{mean} - 1)$, corresponding to Eq. (3). The rates are obtained from the measurements at $t = 60$ and 120 min for 185 particles. The error bars indicate the estimated measurement error. For the best fitted line included in (b) and (c), the R^2-value is 0.42 and 0.39, respectively.

To further elaborate on deviations from the mean-field models, the rates in Fig. 4a are replotted in Fig. 4b as a function of $1/r^2 \cdot (r/r_{mean} - 1)$. For interface-controlled ripening, Eq. (2) predicts a linear relationship for Fig. 4b with a slope corresponding to α, and an offset $dr/dt = 0$ at $r = r_{mean}$. Fig. 4b includes the best linear fit to the rates, which was obtained for $\alpha = 0.025\ \mathrm{nm^{-1}\ min^{-1}}$, in agreement with the α-value from the PSD simulations and with an offset of 0.0005 nm/min, very close to the origin. Apparently, Fig. 4b shows an overall linear trend of the data, but the data spread further emphasizes deviations from the mean-field model. A similar analysis based on the diffusion-controlled ripening model, Eq. (3), is included in Fig. 4c. That is, Fig. 4c shows the rates in Fig. 4a replotted as a function of $1/r^3 \cdot (r/r_{mean} - 1)$. Assuming the term $\ln(L/r)$ in Eq. (3) is constant, the best linear fit to the data in Fig. 4c has a slope $\alpha'/\ln(L/r) = 0.027\ \mathrm{nm^{-1}\ min^{-1}}$, which is in reasonable agreement to $\alpha'/\ln(L/r) = 0.067\ \mathrm{nm^{-1}\ min^{-1}}$ from the PSD simulations, and an offset of 0.0002 nm/min, which is close to the origin. The mean-field model for diffusion-controlled ripening also captures an overall linear trend of the observations, but a significant data spread beyond the mean-field model expectation is apparent.

3.4. Temporal evolution of the nanoparticle sizes

To further examine the apparent discrepancies between the observed dynamic changes of the individual Pt nanoparticles and the mean-field models, a selection of Pt nanoparticles was examined through the entire time-lapsed image series of a specific area of the model catalyst. Fig. 5a shows the selected particles in the TEM frame from Fig. 2a. For each particle, the projected radius, r, of these particles as well as the mean radius for the entire TEM image, r_{mean}, was obtained as a function of time. Fig. 5b shows that the mean particle radius increased as a function of time and that nanoparticles with $r > r_{mean}$ grew and nanoparticles with $r < r_{mean}$ decayed. These general trends are overall consistent with the mean-field models. However, discrepancies are also apparent from a comparison of the observed particle radii of particles 1–9 with the calculated radii. Specifically, the time-dependency of the particle radii was calculated using the interface-controlled mean-field model (Eq. (2)) with the observed radii of particles 1–9 at $t = 5$ min (Fig. 5b) as initial radii and $\alpha = 0.03\ \mathrm{nm^{-1}\ min^{-1}}$. Fig. 5c shows the calculated time-dependency of the particle radii and demonstrates that the growth or decay rates are directly related to the particle size. However, the pattern differs from the observations: Despite comparable initial radii, the particles 4–6 decayed significantly slower than particles 7–9. Moreover, the observed order by which particles 4–9 decayed also differs from the calculated order.

3.5. Ripening models including local correlations

As discussed earlier, a possible cause for the discrepancy between the observations and the mean-field model predictions could be that the particle ripening is not governed by a mean-field concentration of diffusing species, but by the local concentration of diffusing species provided by the neighboring nanoparticles due to the close proximity of the Pt nanoparticles in the present model system [17,18]. To address the influence of the local nanoparticle configuration on the particle ripening, the observations in Fig. 5 will in the following be compared with predictions of ripening models incorporating local correlations in the atom-exchange process [19,20,25]. Specifically, Bartelt et al. established a local correlation framework for interface-controlled ripening [19,20], and Zheng and Bigot developed a framework for diffusion-controlled ripening [25]. Both frameworks are considered because interface- or diffusion-controlled ripening described the previous observations well.

For both models, the size-evolution of a particle i is calculated on the basis of the contribution to the concentration of atomic species from i's nearest neighbor particles. Here, we adopt the approach used by Bartelt et al. and define the nearest neighbors by the Voronoi construction [19,20]. In the Voronoi construction, the support plane is decomposed into cells in such a way that the Voronoi cell of particle i is obtained as the inner envelope of all line segments of points being equidistantly located between the centers of i and another particle [38]. Fig. 6 illustrates the Voronoi construction for an area of the present sample. The nearest neighbors of a particle i are those particles j with a Voronoi cell, which have a segment in common with the cell of i. Moreover, the Voronoi construction has a time-dependency, because cells vanish as the immobile, decaying particles eventually disappear (Fig. 6).

The interface-controlled ripening model derived by Bartelt et al. concerns two-dimensional islands [19,20]. Here, we consider a similar model for ripening of three-dimensional particles on a two-dimensional support based on the expression for the net flux of atomic species, J, onto the particle i [4]:

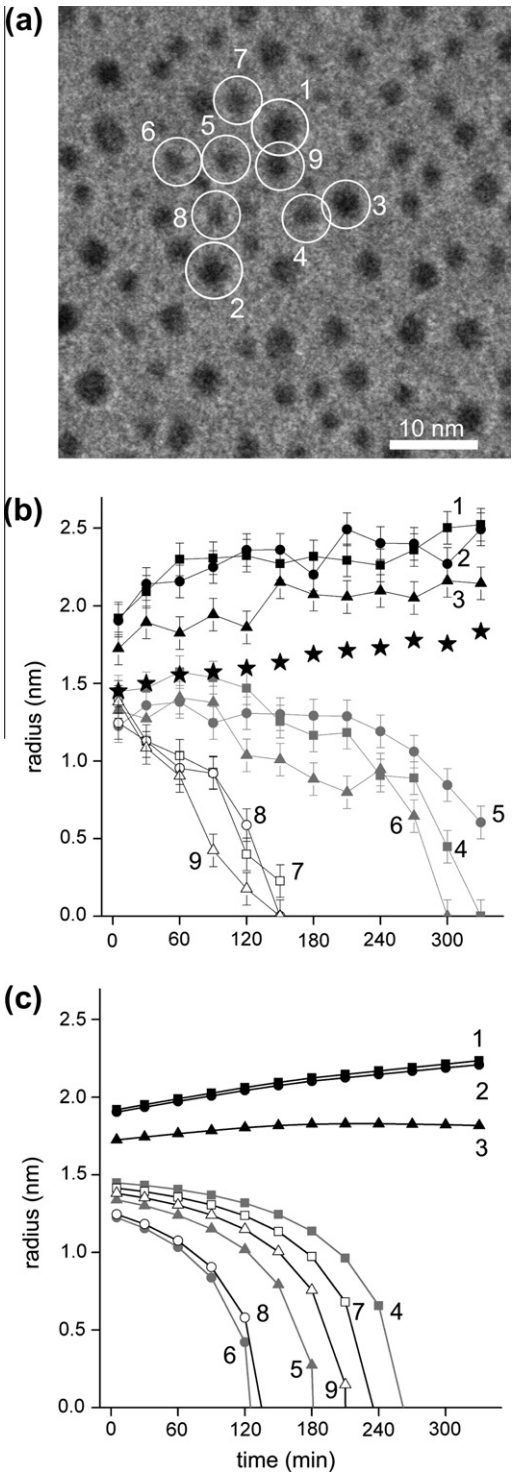

Fig. 5. (a) An outline of the nine selected particles in Fig. 2a (white circles). (b) The particle radii for the particles 1–9 (a) as a function of time in the experiment. The error bars indicate the estimated measurement errors. The mean radius for the whole TEM image (stars) is also presented. (c) Calculated time-dependent particle radii for the particles 1–9. The calculations used the interface-controlled ripening model based on the mean-field assumption (Eq. (2)).

$$J_i = 2\pi r_i a \beta(\rho_{local} - \rho_{r_i}) \tag{4}$$

Here, a is the inter-atomic spacing of Pt on the substrate at the particle edge, r_i the radius of particle i, and ρ the surface concentration of diffusing species, according to Eq. (1). For the diffusion rate $\beta = \nu \cdot \exp(-E_s/kT)$, ν is the vibrational frequency at the substrate sites, E_s the energy barrier for a Pt atom to jump from a support site to a particle edge site, k Boltzmann's constant, and T the temperature. ρ_{local} is the local surface concentration of atomic species, which only depends on i's nearest neighbor particles. The contributions to ρ_{local} from each nearest neighbor j are approximated by the mean of ρ_r for i and j, weighted by the opening angle, Φ_{ij}, of the Voronoi cell of particle i, (defined in Fig. 6):

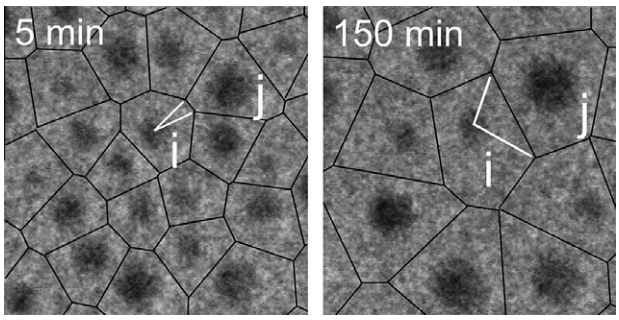

Fig. 6. The Voronoi construction (black lines) superimposed on a close-up on Fig. 2. For the Voronoi cell of particle i, the opening angle Φ_{ij} (indicated by white lines) with respect to the neighbor particle j is defined by the common line of the two adjacent cells with respect to the center of mass of particle i. i corresponds to particle No. 5 in Fig. 5.

$$\rho_{local} = \sum_j 1/2\left(\rho_{r_i} + \rho_{r_j}\right)\frac{\Phi_{ij}}{2\pi} \tag{5}$$

Thus, the model effectively operates with a "local" mean concentration of atomic species, determined by the nearest neighbor particles, contrary to the "global" mean-field concentration, which is spatially invariant and determined through the average particle size. The particle volume change rate can be calculated from Eqs. (4) and (5):

$$\frac{dV_i}{dt} = \Omega J_i \tag{6}$$

Here, Ω is the atomic volume of bulk Pt ($\Omega = 1.5 \cdot 10^{-2}$ nm^3). By Eq. (6), $r(t)$ can be calculated numerically for the particles 1–9 in Fig. 5, as described in detail in the following.

The diffusion-controlled ripening model developed by Zheng and Bigot is based on the following expression for the diffusion-limited flux from a particle i to a neighbor particle j [25]:

$$J_{ij} = \frac{2\pi D}{\ln(l_{ij}^2/r_i r_j)}(\rho_{r_i} - \rho_{r_j}) \tag{7}$$

Here, D is the surface diffusion constant for Pt diffusion on SiO_2 and l_{ij} the distance between the island centers. Thus, this model operates with a pairwise atom-exchange from a particle i to its neighbors j instead of describing the particle ripening as a result of the interaction with a local mean concentration of atomic species established by the neighbors. Here, we adopt the model by Zheng and Bigot and include the detailed neighborhood of nanoparticles by weighting the flux contribution by means of the Voronoi geometry. Thus, the change in volume of a given particle i can be described as:

$$\frac{dV_i}{dt} = -\Omega J_i = \sum_j J_{ij}\frac{\Phi_{ij}}{2\pi} \tag{8}$$

Here, Ω is the atomic volume of Pt and Φ_{ij} the opening angle of the Voronoi cell of particle i. As for Eqs. (6), also Eq. (8) allows $r(t)$ to be calculated numerically for the nine particles of Fig. 5.

The two ripening models presented here include correlations between neighboring particles with a weighting scheme based on the Voronoi construction. The Voronoi construction treats the particles as point sources or sinks for atomic species, so only the distances between the particle centers play a role. However, for the present model catalyst, the distances between the particles

were comparable with their sizes. As the exchange of Pt is considered to occur at the particle edges, the correlated ripening of particle i may therefore be expected to depend on both the separation and the size of the neighboring particles, j. Specifically, for a pair of neighboring particles of radii r_i and r_j and with a center separation l_{ij}, the inter-particle distance may be better represented by the distance between the edges $l_{ij} - r_i - r_j$ than l_{ij}. Moreover, for the exchange of atomic species, the particle i effectively interacts with sites at j's edge; the number of which scales with j's circumference $2\pi r_j$. Based on these considerations, an alternative weighting scheme is proposed in which the contributions to the correlated ripening of i are weighted by the ratio of the circumference of the neighbor particle j to the distance between the edges of the particles i and j. In the following, this scheme is referred to as the "size-dependent" weighting method and it is included in Eqs. (6) and (8) by the transformation:

$$\frac{\Phi_{ij}}{2\pi} \rightarrow \frac{2\pi r_j/(l_{ij} - r_i - r_j)}{\sum_{j'} 2\pi r_{j'}/(l_{ij'} - r_i - r_{j'})} \tag{9}$$

Here, j and j' denote particle i's nearest neighbors, as defined by the Voronoi construction and the sum in the denominator normalizes the weight factor.

Based on Eqs. 6, 8, and 9, the time-evolution of the radii of particles 1–9 (Fig. 5) can be calculated with four schemes based on the interface- or diffusion-controlled ripening models including local correlations based on the Voronoi or size-dependent weighting methods. Specifically, for each scheme, the $r_i(t)$ is calculated using the rate for volume change, dV_i/dt, an assumption of hemispherically shaped particles, and with initial radii corresponding to the measured radii at $t = 5$ min (Fig. 5b). The calculations progressed with time-steps of 30 min corresponding to the time-steps in the time-lapsed image series. The calculations rely on a determination of the surface energy γ and the parameters $\beta \cdot \rho_\infty$ (interface-controlled schemes) or $D \cdot \rho_\infty$ (diffusion-controlled schemes). Clearly, the models are more sensitive to changes of γ, due to the exponential dependency (Eq. (1)), than to the proportional dependency of $\beta \cdot \rho_\infty$ or $D \cdot \rho_\infty$. Therefore, to estimate these parameters for the four schemes, an iterative process was applied in which $r_i(t)$ is calculated for varying values of $\beta \cdot \rho_\infty$ or $D \cdot \rho_\infty$ for a fixed value of γ. The calculations were repeated with other values of γ, close to the surface energy of Pt ($\gamma = 2.1$ J/m^2 [39]), until the best fit to the data in Fig. 5b was obtained. The calculations show that the models are indeed very sensitive to γ and that the models only come close to the observations in Fig. 5b for $\gamma = 0.5$–0.6 J/m^2. The lower surface energy of the Pt nanoparticles compared with metallic Pt is expected as the Pt nanoparticles should be covered with oxygen [40–42]. DFT calculations suggest that the surface energy of the O-terminated Pt sites is ca. 0.4–1.2 J/m^2 [43]. Moreover, the best fit to the radius of particles 1–9 is obtained with the following parameters: For the interface-controlled ripening model, (a) $\gamma = 0.5$ J/m^2, $\beta \cdot \rho_\infty = 2.7$ s^{-1} nm^{-2} with Voronoi weighting and (b) $\gamma = 0.6$ J/m^2, $\beta \cdot \rho_\infty = 4.1$ s^{-1} nm^{-2} with size-dependent weighting. For the diffusion-controlled ripening model, (c) $\gamma = 0.5$ J/m^2, $D \cdot \rho_\infty = 1.4$ s^{-1} with Voronoi weighting and (d) $\gamma = 0.55$ J/m^2, $D \cdot \rho_\infty = 1.6$ s^{-1} with size-dependent weighting. Fig. 7a–d presents the calculated time-evolution of the particle radius for particles 1–9 of Fig. 5. The model parameters were found to give a good description of the growth and decay trends of nine additional particles at a different area of the model catalyst, which confirms the robustness of the fitting procedure.

Fig. 7 shows that all four schemes for correlated ripening capture the growth of the particles 1–3 as depicted in Fig. 5b. However, the schemes differ mainly in the description of the decay and disappearance of particles 4–9. For the interface-controlled model weighted by the Voronoi opening angle, Fig. 7a shows that only particles 5 and 7 disappear whereas particles 4, 6, 8, and 9 remain without significant change during the observation period. The interface-controlled model weighted by the size-dependent weighting method instead predicts that all particles (4–9) decay and vanish (Fig. 7b), as observed (Fig. 5b). In fact, the calculated decay for the particles 4, 6, 7, and 8 matches the observations quantitatively well. However, some deviation is also apparent: Particle 9 decayed faster in the experiment than according to the calculations, and the decay of particle 5 is better described by the Voronoi weighting scheme. For the diffusion-controlled model, as calculated using the Voronoi opening angle or the size-dependent weighting method, the trends for the decaying particles in Fig. 7c and d are similar to the calculated decay using the interface-controlled model in Fig. 7a and b, respectively.

For the present experimental conditions, the description of the time-evolution of the individual particles by the interface- and the diffusion-controlled ripening models, including either weighting scheme, is similar and can thus not be distinguished. However, the local correlations are shown to strongly affect the particle decay and the decay is strongly dependent on the weighting method. Specifically, the models, including the proposed size-dependent weighting method, match better most of the observed particle decays in Fig. 5b than the mean-field models, although deviations are apparent for the particles 5 and 9: A close inspection of the TEM images reveals that particle 5 was more distantly situated from smaller neighbor particles, which may explain why the Voronoi scheme gives a better description, and that particle 9 had one close and larger neighbor particle, which may explain why the size-dependent weighting method described the decay of this particle better. These considerations may suggest that the optimal weighting method depends on the detailed size and location of neighboring particles. Modeling the particle growth or decay may therefore intimately depend on the local conformation of the particle ensemble, and the lack of a generally applicable weighting scheme thus seems to complicate the detailed description of local correlation effects in ripening.

4. Discussion

The present *in situ* TEM observations of a Pt/SiO_2 model catalyst provide unique mechanistic and kinetic information on Pt nanoparticle ripening. This information enables a detailed comparison of the temporal evolution of the nanoparticle sizes with predictions made from different ripening models. Although the time-dependency of the nanoparticle sizes (Figs. 3–5) overall is well described by kinetic models based on the mean-field assumption, deviations are revealed at the individual nanoparticle level. The deviations are proposed to reflect that the atom-exchange in the growth or decay of the individual nanoparticles was influenced by the size and location of the neighboring nanoparticles due to the high particle density in the present model catalyst. Including such local correlations between the neighboring particles in the kinetic models gives a more satisfactory description of the individual nanoparticle sizes (Figs. 5 and 7). The effect of such local correlations is expected to also affect ripening in industrial catalysts with high particle density. Highly dense particle ensembles may result from the synthesis of catalysts with a high or inhomogeneous metal loading.

Although the kinetic behavior of the individual nanoparticles exposed a deviation from the mean-field ripening models, an ensemble property such as the particle size distribution is well described in that framework (Fig. 3). Due to the initial uniform particle density and highly monodispersed size of the Pt nanoparticles, it is possible that the ensemble properties average over a sufficiently large ensemble of different local configurations of nanoparticles to blur the distinct effect of the local correlations. Thus, for catalysts containing a more inhomogeneous nanoparticle

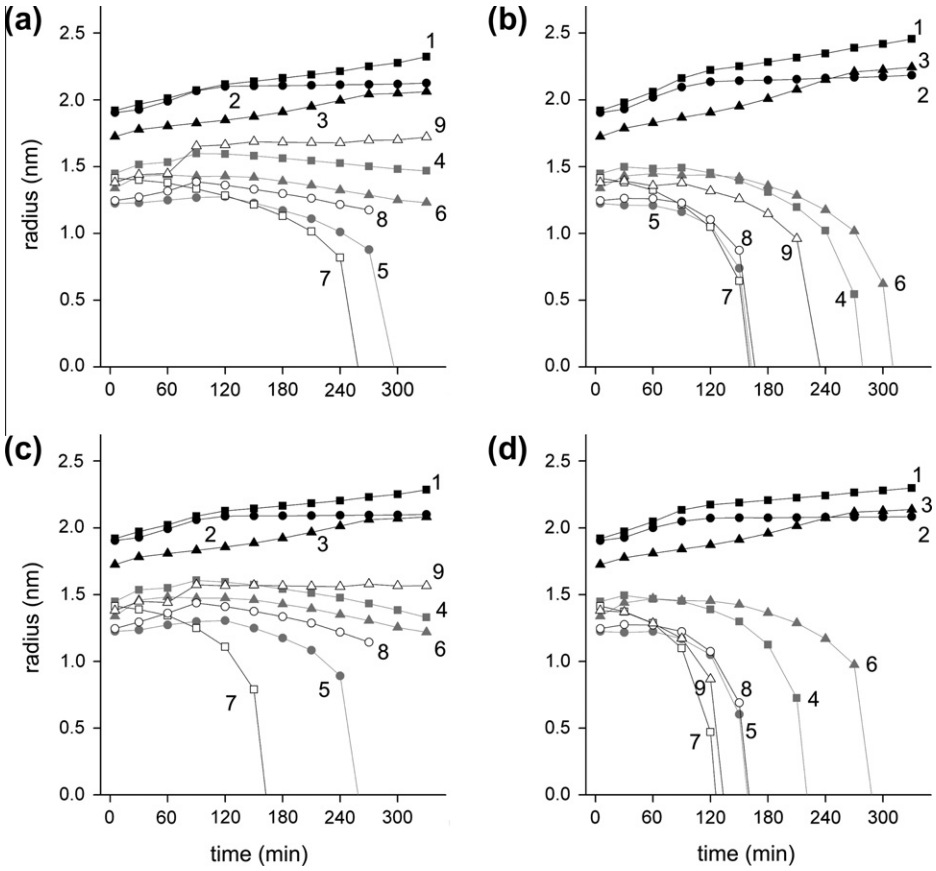

Fig. 7. (a–d) Calculated particle radii as a function of time. The calculations are based on (a and b) the interface-controlled and (c and d) the diffusion-controlled ripening model including local correlations in the atom-exchange process. The local correlations are included by (a and c) the Voronoi and (b and d) the size-dependent weighting methods.

ensemble, local correlations in ripening may be speculated to have a more distinct effect on the time-dependency of ensemble properties. The detailed relationship between the individual nanoparticle behavior and the ensemble properties could in principle be examined for the present model catalyst by integrating the results of an extended analysis similar to that presented in Fig. 5. Here, we limit the discussion to a basic description of local correlation effects in interface- and diffusion-controlled ripening.

The present work focuses on the mean-field assumption underlying the ripening models Eqs. (2) and (3) and has not addressed other assumptions of the models that could also be of importance. Common for the ripening models is the assumption of a homogeneous metal-support adhesion energy and a hemispherical nanoparticle shape. Although the flat and amorphous SiO_2 approaches a homogeneous support, the presence of surface inhomogeneities or defects cannot be excluded. Such features may result in an inhomogeneous metal adhesion with an impact on the concentration or diffusion of atomic species as well as on the shape and orientation of the metal nanoparticles [44–48]. These detailed structural features may also be important for determining the rates of nanoparticle growth or decay in the presence of a reactive gas environment [4,6,35]. The TEM images generally show a similar contrast level of particles with similar size as well as a uniform contrast over the support. A detailed interpretation of the image contrast is, however, complicated by the projection geometry and the convolution of mass-thickness and diffraction contrast phenomena. The present TEM images are therefore likely insensitive to surface inhomogeneities at the atomic-level.

Furthermore, the ripening models are applied irrespective of the nanoparticle sizes in the present analysis. As Pt nanoparticles with a radius below 0.5 nm contain less than 30 atoms, the geometrical surface curvature is not a well-defined parameter. In this size-regime, the Gibbs–Thomson relation (Eq. (1)), being a continuum model, breaks down per definition. Thus, although the size-dependency reflected by Eq. (1) is generally accepted to be valid for larger particles, it is likely insufficient for the smallest particle sizes [9,13,22,49]. The size-dependent ripening of the smallest particles has been subject to debate: Datye et al. emphasized that, even within the Gibbs–Thomson model, Eqs. (2) and (3) are imprecise for small particles because the equations rely on a first-order Taylor expansion of Eq. (1) [9]. The models, Eqs. (4) and (7), apply Eq. (1) directly and should thus better describe the smaller particles. For a particle sufficiently smaller than r^*, Yang et al. suggested that dr/dt is determined by the particle's own chemical potential and is thus less dependent on the neighbor particle configuration resulting in an accelerated decay trend of the smallest particles described by the exponential Gibbs–Thomson relation (Eq. (1)) [22]. A faster decay of small particles will also happen if the surface energy increases with decreasing particle size, as suggested by Campbell et al. [12]. For the present study, a part of the smallest particles revealed in fact an almost linear decay of the particle radius with time, e.g., particle 7 and 9 in Fig. 5b, contrary to the accelerated decay rate predicted by the exponential term in Eq. (1) (Figs. 5c and 7a–d). For 50 additional particles with a radius below ca. 1 nm, a similar linear decay was observed for about half of these particles in the present experiment. It remains to be addressed if this observed linear particle decay can be accounted for by a size-dependent surface energy of the nanoparticles. Modeling the surface energy may be further complicated by the size-dependent surface oxidation of the Pt nanoparticles [40–42].

5. Conclusions

By means of *in situ* TEM, the sintering of Pt nanoparticles dispersed on a planar SiO_2 support was monitored during the exposure to 10 mbar synthetic air at 650 °C. A time-lapsed image series shows that the nanoparticle sintering was dominated by Ostwald ripening and provides detailed information about the nanoparticle growth or decay. Specifically, the time-dependent particle size distributions, the nanoparticle growth rates and the time-evolution in nanoparticle sizes, are found to be overall well described by kinetic models based on a mean-field assumption for the atomic species mediating diffusion-controlled or interface-controlled ripening. However, for the individual nanoparticles, deviations are observed from the mean-field model predictions. Due to the high particle density, it is suggested that the nanoparticle ripening is influenced by the size and location of the neighbor particles. Ripening models including such local correlations in the so-called Voronoi and size-dependent weighting schemes are established and shown to describe well the observed time-evolution of individual nanoparticle sizes.

Acknowledgements

We gratefully acknowledge Bengt Kasemo, Jonas Andersson, Elin Larsson and Laurent Feuz (Chemical Physics Group) as well as Eva Olsson (Microscopy and Microanalysis Group) at Chalmers University of Technology for contributing to sample preparations. We thank the MC2-Access project for financial support. We acknowledge Lone Beck and John Larson (CINF) at Technical University of Denmark for help with the XPS analysis. We acknowledge the participation of the CTCI Foundation, Taiwan, in the establishment of the *in situ* TEM facility at Haldor Topsøe A/S. CINF is funded by The Danish National Research Foundation.

Appendix A. Supplementary material

Supplementary data associated with this article can be found, in the online version, at doi:10.1016/j.jcat.2011.04.011.

References

[1] A.T. Bell, Science 299 (2003) 1688.
[2] Y. Li, G. Somorjai, Nanolett. 10 (2010) 2289.
[3] J.A. Moulijn, A.E.v. Diepen, F. Kapteijn, in: G. Ertl, H. Knözinger, F. Schüth, J. Weitkamp (Eds.), Handbook of Heterogeneous Catal, 2nd Ed., vol. 4, Wiley-VCH Verlag GmbH & Co KGaA, Weinheim, 2008. Chapter 7.
[4] P. Wynblatt, N.A. Gjostein, Prog. Solid State Chem. 9 (1975) 21.
[5] C.H. Bartholomew, Appl. Catal. A 212 (2001) 17.
[6] S.E. Wanke, P.C. Flynn, Catal. Rev. Sci. Eng. 12 (1975) 93.
[7] B.K. Chakraverty, J. Phys. Chem. Solids 28 (1967) 2401.
[8] R. Finsy, Langmuir 20 (2004) 2975.
[9] L.R. Houk, S.R. Challa, B. Grayson, P. Fanson, A.K. Datye, Langmuir 25 (2009) 11225.
[10] A.K. Datye, Q. Xu, K.C. Kharas, J.M. McCarty, Catal. Today 111 (2006) 59.
[11] C.G. Grandqvist, R.A. Burhman, J. Catal. 42 (1976) 477.
[12] C.T. Campbell, S.C. Parker, D.E. Starr, Science 298 (2002) 811.
[13] S.E. Wanke, J. Catal. 40 (1977) 234.
[14] E. Ruckenstein, D.B. Dadyburjor, J. Catal. 48 (1977) 73.
[15] S.D. Coughlan, M.A. Fortes, Scr. Metall. Mater. 28 (1993) 1471.
[16] G.A. Fuentes, E. Salinas-Rodríguez, in: J.J. Spivey, G.W. Roberts, B.H. Davis (Eds.), Studies in Surface Science and Catalysis, vol. 139, Elsevier, Amsterdam, 1991, p. 503.
[17] P.W. Voorhees, J. Stat. Phys. 38 (1985) 231.
[18] D.B. Dadyburjor, S.P. Marsh, M.E. Glicksman, J. Catal. 99 (1986) 358.
[19] W. Theis, N.C. Bartelt, R.M. Tromp, Phys. Rev. Lett. 75 (1995) 3328.
[20] N.C. Bartelt, W. Theis, R.M. Tromp, Phys. Rev. B 54 (1996) 11741.
[21] K. Morgenstern, G. Rosenfeld, G. Comsa, Surf. Sci. 441 (1999) 289.
[22] F. Yang, M.S. Chen, D.W. Goodman, J. Phys. Chem. C 113 (2009) 254.
[23] S.B. Simonsen, I. Chorkendorff, S. Dahl, M. Skoglundh, J. Sehested, S. Helveg, J. Am. Chem. Soc. 132 (2010) 7968.
[24] M. Chen, L.D. Schmidt, J. Catal. 55 (1978) 348.
[25] X. Zheng, B. Bigot, J. Phys. II (France) 4 (1994) 743.
[26] A.W. Grant, Q.-H. Hu, B. Kasemo, Nanotechnology 15 (2004) 1175.
[27] C.D. Wagner, W.N. Riggs, L.E. Davis, J.F. Moulder, in: G.E. Muilenberg (Ed.), Handbook of X-ray Photoelectron Spectroscopy, Perkin-Elmer Corporation, Minnesota, 1979, p. 52.
[28] P.L. Hansen, A.K. Datye, S. Helveg, Adv. Catal. 50 (2006) 77.
[29] R.T.K. Baker, C. Thomas, R.B. Thomas, J. Catal. 38 (1975) 510.
[30] T.A. Dorling, R.L. Moss, J. Catal. 5 (1966) 111.
[31] T.A. Dorling, B.W.J. Lynch, R.L. Moss, J. Catal. 20 (1971) 190.
[32] T.J. Lee, Y.G. Kim, J. Catal. 90 (1984) 279.
[33] W. Zou, R.D. Gonzalez, Appl. Catal. A 102 (1993) 181.
[34] P. Lööf, B. Stenbom, H. Nordén, B. Kasemo, J. Catal. 144 (1993) 60.
[35] C.H. Bartholemew, in: J.J. Spivey, S.K. Argarwal (Eds.), Catalysis – A Specialist Periodical Report, vol. 10, Athenaeum Press Ltd., Newcastle upon Tyne, 1993. Chapter 2.
[36] Y.D. Smet, L. Deriemaeker, R. Finsy, Langmuir 13 (1997) 6884.
[37] P.C. Flynn, S.E. Wanke, J. Catal. 34 (1974) 400.
[38] G. Voronoi, J. Reine, Angew. Math. 134 (1908) 556.
[39] M. McLean, E.D. Hondros, J. Mater. Sci. 6 (1971) 19.
[40] P. Lööf, B. Kasemo, L. Björnkvist, S. Andersson, A. Frestad, in: A. Crucq (Ed.), Studies in Surface Science and Catalysis, vol. 71, Elsevier, Amsterdam, 1991, p. 253.
[41] C.-B. Wang, H.-K. Lin, S.-N. Hsu, T.-H. Huang, H.-Chi. Chiu, J. Mol. Catal. A 188 (2002) 201.
[42] R.W. McCabe, C. Wong, H.S. Woo, J. Catal. 114 (1988) 354.
[43] N. Seriani, W. Pompe, L.C. Ciacchi, J. Phys. Chem. B 110 (2006) 14860.
[44] R. Hardeveld, F. Hartog, Surf. Sci. 15 (1969) 189.
[45] L. Wand, A. Roudgar, M. Eikerling, J. Phys. Chem. C 113 (2009) 17989.
[46] Z. Sljivancanin, B. Hammer, Surf. Sci. 515 (2002) 235.
[47] J.H. Kwak, J. Hu, D. Mei, C.-W. Yi, D.H. Kim, C.H. F Peden, L.F. Allard, J. Szanyi, Science 325 (2009) 1670.
[48] P.L. Hansen, J.B. Wagner, S. Helveg, J. Rostrup-Nielsen, B.S. Clausen, H. Topsøe, Science 295 (2002) 2053.
[49] S.C. Parker, C.T. Campbell, Phys. Rev. B 75 (2007) 035430.

Paper III

Effect of particle shape on the ripening of supported Pt nanoparticles

Søren B. Simonsen[1,2], Ib Chorkendorff[2], Søren Dahl[2], Magnus Skoglundh[3], Kristoffer Meinander[4], Thomas N. Jensen[4], Jeppe V. Lauritsen[4], and Stig Helveg[1,]*

[1]Haldor Topsøe A/S, Nymøllevej 55, DK-2800 Kgs. Lyngby, Denmark, [2]CINF, Department of Physics, Technical University of Denmark, DK-2800 Kgs. Lyngby, Denmark, [3]Competence Centre for Catalysis (KCK), Chalmers University of Technology, SE-41296, Göteborg, Sweden and [4]Interdisciplinary Nanoscience Center (iNANO), Aarhus University, DK-8000 Aarhus C, Denmark

*Address correspondence to sth@topsoe.dk

RECEIVED DATE

ABSTRACT: Sintering of nanoparticles is one main cause of catalyst deactivation. Nanocatalysts exploiting strong size- or shape-dependent catalytic properties rely completely on a stable nanoparticle morphology, and research aimed at understanding the fundamental principles of nanoparticle sintering is therefore needed to advance the development of novel nanocatalysts with enhanced long-term stability. To provide fundamental understanding of the prevailing sintering processes in a model system for diesel and lean-burn engine exhaust aftertreatment catalysts, we here present results from oxygen-induced sintering of Pt nanoparticles dispersed on a planar Al_2O_3 support. The analysis of images from scanning transmission electron microscopy (STEM) and atomic force microscopy (AFM) suggest that the Pt nanoparticles have size-dependent three-dimensional (3D) shapes on the Al_2O_3 substrate after sintering in an oxidizing environment, because the results are consistent with a decreasing height-to-diameter ratio for increasing particle diameters. To relate the observed size-dependence of the particle shape to the ripening process, particle size distributions (PSDs) were extracted from transmission electron microscopy (TEM) images and presented as a function of ageing temperature. The PSDs are compared with computer simulations based on a simple kinetic model for ripening, and the comparison shows that the size-dependence of the particle shape offers an explanation for the observed bimodal PSD forms.

KEYWORDS: Particle shape, sintering, Ostwald ripening, nanoparticles, Pt, Al_2O_3, TEM, STEM, AFM.

The physicochemical properties of a nanoparticle may strongly depend on its size, shape and composition [1]. For application as heterogeneous catalysts, the nanoparticle edges and kinks often play an important role for the catalytic activity and these sites are predominant for the smallest nanoparticles [1-3]. To preserve the active sites and to avoid loss of the total surface area of the catalytically active phase, it is important to stabilize the supported nanoparticles, with sizes of a few nanometers, during operational conditions at often high temperatures in the relevant gas environments [4].

Although a variety of techniques allow well-defined nanoparticles to be synthesized, the nanoparticles are inherently unstable due to their high surface area and thus there is a thermodynamic drive for coarsening of the nanoparticles [5-8]. A vast amount of the published coarsening studies has focused on the evolution of the nanoparticle sizes as a function of time and process conditions [5-20]. A prototypical nanocatalyst system for studying coarsening consists of Pt nanoparticles supported on an Al_2O_3 material

which is relevant as an oxidation catalyst in diesel and lean-burn engine exhaust after-treatment technologies. Previous microscopy studies demonstrated that Pt nanoparticles on Al_2O_3 coarsen via the Ostwald ripening mechanism in oxidizing environment [13,21,22]. In the Ostwald ripening process, atomic species are exchanged among immobile nanoparticles driven by a difference in the chemical potential of atoms in the nanoparticles with different radius of curvatures, as described by the Gibbs-Thomson equation. Nanoparticles with a larger or smaller radius of curvature have a lower or higher chemical potential, respectively, which results in a net mass-transport from the smaller to the larger nanoparticles [5-8].

In addition to the metal nanoparticle size, the shape and metal-support interactions have also been addressed for heterogeneous catalysts [12,13,23-27]. However, no experimental studies have addressed the detailed influence of the 3D geometrical shape of the supported nanoparticles on the ripening process, although Wynblatt and Gjostein, in their pioneering work [6], emphasized that the growth/shrinkage rate of individual nanoparticles depends on the particle radius of curvature, the surface-to-volume ratio and the perimeter of the particle-support interface.

In this paper we address the effect on ripening of the shape of Pt nanoparticles supported on a planar, amorphous Al_2O_3 substrate. The evolution in the form of the PSD is determined with TEM as a function of ageing temperature after thermal ageing in air. Characterization by STEM and AFM suggests that the Al_2O_3-supported Pt nanoparticles adopt size-dependent 3D shapes after thermal ageing. Specifically, it is suggested that the height-to-diameter ratio surprisingly decreases with the nanoparticle size. The relationship between the form of the PSDs and the shape of the nanoparticles is discussed in the light of a simple kinetic model for ripening, and it is shown that the observed evolution of the form of the PSD can be simulated when the size-dependence of the height-to-diameter ratio is taken into account. The analysis proposes an explanation for the previously reported time-dependent evolution in PSD forms of Al_2O_3-supported Pt nanoparticles when aged thermally in air [21].

RESULTS AND DISCUSSION

The planar Pt/Al_2O_3 model catalysts were aged in a tube furnace in 1 bar 0.2 % O_2 in N_2 for 3 hours at 450 °C, 550 °C, 600 °C or 650 °C. Figure 1a-e shows TEM images of the as-prepared and the aged samples. In the TEM images, the Pt nanoparticles are identified as the darker contrast features and the planar, amorphous Al_2O_3 support is associated with the brighter areas. In the as-prepared state, the Pt nanoparticles appear almost mono-dispersed with a homogeneous distribution over the support area (fig. 1a). The TEM images reveal that the thermal ageing resulted in an increase of the mean particle size and in a reduction of the particle density (fig. 1b-e). These changes can be observed at ca. 600 °C in agreement with [5,7,8,11,14,18,22,28,29].

Figure 1f-j presents PSDs extracted from the TEM images corresponding to the ageing conditions in figure 1a-e. In the as-prepared samples, the Pt nanoparticles have a mean projected diameter of 2.7 nm. After ageing at 600 °C, the PSD is asymmetric with a remarkable shoulder to the large particle side of the main peak (fig. 1i). After ageing at 650 °C the asymmetric PSD form has flipped over so that the main peak is associated with a tail towards the smaller particle sizes (fig. 1j).

Ripening is often described by the so-called Lifshitz-Slyozov-Wagner (LSW) model [30,31]. A LSW model, which is modified to describe a two-dimensional system [32], is fitted to the PSD at 650 °C in fig. 1j and found to describe the PSD form well. The agreement is expected since the Al_2O_3 support is planar and homogeneous which closely matches the assumptions of the LSW model. Thus the PSD shape after ageing at 650 °C is therefore consistent with the ripening mechanism. On the contrary, the form of LSW-distribution will obviously not fit the PSD form at 600 °C or below well (fig. 1i), which suggests a non-trivial ripening mechanism. Our previous *in situ* TEM study of the same type of Pt/Al_2O_3 model catalyst in 10 mbar air at 650 °C showed that ripening leads to a temporal evolution of the PSD forms similar to those presented in figure 1f-j [21]. Specifically, as a function of ageing time, a transition shifted the initial monodispersed PSD form into a form, characterized by the appearance of a shoulder to the large particle side of the main peak, and subsequently into a form with a tail to the small particle side of the main peak, which was described by the LSW-model [21]. The present *ex situ* and the previous

in situ results therefore show that ripening leads to the characteristic LSW-form and that the transition forms involved are unexpected bimodal PSD forms, which can not directly be explained by the LSW theory. The apparent discrepancy between the observations and theory may result from the assumption in the theoretical model of a constant 3D shape for all particle sizes, whereas a size-dependent nanoparticle shape is observed in the experiments, which may influence the ripening process [6].

To estimate the 3D shape of the individual Pt nanoparticles, STEM images of the samples were acquired. Figure 2a presents a STEM image of the sample after thermal ageing at 650 °C, where the particles can be identified as the bright area projections and the oxide support corresponds to the larger black area. Since the integrated STEM signal intensity from a nanoparticle corresponds to the nanoparticle volume [33,34], any size-dependent variation in the shape of the supported Pt nanoparticles can directly be revealed from a plot of the nanoparticle intensity versus diameter. In figure 2b, the STEM signal intensity for individual nanoparticles is presented in arbitrary units as a function of their diameter. The relation between the particle volume and diameter depends on the exact 3D particle shape. Since the 3D shape of the Al_2O_3-supported Pt nanoparticles is not known *a priori*, a spherical cap is here used as a tentative approximation to the nanoparticle shape. The spherical cap represents a shape that is uniquely defined by one descriptor, namely by a metal-support contact angle, θ, or alternatively by the ratio of the particle height and diameter, *h/d* (defined in the insert of figure 2a). The volume of a spherical cap with a constant height-to-diameter ratio as a function of the particle size is fitted to the experimental observations in figure 2b (dashed black) by varying the constant C and shape factor (fig. 2, figure caption) until the total square difference between the modeled and measured data is minimized, resulting in $R^2 = 0.95$. Figure 2b shows that the volume of a spherical cap with a constant shape increases faster with the diameter than the volume of the observed Pt nanoparticles. The shape of the observed particles is therefore not fully consistent with a spherical cap with a constant height-to-diameter ratio for all particle sizes. One explanation for this difference is that the height-to-diameter ratio for the observed particles decreases with increasing particle diameter. However, since the calibration constant, *C* (fig. 2, figure caption) relating the particle volume to the STEM signal intensity is unknown, the true relation between the particle heights and diameters cannot be determined from figure 2b alone.

To directly measure the absolute heights of the nanoparticles, AFM measurements have been performed under ultra-high vacuum (UHV) conditions. An AFM image recorded of the sample after thermal ageing at 650 °C is presented in figure 3a. In the image, the AFM tip height relative to the oxide support is depicted by a grey scale in such a way that the Pt nanoparticles are identified as brighter protrusions on the darker background corresponding to the Al_2O_3 support. The significantly larger (> 20 nm), bright features represent impurities on the surface, possibly induced during sample transfer to the UHV chamber of the AFM. Pt nanoparticles at or in close vicinity of such regions were avoided in the data analysis. By individually measuring the height and width of all particles in the AFM images the cluster dimensions were obtained and presented in fig. 3 as the particle height distribution (PHD) (b) and the PSD (c).

The particle diameters measured by AFM (fig. 3c) are generally larger relative to the diameters as measured by TEM (fig. 1j). This difference can be attributed to the well-known effect of tip broadening in AFM for objects with a size comparable to the tip apex dimensions. Therefore, in order to obtain a direct correlation plot of the nanoparticle heights vs. the diameters, the PSD measured by AFM was aligned with the analogous PSD from TEM. The alignment was performed by minimization of the total squared difference between the column heights in the PSDs from AFM and TEM and obtained by the multiplication by a factor 0.7 and the subtraction of the value 2.4 nm (figure 4a). This overestimate of the cluster width of 2.4 nm (2 x 1.2 nm) is in good correspondence with the value expected from the nominal width of the carbon nanotube AFM tips of ca. 1 nm. The effect of AFM tip broadening is graphically illustrated in figure 4b, which shows circles superimposed on the particle positions in a TEM image corresponding to the non-calibrated AFM diameters. Figure 4b serves to illustrate that the broadening is sufficiently small to allow the detection of small particles in the vicinity of larger ones. Figure 4c presents the final plot for the particle height as a function of the nanoparticle diameters

corrected for tip broadening. Interestingly, the majority of the data points lies in the region between the lines corresponding to a spherical (full grey) and a hemispherical (dashed grey) particle shape (fig. 4c). The Al_2O_3-supported Pt nanoparticles are therefore generally flatter than spheres, but higher than hemispheres. Assuming a linear height-to-diameter relation as a first approximation, two straight lines can be fitted to the data: one which is unconstrained (full black) for which $R^2 = 0.48$ and one which is constrained through the origin (dashed black) for which $R^2 = 0.46$. From the fitted lines in figure 4c the size-dependent height-to-diameter ratio was calculated and presented in figure 4d (full black and dashed black). The unconstrained fitted line corresponds to a height-to-diameter ratio that indeed decreases as a function of particle size, reflecting a size-dependent Pt nanoparticle morphology. The AFM data does not describe the height-to-diameter ratio for particle sizes below 2 nm (fig. 4c-d). Extending the unconstrained fit in figure 4c below the limit of 2 nm will result in a height-to-diameter ratio > 1 for diameters < 2 nm, which seems unreasonable. It is therefore more likely that the height-to-diameter ratio is constant for the smallest particle sizes. For the constrained fit, the line corresponds to a constant height-to-diameter ratio for all particle sizes. Since both the unconstrained and the constrained line fits describe the data almost equally well, the AFM results indicate a size-dependence of the height-to-diameter ratio as a possibility. For comparison with the STEM data, the volume of a spherical cap including the size-dependent height-to-diameter ratio, corresponding to the unconstrained fitted line in figure 4d, is fitted to figure 2b (full black) resulting in $R^2 = 0.96$. Similarly, the constrained fitted line in figure 4d corresponds to the previously fitted volume of a spherical cap with constant height-to-diameter ratio (figure 2b (dashed black)). The nanoparticle volume, including the size-dependent height-to-diameter ratio, fits the STEM data slightly better than the fitted volume corresponding to the constant nanoparticle shape. The difference between the two fits based on the AFM data seems relatively small (fig. 2b), compared to the trend of the STEM data which indicates a stronger size-dependence of the nanoparticle shape (fig. 4c). To demonstrate the stronger size-dependence as observed by STEM, the volume of a spherical cap was again fitted to the STEM data (fig. 2b), assuming a linear relation between the height and diameter, but in this case with an unconstrained slope and a $h/d = 1$ for $d = 2$ nm, consistent with the unconstrained fit to the AFM data. The fit is optimized by varying the slope of the linear height-to-diameter relation until the total squared difference between the modeled and measured data points was minimized. The resulting fit to the STEM data has $R^2 = 0.99$ and is indicated by the black dotted line in figure 2b. The stronger size-dependence of the height-to-diameter relation according to the STEM data can be appreciated by re-plotting the black dotted line from figure 2b in figure 4d (black dotted line). In summary, the combined STEM and AFM data suggests that the Al_2O_3-supported Pt nanoparticles generally are flatter than spheres and that the height-to-diameter ratio decreases with the particles size, although the two data sets differ on the degree of the size-dependence of the height-to-diameter ratio.

A size-dependence of the shape of the supported Pt nanoparticles may influence the ripening process in several ways. Firstly, the observed growth or shrinkage of the projected nanoparticle areas in the TEM images depends on the nanoparticle volume which is described in terms of the height-to-diameter ratio. Secondly, different nanoparticle shapes imply that the nanoparticle perimeter at the Pt-oxide interface, and thus the total number of sites that can emit or absorb diffusing species, varies. Thirdly, the nanoparticle shape influences the concentration of atomic species via the Gibbs-Thomson relation, which depends on nanoparticle surface curvature. To address how size-dependent nanoparticle shapes may influence ripening, a simple description is considered in the following, based on the mean-field kinetic model for interface-controlled ripening [6]:

$$\frac{dR}{dt} = \alpha \frac{\alpha'}{R^2}\left(\frac{R}{R*} - 1\right) \qquad \text{eq. 1}$$

Here the shape of each particle is approximated by a spherical cap where R is the radius of curvature (defined in the insert of figure 2a) and $\alpha = \sin(\theta)/(1/2 - 3/4\cos(\theta) + 1/4\cos^3(\theta))$ is the geometrical factor

in which the particle shape is defined by the metal-oxide contact angle, θ. α' describes the system specific parameters, such as the diffusion energy barriers for crossing the metal-support interface as well as the metal surface energy, the atomic volume and the temperature. R^* is the critical radius of curvature corresponding to the particle size which is in equilibrium with the mean-field concentration of diffusing atomic species [6,20]. Based on eq. 1, the evolution of the PSD can be simulated for varying α and α'.

Two simulations are performed: In the first simulation α is set to capture the main trends of the size-dependence of the height-to-diameter ratio, resulting from the unconstrained linear fit to the AFM data, by using a continuous height-to-diameter-trace corresponding to the grey dotted line in fig. 4d. This trace, which resembles the AFM data rather than the STEM data, was chosen to examine the effect of the least size-dependent variations in the height-to-diameter ratio. In the second simulation, α has a constant value identical to the dashed black line in figure 4d, corresponding to the constrained linear fit to the AFM data. To fixate the time-scale in the simulations, α' is adopted so that the final mean nanoparticle diameter corresponds to that observed after 3 hours ageing at 650 ºC. The time steps in the simulation corresponds to units of $\alpha'^{-1} \cdot nm^3$. In the model eq. (1), time couples to temperature through α' in such a way that a long simulated ageing time (many calculation steps) at a low temperature corresponds to a short ageing time (few calculation steps) at a higher temperature. Since R^* in eq. 1 equals the mean radius of curvature [35], this parameter is equaled to the arithmetic mean of R for the particle ensemble in the simulations. The PSD corresponding to the as-prepared Pt/Al_2O_3 sample (fig. 1f) was used as the initial PSD for the simulations. Figure 5a-c presents the simulated PSDs based on the size-dependent height-to-diameter ratio. Here, the initial PSD evolves via bimodal forms, with an additional peak towards the larger particle sizes, into a form of the LSW-type having a main peak shifted towards the large particle sizes and with a tail towards the small sizes (fig. 5a-c). As time and temperature are linked in the simulations, i.e. the effect of temperature can be compensated for with time, it is thus intriguing that the simulated time-evolution in the PSD form matches the experimental evolution as a function of temperature. Similarly, the simulated PSD forms match the experimental time-dependent observations in a previous in situ TEM study of the same type of Pt/Al_2O_3 [21]. In comparison, figure 5d-f presents the simulated PSDs based on the constant height-to-diameter ratio. In this case, the PSDs are characterized by a single peak that gradually shifts toward larger nanoparticle size and by the appearance of a tail toward smaller nanoparticle sizes as the ageing time increases. The transition of the PSD toward the LSW-form does not indicate any development of an additional peak. Thus, according to the simulations in figure 5, the additional peak in the PSD therefore only develops for the particles with a size-dependent height-to-diameter ratio.

In the spherical cap approximation for the 3D nanoparticle shape, a size-dependence of the height-to-diameter ratio corresponds to a size-dependent degree of wetting. It has previously been reported that surface defects at an alumina support can influence the morphology of the supported nanoparticles [36]. A physical reason for a size-dependent wetting could therefore be speculated to result from a dependence of the interaction with support defects on the nanoparticle size, but the present observations do not directly address this possibility. Describing the nanoparticle shape by a single parameter such as the contact angle alone may be an oversimplified approximation and shapes described by additional parameters could be considered. One such example is the spherical cap combined with a metal layer in the interface between the spherical cap and the oxide support. The existence of such an interface layer has been reported for Cu-supported Ag nanoparticles [37]. With this model the observed size-dependence of the height-to-diameter ratio can be described by a constant height of the interface layer while maintaining a constant contact angle. The presented STEM (fig. 2b) and AFM (fig. 4c) data can be fitted equally well using this two-parameter shape description as using the single parameter description. Similarly, additional simulations based on the two-parameter model reproduce the trends in the evolution of the PSD form as for the single parameter description, although the additional peak towards the large particle side of the main peak is less pronounced. The presence of such alternative nanoparticle shapes cannot be excluded and it will require further nano-scale tomographic investigations in order to determine the detailed 3D nanoparticle shape. Moreover, the shape estimation based on STEM may also be slightly affected by a size-dependent Pt surface oxidation of the nanoparticles [38,39], that would result

in a size-dependent change of the mass-thickness contrast. However, as the Pt nanoparticles are at the highest surface oxidized under the present conditions, this effect should be of minor importance.

In conclusion, by combining STEM and AFM measurements, we have shown that Pt nanoparticles supported on Al_2O_3 sinter in an oxidizing environment and adopt size-dependent. Specifically, the measurements suggest that the nanoparticles are generally flatter for the larger nanoparticle sizes. The relationship between nanoparticle ripening and shape is discussed in the light of a kinetic model for ripening, which indeed shows that the PSD forms after ripening are influenced by the size-dependent 3D shape of the supported nanoparticles. The size-dependence of the supported nanoparticle shape therefore offers a possible explanation for the bimodal forms in transition of the PSD toward the LSW-form.

METHODS

The Pt/Al_2O_3 model catalysts consisted of Pt nanoparticles dispersed on a flat, amorphous Al_2O_3 support. The catalysts were supported on Si wafers with amorphous and electron transparent Si_3N_4 windows. Preparation details are described in ref. [21].

A series of thermal ageing experiments at the temperatures 450 °C, 550 °C, 600 °C and 650 °C were carried out with the Pt/Al_2O_3 samples in 0.2 % O_2 in N_2 with a total pressure of 1 bar and a flow of 120 ml/min by using a tube furnace (Carbolite CFT). In the experiments, the samples were placed in a porcelain boat in the centre of the tube furnace. By using an ADM2000 universal gas flowmeter (Agilent Technologies), the gas flow was set at room temperature and it was confirmed after the sintering experiment as room temperature again was reached. After the establishment of the gas flow, the furnace was heated by 5 °C/min until the ageing temperature was reached. After 3 hours at the ageing temperature, the furnace was cooled down by turning off the furnace resulting in a cooling rate of ca. -2 °C/min for the first 200 °C. The furnace temperature was measured with an estimated error of ± 7 °C as determined by inserting an additional thermocouple in the tube furnace near the sample in one experiment.

TEM was performed by using an image aberration corrected Titan 80-300 SuperTwin transmission electron microscope (FEI Company) operated at 300 kV with an information limit of ca. 0.10 nm. TEM images were acquired using bottom-mounted 2k x 2k CCD cameras at magnifications corresponding to pixel sizes of 0.09 nm. From the TEM images, Pt particle sizes (diameters) were measured by using a circular approximation to their projected area. The measurements were performed automatically as described in ref. [21]. The estimated measuring error is a systematic error of 10 % of the particle diameters due to calibration of the TEM and a random error of 0.5 nm for all particle diameters due to the automatic image analysis.

The STEM characterization was performed using a Titan 80-300 electron microscope. The microscope was operated at 300 kV and with an electron probe size less than 0.23 nm, as calibrated towards the Pt(111) lattice fringe spacing. A high-angle annular dark field (HAADF) detector was used to collect scattered electrons and ensure high contrast of the Pt nanoparticles. Images were recorded at a magnification corresponding to a pixel size of 0.16 nm. Furthermore all images were recorded with the same contrast and brightness level for proper comparison of different images. From the STEM images, the particle diameters were measured as described for the TEM images. The nanoparticles' signal intensity was integrated over the projected area corresponding to each particle and the signal contribution from the background generated by the support material was subtracted.

Non-contact atomic force microscopy (NC-AFM) was performed at room temperature on the Pt/Al_2O_3 sample after thermal ageing at 650 °C in an UHV chamber with a base pressure below 1×10^{-10} mbar using a beam deflection NC-AFM described in [40]. The very sensitive non-contact operation mode of the AFM was chosen in order to minimize tip-induced movements of the nanoparticles. The sample was fixed on a standard Ta sample plate and introduced to the UHV chamber through a vacuum load lock. No further sample processing was performed. The NC-AFM images were recorded in the topography mode by keeping the mean frequency shift (Δf), due to the tip-surface interaction, constant relative to a preset frequency shift value and recording the feedback signal of the tip-surface distance control as it traces the surface. A voltage was applied to the tip, relative to the sample holder, U_{bias}, which was

adjusted to minimize the electrostatic forces arising from the contact potential difference [41]. To optimize the AFM resolution and to reduce the risk of mechanically pushing the clusters, we used the high aspect ratio carbon nanotube (CNT) terminated silicon probes (Nanosensors, CNT-NCH type) with cantilever spring constants of ca. 42 N/m and resonance frequencies of ca. 330 kHz [42]. Kelvin probe (KPFM) measurements, in which active regulation of the tip-sample bias voltage was included [43], showed negligible effects on the height in topographical images.

Based on eq. 1 computer simulations of the temporal evolution of the PSDs were performed following the procedure of Smet et. al. [44]. For comparison with the TEM data, the radii of curvature, *R*, were converted to the projected diameters, $d = 2R$ for $\theta > \pi/2$. The PSD of the as-prepared Pt/Al_2O_3 sample (fig. 1f) generated from the TEM data was used as the initial PSD. The simulations employed three different particle shapes. First, the particle shape corresponding to the grey dotted line in figure 4d was included by converting the height-to-diameter ratio to values for the contact angle, θ. Secondly, the height-to-diameter ratio was maintained constant (corresponding to the black dashed line in figure 4d) for all particle sizes. Thirdly, a particle shape consisting of a spherical cap with an interface layer between a spherical cap and the oxide support was employed. With this shape model, eq. 1 becomes,

eq. 2
$$\frac{\sin(\theta)\alpha'}{2R^2\left(\frac{1}{2}-\frac{3}{4}\cos(\theta)+\frac{1}{4}\cos^3(\theta)\right)+H\cdot R\sin^2\theta}\left(\frac{R}{R^*}-1\right)$$

where *R* is the radius of curvature, θ the contact angle between the spherical cap and the interface layer, *H* the height of the interface layer, *R** the critical radius of curvature and α' describes the system specific parameters. In the simulations based on eq. 2, the effect of the interface layer was described by $\theta = 0.6\pi$ and $H = 0.7$ nm which corresponds to the best fit to the AFM data (full black line) in fig. 4c. For all simulations, the calculation steps correspond to the time units, $\alpha'^{-1}\cdot nm^3$. Simulations were performed in an iterative way by varying α', until the simulated mean diameter for the last simulation step equaled the observed mean diameter after sintering at 650 °C.

ACKNOWLEDGEMENT

We gratefully acknowledge Bengt Kasemo, Jonas Andersson, Elin Larsson and Laurent Feuz (Chemical Physics Group) as well as Eva Olsson (Microscopy and Microanalysis Group) at Chalmers University of Technology for contributing to sample preparations. We thank the MC2-Access project for financial support. We acknowledge the participation of the CTCI Foundation, Taiwan, in the establishment of the in situ TEM facility at Haldor Topsøe A/S. CINF is funded by The Danish National Research Foundation. JVL, KM and TNJ gratefully acknowledge financial support from the European Research Council (ERC starting grant no. 239834).

REFERENCES

1 Li, Y.; Somorjai, G. A. Nanoscale Advances in Catalysis and Energy Applications. Nanolett. **2010**, *10*, 2289-2295.

2 Nørskov, J. K.; Bligaard, T.; Abild-Pedersen, F.; Chorkendorff, I.; Christensen, C. H. The nature of the active site in heterogeneous metal catalysis. Chem. Soc. Rev. **2008**, *37*, 2163-2171.

3 Jones, G.; Jakobsen, J. G.; Shim, S. S.; Kleis, J.; Andersson, M. P.; Rossmeisl, J.; Abild-Pedersen, F.; Bligaard, T.; Helveg, S.; Hinnemann, B.; Rostrup-Nielsen, J. R.; Chorkendorff, I.; Sehested, J.; Nørskov, J. K. First Principles Calculations and Experimental Insight into Methane Steam Reforming over Transition Metal Catalysts. J. Catal. **2008**, *259*, 147-160.

4 Moulijn, J. A.; Diepen, A. E. v.; Kapteijn, F. Activity Loss. In *Handbook of Heterogeneous*

Catalysis; Ertl, G.; Knözinger, H.; Schüth, F.; Weitkamp, J.; Eds., 2nd Edition., Vol. 4, Wiley-VCH Verlag GmbH & Co KGaA, Weinheim, 2008; pp 1829-1871.

5 Flynn, S. E.; Wanke, P. C. The Sintering of Supported Metal Catalysts. Catal. Rev. Sci. Eng. **1975**, *12*, 93-135.

6 Wynblatt, P.; Gjostein, N. A. Supported metal crystallites. Prog. Solid State Ch. **1976**, *9*, 21-58.

7 Baker, R. T. K.; Bartholomew, C. H.; Dadyburjor, D. B. Sintering and Redispersion: Mechanisms and kinetics. In *Stability of Supported Catalysts: Sintering and Redispersion*; Horsley, J. A.; Ed.; Catalytica Inc: Mountain view, California, 1991; pp 169-225.

8 Bartholomew, C. H. *Catalysis – A Specialist Periodical Report,* volume 10; The Royal Society of Chemistry: Cambridge, 1993; pp 41-82.

9 Nakamura, M.; Yamada, M.; Amano, A. Size Distribution of Platinum Dispersed on Charcoal and Its Effect on the Dehydrogenation of 2,3-Dimethylbutane. J. Catal. **1975**, *39*, 125-133.

10 Granqvist, C. G.; Buhrman, R. A.; Size Distributions for Supported Metal Catalysts. Coalescence Growth versus Ostwald ripening. J. Catal. **1976**, *42*, 477-497.

11 Lee, T. J.; Kim, Y. G. Redispersion of Supported Platinum Catalysts. J. Catal. **1984**, *90*, 279-291.

12 Harris, P. J. F. The Sintering of Platinum Particles in an Alumina-Supported Catalyst: Further Transmission Electron Microscopy Studies. J. Catal. **1986**, *97*, 527-542.

13 Richard, J. M.; Genovese, L.; Moata, A.; Nitsche, S. Redispersion of Platinum on Pt/Al_2O_3 Model Catalyst in Oxygen Studied by Transmission Electron Microscopy. J. Catal. **1990**, *121*, 141-152.

14 Lööf, P.; Stenbom, B.; Nordén, H.; Kasemo, B. Rapid Sintering in NO of Nanometre-Sized Pt Particles on γ-Al_2O_3 Observed by CO Temperature-Programmed Desorption and Transmission Electron Microscopy. J. Catal. **1993**, *144*, 60-76.

15 Fuentes, G. A.; Salinas-Rodríguez, E. Realistic Particle Size Distributions during Sintering by Ostwald Ripening. In *Studies in Surface Science and Catalysis*, volume 139; Spivey, J. J.; Roberts, G. W.; Davis, B. H.; Eds.; Elsevier Science B. V., Amsterdam, 2001; pp 503-510.

16 Sehested, J.; Carlsson, A.; Janssens, T. V. W.; Hansen, P. L.; Datye, A. K. Sintering of Nickel Steam-Reforming Catalysts on $MgAl_2O_4$ Spinel Supports. J. Catal. **2001**, *197*, 200-209.

17 Campbell, C. T.; Parker, S. C.; Starr, D. E. The Effect of Size-Dependent Nanoparticle Energetics on Catalyst Sintering. Science **2002**, *298*, 811-814.

18 Datye, A. K.; Xu, Q.; Kharas, K. C.; McCarty, J. M. Particle size distributions in heterogeneous catalysts: What do they tell us about the sintering mechanism? Catal. Today **2006**, *111*, 59-67.

19 Yang, F; Chen, M. S.; Goodman, D. W. Sintering of Au Particles Supported on TiO_2(110) during CO Oxidation. J. Phys. Chem. C **2009**, *113*, 254-260.

20 Houk, L. R.; Challa, S. R.; Grayson, B.; Fanson, P.; Datye, A. K. The Definition of "Critical Radius" for a Collection of Nanoparticles Undergoing Ostwald Ripening. Langmuir **2009**, *25*, 11225-11227.

21 Simonsen, S. B.; Chorkendorff, I.; Dahl, S.; Skoglundh, M.; Sehested, J.; Helveg, S. Direct Observations of Oxygen-induced Platinum Nanoparticle Ripening Studied by In Situ TEM. J. Am.

Chem. Soc. **2010**, *132*, 7968-7975.

22 Baker, R. T. K.; Thomas, C.; Thomas, R. B. Continuous Observation of the Particle Size Behavior of Platinum on Alumina. J. Catal. **1975**, *38*, 510-513.

23 Arai, M.; Ishikawa, T.; Nakayama, T.; Nishiyama, Y. Effects of Metal-Support Interactions and Temperature on the Sintering of Pt and Ag Particles Supported on Inorganic Solids. J. Colloid Interf. Sci. **1984**, *97*, 254-265.

24 Wang, T.; Lee, C.; Schmidt, L. D. Shape and orientation of supported Pt particles. Surf. Sci. **1985**, *163*, 181-197.

25 Lee, W. H.; Vanloon, K. R.; Petrova, V.; Woodhouse, J. B.; Loxton, C. M.; Masel, R. I. The Equilibrium Shape and Surface Energy Anisotropy of Clean Platinum. J. Catal. **1990**, *126*, 658-671.

26 Hansen, P. L.; Wagner, J. B.; Helveg, S.; Rostrup-Nielsen, J. R.; Clausen, B. S.; Topsøe, H. Atom-Resolved Imaging of Dynamic Shape Changes in Supported Copper Nanocrystals. Science **2002**, *295*, 2053-2055.

27 Kwak, J. H.; Hu, J.; Mei, D.; Yi, C.-W.; Kim, D. H.; Peden, C. H. F.; Allard, L. F.; Szanyi, J. Coordinatively Unsaturated Al^{3+} Centers as Binding Sites for Active Catalyst Phases of Platinum on γ-Al_2O_3. Science **2009**, *325*, 1670-1673.

28 Ruckenstein, E.; Chu, Y. F. Redispersion of Platinum Crystallites Supported on Alumina – Role of Wetting. J. Catal. **1979**, *59*, 109-122.

29 Harris, P. J. F. Growth and Structure of Supported Metal Catalyst Particles. Int. Mater. Rev. **1995**, *40*, 97-115.

30 Lifshitz, I. M.; Slyozov, V. V. The kinetics of precipitation from supersaturated solid solutions. J. Phys. Chem. Solids **1961**, *19*, 35-50.

31 Wagner, C. *Z.* Theorie der alterung von niederschlagen durch umlosen (Ostwald-reifung). Elektrochemie **1961**, *65*, 581-591.

32 Rogers, T. M.; Desai, R. C. Numerical study of late-stage coarsening for off-critical quenches in the Cahn-Hilliard equation of phase separation. Phys. Rev. B **1989**, *39*, 11956-11964.

33 Carlsson, A.; Puig-Molina, A.; Janssens, T. V. W. New Method for Analysis of Nanoparticle Geometry in Supported fcc Metal Catalysts with Scanning Transmission Electron Microscopy. J. Phys. Chem. B **2006**, *110*, 5286-5293.

34 Li, Z. Y.; Young, N. P.; Vece, M. D.; Palomba, S.; Palmer, R. E.; Bleloch, A. L.; Curley, B. C.; Johnston, R. L.; Jiang, J.; Yuan, J. Three-dimensional atomic-scale structure of size-selected gold nanoclusters. Nature **2008**, *451*, 46-48.

35 Finsy, R. On the Critical Radius in Ostwald Ripening. Langmuir **2004**, *20*, 2975-2976.

36 Kwak, J. H.; Hu, J.; Mei, D.; Yi, C.-W.; Kim, D. H.; Peden, C. H. F.; Allard, L. F.; Szanyi, J. Coordinatively Unsaturated Al^{3+} Centers as Binding Sites for Active Catalyst Phases of Platinum on γ-Al_2O_3. Science **200**9, *325*, 1670-1673.

37 Yeadon, M.; Yang, J. C.; Ghaly, M.; Averback, R. S.; Gibson, J. M. Novel interactions of supported clusters: contact epitaxy. Mater. Sci. Eng. B **1999**, *67*, 76-79.

38 Wang, C.-B.; Lin, H.-K.; Hsu, S.-N.; Huang, T.-H.; Chiu, H.-C. Enthalpies of reduction-oxidation

of alumina-supported platinum. J. Mol. Catal. A **2002**, *188*, 201-208.

39 McCabe, R. W.; Wong, C.; Woo, H. S. The Passivating Oxidation of Platinum. J. Catal. **1988**, 114, 354-367.

40 Enevoldsen, G. H.; Foster, A. S.; Christensen, M. C.; Lauritsen, J. V.; Besenbacher, F. Noncontact Atomic Force Microscopy Studies of Vacancies and Hydroxyls of TiO_2(110): Experiments and atomistic simulations. Phys. Rev. B **2007**, *76*, 205415.

41 Gritschneder, S.; Namai, Y.; Iwasawa, Y.; Reichling, M. Structural Features of CeO_2(111) Revealed by Dynamic SFM. Nanotechnology **2005**, *16*, S41-S48.

42 Barwich, V.; Bammerlin, M.; Baratoff, A.; Bennewitz, R.; Guggisberg, M.; Loppacher, C.; Pfeiffer, O.; Meyer, E.; Güntherodt, H.-J.; Salvetat, J.-P.; Bonard, J.-M.; Forró, L. Carbon nanotube tips in non-contact SFM. Appl. Surf. Sci. **2000**, 157, 269-273.

43 Sadewasser, S.; Lux-Steinger, M. C. Correct Height Measurement in Noncontact Atomic Force Microscopy, Phys. Rev. Lett. **2003**, *91*, 266101.

44 Smet, Y. D.; Deriemaeker, L.; Finsy, R. A Simple Computer Simulation of Ostwald Ripening. Langmuir **1997**, *13*, 6884-6888.

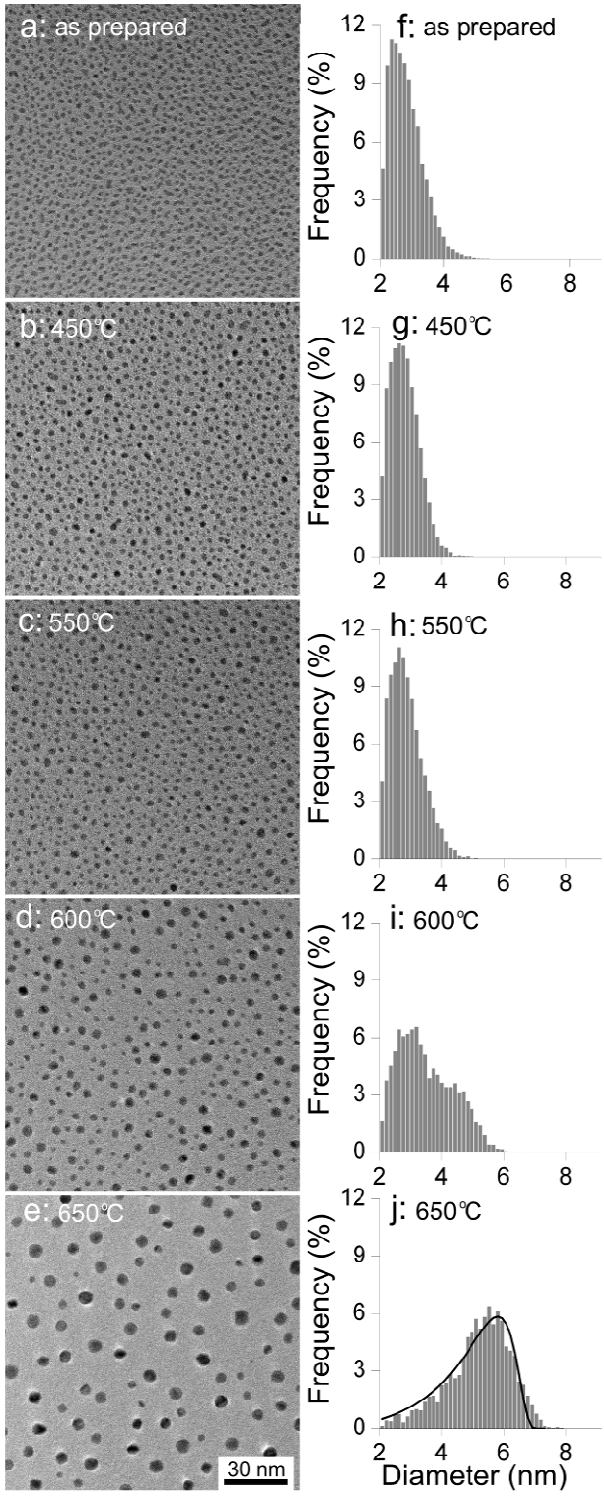

Fig. 1. (a-e) Representative TEM images of the Pt/Al_2O_3 samples after ageing in a tube furnace in 1 bar 0.2 % O_2 in N_2 for 3 hours. The samples were aged at 450 ºC, 550 ºC, 600 ºC, 650 ºC as indicated in the figure. (f-j) Particle size distributions based on measurements from a larger number of TEM images. The number of measured particles are (f) 14243, (g) 11204 (h) 8310, (i) 7606 and (j) 2954. For the ageing temperature 650 °C (j), a two-dimensional LSW distribution function [32] is fitted to the particle size distribution.

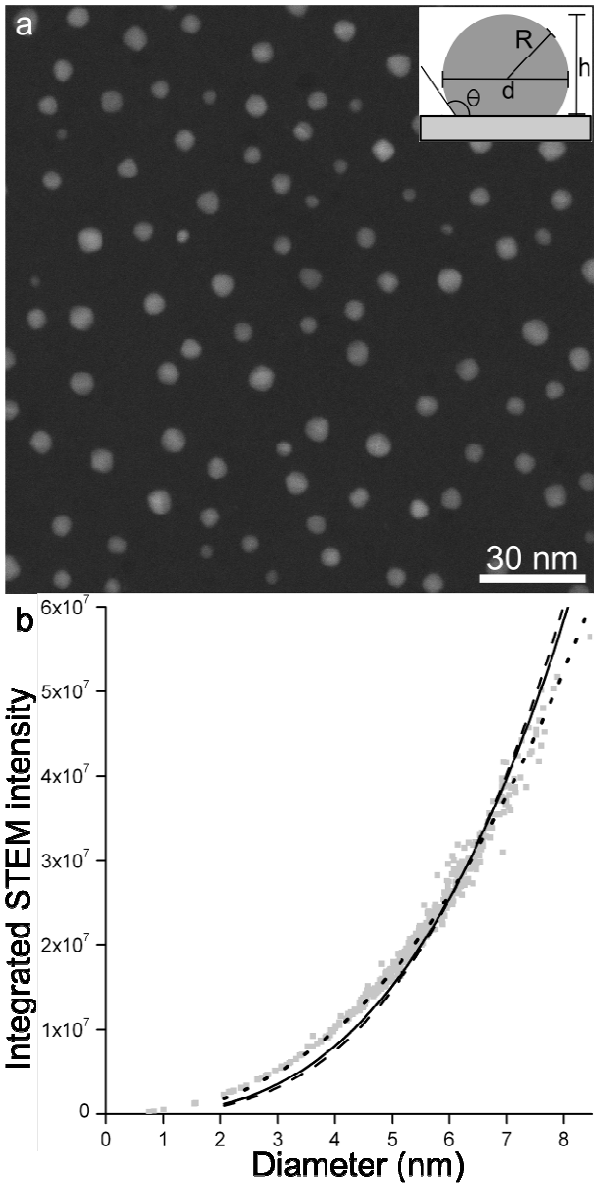

Fig. 2. (a) A representative STEM image of the Pt/Al2O3 sample after ageing in a tube furnace in 1 bar 0.2 % O2 in N2 for 3 hours at 650 °C. The insert illustrates a supported Pt nanoparticle in profile and defines the geometrical parameters: the curvature of radius, R; the particle diameter, d; the particle height, h; and the metal-support contact angle, θ. (b) The STEM signal intensity integrated over the projected area of the particles plotted in arbitrary units against the particle diameter, d (grey dots). The volume of a spherical cap, $V(d) = C \cdot [1/2 - 3/4\cos(\theta) + 1/4\cos3(\theta)] \cdot 1/6\pi d3$ is fitted to the data with R2 = 0.95 (dashed line). Here C is a calibration factor for converting particle volumes to the STEM signal intensities and θ is the metal-oxide contact angle, which is kept constant for all particle sizes. In addition, V(d) is plotted with a size-dependent θ corresponding to the size-dependent height-to-diameter ratio presented in figure 4d resulting in R2 = 0.96 (full line). Finally, V(d) with a size-dependent θ is fitted to the STEM data by assuming a linear relation between the particle height and diameter and that particles for which d = 2 are spherical, resulting in R2 = 0.99 (dotted line). All fits are based on data points corresponding to diameters above 2 nm.

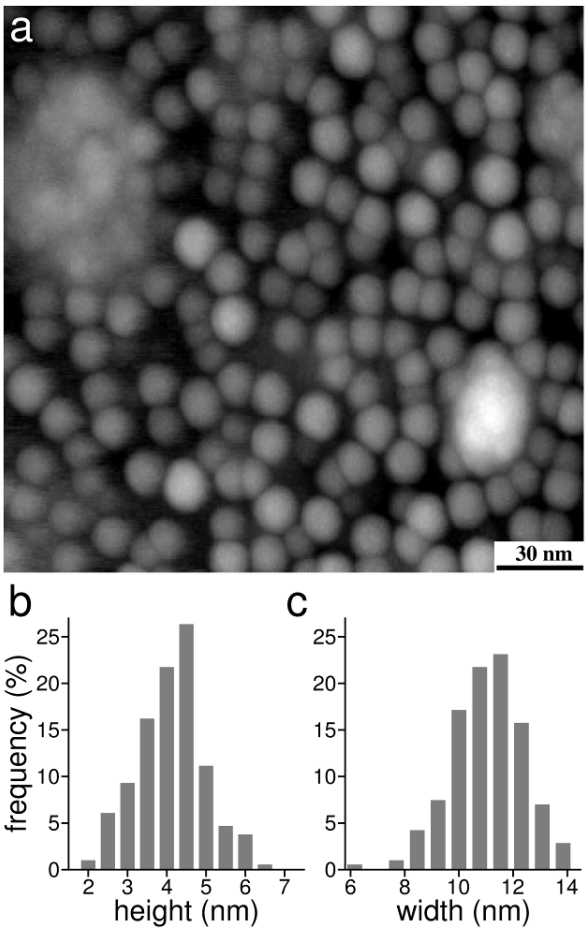

Fig. 3 (a) A representative AFM image of the Pt/Al2O3 sample after ageing in a tube furnace in 1 bar 0.2 % O2 in N2 for 3 hours at 650 °C. (b) Particle height distribution and (c) particle size distribution based on measurements from a number of AFM images. The number of measured particles is 217.

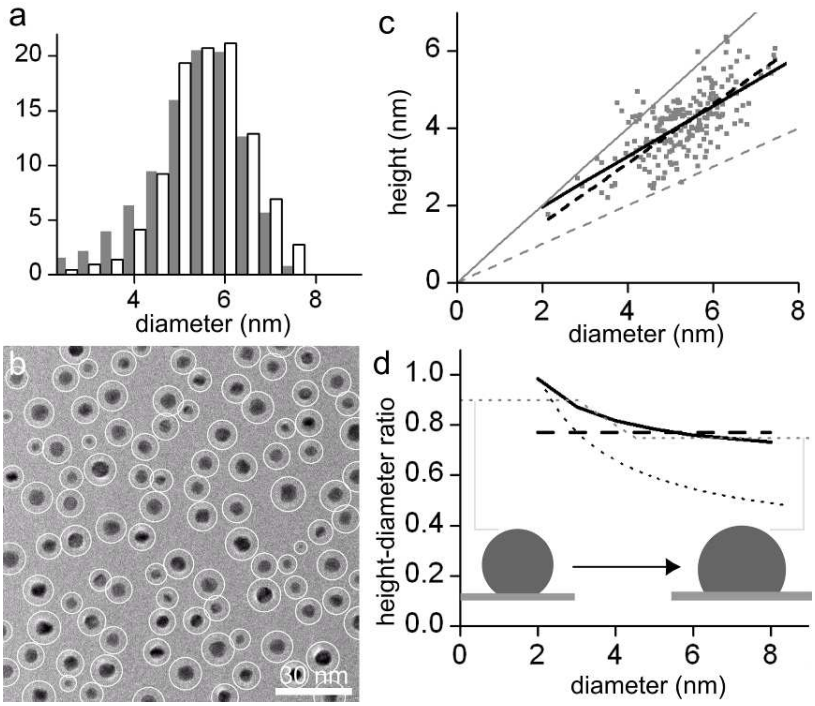

Fig. 4. (a) Particle size distributions from the calibrated AFM measurements (white) and TEM measurements (grey). (b) TEM image of the Pt/Al2O3 sample after ageing at 650 °C. The circles indicate the none-calibrated AFM diameters. (c) The nanoparticle height presented as a function of the calibrated nanoparticle diameter. Two straight lines are fitted to the dataset: One without any constraints (full black) and one constrained to include the origin (dashed black). For comparison, lines corresponding to a spherical (full grey) and a hemispherical (dashed grey) particle shape are indicated. (d) The height-to-diameter ratio is presented as a function of nanoparticle size based on the unconstrained (full black) and the constrained (dashed black) fitted lines in (c). The black dotted line corresponds to the black dotted line in figure 2b and represents the best fit to the STEM data. The height-to-diameter ratio values used in the simulation is indicated (dotted grey) and the nanoparticle shapes corresponding to the highest and lowest values of the height-to-diameter ratio are illustrated.

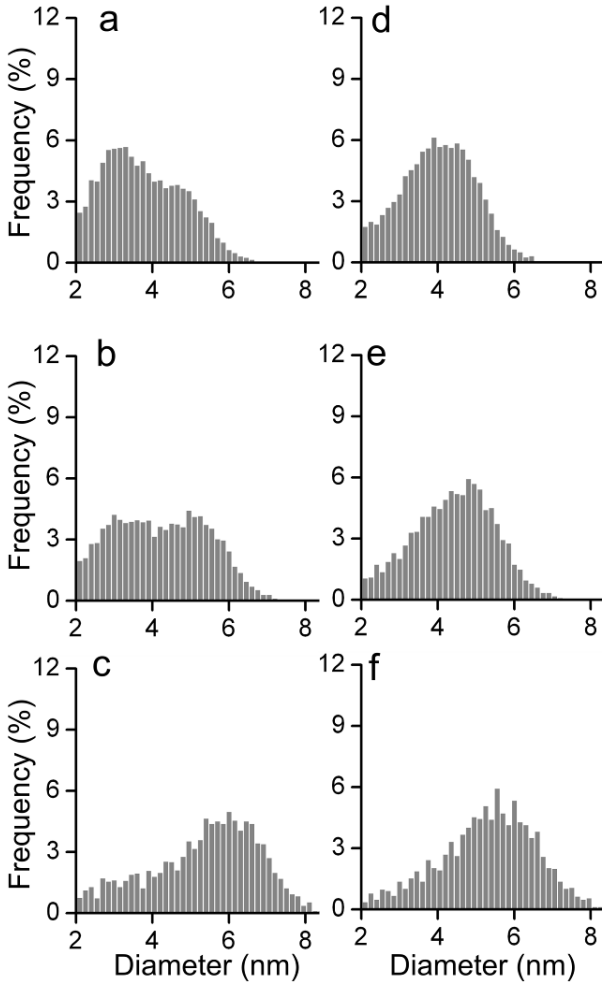

Fig. 5. Simulated particles size distributions based on eq. 1 for particles with a decreasing (a-c) and a constant (d-f) height-to-diameter ratio. The metal-support contact angle, θ (eq. 1) used in the simulations, is calculated from the height-to-diameter ratio indicated by (a-c) the grey dotted or (d-f) the black dashed line in figure 4d. The number of calculation steps for each simulation, corresponding to the sintering time in arbitrary time units, is (a, d) 20, (b, e) 30 and (c, f) 60. The initial distributions are identical to the initial distribution of the Pt/Al2O3 sample (fig. 1f). The number of particles in each distribution is (a) 6651, (b) 5220, (c) 2807, (d) 5439, (e) 4208 and (f) 2570.